Theoretical Investigation of Doped Silicon Nanomaterials Synthesis and Properties

by

Yeseul Choi

A thesis submitted to the Graduate Faculty of
Auburn University
in partial fulfillment of the
requirements for the Degree of
Master of Science

Auburn, Alabama
August 3, 2019

Keywords: DFT, Machine learning, Thermochemistry, Silicon-germanium alloys, Silicon-nitrides, Reactivities

Approved by

Dr. Andrew J. Adamczyk, Chair, Assistant Professor, Department of Chemical Engineering, Auburn University, Auburn, AL, USA
Dr. Mario Eden, Department Chair, Joe T. and Billie Carole McMillan Professor, Department of Chemical Engineering, Auburn University, Auburn, AL, USA
Dr. Xinyu Zhang, Associate Professor, Department of Chemical Engineering, Auburn University, Auburn, AL, USA
Dr. Thomas J. Preston, Staff Scientist, Institute for Energy Technology, Kjeller, Norway

Abstract

With the advent of the fourth industrial revolution and 5G technology era, demand for semiconducting chips is expected to increase explosively. Most semiconductor devices are produced through hundreds of stages of chemical vapor deposition (CVD) method, but the fundamental explanation of the synthesis is still vague. In order to propose a desirable semiconducting material, the first step is considered to understand the properties of molecules, which can be used as a precursor. However, there are limited studies available that predict the properties of silicon alloy hydrides. For this purpose, we conducted a computational study of 46 hydrogenated SiGe clusters and 59 hydrogenated SiN clusters ($Si_xM_yH_z$, M=Ge or N, $1<X+Y\leq6$) to predict the structural, thermochemical, and electronic properties. The optimized geometries of the $Si_xM_yH_z$ clusters were investigated using quantum chemical calculations and statistical thermodynamics.

The SiGe clusters contained 6 to 9 fused Si-Si, Ge-Ge, or Si-Ge bonds, i.e., bonds participating in more than one 3- to 4-membered rings, and different degrees of hydrogenation, i.e., the ratio of hydrogen to Si/Ge atoms varied depending on cluster size and degree of multifunctionality. The 59 hydrogenated SiN nanostructures contained 1 to 9 fused Si-Si or Si-N bonds i.e., bonds participating in acyclic structures or in more than one 3- to 6-membered rings, and different degrees of hydrogenation, the numbers of nitrogen atoms contributed to stability of molecules. Our studies have established trends in standard enthalpy of formation, standard entropy, and constant pressure heat capacity as a function of cluster composition and structure. A novel bond additivity correction model for SiGe chemistry was regressed from experimental data on 7 acyclic Si/Ge/SiGe species to improve the accuracy of the standard enthalpy of formation predictions. Internal rotation correction was employed for acyclic SiN molecules. Electronic properties were investigated by analysis of the HOMO–LUMO energy gap to study the effect of elemental composition on the electronic stability of $Si_xM_yH_z$ clusters. These properties will be discussed in the context of tailored nanomaterials design and generalized using a machine learning approach for $Si_xGe_yH_z$ clusters. The stability of $Si_xN_yH_z$ was explained with natural bond orbital (NBO) analysis.

Acknowledgments

For his technical guidance during my master study at Auburn University, I would like to sincerely thank my advisor, Prof. Andrew J. Adamczyk. I have learned a lot from his hardworking spirit, thoughtful nature and patience. When I had trouble in my academic status or when I had questions about my research, he always steered me in the right direction and supported me. It wouldn’t be possible for me to pursue a study without him.

For their guidance and suggestions during my studies, I would like to thank my Master thesis committee members: Prof. Mario Eden, Prof. Xinyu Zhang, and Dr. Thomas J. Preston. Especially, I am gratefully indebted to Dr. Preston for his valuable comments on my project. I would like to acknowledge Admaczyk group members, Ashraf Ali, Katherin Lawson, Siyuan Wu, and Tanzina Azad, for frequent technical discussions. Also, I would like to thank my friends, classmates and Chemical Engineering department faculty and staff at Auburn including Elaine R. Manning for providing warm-hearted vibe.

I would like to thank my previous advisor, Prof. Jung Kyoo Lee. Without his encouragement and support, it wouldn’t be possible for me to study at Auburn.

I would like to express profound gratitude to my parents and family for providing me with unfailing support and continuous encouragement throughout my master program. This accomplishment would not have been possible without them. Thank you.

Table of Contents

Abstract ii

Acknowledgments iv

List of Tables viii

List of Figures x

List of Abbreviations xii

Chapter 1 Motivation 1

Chapter 2 Background 7

- 2. 1 **Overview of computational chemistry** 7
- 2. 2 **Basic Background** 9
- 2. 3 Structure-Property relationship and the machine learning approach 17
- 2. 4 Natural Bond Orbital (NBO) Analysis 18

Chapter 3 Hydrogenated Si, Ge, and SiGe Nanocluster 19

- 3. 1 Introduction 19
- 3. 2 Computational method 24
- 3. 3 Structures and Vibrational Frequencies 34

3. 4 Thermochemical Properties 43

3. 5 Electronic Properties and Chemical Stability 52

3. 6 Generalization of Electronic properties using a machine learning approach 62

Chapter 4 Hydrogenated Si and SiN Nanoclusters 68

4. 1 Introduction 68

4. 2 Computational method 82

4. 3 Structures and Vibrational Frequencies 62

4. 4 Thermochemical Properties 88

4. 5 Electronic Properties and Chemical Stability 98

4. 6 Natural Bond Orbitals (NBO) analysis 106

Chapter 5 Summary of Conclusion 107

5. 1 Si, Ge and SiGe nanoclusters 107

5. 2 Si and SiN nanoclusters 109

References 111

Appendix A1. Calculated standard entropies and constant pressure heat capacities at elevated temperatures using the G3//B3LYP method for all hydrogenated Si, Ge, and SiGe clusters and acyclic species 118

Appendix A2. Calculated contour surfaces of frontier molecular orbitals (HOMO, LUMO) for all Hydrogenated Si and SiGe clusters using the G3//B3LYP level of theory 122

Appendix. B.1. Calculated standard entropies and constant pressure heat capacities at elevated temperatures using the G3//B3LYP method for all hydrogenated Si and SiN clusters and acyclic species 126

Appendix B2. Thermodynamic properties with internal rotation correction 130

Appendix B3. Calculated contour surfaces of frontier molecular orbitals (HOMO, LUMO) for all Hydrogenated Si and SiN clusters using the G3//B3LYP level of theory. 133

List of Tables

Table 3.1 Calculated singlet-triplet splitting values of selected Si, Ge, and SiGe species using the G3//B3LYP level of theory 27

Table 3.2 Comparison of calculated standard enthalpy of formation, standard entropy, and constant pressure heat capacity at 298 K to available experimental data 33

Table 3.3 Comparison of experimental vibrational modes for SiH_4, Si_2H_6, GeH_4, and Ge_2H_6 to unscaled harmonic vibrational modes. 41

Table 3.4 Comparison of calculated thermodynamic properties of hydrogenated Si, Ge, and SiGe clusters using the G3//B3LYP method with and without the bond-additivity corrections 45

Table 3.5 Summary of regressed parameters for the Bond Additivity Correction (BAC) 47

Table 3.6 Calculated quantum chemical molecular descriptors for hardness (η), chemical potential (μ), and softness (σ) 59

Table 3.7 Regression analysis results 65

Table 4.1 Calculated Singlet-Triplet Splitting Values of Selected Si and SiN Species Using the G3//B3LYP Level of Theory 75

Table 4.2 Comparison of Calculated Standard Enthalpy of Formation, Standard Entropy, and Constant Pressure Heat Capacity at 298 K to Available Experimental Data for Small Acyclic Hydrogenated Silicon and Nitrogen Species 79

Table 4.3 Comparison of Experimental Vibrational Modes for NH_3 and SiN_3NH_2 to Unscaled Harmonic Vibrational Modes 87

Table 4.4 Comparison of Calculated Thermodynamic Properties of Hydrogenated Si and SiN Clusters Using the G3//B3LYP Method with Calctherm modification 90

Table 4.5 Calculated Quantum Chemical Molecular Descriptors for Hardness (η), Chemical Potential (μ), and Softness (σ)... 103

List of Figures

Figure 3.1 Optimized $Si_xGe_yH_z$ $(x+y=6)$ cluster geometries.................... 26

Figure 3.2 Parity plots of standard enthalpy of formation for the 46 hydrogenated Si, Ge, and SiGe clusters in this study:.................... 48

Figure 3.3 (a) Standard entropies and (b) constant pressure heat capacities of all hydrogenated Si, Ge, and SiGe clusters 50

Figure 3.4 Comparison of calculated HOMO-LUMO energy gaps for pure silicon and germanium clusters.................... 54

Figure 3.5 Comparison of calculated HOMO-LUMO energy gaps for all hydrogenated Si, SiGe, and Ge clusters 55

Figure 3.6 Comparison of calculated contour surfaces of frontier molecular orbitals (HOMO, LUMO) for the TBP-1 cluster.................... 57

Figure 3.7 Representative energy level diagrams of two optoelectronic processes determined by singlet-triplet splitting ($\Delta E'_{ST}$) between energies of the lowest singlet (E_{S1}) and triplet (E_{T1}) excited states. 61

Figure 3.8 Contour map of the calculated fractional electrons transferred in eV (ΔN) for molecular interactions of all 53 molecules in this study. 63

Figure 3.9 Parity plot of fractional electrons transferred for the training set of 2809 molecular interactions 66

Figure 4.1 Optimized $Si_xN_yH_z$ (x + y = 6) cluster geometries 74

Figure 4.2 Heat of formation of (a) acyclic silicon nitride hydrides and (b) hydrogenated silicon nitride clusters in this study 92

Figure 4.3 Standard entropies of (a) acyclic silicon nitride hydrides and (b) hydrogenated silicon nitride clusters 93

Figure 4.4 Constant pressure heat capacities of (a) acyclic silicon nitride hydrides and (b) hydrogenated silicon nitride clusters 95

Figure 4.5 Comparison of calculated HOMO−LUMO energy gaps for all hydrogenated Si and SiN clusters... 100

Figure 4.6 Contour map of the calculated fractional electrons transferred in eV (ΔN) for molecular interactions of all 59 molecules.. 105

List of Abbreviations

AO	atomic orbitals
BAC	bond additivity correction
BD	bonding
CC	coupled cluster theory
CMOS	complementary metal-oxide semiconductor
CR	core
CVD	chemical vapor deposition
DFT	density functional theory
E_{el}	electronic energies
HN	hexagonal planar (SiN)
HOMO	highest occupied molecular orbital
ICT	intramolecular charge transfers
IoT	Internet of things
KS-DFT	Kohn-Sham density functional theory
LED	light-emitting diodes
LP	Lone pair
LUMO	lowest unoccupied molecular orbital
MO	molecular orbital
MOSFETs	metal oxide semiconductor field effect transistor
MP	Møller–Plesset perturbation theory
MP2	Møller–Plesset second order perturbation

NBO	Natural bond orbital
NLS	natural Lewis structure
NMOS	n-channel metal-oxide semiconductor
PES	potential energy surface
PN	pentagonal planar (SiN)
Pri	prismane geometries (SiGe)
PriN	prismane geometries (SiN)
RAM	random access memory
RY	Rydberg
SCF	self-consistent field
SEM	Scanning Electron Microscopy
Si:C S/D	silicon–carbon source/drain stressors
SiGe HBT	silicon-germanium heterojunction bipolar transistor
SN	square planar (SiN)
ST	substituted trigonal planar (SiGe)
STN	substituted trigonal planar (SiN)
STS	strain-transfer structure
T	trigonal planar (SiGe)
TBP	trigonal bipyramidal geometries (SiGe)
TBPyN	trigonal bipyramidal geometries (SiN)
TEM	Transmission electron microscopy
TN	trigonal planar (SiN)
TP	trigonal pyramidal (SiGe)
TPyN	trigonal pyramid (SiN)
ZPE	zero-point vibrational energy

Chapter 1: Motivation

Semiconductors, which are the most important components in electronic devices such as smart phones, computers, and tablets that are indispensable in our everyday life, are electronic device components with functions of amplification, rectification and switching of electrical signals. With the advent of the 5G technology era, demand for semiconducting chips for communication is increasing. Demand for semiconductor devices is expected to increase explosively due to the development of autonomous vehicles and advent of the internet of things (IoT) era. In addition, due to the development of information and communication technology that will lead the fourth industrial revolution, mobile devices and large servers generate vast amounts of data. The technology for mobile internet, big data, and artificial intelligence is developing as well. The fourth industrial revolution which brings hyper-connected and super intelligent society will be realized by the further development of semiconductor materials.

Semiconductors are classified by functions. There are memory semiconductors, system semiconductors and special semiconductors such as discrete devices or optical devices. As examples of different functions of semiconductor, there are random access memory (RAM), transistors, light-emitting diode (LED), and solar cells respectively.

H. W. Brattain, J. Bardeen, and W. Shockely in Bell Laboratories made the first semiconductor with germanium in 1947, but silicon has replaced for main semiconducting material with thermal stability at high temperature. After the metal oxide semiconductor field effect transistor (MOSFETs) were developed using silicon and silicon oxides in the 1960s, the size of transistors has been reduced by the results that the number of transistor per chip area has been successfully integrated by about two times every two years. At present, it has been minimized to the size of less than 10 nm scale[1, 2], but the technique of lowering the driving voltage has not been developed relatively compared to the integration techniques. As an example of a few nanoscale sizes of SiGe material, author Pi and coworkers synthesized 3nm diameter size of SiGe crystals (Figure 1.1). The fundamental reason why information and communication devices and services consume enormous amounts of energy and power is because MOSFETs consume considerable power. Replacing silicon-germanium heterojunction bipolar transistor (SiGe HBT) with complementary metal-oxide semiconductor (CMOS) enabled to achieve higher performance. K-W Ang et al.[3] demonstrated n-channel metal-oxide semiconductor (NMOS) transistor with SiGe heterostructure embedded beneath the channel and silicon-carbon source/drain (Si:C S/D) stressors. The additional strain effect by SiGe structure from the S/D stressors to Si channel enabled improvement of 40% in drive current compared to unstrained control devices. Figure 1.2 (a) is the cross-sectional transmission electron microscopy (TEM) image of a completed strained transistor with Si:C S/D stressors and embedded SiGe region as an strain-transfer structure (STS). Figure 1.2 (b) is the electron dispersion spectroscopy (EDS) measurement results which shows no Ge out-diffusion to gate dielectric interface due to optimized strained-Si channel thickness.

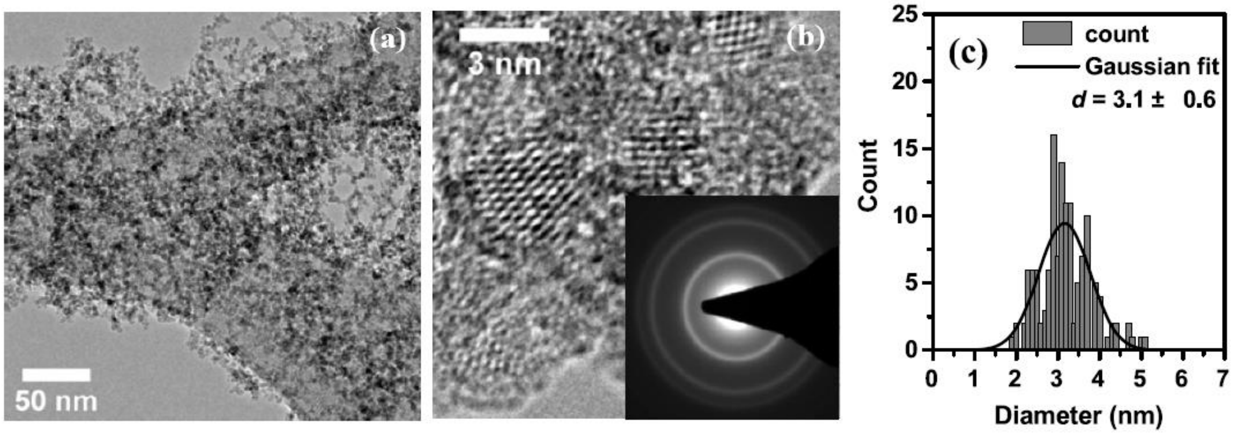

Figure 1.1. $Si_{0.45}Ge_{0.55}$ alloy nanocrystals on a lacy-carbon grid examined by (a) low-resolution and (b) high-resolution TEM. A selected area electron diffraction pattern is shown as the inset of (b). The (c) size distribution is Gaussian with a mean size of 3.1 nm and a standard deviation of 0.6 nm.[2]

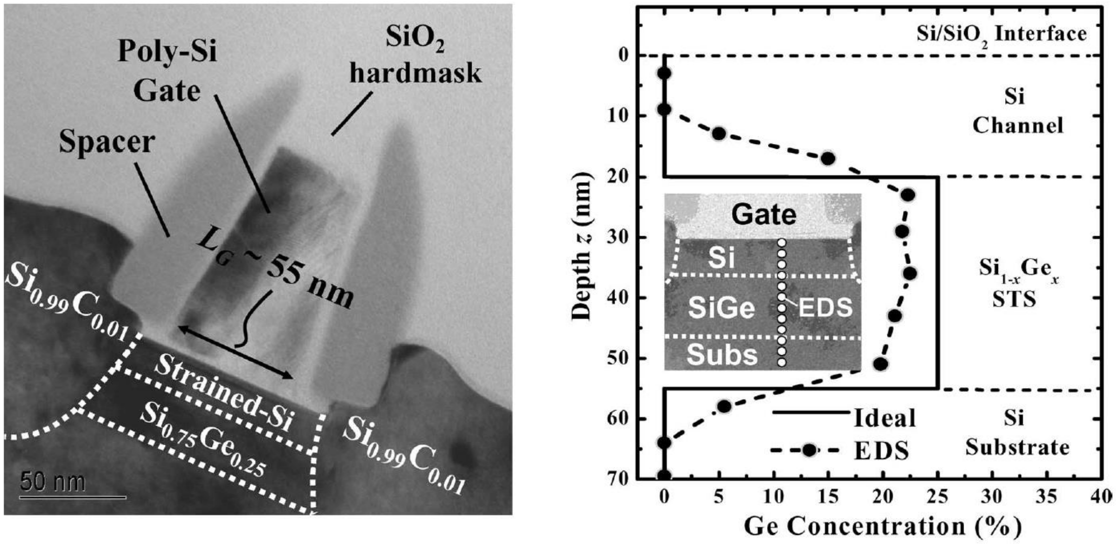

(a)

(b)

Figure 1.2 (a) Transmission electron microscopy (TEM) image of a strained n-MOSFET with silicon-germanium strain-transfer structure (SiGe STS) and silicon–carbon source/drain (Si:C S/D) stressors. No misfit dislocations were observed at the vertical heterojunction between the Si:C S/D and the embedded SiGe STS, indicating a pseudomorphic epitaxy growth. (b) Ge concentration profile as a function of depth obtained using electron dispersion spectroscopy (EDS) measurements. A well-controlled thermal budget and an optimum choice of strained-Si channel thickness prevent Ge out-diffusion to the Si/SiO$_2$ interface, which is important for the achievement of good gate dielectric quality and high electron mobility.[3]

For the Silicon-nitride materials, it has been widely used for the electronic devices such as oxidation masks, passivation layers, gate insulating layers, dielectric layers and antireflection coatings with a wide band-gap (5.3 eV). Silicon nitride is mostly used for inactive materials,[4-7] however, several groups have reported potential of silicon nitride for anode material of lithium ion battery.[8, 9] Ulvestada et al.[10, 11] suggested silicon nitride conversion reaction with lithium ion and demonstrated electrochemical performance of a-SiN_x thin films with compositions ranging from pure Si to $SiN_{0.89}$. The optical and scanning electron microscopy (SEM) images of $SiN_{0.89}$ thin films by Ulvestada were represented in Figure 1.3.

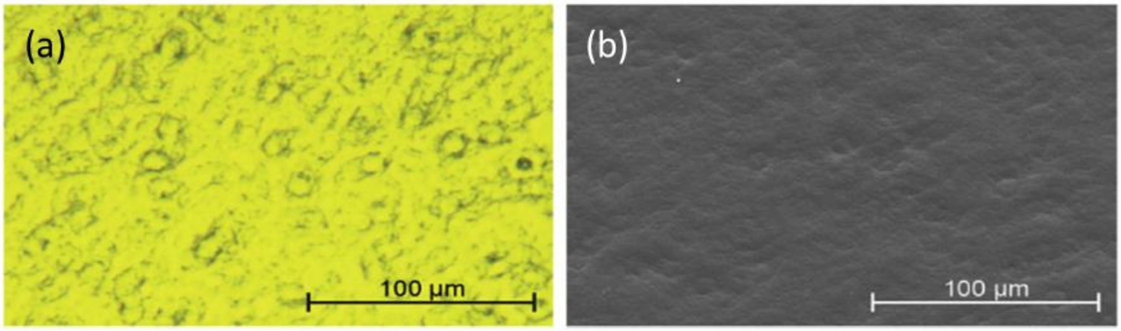

Figure. 1.3. Plane view optical (a) and SEM (b) micrographs of the 156 nm $SiN_{0.89}$ film. The structure of the surface is related to the structure of the rolled copper substrate.

In order to produce more efficient semiconductors, there have been conducted numerous research, but understanding fundamental mechanism of semiconducting material formation is still deficient. The chemical vapor deposition (CVD) method has been widely used for the synthesis of semiconducting materials by the pyrolysis[12] or non-thermal plasma from precursor gases[2]. Understanding nucleation reaction, which occurs during pyrolysis, is important to produce semiconducting materials with desirable properties. Undesired defects can arise in semiconductor processing because these nanoclusters deposit on the growing substrate as illustrated in Figure 1. 4.

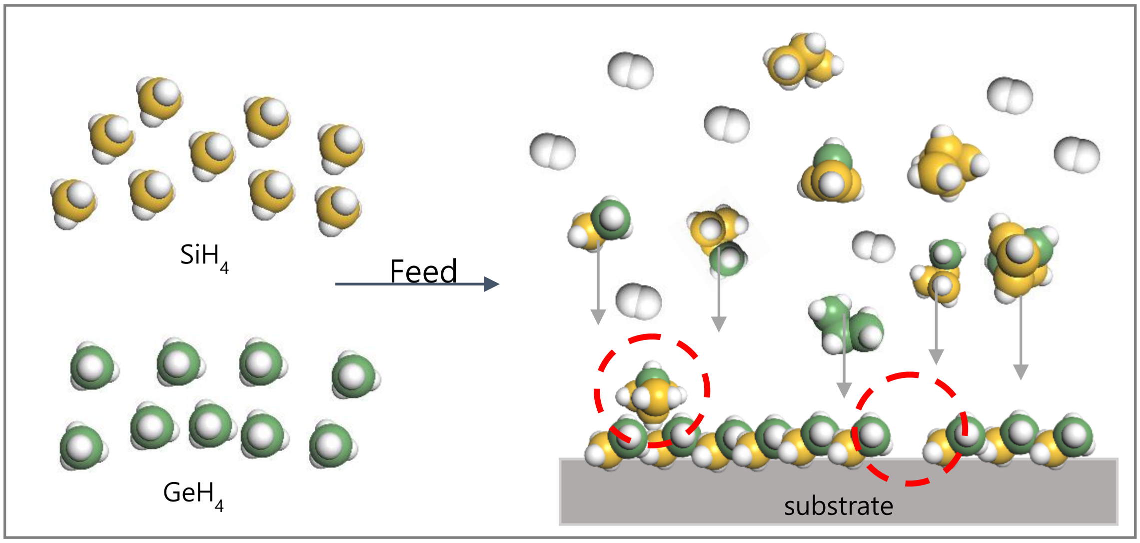

Figure 1.4. Graphic illustration of defect arise during CVD process.

The first step of understanding nucleation mechanism begins figuring the thermodynamic and electrical properties of nanoclusters. Using calculated thermodynamic properties of materials, we can postulate a kinetic mechanism or kinetic pathway and estimate the reaction rate of the reactant in the system. From that information, we would expect to design more sophisticated semiconductor and simplify the semiconductor manufacturing process. For this purpose, we have strong motivation to predict the thermodynamic and electrical properties of Ge or N-doped silicon clusters.

Chapter 2 Background

2.1 Overview of computational chemistry [13-15]

Computational chemistry is a field of theoretical chemistry that solves chemical problems using computer simulations. Since Heitler and London first performed theoretical calculations in 1927, they developed into practical applications as computer technology developed in the 1940s. In 1956, MIT first performed computations using the *ab initio* Hartree-Fock method. In 1964, empirical calculations were performed according to the Hückel method. Various computer programs in computational chemistry have been developed since the 1970s. In 1998, the Nobel Prize for Chemistry was awarded to Kohn[16] and Pople[17], who developed computational methods in density functional theory (DFT) and quantum chemistry, because the field of computational chemistry was established as a discipline. In 2013, Karplus,[18] Levitt[19], and Warshel[20] were awarded the Nobel Prize for developing multiscale models for complex chemical systems.

We can build molecular geometries and calculate energies of the molecules and transition states intermediate molecules. From the energy information, we also are able to predict reactivities of the molecules, spectra, interaction between the molecules and physical properties of molecules. As the tools of computational chemistry, there are mainly four classes: molecular mechanics, *ab initio* methods, semiempirical calculations, and density functional calculation.

Molecular mechanics, which is based on a model of a molecule as a collection of balls (atoms), held together by springs (bonds) compute the potential energy surface for a molecule using classical physics. Since it requires less of computer power than quantum mechanical methods, it is useful for large molecules such as proteins. However, it is not applicable for electronic properties and it restricted by parameters of equation depends on a force-field for different types of atoms or systems. Molecular dynamics calculations depicts physical movements of atoms and molecules with the laws of motion from classical physics.

Ab initio methods are based on the Schrödinger equation which describes how the electrons in a molecule behave. The *ab initio* method solves the Schrodinger equation for a molecule and gives us an energy and wavefunction. The wavefunction is a mathematical function that can be used to calculate the electron distribution. Using *ab initio* the Schrödinger equation is solved for only hydrogen, which has one electron. It is impossible to calculate the repulsive force when there are two or more electrons. In order to calculate electronic energy of any molecule which has more than two electrons, instantaneous coulombic electron-electron repulsion is not taken into account, only average effect (mean field) is included in the calculation. As the simplest type of *ab initio* calculation is the Hartree-Fock method, many types of calculations begin with a Hartree-Fock calculation and subsequently corrected for electron-electron repulsion. Moller-Plesset perturbation theory (MPn) and coupled cluster theory (CC) are examples of post-Hartree-Fock methods.

Adding approximations to reduce the numbers of parameters and using available experimental values are able to predict results with economical time. This is called the semiempirical calculations, it is mixing of theory and experiment values. Common semi-empirical methods for electronic structure prediction are the AM1[21], PM3[22], PM6[23], methods.

Density Functional Theory (DFT) are also based on the Schrödinger equation, but DFT dose not calculate a wavefunction, but rather drives the electron distribution which means electron density. DFT is relatively new methodology, but it became more popular than *ab initio* and semiempirical method due to its temporal economics and relatively accurate calculations compared to both of them. [13-15]

2.2 Basic Background

Classical mechanics which is known as Newtonian mechanics, describes the motion of macroscopic objects such as spacecraft, planets, stars, and galaxies. In classic mechanics, events are continuous and deterministic which means, if the present state of an object is known, it is possible to predict how it will move forward by the laws of classical mechanics and how it has moved in the past. However, the classical mechanics cannot be applied to extremely small particles moving at very high speed; in this case quantum mechanics is necessary.

Quantum mechanics describes nature at the smallest scales of energy levels of atom and subatomic particles. What quantum mechanics differs from classical mechanics is quantized properties which are energy, momentum, angular momentum and other quantities of a bound system. All object have characteristics of both particles and waves, wave-particle duality. By the uncertainty principle, there are limits to the precision with which quantities can be measured; the more precisely an electron's position is known, the less precisely its speed can be known, and vice versa. In quantum mechanics, events are unpredictable but the wave function provides information about the probability.

All matter in the universe is comprised of atoms. The atom consists of elemental particles some of which are charged or neutral. These particles interact with each other, there are only four conservative force; weak interaction which governs the decay of beta particles, strong interaction that is responsible for binding nuclei together, gravitational interaction which is (always small) attraction between objects with mass and electromagnetic interaction that occurs between all charged particle due to their charges. At the atomic and molecular scale, only electromagnetic interaction is significant, this is because the mass of proton and electron is much smaller compared to their charges. Hence, it is important to consider electromagnetic interaction between nuclei and electrons because this interaction is the cause of all the chemical phenomena.

The electromagnetic interaction between particles can be described in terms of either a force (F) or a potential (U). These are equivalent, as the force is the derivative of the potential with respect to the position r. [15]

$$F(r) = -\frac{\partial U}{\partial r} \qquad \text{(eq 2.1)}$$

$$U_{elec}(r_{ij}) = C_{elec}\frac{q_i q_j}{r_{ij}} \qquad \text{(eq 2.2)}$$

In other words, under the influence of a constant force, a particle which mass is m, moves in a direction with instant speed v. At this point, the Kinetic energy is $\frac{1}{2}mv^2$. Total energy(ε) which is the sum of kinetic and potential energy(U) is conserved, according to the law of conservation of energy. If the total energy is constant in time, then $\frac{d\varepsilon}{dt} = 0$.

$$\varepsilon = \frac{1}{2}mv^2 + U \qquad \text{(eq 2.3)}$$

Differentiation of Equation (eq3) with respect to time gives

$$\frac{d\varepsilon}{dt} = mv\frac{dv}{dt} + \frac{dU}{dt} \qquad \text{(eq 2.4)}$$

And by the chain rule

$$\frac{d\varepsilon}{dt} = mv\frac{dv}{dt} + \frac{dU}{dx}\frac{dx}{dt} \qquad \text{(eq 2.5)}$$

If the energy ε is constant, then its first differential with respect to time is zero, and v is just dx/dt. Likewise, dv/dt is the acceleration and so

$$0 = \left(m\frac{d^2x}{dt^2} + \frac{dU}{dx}\right)\frac{dx}{dt} \qquad \text{(eq 2.6)}$$

Since the speed is not zero, the terms in parenthesis should be zero to make eq 2.6 is true. According to Newton's second law of motion, mass times acceleration is force, and so

$$F = -\frac{dU}{dx} \qquad \text{(eq 2.7)}$$

Which gives us the relation between force and mutual potential energy. When the particle moves in three dimensions, the force and potential energy will look like below.

$F = -\mathbf{grad}\ U$, where the grad U is $\mathbf{grad}\ U = \frac{\partial U}{\partial x} e_x + \frac{\partial U}{\partial y} e_y + \frac{\partial U}{\partial z} e_z$ and the gradient of U is given Cartesian coordinates. [24]

When considering the potential energy of a molecule, the electromagnetic interaction is not only a factor, but also electric multipoles, electrostatic potential, polarization, many-body forces among each particles are factors, which should be considered all together. Mechanics is traditionally the study of the behavior of moving objects under the certain action of force. Molecules made of nuclei and electrons are understood fundamentally, with the motion of nuclei and electrons under the influence of the electromagnetic force exerted by their charges. In quantum mechanics, wavefunction that describes the state of particles(nuclei and electrons) can be derived using the Schrödinger equation. The Schrödinger equation of the general form is,

$$H\Psi = E\Psi \qquad \text{(eq 2.8)}$$

where H is Hamiltonian operator, Ψ is wave function.

The wave function obtained by solving the Schrodinger equation can be expressed as $\Psi(\vec{r}, t)$, which depends on time and space. However, we only take account into the time independent non-relativistic Schrödinger equation here. Solving the Schrodinger equation for a molecule gives us better understanding of the behavior of particles (mainly electrons) in molecules, and thus of the structures and reactivity of molecules.

Hamiltonian represents to the total energy of the target system. When the Hamiltonian expressed in a mathematical form, it becomes a Schrödinger equation which is expressed in the form of a second-order differential equation. By solving this equation, we are able to obtain the energy level, the wave function, and the electron density of the electrons. The typical form of the Hamiltonian operator takes into account five contributions to the total energy of a molecular system: the kinetic energies of the electrons and nuclei, the attraction of the electrons to the nuclei, and the interelectronic and internuclear repulsions.

So, denoting the Hamiltonian operator into mathematical form,

$$H = -\sum_{i} \frac{\hbar^2}{2m_{\mathrm{e}}} \nabla_i^2 - \sum_{k} \frac{\hbar^2}{2m_k} \nabla_k^2 - \sum_{i} \sum_{k} \frac{e^2 Z_k}{r_{ik}} + \sum_{i<j} \frac{e^2}{r_{ij}} + \sum_{k<l} \frac{e^2 Z_k Z_l}{r_{kl}} \qquad \text{(eq 2.9)}$$

where i

and j are electrons, k and l are nuclei, ħ is Planck's constant divided by 2π, m_e is the mass of electron, m_k is the mass of nucleus k, ∇^2 is the Laplacian operator, e is the charge on the electron, Z is an atomic number, and r_{ab} is the distance between particles a and b. Note that Ψ is a function of 3n coordinates where n is the total number of particles (nuclei and electrons), e.g., the x, y, z Cartesian coordinates specific to each particle. If we work in Cartesian coordinates, the Laplacian has the form

$$\nabla_i^2 = \frac{\partial^2}{\partial x_i^2} + \frac{\partial^2}{\partial y_i^2} + \frac{\partial^2}{\partial z_i^2} \qquad \text{(eq 2.10)}$$

In fact, accurate wave functions for a molecule that has more particles than hydrogen does are extremely difficult to express because of the correlated motions of particles. In order to simplify this problem, we are requested to employ the Born–Oppenheimer approximation.[25] The Born–Oppenheimer approximation is the assumption that the electronic motion and the nuclear motion in molecules can be separated, because the time scale which the electrons reach equilibrium on is short comparted to the time scale on which the nuclei move. The nuclei of molecular systems are moving much slower than the electrons due to their mass (nuclei are about 1800 times more massive than electrons are). The approximation separates the states into independent states for nuclei Ψ_n and electrons Ψ_e, with energies E_n and E_e. The Hamilitonian is split into corresponding terms, H_n and H_e. The interaction energy between nuclei and electrons is placed in the electronic part. The result is

$$\Psi = \Psi_n \Psi_e\,, \quad \mathrm{H} = \mathrm{H}_n + \mathrm{H}_e \qquad \text{(eq 2.11)}$$

$$H_n \Psi_n = \mathrm{E}_n \Psi_n \qquad \text{(eq 2.12)}$$

$$H_e \Psi_e = \mathrm{E}_e \Psi_e \qquad \text{(eq 2.13)}$$

$$H_e = T + U + V = F + V \qquad \text{(eq 2.14)}$$

As such, it is convenient to separate electrons and nuclei motions and compute electronic energies for fixed nuclear positions. That is, the nuclear kinetic energy term is taken to be independent of the electrons, correlation in the attractive electron–nuclear potential energy term is eliminated, and the repulsive nuclear–nuclear potential energy term becomes a simply evaluated constant for a given geometry.

$$H_{el} = -\sum_i \frac{\hbar^2}{2m_e}\nabla_i^2 - \sum_i \sum_k \frac{e^2 Z_k}{r_{ik}} + \sum_{i<j} \frac{e^2}{r_{ij}}$$

(eq 2.15)

$$(H_{\text{el}} + V_N)\Psi_{\text{el}} = E_{\text{el}}\Psi_{\text{el}}$$

(eq 2.16)

Here the subscript ‘el’ emphasizes the invocation of the Born–Oppenheimer approximation and H_{el} includes only electron-related terms from eq9, V_N is the nuclear–nuclear repulsion energy. The eigenvalue of the electronic Schrodinger equation is called the ‘electronic energy’. Note that the term V_N is a constant for a given set of fixed nuclear coordinates. Wave functions are invariant to the appearance of constant terms in the Hamiltonian, so in practice one almost always solves eq12 without the inclusion of V_N, in which case the eigenvalue is sometimes called the ‘pure electronic energy’, and one then adds V_N to this eigenvalue to obtain E_{el}. Introducing the Born-Oppenheimer approximation is one of the cornerstones in Computational Chemistry, this is because (1) it makes the concept of molecular shape (geometry) meaningful, (2) it makes possible the concept of a potential energy surface(PES), and (3) it simplifies the application of the Schrodinger equation to molecules by allowing us to focus on the electronic energy and then add the nuclear repulsion energy later. Without the Born–Oppenheimer approximation, we would lack the concepts of equilibrium and transition state geometries, which are significant in terms of chemical reaction phenomena, since these are defined as critical points on the PES.

This Schrodinger equation was greatly simplified considering only electrons, but it was difficult to solve in Hamiltonian, especially because the interaction between electrons still had to deal with a large number of electrons. One way to solve this problem is solving the Schrodinger equation which Hamiltonian assumes all electrons or particles move independently without interacting each others. This is called one electron approximation, and the methods which uses this approximation are Hartree approximation, Hartree-Fock approximation and DFT.

The Hartree approximation[26] and the Hartree-Fock approximation are approximations based on the assumption that each electron has independent motion and is only influenced by the average charge density exerted by the other electrons. The Hartree-Fock approximation has been used mainly for small molecules, and the DFT has been used for quantum computation for solids. DFT is the theory that the total energy of a system with many electrons is obtained by knowing the electron density in the space without finding all the wave functions of the electrons, and it was proposed by Walter Kohn with Hohenberg in 1964[27]. The first Hohenberg–Kohn theorems demonstrates that the ground state properties of a many-electron system are uniquely determined by an electron density that depends on only three spatial coordinates. The second Hohenberg–Kohn theorems defines an energy functional for the system and proves that the correct ground state electron density minimizes this energy functional. From this idea, the Schrödinger equation based on more specific electron density function was proposed by Kohn-Sham equation in 1965.[16] By Kohn-sham theorem, the intractable many-body problem of interacting electrons in a static external potential is reduced to a tractable problem of non-interacting electrons moving in an effective potential. A stationary electronic state is then described by a wavefunction satisfying the many-electron time-independent Schrödinger equation,

$$H\Psi = E\Psi \quad ,$$

$$\boldsymbol{H} = -\frac{\hbar^2}{2m}\nabla^2 + \boldsymbol{V}_{ext}(\boldsymbol{x}) + \boldsymbol{V}_{H}(\boldsymbol{x}) + \boldsymbol{V}_{xc}(\boldsymbol{x})$$

$$V_s = V_{ext}(x) + V_H(x) + V_{xc}(x)$$

(eq 2.17)

where the V_H term denotes the Hartree term describing the electron–electron coulomb repulsion, while the last term V_{xc} is called the exchange–correlation potential. Here, V_{xc} includes all the many-particle interactions. Since the Hartree term V_H and V_{xc} depend on the density of the original many-body system, which depends on the orbitals φ_i, which in turn depend on the effective single-particle potential, V_s, the problem of solving the Kohn–Sham equation has to be done in a self-consistent way. Usually one starts with an initial guess for electron density, then calculates the corresponding Vs and solves the Kohn–Sham equations for the φi. From these one calculates a new density and starts again. This procedure is then repeated until convergence is reached.

DFT method expresses the total energy function (Hamiltonian) of the system consisting of many electrons in terms of electron density of the system which assumed to be composed of virtual particles that do not interact with each other. Unlike the Hartree-Fock method, DFT does not find the wave function of the Schrödinger equation. The electron density for the ground electronic state at an arbitrary space $(\vec{r})$ is obtained from the solution of this Kohn-Sham equation. With the accurate electron density prediction of molecule which contribute to calculate other physical properties, DFT has become one of the most popular computational methods.[28]

2.3 Structure-Property relationship and the machine learning approach

Structure of a molecule determines its chemical and physical properties. The molecular formula e.g. Si_2H_6, tells us which elements are present and in what ration in the molecule. We can estimate relative overall size and steric properties from the structure geometry as well. Functional groups in the molecule indicated electrostatic properties such as polarity and hydrogen bonding. From the structure information, we can predict a relative reactivity between molecules.

Machine learning is the idea that there are generic algorithms that can tell us something interesting about a set of data without writing any custom code specific to the problem. Instead of writing code, we put data to the generic algorithm and it builds its own logic based on the data. As the structure information, we used molecular weight and degree of hydrogen passivation. As a reactivity index, the HOMO-LUMO energy data were used from DFT calculation, which is important for reacting chemical system in molecular orbital (MO) theory. The relationship between each molecular weight and passivation of each reactant as independent variables and the fractional electron transfer index as a dependent variable were found to be a statistically significant model by multiple regression analysis of the data. A general model for predicting reactivity of similar nanocluster, which is not included in this thesis, is presented with machine learning approach.

2.4 Natural Bond Orbital (NBO) Analysis [29, 30]

Natural bond orbital (NBO) analysis is one way to translate computational solutions of Schrödinger's wave equation into the familiar language of chemical bonding concepts. In these methods, molecular properties are expressed in terms of a natural Lewis structure (NLS) depiction of the wave function, in direct correspondence to the elementary Lewis dot diagram. NBO analysis provides a bridge between molecular orbital and valence bond theory.

A NBO is a calculated bonding orbital with maximum electron density. The NBO analysis provide useful information for understanding of intra- and inter-molecular bonding, bond species and interactions among bonds. It is used for investigating of hyperconjugation interactions (or intramolecular charge transfers, ICT) between Lewis type (bonding or lone pair) filled orbitals and non-lewis type (antibonding and Rydgberg) vacancy orbitals in molecular system.

Chapter 3 Hydrogenated Si, Ge, and SiGe Nanocluster Properties using Theoretical Calculations and a Machine Learning Approach

3.1 Introduction

Studies of semiconducting silicon-germanium (SiGe) materials are of technological interest because of their practical application in the microelectronics industry.[31] Moreover, SiGe clusters have attracted great interest for their use in optoelectronic, sensor, and photovoltaic applications.[32-36] Understanding semiconducting nanomaterials formation from the pyrolysis of mixtures of silane (SiH_4) and germane (GeH_4) at even the mildest conditions is still incomplete.[37-42] Homogenous gas-phase nanomaterials formation is a complex phenomenon in which hundreds, or possibly thousands of species, undergo simultaneous reaction. During the chemical vapor deposition of SiGe semiconducting nanomaterials, surface reactions play an important role. However, undesired defects can arise in semiconductor processing because these SiGe clusters deposit on the growing substrate. Since these clusters are important for the fine processing of semiconductors and the synthesis of novel materials, computational modeling can play a very important role in narrowing the gap between controlled experimental studies and practical operating conditions. Similarly, intentional synthesis of SiGe semiconducting nanomaterials in the gas phase can benefit from an improved mechanistic understanding of formation to tailor efforts in materials design, particularly for self-assembling molecular systems and nanocomposites.

Due to tunable semiconductor properties, Si, Ge, and SiGe clusters have also attracted great interest for the development of new materials in nanoscale applications as fundamental building blocks.[43] Both Si and Ge clusters have widely been studied because the structure and bonding of bulk Ge materials are very similar to that of bulk Si materials. Pristine Si and Ge clusters without hydrogen content are chemically reactive and thus not suitable as a building block for self-assembled materials.[44] However, this reactivity can be reduced with surface passivation by hydrogen or other suitable functional groups, such as alkyl functionalities. Si clusters have been studied extensively for their promising structural, thermochemical, and electronic properties.[45-51] For Ge clusters, there have been reported cage types of pure Ge structures with metal-doping.[52-54] Most Ge cluster studies have been conducted to investigate the geometric strain effect of clusters upon increased Ge content for medium to large cluster sizes.[36] However, to the best of our knowledge, analogous studies have not been reported for small- to medium-sized hydrogenated SiGe clusters.

Furthermore, nanocrystals of Ge have received significant interest in recent years.[35] Self-organized quantum dots of Ge were grown on Si substrates. It was observed in Si/Ge superlattices and in Ge quantum dots grown on Si that interdiffusion between Si and Ge may occur to form alloys under certain growth conditions. Detailed knowledge of the thermodynamics and the nature of Ge–Si bonding is still needed to understand the spontaneous processes leading to the formation of self-organized structures. Compared to the vast data available on solid-state materials, theoretical solid-state studies on materials possessing Si-Ge bonds and comprehension of the SiGe chemistry, especially for small clusters, are very rare. The limited results which are available on such model clusters are confined to thermodynamic investigations of the clusters of small sizes less than four atoms, measurement of optical properties of SiGe materials, and a few advanced *ab initio* calculations on SiGe dimers. Structural characteristics were also determined theoretically for several selected larger clusters by applying semi-empirical methods which include tight-binding molecular dynamics approaches, density functional theory (DFT), and Møller–Plesset second order perturbation (MP2) theories. So far, no theoretical thermodynamic data, which could indirectly validate the calculated structures through comparison against the existing experiments, are available. Thus, detailed theoretical studies connecting the structures, bonding, and thermodynamic properties of Si, Ge, and SiGe clusters are critically needed.

Recently, automated network generation techniques have allowed the kinetics of inorganic cluster and nanoparticle formation, such as Si clusters and nanoparticles, to be described at the mechanistic level. Rate coefficients must be estimated for every elementary step comprising the mechanistic model, and kinetic correlations are used to make this tractable. One common method for predicting activation barriers (E_a) is the Evans-Polanyi correlation; however, these structure-activity correlations require detailed thermochemical information for each reacting species. Recently, the existing group additivity database for the prediction of thermochemical properties of hydrogenated silicon clusters was revised and augmented with new atom-centered groups, ring corrections, and bond-centered groups to accurately capture more complex species. Conversely, there are limited studies available that predict the thermochemical properties of SiGe and Ge clusters, which is the next step for expanding our thermochemistry database for semiconducting nanoparticle formation.

For this purpose, we conducted a computational study of hydrogenated Si, Ge, and SiGe alloy clusters ($Si_xGe_yH_z$, $1<X+Y\leq 6$) to predict structures, thermochemistry, and electronic properties. This paper presents the thermochemical properties of 46 cyclic and polycyclic Si, Ge, and SiGe clusters and 7 acyclic Si, Ge, and SiGe species, i.e., standard enthalpies of formation, standard entropy values, and constant pressure heat capacities, and specifically examines both multifunctional and monofunctional molecules containing between one and six Si and/or Ge atoms. The hydrogenated clusters in this study involved different degrees of hydrogenation, i.e., the ratio of hydrogen to Si and Ge atoms varied widely depending on the size of the cluster and/or degree of multifunctionality. Species containing different numbers of fused rings comprised of three to four Si or Ge atoms were considered. The composite method of G3//B3LYP was used to calculate the electronic energy, and then statistical thermodynamics was applied to all the hydrogenated Si, Ge, and SiGe clusters to incorporate temperature effects. Enthalpies of formation at 1 atm and 298 K were calculated using atomization energies and corrected with a novel bond additivity correction model. Standard entropies and constant pressure heat capacities were calculated using a temperature-dependent scaling factor for the vibrational frequencies to account for anharmonicity. Our studies have established trends in thermodynamic properties (standard enthalpy of formation (ΔH^o_f), standard entropy (S^o), and constant pressure heat capacity (C_p)), as a function of cluster composition and structure. Furthermore, we compared HOMO-LUMO energy gaps and HOMO and LUMO electron distributions in order to gain insight into the electronic stability of the hydrogenated Si, Ge, and SiGe clusters. Quantum chemical parameters such as electronic chemical potential μ, global hardness η, and the softness σ were also calculated to provide valuable information about chemical stability. These quantum chemical parameters were generalized using a machine

learning approach to assess charge transfer during molecular interaction of hydrogenated Si, Ge, and SiGe clusters in the gas phase.

Studies of semiconducting silicon-germanium (SiGe) materials are of technological interest because of their practical application in the microelectronics industry.[31] Moreover, SiGe clusters have attracted great interest for their use in optoelectronic, sensor, and photovoltaic applications.[32-36] Understanding semiconducting nanomaterials formation from the pyrolysis of mixtures of silane (SiH_4) and germane (GeH_4) at even the mildest conditions is still incomplete.[37-42] Homogenous gas-phase nanomaterials formation is a complex phenomenon in which hundreds, or possibly thousands of species, undergo simultaneous reaction. During the chemical vapor deposition of SiGe semiconducting nanomaterials, surface reactions play an important role. However, undesired defects can arise in semiconductor processing because these SiGe clusters deposit on the growing substrate. Since these clusters are important for the fine processing of semiconductors and the synthesis of novel materials, computational modeling can play a very important role in narrowing the gap between controlled experimental studies and practical operating conditions. Similarly, intentional synthesis of SiGe semiconducting nanomaterials in the gas phase can benefit from an improved mechanistic understanding of formation to tailor efforts in materials design, particularly for self-assembling molecular systems and nanocomposites.

3.2 Computational Methodology

Quantum chemical calculations were performed with the *Gaussian 16* software.[55] All electronic energies for the hydrogenated Si, Ge, and SiGe clusters and acyclic species were calculated using the G3//B3LYP composite method,[56, 57] which uses B3LYP/6-31g(d) geometries and higher-level corrections based on single point energies. To assess different levels of theory, we employed the *Gaussian 16* software to perform quantum chemical calculations using the CBS-QB3, G3//B3LYP and G4//B3LYP composite methods. The primary difference between the Gn and CBS methods is how the correlation energy is estimated. The Gn methods assume basis set additivity and add an empirical correction to recover part of the remaining correlation energy. The complete basis set (CBS) procedures, on the other hand, attempt to perform an explicit extrapolation of the calculated values.[58] All electronic energies for the hydrogenated Si, Ge, and SiGe acyclic species in this study were calculated using these three levels of theory.

The optimized structures for all 46 hydrogenated Si, Ge, and SiGe clusters investigated in this study are depicted in Figure 3.1. The hydrogenated clusters of this study can exist in the singlet state and triplet state.[37, 59-61] As shown in Table 3.1, using the G3//B3LYP method, triplet-singlet splitting values of linear and cluster species were investigated. These calculated triplet-singlet splitting values suggest that the singlet potential energy surface is significantly lower in energy than the triplet potential energy surface. Thus, for all results reported in this study, the electronic wave functions for the hydrogenated Si, Ge, and SiGe clusters were optimized in the singlet state. Geometries and harmonic vibrational frequencies are confirmed local minima on the singlet potential energy surface, i.e., all of the vibrational frequencies are real. It is well-established that hydrogenated Si, Ge, and SiGe nanostructures pass through metastable configurations (or transient chemical species) before reaching a global minimum from molecular dynamics simulations,[62] but detailed knowledge of the structure and thermochemistry of a wide range of hydrogenated clusters is still needed. The harmonic vibrational frequencies and zero-point vibrational energy (ZPE) were linearly scaled by a temperature-dependent scaling factor of 0.98, respectively, to account for anharmonicity in the normal vibrational modes as a function of temperature as suggested by Scott and Radom and Alecu and co-workers.[63, 64] Using conventional statistical thermodynamics, molecular partition functions based on the harmonic oscillator and rigid rotor approximations were used to calculate thermodynamic properties as a function of temperature.

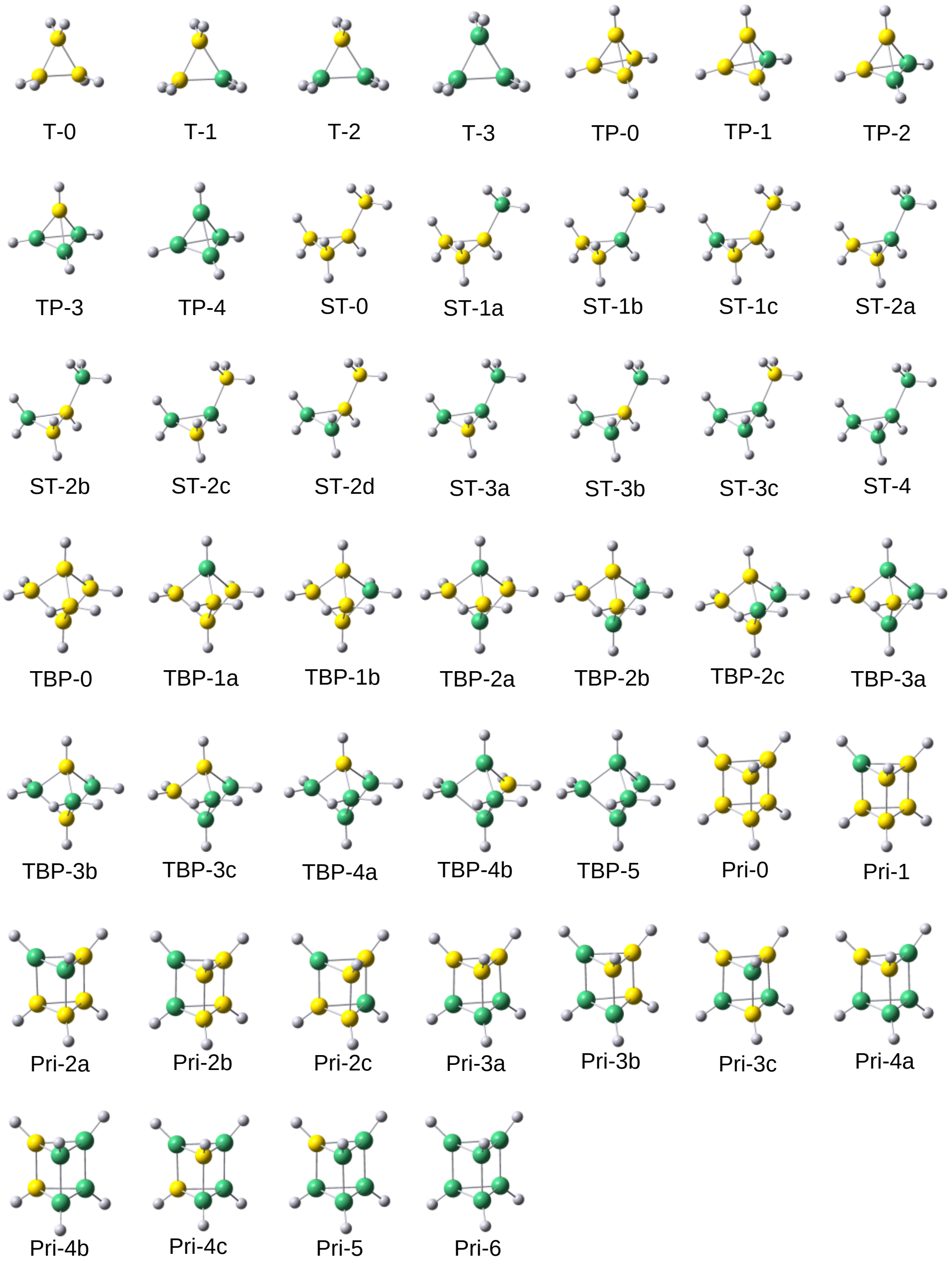

Figure 3.1. Optimized $Si_xGe_yH_z$ $(x+y=6)$ cluster geometries using the G3//B3LYP level of theory. The clusters are denoted by T for trigonal planar, TP for trigonal pyramidal, ST for substituted trigonal planar, TBP for trigonal bipyramidal, and Pri for prismane geometries. The indices are incremented by integer values to correspond with the replacement of a Si (yellow) atom by a Ge (green) atom from 0 to N, where 0 is the pure Si cluster and N is the pure Ge cluster. The lower case letter symbol denotes isomers.

Table 3.1. Calculated singlet-triplet splitting values of selected Si, Ge, and SiGe species using the G3//B3LYP level of theory, where the splitting value is defined as the difference in total energy of the species between the singlet ground state (S_0) and the first excited triplet state (T_1). The nomenclature to identify molecular geometries is the same as in Figure 3.1, and representative energy level diagrams can be found in Figure 3.7. ZPE denotes zero-point vibrational energy.

	G3//B3LYP Electronic energies with ZPE correction				
		Spin multiplicity			
Species	Index	Singlet (Hartrees)	Triplet (Hartrees)		Singlet-triplet splitting (eV)
Si_1H_4	L-1	-291.7112	-291.5693	[a]	3.9
Ge_1H_4	L-5	-2078.819	-2078.6874	[b]	3.6
Si_3H_6	T-0	-871.5746	-871.5151		1.6
Ge_3H_6	T-3	-6232.9354	-6232.8851		1.4
Si_5H_8	TBP-0	-1451.5169	-1451.4273		2.4
Si_4GeH_8	TBP-1a	-3238.6407	-3238.5581		2.2
$Si_3Ge_2H_8$	TBP-2b	-5025.7602	-5025.6793		2.2
$Si_4Ge_2H_6$	Pri-2b	-5313.8816	-5313.8201		1.7
$Si_3Ge_3H_6$	Pri-3c	-7101.0080	-7100.9437		1.7

---

[a] This molecule exists in a form of dissociation of $\cdot SiH_3$ and $\cdot H$

[b] This molecule exists in a form of dissociation of $\cdot GeH_3$ and $\cdot H$

A closer investigation of the 46 cluster structures in this study reveals no dangling Si-Si, Ge-Ge, and Si-Ge σ bonds capable of internal rotation for the clusters with the exception of the substituted trigonal planar geometry. Aside from the temperature-dependent scaling factor, anharmonic movements in torsional vibrational modes for the linear chemical species (Si_2H_6, Ge_2H_6, $SiGeH_6$, Si_3H_8, and Ge_3H_8) and the substituted trigonal planar cluster geometries were not treated. Similarly, anharmonic small ring movements (e.g., the pseudorotation of cyclopentasilanes and the ring puckering of cyclotetrasilanes incorporated into the multifunctional polycyclic structures) were not treated aside from the temperature-dependent scaling factor.[65, 66] The protocol in our study was implemented because (1) there are reduced anharmonic small ring movements for the more rigid structures in this study, which was verified by the animation of key vibrational modes, (2) the calculation of a revised partition function to account for anharmonic torsional modes and small ring movements was beyond the scope of this study. Enthalpy, H, and entropy, S, are calculated using standard formulas.[67] Calculation of thermochemical properties was performed automatically using the CalcTherm script, which interfaces with electronic structure codes to provide thermochemical properties (S, C_p , H) of individual species at elevated temperatures.[68] The external symmetry numbers for the hydrogenated Si-Ge clusters examined in this study impact the molecular partition function for rotation and reduce the rotational entropy by an amount equivalent to R ln σ_{rot},[67] where σ_{rot} is the external symmetry number of the molecule and R is the ideal gas constant.

The enthalpy of formation of a given molecule $Si_xGe_yH_z$ can be calculated from its atomization energies using Eq (3.1):[37]

$$\Delta H^{\circ}{}_{f,298}(Si_xGe_yH_z) = [x\Delta H^{\circ}{}_{f,298}(Si) + y\Delta H^{\circ}{}_{f,298}(Ge) + z\Delta H^{\circ}{}_{f,298}(H)] - \Delta H^{\circ}{}_{a,298}(Si_xGe_yH_z) \quad (3.1)$$

where the formation enthalpies of atomic silicon, germanium and hydrogen are the experimental values obtained from the JANAF tables ($\Delta H^{\circ}{}_{f,298}(Si)$ = 450 kJ mol^{-1}, $\Delta H^{\circ}{}_{f,298}(Ge)$ = 372 kJ mol^{-1}, $\Delta H^{\circ}{}_{f,298}(H)$ = 217.999 kJ mol^{-1}) and $\Delta H^{\circ}{}_{f,298}(Si_xGe_yH_z)$. The atomization energy defined as the enthalpy change upon decomposition of a molecule into its component atoms can be evaluated using Eq (3.2):

$$\Delta H^{\circ}{}_{a,298}(Si_xGe_yH_z) = [xH_{a,298}(Si) + yH_{a,298}(Ge) + zH_{a,298}(H)] - H^{298}(Si_xGe_yH_z) \quad (3.2)$$

where H_{298}(Si), H_{298}(Ge) and H_{298}(H) are the enthalpies of atomic silicon, germanium and hydrogen at 298 K, respectively, and $H_{298}(Si_xGe_yH_z)$ is the enthalpy of $Si_xGe_yH_z$ at the same temperature. These enthalpies can be calculated as the sum of the electronic energies (E_{el}), zero point energies (ZPE), and thermal corrections ($E_{vib}{}^{298}$, $E_{trans}{}^{298}$, and $E_{rot}{}^{298}$) at 298 K, as follows from canonical molecular partition functions assuming an ideal gas at 1 atm using Eq. 3.3:

$$H^{298} = E_{el} + ZPE + E_{vib}^{298} + E_{trans}^{298} + E_{rot}^{298} + \Delta PV \quad (3.3)$$

All of the quantities on the right-hand side of Eq 3.3 are obtained from quantum chemical calculations, and the standard enthalpy of formation of $Si_xGe_yH_z$ is then calculated.

The isodesmic bond additivity correction (BAC) proposed by Petersson et al.[69] and applied to silicon hydride chemistry by Wong et al. was extended in our calculations of standard enthalpy of formation for SiGe and Ge species. This approach uses a set of reference molecules that have experimental data available which then are compared to G3//B3LYP enthalpies of formation from homodesmotic reactions to calculate a set of correction parameters. The inclusion of these correction parameters was shown to lead to values that very closely approximate standard enthalpies of formation based on available experimental data and data calculated using the method of homodesmotic reactions.[70] The novel BAC parameters used in this study to calculate enthalpies of formation for Si, Ge, and SiGe species are regressed and presented in the Results and Discussion section and follow Eq 3.4.

$$\Delta H^{\circ}_{f,298}(\mathrm{BAC}) = \Delta H^{\circ}_{f,298}(\mathrm{calculated}) + \sum_{i} N_i \mathrm{BAC}_i \tag{3.4}$$

BAC_i is the BAC parameter of a certain bond type i, and the standard enthalpy of formation estimated from BACs, ΔH^o_f,298 (BAC), can be defined as the standard enthalpy of formation calculated on the basis of atomization energies, ΔH^o_f,298 (calculated), corrected by the summation of the BAC_i parameters multiplied by the number of bonds of that type (N_i).

In order to test the accuracy of our calculations, calculations were carried out on small acyclic Si, Ge, and SiGe hydrides using the CBS-QB3, G3//B3LYP, and G4//B3LYP methods and summarized in Table 3.2. The calculated results from the G3//B3LYP and G4//B3LYP composite methods were found to be in reasonable agreement with available experimental data for standard enthalpy of formation at 298 K. The performance summary for prediction of thermochemical properties for small acyclic Si, Ge, and SiGe hydride chemistries indicated that the G3//B3LYP and G4//B3LYP composite methods outperform the CBS-QB3 method on estimating standard enthalpy of formation when compared to available experimental data. Calculation of the standard enthalpy of formation at 298 K has been underestimated with CBS-

QB3, G3//B3LYP and G4//B3LYP composite methods. In the case of estimating standard entropy values of the acyclic species, all predicted standard entropies were estimated between 0.5 and 3.8 J mol^{-1} K^{-1} in average absolute deviation when compared to available experimental data. For constant pressure heat capacity, however, the calculations for all three methods were very accurate with a highest average absolute deviation of 1.1 J mol^{-1} K^{-1} when compared to available experimental data.

Analogously, a previous study on silicon hydrides from our group compared W-1 and G3//B3LYP standard enthalpies of formation at 298 K to available experimental data. The G3//B3LYP composite method agrees with available experimental data within an average absolute deviation of 1.0 kcal mol^{-1} while the W-1 method captures available experimental data within an average absolute deviation of 2.0 kcal mol^{-1}. The W-1 method was developed to be an affordable and accurate method for the determination of thermochemistry; however, the improved predictions by the G3//B3LYP method can be attributed to the use of a higher level correction based upon a regression of correction parameters from an experimental data set of 299 energies containing enthalpies of formation, ionization potentials, electron affinities, and proton affinities. Additionally, the G3//B3LYP method was a reasonable choice because the cluster property data set from this study is intended to be used in conjunction with an existing G3//B3LYP database developed by our group for the estimation of silicon hydride thermochemical properties. The G4//B3LYP method did exhibit superior accuracy for the small acyclic species examined with available experimental data; however, we experienced significant self-consistent field (SCF) energy convergence issues for structures larger than four Si and/or Ge atoms in the latest revision of the Gaussian software and this method was not pursued.

Table 3.2. Comparison of calculated standard enthalpy of formation, standard entropy, and constant pressure heat capacity at 298 K to available experimental data for small acyclic hydrogenated silicon and germanium species using the CBS-QB3, G3//B3LYP, and G4//B3LYP composite methods. Deviation is defined as experiment minus theory. AAD denotes average absolute deviation.

Molecules	net charge	spin multiplicity	$\Delta H^{\circ}_{f,298K}$ (kJ mol^{-1})						
level of theory			Exp^{a}	CBS-QB3	Deviation	G3B3	Deviation	G4	Deviation
Si_1H_4	0	1	34.3	22.57	11.7	31.22	3.1	31.52	2.8
Si_2H_6	0	1	80.3	65.39	14.9	75.69	4.6	75.03	5.3
Si_3H_8	0	1	120.9	100.38	20.5	112.46	8.4	111.49	9.4
AAD					15.7		5.4		5.8
$SiGeH_6$	0	1	116.3	71.70	44.6	107.26	9.1	108.62	7.7
Ge_1H_4	0	1	90.8	47.48	43.3	80.71	10.1	81.46	9.3
Ge_2H_6	0	1	162.3	79.07	83.2	139.71	22.6	142.23	20.1
Ge_3H_8	0	1	226.8	108.68	118.1	192.40	34.4	196.51	30.3
AAD					81.6		22.4		19.9

S^{298K}
(J mol^{-1} K^{-1})

			Exp^{a}	CBS-QB3	Deviation	G3B3	Deviation	G4	Deviation
Si_1H_4	0	1	204.6	204.38	0.2	204.56	0.0	204.48	0.1
Si_2H_6	0	1	272.7	273.82	-1.1	273.57	-0.9	274.10	-1.4
Si_3H_8	0	1	N.A.	346.58	-	347.08	-	347.38	-
AAD					0.7		0.5		0.8
$SiGeH_6$	0	1	N.A.	292.66	-	294.27	-	292.91	-
Ge_1H_4	0	1	217.1	217.31	-0.2	217.48	-0.4	217.41	-0.3
Ge_2H_6	0	1	297.0	300.47	-3.5	304.20	-7.2	300.88	-3.9
Ge_3H_8	0	1	N.A.	388.09	-	419.08	-	389.24	-
AAD					1.9		3.8		2.1

C_p
(J mol^{-1} K^{-1})

			Exp^{a}	CBS-QB3	Deviation	G3B3	Deviation	G4	Deviation
Si_1H_4	0	1	42.8	42.52	0.3	42.71	0.1	42.70	0.1
Si_2H_6	0	1	80.0	79.73	0.3	79.49	0.5	79.85	0.2
Si_3H_8	0	1	N.A.	117.55	-	117.13	-	117.71	-
AAD					0.3		0.3		0.2
$SiGeH_6$	0	1	N.A.	82.37	-	82.95	-	82.65	-
Ge_1H_4	0	1	45.0	44.78	0.2	44.88	0.1	45.06	-0.1
Ge_2H_6	0	1	84.9	85.16	-0.3	86.15	-1.2	85.60	-0.7
Ge_3H_8	0	1	N.A.	126.17	-	128.35	-	126.92	-
AAD					0.3		1.1		0.4

Any chemical system (e.g., an atom, molecule, ion, or radical) is characterized by its electronic chemical potential, μ, and by its absolute hardness, η. Thus, the calculated quantum chemical parameters such as the highest occupied molecular orbital energy E_{HOMO}, the lowest unoccupied molecular orbital energy E_{LUMO}, energy gap ΔE, electronic chemical potential μ, global hardness η, and the softness σ were calculated in our study. The concept behind the derivation of these parameters is related to each other through frontier molecular orbital theory,[71-76] and this concept can be approximated as Eqs 3.5 and 3.6.

$$-\mu = \frac{I+A}{2} = \chi \tag{3.5}$$

$$\eta = \frac{I-A}{2} \tag{3.6}$$

Here I is the ionization potential and A is the electron affinity. The inverse values of the global hardness are designated as the softness $\sigma = 1/\eta$. According to Koopmans' theorem, the frontier orbital energies are given by $-E_{HOMO} = I$ and $-E_{LUMO} = A$. It is well-known and controversial that application of Koopmans' theorem to Kohn–Sham (KS) Density Functional Theory (KS-DFT) requires a tuning procedure to be able to "impose" Koopmans' theorem on DFT approximations, thereby improving many of its related predictions in actual applications. Here hybrid functionals systematically calculate HOMO energies that underestimate the first ionization potential values by several electron volts. Nevertheless, these tabulated quantum chemical parameters can be used in two possible ways: as a rank ordering of similar acids (electrophiles) or bases (nucleophiles) to predict relative properties or as a source of values to use in relevant equations such as Eq 3.7. If two systems or molecules, A and B are brought together, electrons will flow from that of lower χ to that of higher χ, until the chemical potentials become equal. As a first approximation, the (fractional) number of electrons transferred, ΔN, will be given by Eq 3.7. The difference in electronegativity drives the electron transfer, and the sum of the hardness parameters acts as a resistance. This reactivity index was then generalized beyond the species in this study using a machine learning approach based on multiple linear regression and detailed sensitivity analysis.

$$\Delta N = \frac{\chi_B - \chi_A}{2(\eta_B + \eta_A)} \tag{3.7}$$

3.3 Structures and Vibrational Frequencies

The structures for the 46 hydrogenated Si, Ge, and SiGe clusters and 7 acyclic Si, Ge, and SiGe species that were investigated in the present study were optimized using the B3LYP/6-31G(d) level of theory. The optimized structures for all of the clusters showed complex polycyclic or cyclic nature and a varying level of surface passivation with hydrogen atoms, as illustrated in Figure 3.1. High-energy sterically strained structural isomers were calculated in this study to capture the diverse range of strain energies possible in hydrogenated Si, Ge, and SiGe clusters. Acyclic (or linear) Si, Ge, and SiGe structures were calculated for species comprised of one to three Si or Ge atoms. For the cluster structures, hydrogenated trigonal planar, trigonal pyramidal, substituted trigonal planar, trigonal bipyramidal, and prismane geometries comprised of varying numbers of three- and four-membered rings were calculated. All electronic wavefunctions for the structures were optimized in a singlet state. We also calculated all structures in this study in the triplet states (see Table 3.1 for selected structures). It was observed that the clusters and acyclic species changed geometry significantly upon excitation to the triplet state. In the case of trigonal planar structures going to the triplet state from the singlet state, the structures optimized to a linear geometry which has a higher standard enthalpy of formation than its analogue in the singlet state. For the three dimensional structures such as trigonal pyramidal, trigonal bipyramidal, and prismane, the structures transformed to less stereoscopic shapes which appeared similar to cyclohexane in geometry. This strong change in geometry indicated that the structures in this study are very stable in singlet ground state, and thus require significant structural rearrangement to find a stable minima on the triplet potential energy surface. Electronic excitation to a higher spin state may be a viable means to create more reactive intermediates due to the conformational changes in geometry on the path to the triplet state from the singlet state.

Comparison of our predicted values to experiment for geometry parameters are presented here for the acyclic species. For silane, the B3LYP/6-31G(d) predicted Si-H bond distance is 1.486 Å and the experimental value is 1.480 Å.[77] For germane, the predicted Ge-H bond distance is 1.542 Å and the experimental value is 1.525 Å.[78] For disilane, the predicted Si-Si and Si-H bond lengths were 2.350 Å and 1.489 Å, respectively, and experimental values were 2.331 Å and 1.492 Å, respectively. The HSiSi and HSiH bond angles were predicted as 110.6 and 108.3 degrees, respectively, and experimental values were 110.3 and 108.6 degrees, respectively. For digermane, the predicted Ge-Ge and Ge-H bond lengths were 2.448 Å and 1.546 Å, respectively, and experimental values were 2.403 Å and 1.541 Å, respectively. The HGeGe and HGeH bond angles were predicted as 110.7 and 108.2 degrees, respectively, and experimental values were 112.3 and 106.4 degrees, respectively. For H3SiGeH3, the predicted Si-Ge, Si-H, and Ge-H bond lengths were 2.398 Å, 1.488 Å, and 1.546 Å, respectively, and the experimental values were 2.358 Å, 1.494 Å, and 1.538 Å, respectively. The HSiH and HGeH bond angles were predicted as 108.5 and 107.9 degrees, respectively, and experimental values were 108.8 and 108.3 degrees, respectively.[79] All of our predicted values for geometry parameters are very well matched to the experimental data for the acyclic Si, Ge, and SiGe species in this study.

Using the nomenclature introduced in Figure 3.1, an analysis of the geometry parameters for the cluster species are presented herein. For trigonal planar Si_3H_6 (T-0), the equilateral triangle structure is suggested with a Si-Si bond length of 2.345 Å and a Si-H bond length of 1.486 Å.

Substituting Ge atoms systematically for Si atoms in the T-0 geometry, all the mixed SiGe and a pure Ge trigonal planar geometries were created. Addition of a Ge atom to the T-0 geometry increases the length of all the bonds mildly, thereby increasing the size of the full cluster where the fully substituted Ge cluster is the largest in geometric dimensions. For the T-1 geometry, the Ge-Si bond length is 2.405 Å, Si-Si bond length is 2.348 Å, Ge-H bond length is 1.541 Å, and Si Ge-Si apex angle is 58.6 degrees. As observed with the trigonal planar structural series, all other structural geometries (i.e., substituted trigonal planar, trigonal pyramidal, trigonal bipyramidal, and prismane) showed a similar trend of expanding bond lengths when exchanging a Si atom with a Ge atom. Although not presented in Figure 3.2.1, it is noteworthy to discuss the S-0 geometry, or nearly planar cyclic rhombus structure of four Si atoms, which has a Si-Si bond length of 2.371 Å and a Si-H bond length of 1.492 Å. With the angles of the Si-Si-Si bonds at 87.7 and 92.3 degrees and all Si atoms possessing an sp^3 hybridized center, this cyclic structure shows a slightly puckered character and the four-membered ring is not completely planar. Interestingly, the square planar Si_4H_8 is the only structure in the geometry series which showed a stable minimum on the singlet potential energy surface with all real vibrational frequencies. Structures comprised of one four-membered ring and any level of Ge content were unstable, i.e., all structures were found to be higher-order saddle points on the potential energy hypersurface with imaginary vibrational frequencies. A conformational search revealed that a substituted trigonal planar structure in which a hydrogen in the trigonal plane structure is substituted with a silyl or germyl group was a more stable minimum on the singlet potential energy surface with all real vibrational frequencies. We found that the substituted trigonal planar (ST-0) geometries are more stable than the square planar (S-0) geometries, where a smaller three-membered ring in the ST-0 geometry is preferred over a larger four-membered ring in the S-0 geometry. All ST-0 geometries with varying levels of Si and Ge content have real vibrational frequencies. In the case of Si4H8 (ST-0), the average of Si-Si and Si-H bond lengths are 2.346 Å and 1.486 Å, respectively, and the angle between the trigonal plane and the Si atom of the silyl group is 120.6 degrees. These bond distances and angles in the ST-0 structural series are slightly increased as the Si atoms are replaced with Ge atoms.

Compared to the Si atom, the Ge atom has a full 3d shell of 10 electrons and significantly more electrons than the Si atom; however, the respective bond lengths upon Ge substitution are only increased by +3.7% going from the Si-H to Ge-H substitution, respectively, and +2.4% going from Si-Si to Si-Ge substitution, respectively. Another reason for the observed higher stability for the ST-0 geometry than the S-0 geometry can be seen by the fact that the ST-0 geometry has fewer overall spatial constraints than the S-0 geometry. In other words, the ST-0 geometry still has a torsional degree of freedom in vibrational modes for the substituted silyl or germyl group which is lost upon a four-membered ring formation. This explanation could also attribute why the ST-0 geometry is more stable than the TP-0 geometry, which also lacks any torsional degrees of freedom in vibrational modes. The trigonal pyramidal geometry (TP-0) has on average a shorter Si-Si bond length at 2.327 Å and Si-H bond length at 1.479 Å compared to Si clusters in the other geometry series. In the TP-1 structure, the Si-Si bond length on average is 2.332 Å and the Si Ge bond length is 2.399 Å. The fact that the TP-0 geometry has more contracted Si-Si bond distances than the ST-0 geometry supports the stable nature of ST-0 geometry due to an overall lack of polycyclic nature.

Several structures in this study were initially hypothesized to have both pentacoordinated and hexacoordinated Si and Ge centers; however, only stable clusters comprised of hexacoordinated Si and Ge centers were isolated. This type of bonding behavior indicates that both Si and Ge centers would exhibit sp^3d or sp^3d^2 hybridization, respectively. In its least strained hypervalent form, sp^3d hybridized Si and Ge centers will form covalent bonds with five neighboring atoms in a trigonal bipyramidal electron pair coordination. These sp^3d hybridized centers were explored for the square bipyramidal (SBP) geometry series. The sp^3d^2 hybridized Si and Ge centers will form covalent bonds with six neighboring atoms in an octahedral electron pair coordination. These sp^3d^2 hybridized Si and Ge centers were explored for trigonal bipyramidal (TBP) geometries. Structures comprised of pentacoordinated Si and Ge were found to be the unstable in the square bipyramidal geometries and these structures favored prismane geometries (Pri) that were instead comprised of sp^3 hybridized Si and Ge atoms. These SBP structures comprised of pentacoordinated Si and Ge centers were unstable, i.e., all structures were found to be higher order saddle points on the potential energy hypersurface comprised of imaginary vibrational frequencies. The unstable SBP structure constructed to have sp^3d hybridization is supported with similar work done for Si and Ge complexes where Si complexes were found to be more stable in the hypervalent state with a hexacoordinated complex rather than a pentacoordinated complex. This tendency to form a hexacoordinated Si or Ge centers is further supported by our stable trigonal bipyramidal geometries which exhibit a strained hexacoordinated Si or Ge center in the trigonal center plane of the cluster. For the molecules in our study, results show that a similar preference for hypervalent bonding behavior observed for the Si centers also occurs for the Ge centers. This bonding behavior is likely due to the presence of a complete 3d shell of 10 electrons for the Ge atom which would exhibit more facility to form hybridization involving the d orbital than the Si atom. In this study, all of the Si and Ge atoms are passivated with hydrogen or bonded to other Si or Ge atoms to be in the most stable sp^3 and sp^3d^2 hybridization states. As with the trigonal planar (T-0), substituted trigonal planar (ST-0), and trigonal pyramidal (TP) geometries, the expansion of bond lengths and bond angles upon substitution of a Ge atom for a Si atom was also observed for trigonal bipyramidal (TBP) and prismane (Pri) geometries. There are studies in the literature for so-called "ultrastable silicon nanoclusters", or hydrogenated pure silicon prismanes comprised of up to 18 silicon atoms. Katin et al.[80] compared the electronic, optical properties, and kinetic stability of $Si_{18}H_{12}$ with the pristine silicon prismane and prismanes embedded with additional C, Si, and Ge atoms. Comparison of this theoretical study with our current study, clusters with a higher density of atoms are subject to have larger spatial confinements which resulted in shorter Si-Si, Si-Ge, and Ge-Ge bond lengths. A similar tendency in bond contraction can be observed by changing the Si atom to a Ge atom in the structures, as opposed to embedding an additional atom in the center of the polycyclic structure.

At the level of theory considered in our study, modeling results have all real vibrational frequencies and represent stable minima on the potential energy surface. Experimental spectroscopic data for the vibrational frequencies of hydrogenated Si, Ge, and SiGe clusters are limited. The unscaled harmonic vibrational frequencies for linear silicon hydrides (SiH_4 and Si_2H_6) and germanium hydrides (GeH_4 and Ge_2H_8) calculated using two different level of theories (G3//B3LYP and G4//B3LYP) were compared against available spectroscopic experimental data in Table 3.3. The unscaled harmonic frequencies for SiH_4, Si_2H_6, GeH_4, and Ge_2H_6 were determined to have mean percentage deviations from experimental values of -1.7, -1.8, +0.7, and +5.8 %, respectively, at the G3//B3LYP level of theory. The G4//B3LYP method predicts slightly more accurate vibrational frequencies with the mean percentage deviations of -1.3, -0.9, -0.9, and +2.2 % for SiH_4, Si_2H_6, GeH_4, and Ge_2H_6, respectively.

Table 3.3. Comparison of experimental vibrational modes for SiH_4, Si_2H_6, GeH_4, and Ge_2H_6 to unscaled harmonic vibrational modes using the G3//B3LYP and G4//B3LYP composite methods. All vibrational frequency values are reported in cm^{-1}.

(a) Vibrational Modes of SiH_4

mode symmetry	experimental frequency[a]	G3//B3LYP			G4//B3LYP		
		calc. freq.	deviation (exp-calc)	% deviation	calc. freq.	deviation (exp-calc)	% deviation
A_1	2187	2252	-65	-3.0	2238	-51	-2.3
E	975	975	0	0.0	975	0.2	0.0
T_2	2191	2265	-74	-3.4	2248	-56.6	-2.6
T_2	914	917	-3	-0.3	918	-4.3	-0.5
av			-35.5	-1.7		-27.9	-1.3

(b) Vibrational Modes of Si_2H_6

mode symmetry	experimental frequency[b]	G3//B3LYP			G4//B3LYP		
		calc. freq.	deviation (exp-calc)	% deviation	calc. freq.	deviation (exp-calc)	% deviation
A_{1g}	2152	2239	-86.9	-4.0	2217	-65.0	-3.0
A_{1g}	909	930	-21.3	-2.3	926	-17.2	-1.9
A_{1g}	434	433	0.8	0.2	422	11.7	2.7
A_{1u}	131	127	3.6	2.7	127	4.4	3.4
A_{2u}	2154	2229	-75.1	-3.5	2210	-55.9	-2.6
A_{2u}	844	855	-11.5	-1.4	853	-9.0	-1.1
E_g	2155	2239	-83.9	-3.9	2219	-64.0	-3.0
E_g	929	943	-13.8	-1.5	944	-14.6	-1.6
E_g	625	638	-12.7	-2.0	632	-7.3	-1.2
E_u	2179	2252	-72.6	-3.3	2228	-49.0	-2.2
E_u	940	957	-17.2	-1.8	957	-17.2	-1.8
E_u	379	380	-0.6	-0.2	373	6.4	1.7
av			-25.8	-1.8		-16.8	-0.9

(c) Vibrational Modes of GeH_4

mode symmetry	experimental frequency[c]	G3//B3LYP			G4//B3LYP		
		calc. freq.	deviation (exp-calc)	% deviation	calc. freq.	deviation (exp-calc)	% deviation
A_1	2106	2051	54.7	2.6	2153	-46.7	-2.2
E	931	936	-4.9	-0.5	924	6.9	0.7
T_2	2114	2082	32.5	1.5	2160	-45.9	-2.2
T_2	819	824	-5.0	-0.6	819	0.0	0.0
av			19.3	0.7		-21.4	-0.9

(d) Vibrational Modes of Ge_2H_6

mode symmetry	experimental frequency[d]	G3//B3LYP			G4//B3LYP		
		calc. freq.	deviation (exp-calc)	% deviation	calc. freq.	deviation (exp-calc)	% deviation
A_{1g}	2068	2025	42.8	2.1	2124	-55.9	-2.7
A_{1g}	832	835	-2.6	-0.3	838	-5.6	-0.7
A_{1g}	268	238	29.9	11.2	254	14.2	5.3
A_{1u}	146	80	66.0	45.2	105	40.8	28.0
A_{2u}	2077	2031	45.8	2.2	2130	-52.9	-2.5
A_{2u}	756	752	4.4	0.6	753	2.8	0.4
E_u	2091	2067	24.4	1.2	2142	-51.4	-2.5
E_u	879	887	-7.9	-0.9	887	-7.7	-0.9
E_u	370	349	20.7	5.6	354	15.7	4.2
E_g	2081	2058	22.9	1.1	2134	-52.7	-2.5
E_g	880	891	-10.7	-1.2	892	-11.8	-1.3
E_g	567	548	19.4	3.4	557	10.2	1.8
av			21.3	5.8		-12.9	2.2

[a,c] ref[81], [b] ref[82]

3.4 Thermochemical Properties

The thermodynamic properties of 7 acyclic Si, Ge, and SiGe hydrides with experimental data available were estimated using the three different quantum chemical methods mentioned in the Computational Methodology section. The deviations between the calculated and experimental values for standard enthalpy of formation, standard entropy, and constant pressure heat capacity are listed in Table 3.2 for these acyclic species. Among the methods used, the G3//B3LYP method was the most accurate for the standard enthalpy of formation calculation for silicon hydrides with an average absolute deviation of 5.4 kJ mol^{-1} from experimental measurements while the G4//B3LYP method was more accurate for the prediction standard enthalpy of formation values for germanium hydrides with an average absolute deviation of 19.9 kJ mol^{-1} from experimental measurements. The G3//B3LYP method had similar predictive accuracy as the G4//B3LYP method for the standard enthalpy of formation for germanium hydrides with an average absolute deviation of 22.4 kJ mol^{-1}. The largest deviations between experimental and calculated predictions for standard enthalpy of formation values observed for germanium hydrides can be attributed to factors not included in the composite methods discussed. This conclusion is supported by reasonably accurate predictions of geometry parameters and vibrational frequencies for the germanium hydrides discussed in the Structures and Vibrational Frequencies section. The quantum chemical factors that lead to large deviations in standard enthalpy of formation prediction include correlation of core and core-valence electrons and relativistic effects such as spin-orbit coupling which becomes progressively more important as heavier elements like Ge are considered. It should be noted that the G3//B3LYP method does include an experimental spin-orbit energy correction term used for atoms and calculated spin-orbit energy correction term for selected diatomic species. For the G3//B3LYP method, the use of a higher level correction factor based upon a regression of correction parameters from an experimental data set containing standard enthalpies of formation, ionization potentials, electron affinities, and proton affinities differs for Si and Ge hydride species. Namely, there are more Si-based species than Ge-based species in this test set for regression of higher level correction factors, i.e., the test set included species with one or two Si atoms and only one Ge atom.

To the best of our knowledge, there is no extensive investigation of thermochemical property estimation or even of vibrational frequency calculations for optimized hydrogenated Si, Ge, and SiGe clusters outside of the works cited in this paper. A total of 46 molecules up to a moderate cluster size, where $(Si + Ge) \leq 6$, were investigated in this study. The thermochemical properties of all 46 species studied here are reported in the Table 3.4. The most stable ground electronic state for all molecules in this study was found to be the singlet state. As mentioned in the previous section Structures and Vibrational Frequencies, a significant conformational change or spontaneous bond dissociation was observed during optimization of the electronic wavefunction to the triplet state. In all geometries, the addition of Ge atoms to a species increases the standard enthalpy of formation, standard entropy, and constant pressure heat capacity values. The trend based on elemental composition for standard enthalpy of formation predictions by the G3//B3LYP and G4//B3LYP methods was successfully captured for the acyclic hydrides of this study. Due to the semiconducting or non-local nature of electron correlation in the larger clusters with cyclic or polycyclic, rigorous composite methods are required to accurately predict trends in thermochemical properties such as standard enthalpy of formation as function of Si and Ge composition.

Table 3.4. Comparison of calculated thermodynamic properties of hydrogenated Si, Ge, and SiGe clusters using the G3//B3LYP method with and without the bond-additivity corrections (BAC) as denoted in Eq. 3.4. The nomenclature to identify molecular geometries is the same as in Figure 3.1.

Level of Theory									G3//B3LYP			G3//B3LYP (BAC)		
Atoms			Species	Net charge	Spin multi-plicity	Symmetry group	chirality	s_{ext}	$\Delta H^{\circ}_{f,298K}$	C_p	S	$\Delta H^{\circ}_{f,298K}$	C_p	S
Si	Ge	H							KJ/mol	J/mol.K	J/mol.K	KJ/mol	J/mol.K	J/mol.K
Trigonal Planar														
3	0	6	T-0	0	1	D_{3h}		6	261.1	105.4	319.5	268.9	105.3	304.5
2	1	6	T-1	0	1	C_{2v}		2	278.8	110.3	339.1	286.4	110.2	333.3
1	2	6	T-2	0	1	C_{2v}		2	296.1	114.7	358.8	313.2	114.6	352.8
0	3	6	T-3	0	1	D_{3h}		6	313.8	118.7	378.2	349.9	118.6	363.1
Trigonal Pyramidal														
4	0	4	TP-0	0	1	T_d		12	644.0	122.1	352.9	654.1	121.9	331.9
3	1	4	TP-1	0	1	C_{3v}		3	655.2	122.7	359.6	661.4	122.6	350.2
2	2	4	TP-2	0	1	C_{2v}		2	665.7	123.4	367.7	677.5	123.3	361.9
1	3	4	TP-3	0	1	C_{3v}		3	675.1	124.3	376.1	702.4	124.2	366.9
0	4	4	TP-4	0	1	T_d		12	683.5	125.4	384.6	735.7	125.4	363.8
Substituted trigonal planar														
4	0	8	ST-0	0	1	C_S		1	282.7	142.0	381.5	293.3	141.9	381.3
3	1	8	ST-1a	0	1	C_S		1	316.1	145.8	402.6	330.3	145.7	402.4
3	1	8	ST-1b	0	1	C_S		1	285.4	146.2	394.5	292.0	146.1	394.3
3	1	8	ST-1c	0	1	C_1	o	2	300.8	147.0	402.5	311.1	146.9	402.4
2	2	8	ST-2a	0	1	C_S		1	320.0	149.6	417.7	339.8	149.5	417.5
2	2	8	ST-2b	0	1	C_1	o	2	334.2	150.8	425.3	348.2	150.7	425.1
2	2	8	ST-2c	0	1	C_1	o	2	303.1	150.7	413.0	319.1	150.5	412.8
2	2	8	ST-2d	0	1	C_S		1	318.5	151.6	424.0	338.3	151.5	423.8
1	3	8	ST-3a	0	1	C_1	o	2	337.5	154.0	437.4	366.8	153.9	437.2
1	3	8	ST-3b	0	1	C_S		1	351.9	155.3	451.4	375.3	155.2	451.2
1	3	8	ST-3c	0	1	C_S		1	321.0	154.9	431.8	356.1	154.8	431.6
0	4	8	ST-4	0	1	C_S		1	355.2	158.2	464.2	403.6	158.1	464.0
Trigonal Bipyramidal														
5	0	8	TBP-0	0	1	D_{3h}		6	282.4	157.6	373.9	295.7	157.4	358.8
4	1	8	TBP-1a	0	1	C_{3v}		3	290.0	160.3	385.7	299.4	160.1	376.3
4	1	8	TBP-1b	0	1	C_{2v}		2	302.9	162.9	392.0	316.0	162.8	386.2
3	2	8	TBP-2a	0	1	D_{3h}		6	298.1	162.4	396.3	303.5	162.2	381.1
3	2	8	TBP-2b	0	1	C_S		1	309.6	165.4	403.3	328.4	165.2	403.1
3	2	8	TBP-	0	1	C_{2v}		2	323.2	168.4	411.3	336.0	168.3	405.4

			2c											
2	3	8	TBP-3a	0	1	C_{2v}		2	317.0	166.8	412.5	335.3	166.6	406.5
2	3	8	TBP-3b	0	1	D_{3h}		6	343.4	173.8	432.3	356.0	173.7	417.2
2	3	8	TBP-3c	0	1	C_S		1	329.1	170.4	422.0	357.2	170.3	421.9
1	4	8	TBP-4a	0	1	C_{3v}		3	348.4	175.5	442.4	386.0	175.4	433.1
1	4	8	TBP-4b	0	1	C_{2v}		2	335.7	171.4	430.0	379.3	171.2	424.1
0	5	8	TBP-5	0	1	D_{3h}		6	354.2	176.0	448.8	416.8	175.8	433.9
Prismane														
6	0	6	Pri-0	0	1	D_{3h}		6	587.1	171.3	393.8	602.6	171.2	378.7
5	1	6	Pri-1	0	1	C_S		1	589.5	174.0	405.7	601.0	173.8	405.5
4	2	6	Pri-2a	0	1	C_S		1	591.6	176.1	416.7	608.8	176.0	416.5
4	2	6	Pri-2b	0	1	C_{2v}		2	592.7	175.4	415.6	609.9	175.3	409.7
4	2	6	Pri-2c	0	1	C_2	o	4	591.9	176.4	417.8	599.4	176.3	411.8
3	3	6	Pri-3a	0	1	C_{3v}		3	593.5	178.0	427.2	626.0	177.9	417.9
3	3	6	Pri-3b	0	1	C_1	o	2	594.2	177.7	427.2	617.1	177.6	427.0
3	3	6	Pri-3c	0	1	C_S		1	593.9	178.4	428.9	616.8	178.2	428.7
2	4	6	Pri-4a	0	1	C_S		1	595.7	179.7	438.2	633.9	179.6	437.9
2	4	6	Pri-4b	0	1	C_{2v}		2	596.5	178.9	436.9	634.7	178.8	430.9
2	4	6	Pri-4c	0	1	C_2	o	4	595.8	179.7	438.8	624.4	179.6	432.8
1	5	6	Pri-5	0	1	C_S		1	597.3	181.1	448.6	650.9	181.0	448.3
0	6	6	Pri-6	0	1	D_{3h}		6	598.7	182.7	459.0	677.2	182.6	443.9

Petersson et al.[69] proposed the concept of an isodesmic bond additivity correction (BAC) scheme based on the spirit of isodesmic reactions. With this approach, our study compared small acyclic molecules with experimental data available in order to calculate the bond additivity corrections necessary for implementation of Eq. 3.4. The novel BAC parameters for Si, Ge, and SiGe species regressed in our study to calculate standard enthalpies of formation are presented in Table 3.5.

Table 3.5. Summary of regressed parameters for the Bond Additivity Correction (BAC) of different bond types for standard enthalpy of formation at 298 K calculated from atomization energies and the G3//B3LYP level of theory.

	Si-H	Ge-H	Si-Ge	Si-Si	Ge-Ge
BAC values (KJ/mol)	-0.12	1.83	-0.66	1.28	7.06

The regression statistics show that the most statistically significant BAC parameter is for the Ge-H bond followed by the Ge-Ge bond with p-values of 0.007 and 0.011, respectively. The R^2-value for the full regression was 0.9992 with an F-value of 525.8 and a p-value of 0.002. Thus, the full regression model is statistically significant at the 99.5% confidence interval. The BAC parameters are categorized into five different types according to the Si and/or Ge atoms participating in the respective bond. For all 46 hydrogenated Si, Ge, and SiGe clusters, the resulting standard enthalpies of formation using this BAC approach are listed along with the standard enthalpies of formation obtained from atomization energies without the BAC approach in Table 4. Figure 3.2a-f depict parity plots to display trends of the BAC impact on prediction of standard enthalpies of formation for key geometry series (T, ST, TBP, TP, and Pri).

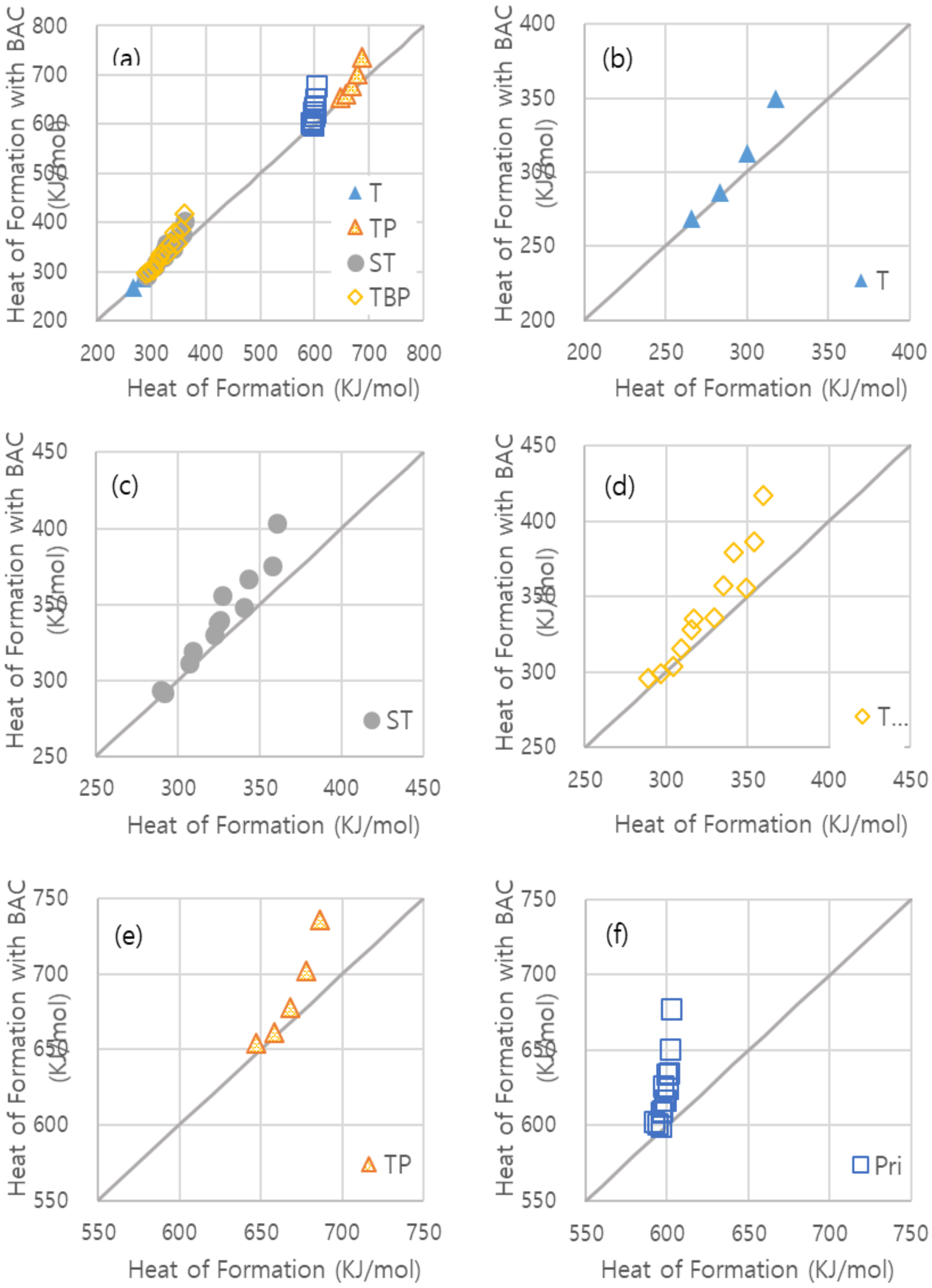

Figure 3.2. Parity plots of standard enthalpy of formation for the 46 hydrogenated Si, Ge, and SiGe clusters in this study: (a) all geometries, (b) trigonal planar group, (c) substituted trigonal

planar group, (d) trigonal bipyramidal group, (e) trigonal pyramidal group, and (f) prismane group.

On average, the standard enthalpy of formation for all clusters in this study increased after implementation of the required BAC parameters. The most pronounced BAC effect on the standard enthalpy of formation prediction was for the clusters comprised of higher Ge atom content than Si atom content, particularly because the G3//B3LYP method systematically underestimates the standard enthalpy of formation of SiGe and Ge hydrides. The absolute difference in standard enthalpies of formation between the Pri-0 and Pri-6 structures before employing the BAC parameters was 10.8 kJ mol^{-1}. After implementation of the BAC parameters, the standard enthalpies of formation of Pri-0 and Pri-6 structures were 602.6 kJ mol^{-1} and 677.2 kJ mol^{-1}, respectively. Upon implementation of the BAC parameters, the absolute difference in standard enthalpies of formation between the Pri-0 and Pri-6 structures become 74.6 kJ mol^{-1}. Thus, species with more X-X bonds (X = Si or Ge) will exhibit a greater impact of the BAC parameters. This trend in correction of standard enthalpy of formation values can be clearly seen by observing the parity plots in Figure 2, particularly Figure 2f for the prismane clusters.

The standard entropies and constant pressure heat capacities for all clusters in this study over the temperature range of 298.15 K to 1500 K are presented graphically in Figure 3.3a-3b and in Appendix A1. The average percent deviations between experimental and calculated values of standard entropy and constant pressure heat capacity for the seven acyclic Si, Ge, and SiGe hydrides were +1.3% and +0.6%, respectively, at the G3//B3LYP level of theory. It is noteworthy to mention that the external symmetry number was identified for all clusters to ensure that accurate standard entropy values were predicted. The effect of external symmetry number on rotational entropy becomes less pronounced at elevated temperatures because the aforementioned correction factor, R ln σ_{rot}, is not a function of temperature.

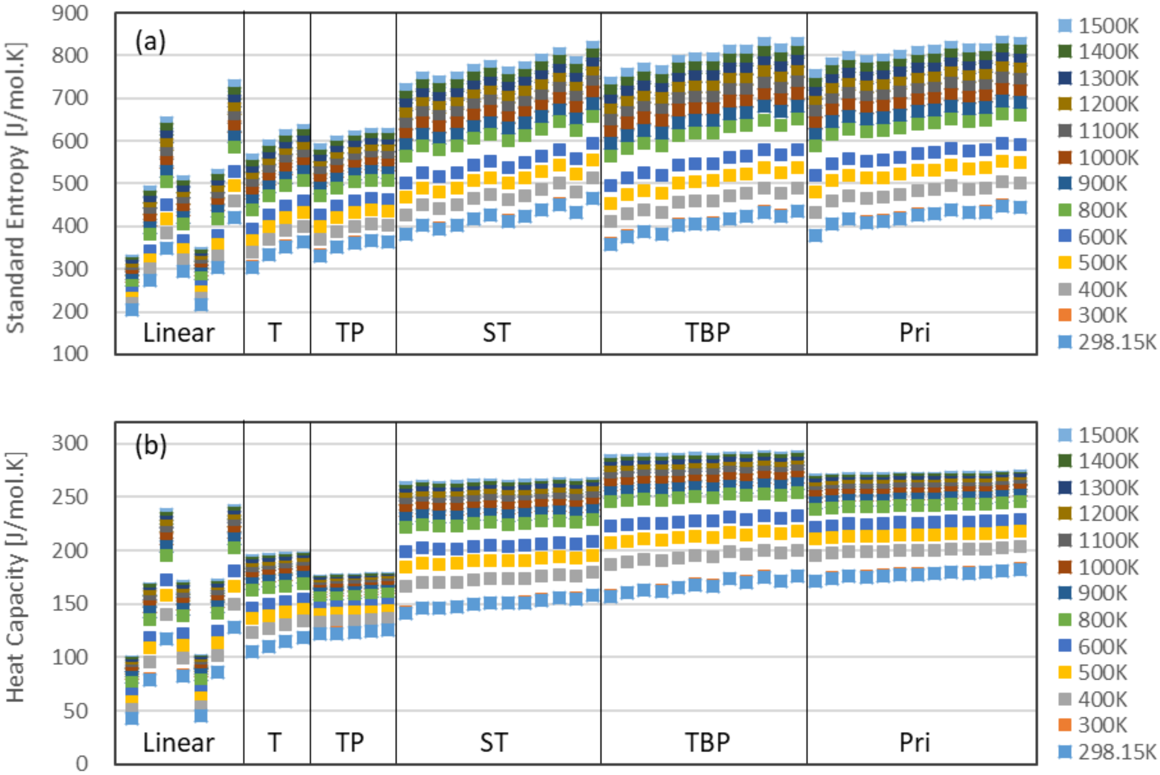

Figure 3.3. (a) Standard entropies and (b) constant pressure heat capacities of all hydrogenated Si, Ge, and SiGe clusters in this study over the temperature range of 298.15K to 1500 K using the G3//B3LYP level of theory.

The clusters with the highest degree of symmetry were the trigonal planar geometries, particularly the pure Si and Ge clusters, TP-0 and TP-4, respectively, which both possess a Td point group symmetry. The D3h point group symmetry was the next most common point group symmetry with a high degree of symmetry in this study, particularly for the trigonal bipyrimidal

(TBP) and prismane (Pri) geometries. Chiral clusters containing at least one Si/Ge atom with four nonidentical substituents were identified in our study. The presence of one chiral center was denoted in Table 4 for four substituted trigonal planar and three prismane clusters. The presence of a chiral center in a cluster increases the external symmetry number by a factor of two. Figure 3.3a-3b display standard entropy and constant pressure heat capacity values, respectively, as a function of temperature and it is interesting to note that standard entropy values are more sensitive to temperature variations than constant pressure heat capacity for the clusters in this study. For both the trigonal planar and trigonal pyramidal geometries, the range of standard entropy and constant pressure heat capacity values from 298 K to 1500 K is lower than the range of standard entropy and constant pressure heat capacity values over the same temperature range for the substituted trigonal planar, trigonal bipyramidal, and prismane geometries. This observation is likely due to the greater number of vibrational degrees of freedom for the larger Si, Ge, and SiGe clusters sizes.

If standard enthalpy of formation values are compared for isomers of a given cluster geometry, relative stabilities can be identified and ranked accordingly. Cluster isomers are present in this study for the substituted trigonal planar (ST), trigonal bipyramidal (TBP), and prismane (Pri) geometries. For instance in Table 4 for the trigonal bipyramidal geometry, one can observe that the isomer TBP-2a is more stable than isomers TBP-2b and TBP-2c where standard enthalpies of formation are 303.5 kJ mol^{-1}, 328.4 kJ mol^{-1}, and 336.0 kJ mol^{-1}, respectively. The isomer TBP-2a differs from TBP-2b and TBP-2c due to the presence of two sp^3-hybridized Ge atoms in TBP-2a compared to two sp^{3}d^2-hybridized Ge atoms in TBP-2b and TBP-2c. A similar trend in cluster stabilities is also observed for the other TBP isomers in the TBP-1, TBP-3, and TBP-4 series of cluster geometries, but the differences between the most stable isomer and the least stable isomer in these geometry series are lower with values of 16.6 kJ mol^{-1}, 21.9 kJ mol^{-1}, and 6.7 kJ mol^{-1}, respectively. The difference in stability of isomers is similarly pronounced for the substituted trigonal planar geometry series; however, the greatest difference for the stability of isomers for this study is in the ST-1 series where the ST-1b isomer is most stable. The ST-1b isomer has the molecular formula of $Si_3Ge_1H_8$ where the Ge is at the center of the cluster and bound to three Si atoms and one H atom. The differences in stability between the most stable isomer and the least stable isomer in the ST-1, ST-2, and ST-3 series are 38.3 kJ mol^{-1}, 20.7 kJ mol^{-1}, and 19.2 kJ mol^{-1}, respectively. The difference in stability of isomers is least pronounced for the prismane clusters with differences ranging 10.5 kJ mol^{-1}, 9.2 kJ mol^{-1}, and 10.3 kJ mol^{-1} for the Pri-2, Pri-3, and Pri-4 series, respectively.

3.5 Electronic Properties and Chemical Stability

The highest occupied and lowest unoccupied molecular orbital energies are very informative properties of a molecule or cluster which can be calculated by quantum chemical methods. These molecular orbitals also assign the electron density as a function of position in the molecule or cluster, where electron density for a given molecular orbital i is defined as the square of the electronic wavefunction, Ψ_i^2. Knowledge of the highest occupied and lowest unoccupied molecular orbital contours is critical for understanding reactions of clusters as well as optoelectronic properties. The foundation of the frontier orbital theory for the prediction of the most reactive positions in multi-electron systems is based on the highest occupied and lowest unoccupied molecular orbitals. Reactive molecules or clusters are characterized by a small highest occupied molecular orbital-lowest unoccupied molecular orbital (HOMO-LUMO) energy gap. Both the HOMO and LUMO are the primary molecular orbitals that can be used as predictors of chemical stability and optoelectronic properties.

In our computational study, the HOMO–LUMO energy gap is considered to investigate the role of cluster composition on the chemical stability of hydrogenated Si, Ge, and SiGe clusters. This energy gap is a critical parameter which characterizes the chemical reactivity of the hydrogenated clusters. This chemical reactivity is related to the facility of a molecule to participate in chemical reactions or to create a novel self-assembled material through non-bonding molecular interactions. The HOMO–LUMO energy gap can describe the ability for electrons to move from HOMO to LUMO and consequently is considered as an important parameter to analyze the chemical stability of clusters. For instance, if the HOMO–LUMO energy gap were large for a given Si, Ge, or SiGe cluster, this value would correspond to a closed shell electronic configuration and high chemical stability. On the other hand, smaller HOMO–LUMO energy gaps for given Si, Ge, and SiGe clusters reflect that the respective cluster may interact easily with other molecules to form a covalent bond and these types of molecules are on average more chemically reactive.

Calculated HOMO-LUMO energy gaps of hydrogenated Si and Ge clusters and acyclic Si and Ge hydrides at the G3//B3LYP level of theory are presented in Figure 3.4. The highest HOMO-LUMO energy gaps are for acyclic Si and Ge hydrides comprised of one or two Si/Ge atoms ranging from 12.4 to 14.6 eV for Si-containing species and 12.0 to 14.2 eV for Ge-containing species. The calculated HOMO-LUMO energy gaps for pure Ge species are always lower than for pure Si species, where the largest absolute difference of 0.62 eV is observed for the trigonal bipyramidal geometry. The smallest absolute difference of 0.06 eV between HOMO-LUMO energy gaps for pure Si and Ge species is observed for the trigonal pyramidal geometry. The trigonal pyramidal geometry is the most strained geometry in our study as previously discussed in the Structures and Vibrational Frequencies section. On average, the HOMO-LUMO energy gap decreases with increase in the polycyclic nature of the pure Si or Ge cluster.

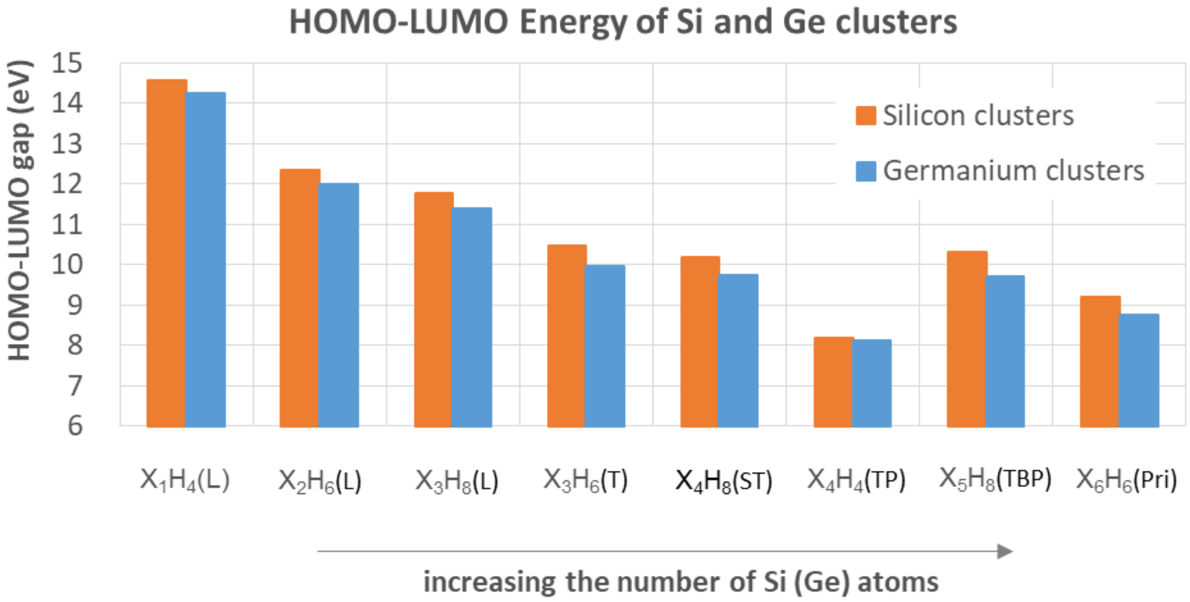

Figure 3.4. Comparison of calculated HOMO-LUMO energy gaps for pure silicon and germanium clusters using the G3//B3LYP level of theory. The nomenclature to identify cluster geometries is the same as in Figure 3.1.

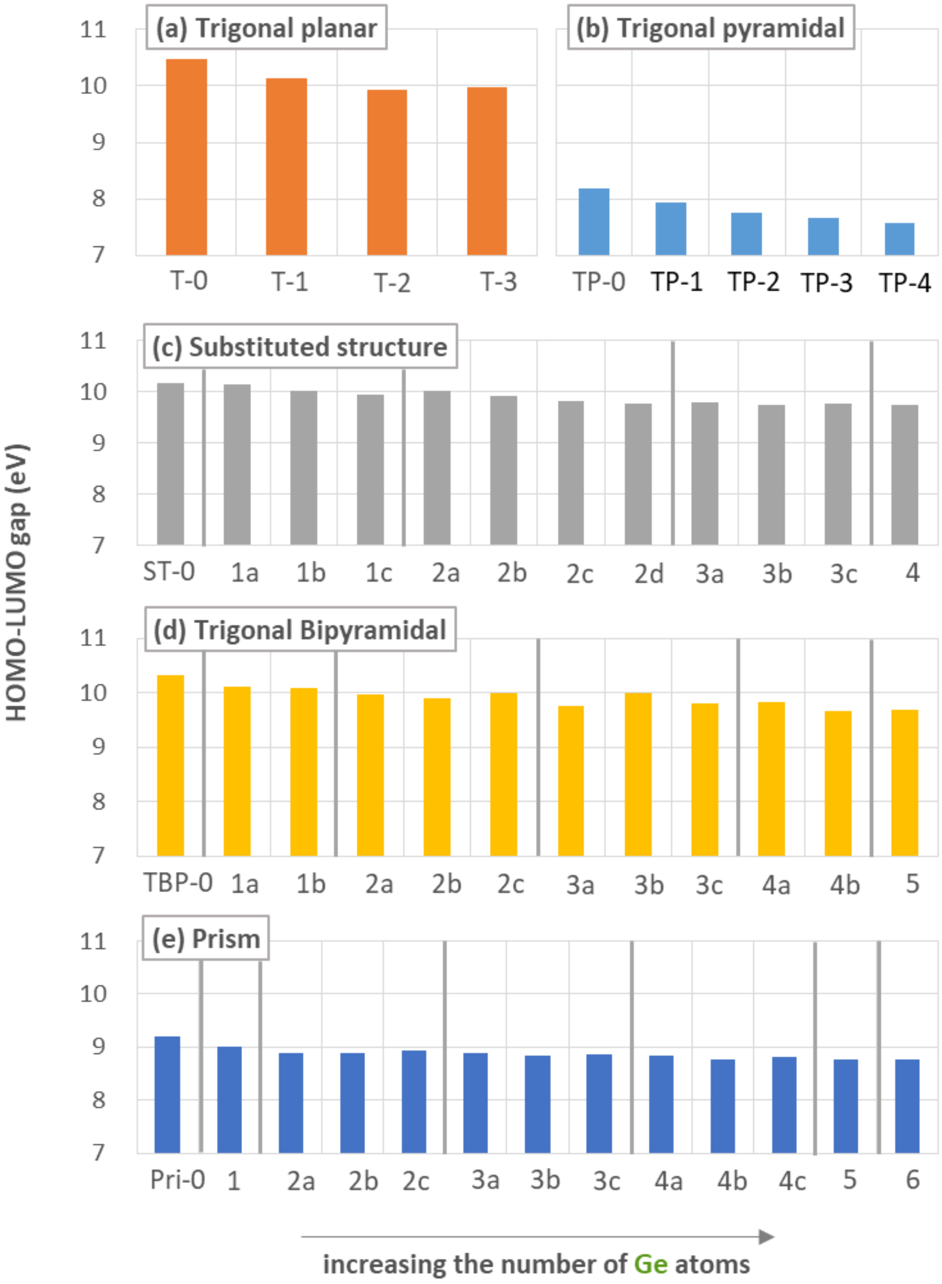

Figure 3.5. Comparison of calculated HOMO-LUMO energy gaps for all hydrogenated Si, SiGe, and Ge clusters in this study using the G3//B3LYP level of theory. The nomenclature to identify cluster geometries is the same as in Figure 3.1.

Figure 3.5a-e present calculated HOMO-LUMO energy gaps of all clusters in our study, particularly highlighting the effects of alloy cluster composition and isomers. The most precipitous fall in HOMO-LUMO energy gap is for the trigonal bipyramidal geometry followed by the trigonal planar, substituted trigonal planar, prismane, and trigonal pyramidal geometries at 0.49, 0.44, 0.44, and 0.43 eV, respectively. It is interesting to note that the corresponding band gap energy of bulk semiconductor materials is lowered at elevated temperatures as increased atomic vibrations increase interatomic spacing which decreases the potential seen by the electrons in the material, thus reducing the size of the observed band gap energy. It can be expected that a similar phenomenon may be observed for the larger clusters in this study. For instance, bulk pure Si has a band gap energy of 1.17 and 1.11 eV at 0 and 300 K, respectively, and bulk pure Ge has a band gap energy of 0.744 and 0.660 eV at 0 and 300 K, respectively.

Many semiconducting materials or material precursors are characterized as hyperpolarizable and are analyzed by means of vibrational spectroscopy, i.e. Infrared or Raman spectroscopy. In the case of Raman spectroscopy, the corresponding analysis of the electronic wavefunction indicates that the electron absorption corresponds to the transition from the ground state to the first excited state and is conventionally described by the one-electron vertical excitation from the HOMO to the LUMO. For most clusters in this study, the HOMO is delocalized over the entire structure. By contrast, the LUMO is still largely delocalized over the entire structure but also extends well beyond the center of mass of the nuclei positions. Consequently, the HOMO-LUMO transition implies an electron density transfer to the limits of the molecular orbitals and this phenomena is consistent with semiconducting material behavior. This extreme delocalization of electron density suggests facile electron density transfer between neighboring clusters in the absence of a formal covalent bond formation, which can be useful for the development of self-assembling nanomaterials. Examples of this LUMO behavior can be seen in Appendix A1 of the Supporting Information for the trigonal planar (T), trigonal pyramidal (TP), and prismane (Pri) geometries, where this behavior is most pronounced in structures that contain one or more Ge atoms. Figure 3.6 presents a comparison of calculated contour surfaces of the frontier molecular orbitals (HOMO, LUMO) for the TBP-1 cluster using the B3LYP/6-31g(d), G3//B3LYP, and G4//B3LYP levels of theory. It is important to highlight how the LUMO contour changes significantly between the B3LYP/6-31g(d) and G3//B3LYP levels of theory; however, the HOMO contour is essentially the same between these two level of theory. The HOMO and LUMO contour predictions at the G4//B3LYP level of theory show the strongest inclusion of electron correlation effects as can be observed in Figure 3.6 for the TBP-1 cluster.

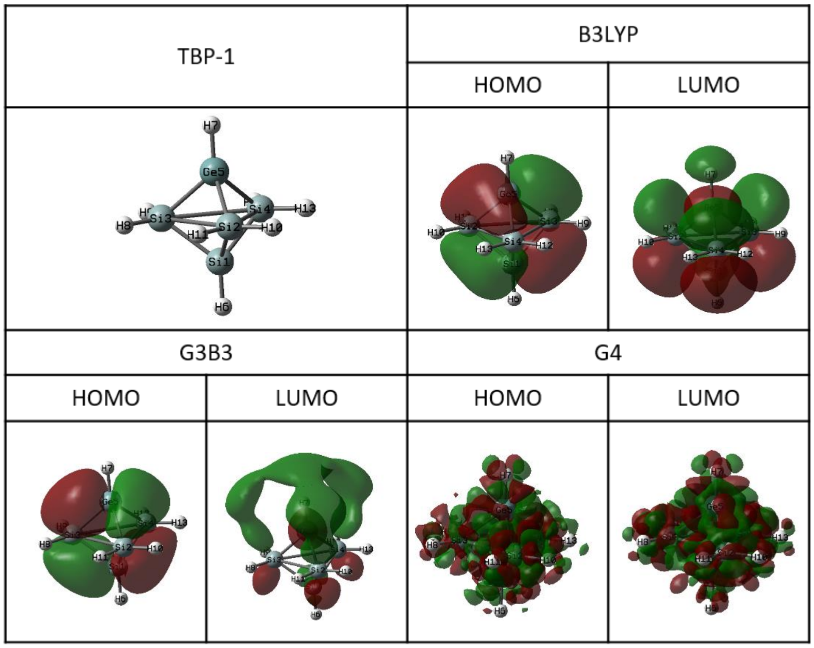

Figure 3.6. Comparison of calculated contour surfaces of frontier molecular orbitals (HOMO, LUMO) for the TBP-1 cluster using the B3LYP/6-31g(d), G3//B3LYP, and G4//B3LYP levels of theory. The HOMO and LUMO orbital distributions are presented using an isovalue of 0.02. The nomenclature to identify cluster geometry is the same as in Figure 3.1.

Since molecular orbital (MO) theory is by far the most widely used by chemists and chemical engineers, it is important to place the HOMO-LUMO energy gap in a MO framework for reacting chemical systems. That is, according to the notation introduced in the Computational Methodology section, hard molecules have a large HOMO-LUMO energy gap, and soft molecules have a small HOMO-LUMO energy gap. A small HOMO-LUMO energy gap is correlated to small vertical excitation energies to the manifold of excited energy states. Therefore, soft molecules, with a smaller energy gap than hard molecules, will be more polarizable by definition. High polarizability is the most characteristic property attributed to soft Si, Ge, and SiGe clusters. HOMO-LUMO energy gaps should be small for the most favorable bonding or non-bonding interaction between molecules or clusters, i.e., both reactants or molecules should exhibit soft character. As listed in Table 3.6, the trigonal pyramidal and prismane Si, Ge, and SiGe clusters are the softest species in this study, and thus most reactive due to smaller energy gaps than the remaining clusters and acyclic species. Consequently, these clusters also have a 1:1 Si-to-H or Ge-to-H atomic ratio, whereas the other species in this study have a lower Si or Ge atomic ratio to H. On average, less passivation with hydrogen will result in a more reactive cluster or acyclic species. As defined in the Computational Methodology section, molecular hardness, softness, and chemical potential calculated from the G3//B3LYP level of theory are presented in Table 3.6.

Table 3.6. Calculated quantum chemical molecular descriptors for hardness (η), chemical potential (μ), and softness (σ) at the G3//B3LYP level of theory for all hydrogenated Si, Ge, and SiGe clusters and acyclic species in this study. Hardness in eV, chemical potential in eV, and softness in eV^{-1}.

Index		η	μ	σ	Index		η	μ	σ
1	L-1	7.3	-5.9	0.14	28	ST-4	4.9	-3.6	0.21
2	L-2	6.2	-4.9	0.16	29	TBP-0	5.2	-3.9	0.19
3	L-3	5.9	-4.6	0.17	30	TBP-1a	5.1	-3.9	0.2
4	L-4	6.1	-4.8	0.16	31	TBP-1b	5	-3.8	0.2
5	L-5	7.1	-5.7	0.14	32	TBP-2a	5	-3.9	0.2
6	L-6	6	-4.7	0.17	33	TBP-2b	4.9	-3.8	0.2
7	L-7	5.7	-4.4	0.18	34	TBP-2c	5	-3.8	0.2
8	T-0	5.2	-3.8	0.19	35	TBP-3a	4.9	-3.8	0.21
9	T-1	5.1	-3.7	0.2	36	TBP-3b	5	-3.9	0.2
10	T-2	5	-3.7	0.2	37	TBP-3c	4.9	-3.8	0.2
11	T-3	5	-3.7	0.2	38	TBP-4a	4.9	-3.8	0.2
12	TP-0	4.1	-2.9	0.24	39	TBP-4b	4.8	-3.8	0.21
13	TP-1	4	-2.9	0.25	40	TBP-5	4.8	-3.8	0.21
14	TP-2	3.9	-3	0.26	41	Pri-0	4.6	-3.4	0.22
15	TP-3	3.8	-2.9	0.26	42	Pri-1	4.5	-3.4	0.22
16	TP-4	3.8	-2.9	0.26	43	Pri-2a	4.4	-3.4	0.22
17	ST-0	5.1	-3.8	0.2	44	Pri-2b	4.4	-3.4	0.22
18	ST-1a	5.1	-3.8	0.2	45	Pri-2c	4.5	-3.4	0.22
19	ST-1b	5	-3.7	0.2	46	Pri-3a	4.4	-3.4	0.22
20	ST-1c	5	-3.7	0.2	47	Pri-3b	4.4	-3.4	0.23
21	ST-2a	5	-3.7	0.2	48	Pri-3c	4.4	-3.4	0.23
22	ST-2b	5	-3.7	0.2	49	Pri-4a	4.4	-3.4	0.23
23	ST-2c	4.9	-3.6	0.2	50	Pri-4b	4.4	-3.4	0.23
24	ST-2d	4.9	-3.6	0.2	51	Pri-4c	4.4	-3.4	0.23
25	ST-3a	4.9	-3.6	0.2	52	Pri-5	4.4	-3.4	0.23
26	ST-3b	4.9	-3.6	0.21	53	Pri-6	4.4	-3.4	0.23
27	ST-3c	4.9	-3.6	0.2					

Developing materials with desired optoelectronic properties has always been at the forefront of the semiconducting electronics industry. The optical properties of Si clusters and nanocrystals have been intensively studied due to the possible technological applications of Si in the semiconductor industry. It has been shown that the large HOMO–LUMO energy gaps of metal encapsulated silicon clusters coupled with their weak reactivity make these structures most suitable for optical absorption and photoluminescence in the visible region. Some of these studies have been driven by the desire to understand the quantum effects of confinement in reduced structural dimensions. To control the triplet/singlet excited states in a designed manner for a desired optoelectronic property, the rational adjustment of the singlet-triplet energy gap ($\Delta E'_{ST}$) between the first singlet (S_1) and triplet (T_1) excited states is the key as depicted in Figure 3.7a-7b. Insight into this latter value can be found by the difference between the HOMO-LUMO energy gap and the singlet-triplet splitting energy value (ΔE_{ST}) between the singlet ground state (S_0) and first excited triplet electronic spin state (T_1). Here we complement and extend optoelectronic studies for Si, Ge, and SiGe clusters by calculating the HOMO-LUMO energy gap, which provides insight into the energy gap between the singlet ground state (S_0) and first excited singlet state (S_1), and relating this energy value to the energy splitting between the singlet ground state (S_0) and first excited triplet electronic spin state (T_1), (ΔE_{ST}).

For instance, examination of Table 1 for the singlet-triplet energy splitting values (ΔE_{ST}) of SiH_4 and GeH_4 reveals values of 3.9 and 3.6 eV, respectively. Examination of Figure 4 for the HOMO-LUMO energy gaps of SiH_4 and GeH_4 reveals values of 14.6 and 14.2 eV, respectively. Similar analysis can be extended to the other species in this study using Table 1 for singlet-triplet splitting energy values (ΔE_{ST}), and Figures 3.4 and 3.5 for HOMO-LUMO energy gap values. On average, our theoretical studies suggest that the Ge-doped clusters will exhibit a lower HOMO-LUMO energy gap and singlet-triplet splitting energy value (ΔE_{ST}). Our results suggest that the vertical excitation energy from a singlet spin state to the excited singlet spin state is positively correlated with the HOMO-LUMO energy gap for a molecule optimized in the ground singlet spin state. Given our preliminary findings on varying levels of passivation, our calculations also suggest that other surface termination schemes may increase cluster chemical stability such that properties of the respective cluster can be used for optoelectronic materials. In Figure 3.7a-7b, representative energy level diagrams of two optoelectronic processes determined by singlet-triplet splitting ($\Delta E'_{ST}$) between energies of the lowest singlet (E_{S1}) and triplet (E_{T1}) excited states are presented for the sake of clarity.

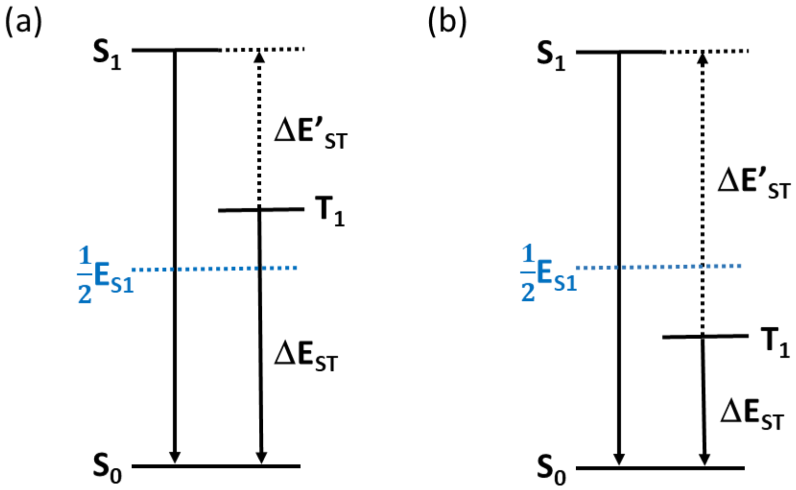

Figure 3.7. Representative energy level diagrams of two optoelectronic processes determined by singlet-triplet splitting ($\Delta E'_{ST}$) between energies of the lowest singlet (E_{S1}) and triplet (E_{T1}) excited states. Process (a) has a small $\Delta E'_{ST}$ value, and process (b) has a large $\Delta E'_{ST}$ value. The singlet-triplet splitting values (ΔE_{ST}) between energy of the ground state singlet (E_{S0}) and first excited triplet state (E_{T1}) which are reported in Table 3.1 for selected species are also labelled for the sake of clarity. Downward arrows are associated with emissions, and upward arrows are associated with transitions.

Rational design and optimization of nanoclusters for semiconducting nanomaterial applications traditionally requires the systematic synthesis and examination of various cluster molecules. This conventional “trial-and-error” approach generally requires considerable time and labor costs. Prediction of the cluster properties with a machine learning approach would facilitate the rational design and optimization of nanomaterials, and this approach would allow the discovery of nanostructures with desired properties rapidly and efficiently. Developing this “nanostructure informatics” approach would create a practical method to develop a robust predictive model for nanocluster reactivity. A convenient set of quantum chemical parameters to train our models using a machine learning approach is the fractional electrons transferred during molecular interaction of reactants which was previously introduced in the Computational Methodology section. The fractional electrons transferred during molecular interaction of reactants, ΔN, is correlated to the degree of nucleophilicity and electrophilicity of the reactants, which is highly desirable for tailored nanomaterials design such as self-assembling nanomaterials.

3.6 Generalization of Electronic properties using a machine learning approach

Implementation of Eq. 3.7 to calculate fractional electrons transferred during molecular interaction of reactants, ΔN, using the quantum chemical parameters in Table 3.6 are presented in Figure 3.8. In Figure 3.8, we present 2809 data points representing ΔN values for the interaction of all 53 hydrogenated Si, Ge, and SiGe species in this computational study. The graphical representation in Figure 3.8 very conveniently visualizes the key nucleophilic and electrophilic characters of all potential molecular interactions in this study. Dark red and dark blue regions of this data set represent interactions with the largest ΔN values. The sign of the ΔN value represents the directionality of the electron transfer process. For instance, if one chooses a reactant B from the x-axis and moves vertically along the y-axis of Figure 3.8, a negative ΔN value signifies that reactant B is a nucleophile when interacting with the corresponding reactant A for the molecular interaction.

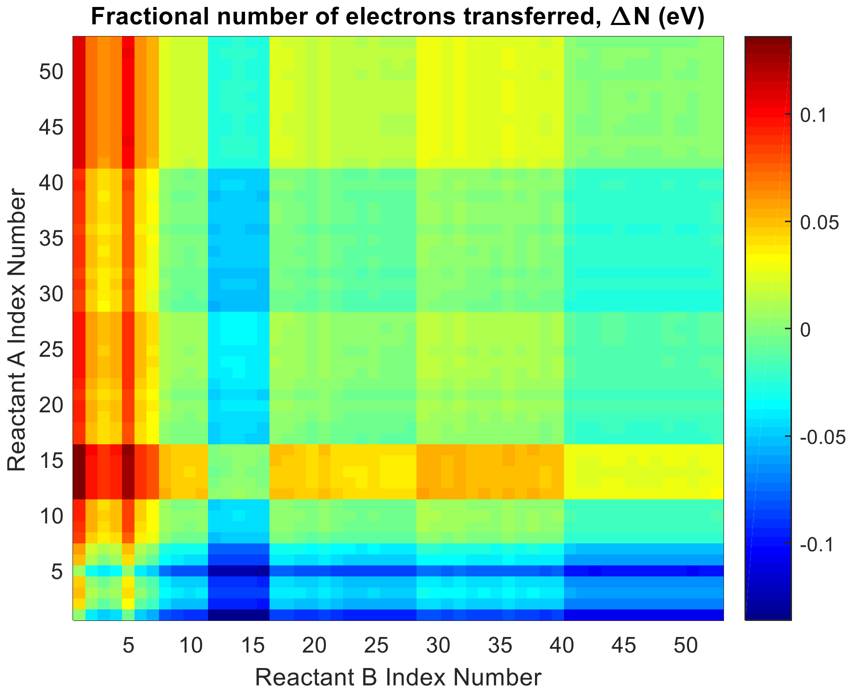

Figure 3.8. Contour map of the calculated fractional electrons transferred in eV (ΔN) for molecular interactions of all 53 molecules in this study. ΔN follows Eq. 3.3 where the frontier molecular orbital energies are calculated using the G3//B3LYP level of theory. The reactant index number follows the numbering scheme of Table 3.6

Conversely, reactant A for that same interaction has more electrophilic character during the interaction. The ΔN values in Figure 3.8 are derived directly from quantum chemical calculations at the G3//B3LYP level of theory; however, our study was generalized beyond these calculations by introducing a machine learning approach to create a robust multiple linear regression equation to predict this ΔN value for molecular interactions not explicitly examined in this study. Eq. 3.8 is proposed for this purpose where ΔN is a function of the molecular weight of reactants A and B, ω_i, the degree of passivation of reactants A and B, π_i, and the regression coefficients, C_i. The degree of passivation of the reactants is defined as the atom count of total heavy atoms, Si and Ge, divided by the atom count of total hydrogen atoms. The use of the molecular weight and degree of cluster passivation allows for the implementation of nanomaterials design efforts independent of the need to perform computationally expensive quantum chemical calculations during the initial screening efforts of nanomaterials design.

$$\Delta N = C_1 * \omega_A + C_2 * \pi_A + C_3 * \omega_B + C_4 * \pi_B \qquad \text{Eq. 3.8}$$

Table 3.7a contains two models which follow Eq. 8 and were regressed using a machine learning approach to statistical data analysis. Table 3.7b also contains the regression analysis including the statistical significance and errors of the different models evaluated. Model 1 is comprised of regression coefficients, C_i, for a training set of all 2809 data points for ΔN in this study. The overall model was deemed significant if the F-test satisfied the 99% confidence level (i.e., the p-value was below $\alpha = 0.01$). In fact, the total regression for Model 1 was statistically significant at the 99.99% confidence interval, and all four regression coefficients, C_i, were also statistically significant at the 99.99% confidence interval despite the total regression for Model 1 having an R^2-value of 0.6660. Although not presented in Table 3.7, an additional set of four cross terms were added to the full regression Eq. 3.8 of the forms, $C_{ij}\,\omega_i\,\omega_j$, $C_{ij}\,\pi_i\,\omega_j$, and $C_{ij}\,\pi_i\,\pi_j$ to determine if the R^2-value could be improved. These additional cross terms did not improve the R^2-value for the full regression and were not statistically significant at the 95% confidence interval. Figure 3.9 displays a parity plot for Model 1 of fractional electrons transferred in eV, ΔN, for the training set of 2809 molecular interactions calculated from the G3//B3LYP level of theory.

Table 3.7. (a) Coefficients for the full regression containing 2809 ΔN values (Model 1) and for the regression containing 10% of the ΔN values randomly removed (Model 2), (b) statistical analysis for the least squares regressions and summary of errors, (c) performance summary of the sensitivity analysis using the refitted coefficients (Model 2) and the coefficients from the full regression (Model 1). AAD denotes average absolute deviation.

(a) Regression coefficients

	C_1	C_2	C_3	C_4
Model 1	0.08245	0.000071	-0.08245	-0.000071
Model 2	0.08309	0.000067	-0.08186	-0.000074

(b)**Training set**

		Regression F-Test			
	R^2-value	F-value	P-value	AAD (eV)	std dev
Model 1	0.6660	1398.46	<0.001	0.0172	0.0144
Model 2	0.6690	1275.56	<0.001	0.0170	0.0143

(c) **Validation set**

Regression parameters	AAD (eV)	std dev
Model 1	0.01879	0.01491
Model 2	0.01881	0.01491

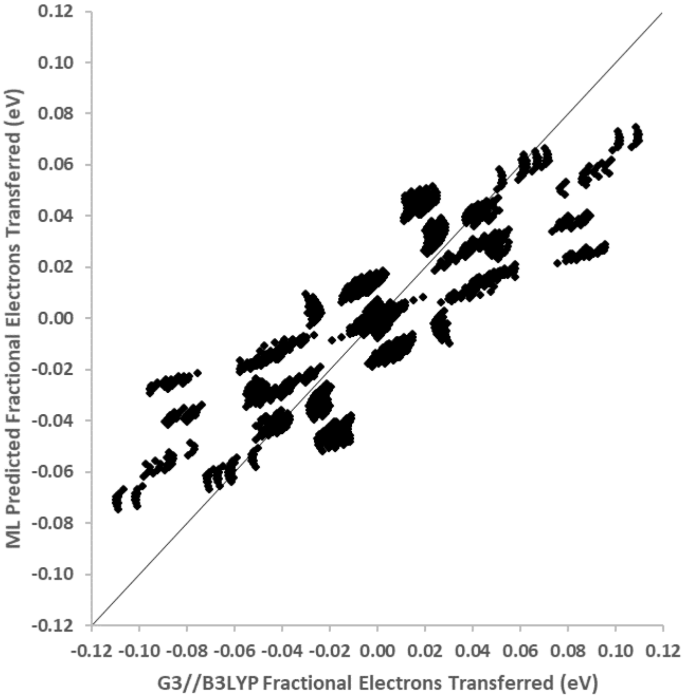

Figure 3.9. Parity plot of fractional electrons transferred in eV for the training set of 2809 molecular interactions from the G3//B3LYP level of theory. ML denotes prediction of fractional electrons transferred using the machine learning model regressed in this study.

Finally, the best predictive model for ΔN values and its four regression coefficients, C_i, were validated using the sensitivity analysis proposed by Mavrovouniotis. This approach removes 10% of the molecular interactions randomly (or 281 ΔN values for our study), and the four regression coefficients are refitted. The new regression coefficients are then used to predict the ΔN values of the removed molecular interactions. The differences between these ΔN values and the values predicted from the original four regression coefficients are then calculated to assess the sensitivity of the regression coefficients. Model 2 presented in Table 3.7 evaluates the sensitivity analysis of the four regression coefficients, C_i, for the prediction of ΔN values. A performance summary for the prediction of ΔN values for the removed molecular interactions using the refitted regression coefficients and the regression coefficients from the full regression containing 2809 molecular interactions is presented in Table 3.7c. The run using the refitted regression coefficients had an average absolute deviation value of 0.01881 eV for the validation set of 281 molecular interactions compared to the G3//B3LYP values, which is a negligibly higher error than the errors obtained using the regression coefficients from the full regression containing 2809 molecular interactions. Namely, the average absolute deviation value of 0.01879 eV was obtained for the validation set of 281 molecular interactions compared to the G3//B3LYP values when using the regression coefficients from Model 1. Thus, the predictive capability of our multiple linear regression model for molecular interactions, or ΔN values, not included in the training set is very good. This generalization for the prediction of molecular interaction properties is necessary because computational and/or experimental investigation of all potential interactions of Si/Ge/SiGe clusters is not feasible.

Chapter 4 Hydrogenated Si and SiN Nanoclusters

4.1 Introduction

Silicon nitride is used in a variety of important technological applications. Due to the high strength, high thermal stability, low density, resistance, silicon nitride (Si_3N_4-based ceramics) has attracted great interest for their multi usages for such as cutting tools, anti-friction bearings in turbine[83-85] and electronic application[4, 5]. Specifically, silicon nitride (Si_3N_4) is a wide band-gap (5.3eV) semiconductor material[5], silicon nitride thin film is used as insulating, masking and passivating materials[6] in integrated circuits in the microelectronics industry.[4, 7, 11]

So far, more than six different crystalline polymorphs of Si_3N_4 including α- and β-Si_3N_4 have been reported in the literature[86, 87]. Silicon nitride which can be prepared in several different synthetic routes is an important material for barrier coatings in electronic devices and amorphous Si_3N_4 powder also occurs as an intermediate during the α-Si_3N_4 synthesis. Basically, four different methods of synthesis of silicon nitride from powders were reported; 1) Direct synthesis from elemental silicon with nitrogen, 2) Carbothermic reduction of SiO_2 and carbon under N_2 flow, 3) Diimide process; $SiCl_4$ is reacted with NH_3 at 0~20 ºC to form amorphous, polymeric silicon diimide ($[Si(NH)_2]_n$) which transforms into amorphous silicon nitride upon annealing at higher than 1000 ºC, 4) Dissociation (pyrolysis/CVD) of volatile silicon compounds such as SiH_4, $SiCl_4$ with NH_3.[88, 89] In addition to these classical routes to Si_3N_4, alternatives have been suggested. These include, for example, Self-propagating high-temperature synthesis (SHS-process), plasma- or laser-enhanced techniques.[90-92] The pyrolysis of silicon-containing polymers, especially polysilazanes gives amorphous as well as crystalline silicon nitride, depending on the pyrolysis temperature[93].

In order to prepare Si_3N_4 materials for the electronic devices such as oxidation masks, passivation layers, gate insulating layers, dielectric layers and antireflection coatings, plasma-enhanced-chemical-vapor-deposition (PECVD)[94, 95] is considered most efficient method comparing to thermal oxidation or low-pressure chemical-vapor-deposition (LPCVD), which take place at temperatures approaching 1000 ºC. Although silicon nitride has been researched intensively and the conditions of silicon nitride synthesis has demonstrated in many studies, it appears that the fundamental understanding of the hydrogenated silicon nitride synthesis process is still unknown. Homogeneous gas-phase nanomaterials formation of silicon nitride is a complex phenomenon in which hundreds, or possibly thousands of species, undergo simultaneous reaction. Besides inactive layer application, silicon-nitride is used as alternative anode material for lithium ion battery. Guzman et al.8 and Ulvestad et al.9 demonstrated the much higher galvanostatic capacity of SiNx, which are 1400 and 1500 mAh g-1 compared to commercial graphite (372 mAh g-1). From the fact that the nitrogen contents affect to the reversible capacity of material and cycling stability which is found by Ulvesta team, I believe that this study could contribute to design silicon nitride anode material with optimized nitrogen content.

Since electronic, optoelectronic and photovoltaic properties of silicon nitride that are controlled or affected by defects, the nature and number of defect sites of silicon nitride may change with the preparation method used. Usually, the deposition of silicon nitride is done from 700 ºC in the vapor phase from the precursors such as SiH_4, $SiCl_4$, SiH_2Cl_2 with NH_3. Surface reactions play an important role during the chemical vapor deposition of $Si_xN_yH_z$. However, understanding semiconducting nanomaterials formation from the co-pyrolysis of silane (SiH_4) and ammonia (NH_3) is still incomplete as well.

Detailed knowledge of the thermodynamics and the nature of Si-N bonding is still required to understand the spontaneous processes leading to the formation of self-organized structures. Compared to the vast data available on solid-state materials, theoretical solid-state studies on materials possessing Si-N bonds and comprehension of the SiN chemistry, especially for small clusters, are very rare. The limited results which are available on such Si-N binary molecules and molecular ions and solid products are found with experimental synthesis conditions, measurement of concentration of formed $Si_xN_yH_z$ via vacuum ultraviolet laser single photon-ionization coupled with time-of-flight mass spectrometry and a few advanced *ab initio* investigation of gas-phase reactions between silane and ammonia[96-101]. However, no theoretical thermodynamic data, which could indirectly validate the calculated structures through comparison against the existing experiments, are available. Thus, detailed theoretical studies connecting the structures, bonding, thermodynamic and electronic properties of Si and SiN clusters are critically needed.

Furthermore, the kinetics of inorganic cluster and nanoparticle formation of Si clusters and nanoparticles[102, 103] has been described at the mechanistic level by automated network generation techniques.[104] Rate coefficients must be estimated for every elementary step comprising the mechanistic model, and kinetic correlations are used to make this tractable. One common method for predicting activation barriers (E_a) is the Evans-Polanyi correlation; however, these structure-activity correlations require detailed thermochemical information for each reacting species. The existing group additivity database[37] for the prediction of thermochemical properties of hydrogenated silicon clusters was revised and augmented with new atom-centered groups, ring corrections, and bond-centered groups to accurately capture more complex species by our group. However, there are still limited studies available that predict the thermochemical properties of hydrogenated silicon nitride clusters, which is the next step for expanding our thermochemistry database for semiconducting nanoparticle formation.

For this purpose, we conducted a computational study of Si and SiN alloy acyclic hydrides and clusters ($Si_xN_yH_z$, $1<X+Y\leq6$) to predict structures, thermochemistry, and electronic properties. This paper presents the thermochemical properties of 32 cyclic and polycyclic Si and SiN clusters and 27 acyclic Si and SiN species, i.e., standard enthalpies of formation, standard entropy values, and constant pressure heat capacities. The hydrogenated clusters in this study involved different degrees of hydrogenation, i.e., the ratio of hydrogen to Si and Ge atoms varied widely depending on the size of the cluster and/or degree of multifunctionality. The composite method of G3//B3LYP[105, 106] was used to calculate the electronic energy, and then statistical thermodynamics was applied to all the hydrogenated Si and SiN clusters to incorporate temperature effects. Enthalpies of formation at 1 atm and 298 K were calculated using atomization energies. Standard entropies and constant pressure heat capacities were calculated using a temperature-dependent scaling factor for the vibrational frequencies to account for anharmonicity. Internal rotations in acyclic hydrogenated silicon nitride and the substituted trigonal clusters that were more appropriately treated as free rotors were quantified using the one-dimensional hindered rotor and free rotor approximations as well. Our studies have established trends in thermodynamic properties (standard enthalpy of formation (ΔH°_{f}), standard

entropy (S°), and constant pressure heat capacity (C_p)), as a function of cluster composition and structure. Furthermore, I compared HOMO-LUMO energy gaps and HOMO and LUMO electron distributions in order to gain insight into the electronic stability of the hydrogenated Si and SiN clusters. Quantum chemical parameters such as electronic chemical potential μ, global hardness η, and the softness σ were also calculated to provide valuable information about chemical stability. These quantum chemical parameters were generalized using a machine learning approach to assess charge transfer during molecular interaction of hydrogenated Si and SiN clusters in the gas phase. Natural bond orbital analysis was conducted to further investigate the effect of nitrogen on the stability of the molecule.

4.2 Computational Methodology

Quantum chemical calculations were performed with the Gaussian 16 software.[55] All electronic energies for the hydrogenated Si and SiN clusters and acyclic species were calculated using the G3//B3LYP composite method,[107] which uses B3LYP/6-31g(d) geometries and higher-level corrections based on single point energies. The Gn methods assume basis set additivity and add an empirical correction to recover part of the remaining correlation energy.

The optimized structures for all 59 hydrogenated Si and SiN clusters investigated in this study are depicted in Figure 4.1. The hydrogenated clusters of this study can exist in the singlet state and triplet state.[37, 59-61] As shown in Table 4.1, using the G3//B3LYP method, triplet-singlet splitting values of acyclic and cluster species were investigated. These calculated triplet-singlet splitting values suggest that the singlet potential energy surface is significantly lower in energy than the triplet potential energy surface. Thus, for all results reported in this study, the electronic wave functions for the hydrogenated Si and SiN clusters were optimized in the singlet state. Geometries and harmonic vibrational frequencies are confirmed local minima on the singlet potential energy surface, i.e., all of the vibrational frequencies are real. The harmonic vibrational frequencies and zero-point vibrational energy (ZPE) were linearly scaled by a temperature-dependent scaling factor of 0.98, respectively, to account for anharmonicity in the normal vibrational modes as a function of temperature as suggested by Scott and Radom and Alecu and co-workers.[63, 64] Using conventional statistical thermodynamics, molecular partition functions based on the harmonic oscillator and rigid rotor approximations were used to calculate thermodynamic properties as a function of temperature. Internal rotations in acyclic hydrogenated silicon nitride and the substituted trigonal clusters that were more appropriately treated as free rotors were quantified using the one-dimensional hindered rotor and free rotor approximations. This procedure was performed automatically using the Calctherm script developed by our group.[68] Anharmonic small ring movements (e.g.,the pseudorotation of cyclopentasilanes and the ring puckering of cyclotetrasilanes) were not treated.

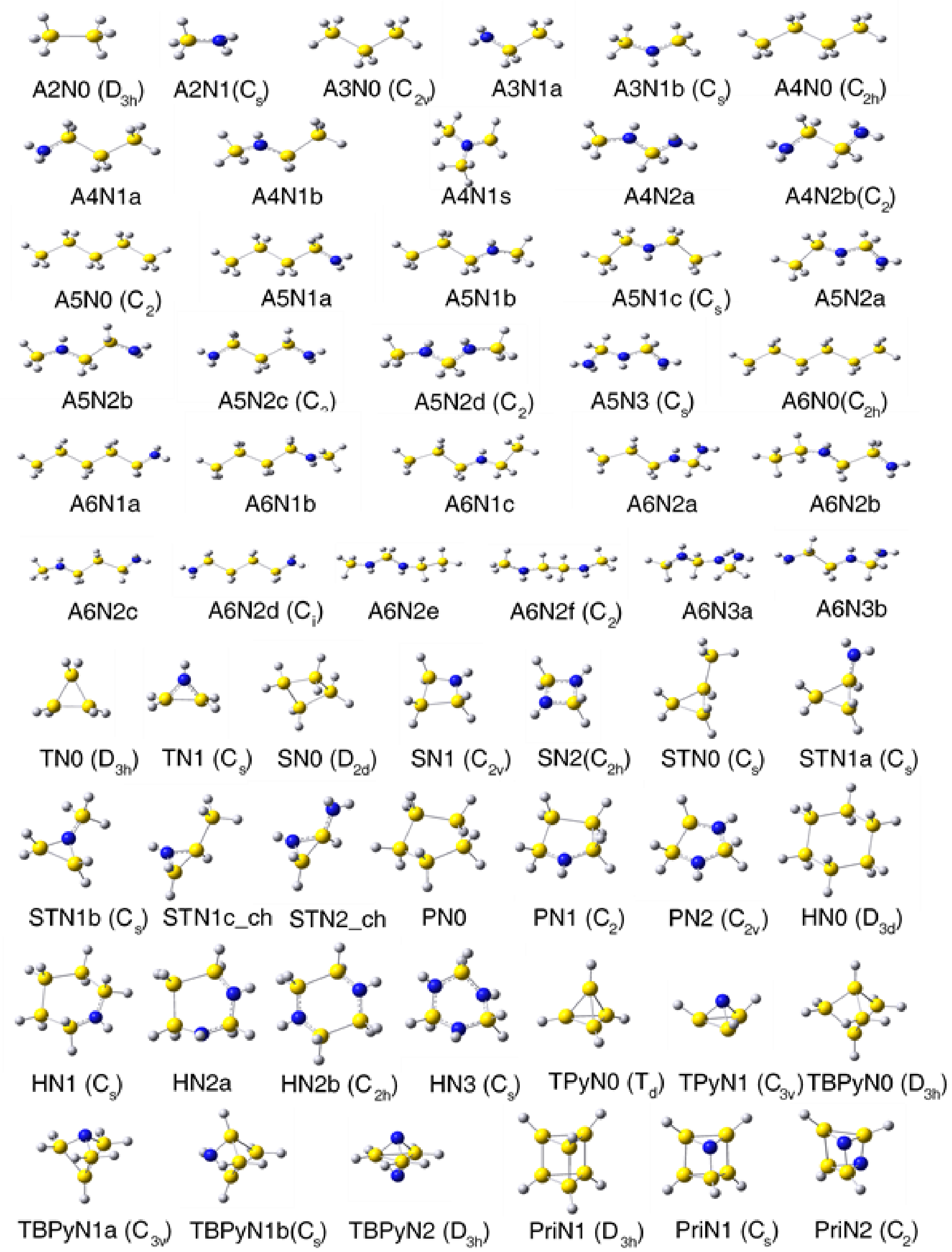

Figure 4.1. Optimized $Si_xN_yH_z$ (x + y = 6) cluster geometries using the G3//B3LYP level of theory. The clusters are denoted by A for acyclic, N for the number of N atoms, TN for trigonal planar, SN for square planar, STN for substituted trigonal planar, PN for pentagonal planar, HN for hexagonal planar, TPyN for trigonal pyramid, PriN for prismane structres, TBPyN for trigonal bipyramidal geometries. The indices are incremented by integer values to correspond with the replacement of a Si (yellow) atom by a N(blue) atom from 0 to 2 or 3, where 0 is the pure Si Cluster. The lower case letter symbol denotes isomers.

Table 4.1. Calculated Singlet-Triplet Splitting Values of Selected Si and SiN Species Using the G3//B3LYP Level of Theory. The nomenclature to identify molecular geometries is the same as in Figure 4.1

	G3B3 electronic energies with zero-point vibrational energies		
	spin multiplicity		
molecules	singlet (Hartree)	triplet[a] (Hartree)	triplet-singlet splitting (eV)
A2N1	-347.0658	-346.9058	4.4
A3N1b	-637.6295	-637.4591	4.6
TN1	-636.3952	-636.3402	1.5
STN0	-1162.1246	-1162.0639	1.7
STN1b	-926.9654	-926.9058	1.6
PN2	-982.3779	-982.2198	4.3
HN1	-1508.0901	-1507.9761	3.1
TPyN1	-924.4658	-924.4579	0.2
TBPyN1a	-1216.3215	-1216.2637	1.6
TBPyN2	-981.1041	-981.0553	1.3
PriN1	-1504.4395	-1504.3949	1.2

[a] All molecules in triplet state exist in a form of dissociation.

Calculation of thermochemical properties was performed automatically using the CalcTherm script, which interfaces with electronic structure codes to provide thermochemical properties (S, C_p , H) of individual species at elevated temperatures.[68] The external symmetry numbers for the hydrogenated SiN clusters examined in this study impact the molecular partition function for rotation and reduce the rotational entropy by an amount equivalent to R ln σ_{rot},[67] where σ_{rot} is the external symmetry number of the molecule and R is the ideal gas constant.

The enthalpy of formation of a given molecule $Si_xN_yH_z$ can be calculated from its atomization energies using Eq (4.1):[37]

$$\Delta H^{\circ}{}_{f,298}(Si_xN_yH_z) = \left[x\Delta H^{\circ}{}_{f,298}\,(Si) + y\Delta H^{\circ}{}_{f,298}\,(N) + z\Delta H^{\circ}{}_{f,298}\,(H)\right] - \Delta H^{\circ}{}_{a,298}\,(Si_xN_yH_z) \quad (4.1)$$

where the formation enthalpies of atomic silicon, nitrogen and hydrogen are the experimental values obtained from the JANAF tables; $\Delta H^{\circ}_{f,298}(Si) = 450$ kJ mol^{-1}, $\Delta H^{\circ}_{f,298}(N) = 473$ kJ mol^{-1}, $\Delta H^{\circ}_{f,298}(H) = 218$ kJ mol^{-1} and $\Delta H^{\circ}_{f,298}(Si_xN_yH_z)$. The atomization energy defined as the enthalpy change upon decomposition of a molecule into its component atoms can be evaluated using Eq (4.2):

$$\Delta H^{\circ}{}_{a,298}(Si_xN_yH_z) = \left[xH_{a,298}\,(Si) + yH_{a,298}(N) + zH_{a,298}(H)\right] - H^{298}(Si_xN_yH_z) \quad (4.2)$$

where $H_{298}(Si)$, $H_{298}(N)$ and $H_{298}(H)$ are the enthalpies of atomic silicon, nitrogen and hydrogen at 298 K, respectively, and $H_{298}(Si_xN_yH_z)$ is the enthalpy of $Si_xN_yH_z$ at the same temperature. These enthalpies can be calculated as the sum of the electronic energies (E_{el}), zero point energies (ZPE), and thermal corrections ($E_{vib}{}^{298}$, $E_{trans}{}^{298}$, and $E_{rot}{}^{298}$) at 298 K, as follows from canonical molecular partition functions assuming an ideal gas at 1 atm using Eq. 4.3:

$$H^{298} = E_{el} + ZPE + E^{298}_{vib} + E^{298}_{trans} + E^{298}_{rot} + \Delta PV \quad (4.3)$$

All of the quantities on the right-hand side of Eq 4.3 are obtained from quantum chemical calculations, and the standard enthalpy of formation of $Si_xN_yH_z$ is then calculated.

In order to test the accuracy of our calculations, calculations were carried out on small acyclic Si and SiN hydrides using the B3LYP/6-31G(d), B3LYP/6-31G(d,p), B3LYP/6-311G(d,p), B3LYP/6-311++G(d,p), G3//B3LYP, G3//B3LYP with Calctherm methods and summarized in Table 4.2. The calculated results from the G3//B3LYP and modified G3//B3LYP with Calctherm composite methods were found to be in reasonable agreement with available experimental data for standard enthalpy of formation at 298 K. The performance summary for prediction of thermochemical properties for small acyclic Si and SiN hydride chemistries indicated that the G3//B3LYP composite methods outperform the B3LYP method with different polarization and diffusion function on estimating standard enthalpy of formation when compared to available experimental data. Calculation of the standard enthalpy of formation at 298 K has been overestimated with all level of methods. In the case of estimating standard entropy values of the acyclic species, all predicted standard entropies were estimated between 0.2 and 15.3 J mol^{-1} K^{-1} in average absolute deviation when compared to available experimental data. For constant pressure heat capacity, all predicted the calculation results for all six methods were estimated between 0.2 and 4.5 J mol^{-1} K^{-1} in average absolute deviation when compared to available experimental data.

Analogously, a previous study[37] on silicon hydrides from our group confirmed that the G3//B3LYP composite method agrees with available experimental data within an average absolute deviation of 1.0 kcal mol^{-1} while the W-1 method captures available experimental data within an average absolute deviation of 2.0 kcal mol^{-1}.[37] Our another previous study on silicon-germanium hydrides from our group compared CBS-QB3 and G3//B3LYP standard enthalpies of formation at 298 K to available data, which demonstrated G3//B3LYP method is more suitable for predicting thermochemical properties of SiGe alloy clusters.[108] In this study, however, due to large electronegativity difference between N and Si, N and H, more flexible basis sets were needed. On this purpose, we added different level of polarization function and diffusion function to B3LYP. B3LYP with polarized triple-zeta 6-311++G(d,p) basis set predicted most accurate standard enthalpy only for ammonia, but prediction for silicon hydrides were poor. On the other hand, G3//B3LYP estimated overall accurate values. This can be seen the attribution of a higher level correction of G3//B3LYP which is based on a regression of correction parameters from an experimental data set of 299 energies containing enthalpies of formation, ionization potentials, electron affinities, and proton affinities.[105, 106] Accordingly, the G3//B3LYP method was a reasonable choice because the cluster property data set from this study is intended to be used in conjunction with an existing G3//B3LYP database developed by our group for the estimation of silicon hydride thermochemical properties.

Table 4.2. Comparison of Calculated Standard Enthalpy of Formation, Standard Entropy, and Constant Pressure Heat Capacity at 298 K to Available Experimental Data for Small Acyclic Hydrogenated Silicon and Nitrogen Species using the B3LYP/6-31G(d), B3LYP/6-31G(d,p), B3LYP/6-311G(d,p), B3LYP/6-311++G(d,p), G3//B3LYP and G3//B3LYP with levels of theory

Molecules	net charge	spin multiplicity							$\Delta H^{\circ}_{f,298K}$ (KJ/mol)							
level of theory			Exp		B3LYP /6-31G(d)	Deviation	B3LYP /6-31G(d,p)	Deviation	B3LYP /6-311G(d,p)	Deviation	B3LYP /6-311++G(d,p)	Deviation	G3B3	Deviation	G3B3 w/ Calctherm	Deviation
NH_3	0	1	-45.9	[a]	-12.1	33.8	-38.1	7.8	-34.7	11.2	-45.9	0.1	-43.0	2.9	-39.4	6.5
Si_2H_6	0	1	80.3	[a]	104.3	24.0	86.8	6.5	103.2	22.9	105.8	25.5	75.7	4.6	80.5	0.2
Si_3H_8	0	1	120.9	[a]	163.2	42.3	139.8	18.9	163.5	42.6	167.1	46.2	112.5	8.4	119.0	1.9
SiN	0	2	403.7	[b]	500.5	96.8	500.5	96.8	495.5	91.8	494.3	90.6	467.2	63.5	467.4	63.7
average						49.2		32.5	54.3	42.1		40.6		19.9		18.1
									S^{298K}	(J/mol K)						
			Exp		B3LYP /6-31G(d)	Deviation	B3LYP /6-31G(d,p)	Deviation	B3LYP /6-311G(d,p)	Deviation	B3LYP /6-311++G(d,p)	Deviation	G3B3	Deviation	G3B3 w/ Calctherm	Deviation
NH_3	0	1	192.8	[a]	192.4	0.4	192.4	0.4	192.3	0.4	192.3	0.4	192.4	0.4	192.4	0.4
Si_2H_6	0	1	272.7	[a]	273.5	0.8	273.5	0.8	273.6	0.9	273.6	0.9	273.6	0.9	273.6	0.9
Si_3H_8	0	1	N.A.	[a]	352.6	-	352.8	-	264.8	-	264.8	-	352.6	-	352.5	-
SiN	0	2	216.8	[b]	216.6	0.2	201.5	15.3	216.6	0.2	216.6	0.2	216.6	0.2	216.6	0.2
average						0.5		5.5		0.5		0.5		0.5		0.5
									C_p	(J/mol K)						
			Exp		B3LYP /6-31G(d)	Deviation	B3LYP /6-31G(d,p)	Deviation	B3LYP /6-311G(d,p)	Deviation	B3LYP /6-311++G(d,p)	Deviation	G3B3	Deviation	G3B3 w/ Calctherm	Deviation
NH_3	0	1	35.6	[b]	34.6	1.0	34.8	0.8	34.9	0.8	34.9	0.8	34.6	1.0	34.6	1.0
Si_2H_6	0	1	80.0	[a]	79.5	0.5	79.4	0.6	79.6	0.4	79.6	0.4	79.5	0.5	79.4	0.6
Si_3H_8	0	1	N.A.		117.1	-	117.1	-	64.6	-	64.6	-	117.1	-	117.0	-
SiN	0	1	30.3	[b]	30.0	0.2	34.8	4.5	30.0	0.2	30.0	0.2	30.0	0.2	30.0	0.2
average						0.6		2.0		0.5		0.5		0.6		0.6

One of the significant features of the density functional theory is its suitability for defining the chemical reactivity; this is called conceptual DFT theory. The Conceptual DFT was developed by Parr et al.[109], which relies on the fact that the ground state energy of an N-electron system as given by the Hohenberg-Kohn theorem. Within the DFT theorem, the electron density can be considered as depending upon the number of electrons N and the external potential v(r), which are themselves determined solely by the density, in other words $E[\rho(r)] = E[N;v(r)]$. When a molecule reacts, its number of electrons increases or decreases according to a counter reagent whether it is nucleophilic or electrophilic. Therefore, the reactivity of a molecule to chemical reactions is determined by its response to changes in N and v(r). The electronic chemical potential, μ can be expressed as the functional derivative of the energy with respect to N when v(r) is kept as constant, which is the opposite of the electronegativity χ.[71]

$$\mu = \left(\frac{\partial E}{\partial N}\right)_{v(r)} \tag{4.4}$$

The quantitative expression for the chemical hardness,η, which can be expressed as the changes of the electronic chemical potential μ of the system with respect to the N at a fixed v(r),[73]

$$\eta = \left(\frac{\partial \mu}{\partial N}\right)_{v(v)} = \left(\frac{\partial^2 E}{\partial N^2}\right)_{v(r)} \tag{4.5}$$

The chemical Hardness η can be thought as a resistance of a molecule to exchange electron density within the environment.[71-74] With the finite difference approximation, Eq 4.6 is obtained.

$$-\mu = \frac{I+A}{2} = \chi \tag{4.6}$$

$$\eta = \frac{I-A}{2} \tag{4.7}$$

Here I and A represent the ionization potential and the electron affinity of a molecule, respectively. The inverse values of the global hardness are designated as the softness $\sigma = 1/\eta$.

Any chemical system (e.g., an atom, molecule, ion, or radical) is characterized by its μ and η. Using the Koopmans' theorem[75, 76] and Kohn–Sham (KS) Density Functional Theory (KS-DFT), these energies can be approached by $-E_{HOMO} = I$ and $-E_{LUMO} = A$. Thus, the calculated quantum chemical parameters such as the highest occupied molecular orbital energy E_{HOMO}, the lowest unoccupied molecular orbital energy E_{LUMO}, energy gap ΔE, electronic chemical potential μ, global hardness η, and the softness σ were calculated in our study. Here hybrid functionals systematically calculate HOMO energies that underestimate the first ionization potential values by several electron volts. Nevertheless, these tabulated quantum chemical parameters can be used in two possible ways: as a rank ordering of similar acids (electrophiles) or bases (nucleophiles) to predict relative properties or as a source of values to use in relevant equations such as Eq 4.8. If two systems or molecules, A and B are brought together, electrons will flow from that of lower χ to that of higher χ, until the chemical potentials become equal. As a first approximation, the (fractional) number of electrons transferred, ΔN, will be given by Eq 4.8. The difference in electronegativity drives the electron transfer, and the sum of the hardness parameters acts as a resistance. This reactivity index was predicted as well in this study.

$$\Delta N = \frac{\chi_B - \chi_A}{2(\eta_B + \eta_A)} \tag{4.8}$$

In order to better understand the stability of hydrogenated SiN alloy clusters, the natural boding orbital (NBO) analysis were conducted using NBO 6.0 program as implemented in the Gaussian 09 package with the B3LYP/6-31G(d) level. NBO calculation is important for the understanding of delocalization effect from the lone pair electrons (donor, i) to anti-bonding orbitals (acceptor,j). The interaction between the donor and acceptor orbitals can be used to measure the degree of intramolecular delocalization or hyperconjugation. The stabilization energy derived from the interactions was estimated by the second order perturbation interaction energy (E2), describe as Eq 4.9.[110]

$$E(2) = \Delta E_{ij} = q_i \frac{F(i,j)^2}{E_{(j)} - E_{(i)}} \qquad (4.9)$$

where q_i is the donor orbital occupancy (2 for closed-shell, 1 for open-shell), $E_{(i)}$ and $E_{(j)}$ are diagonal elements (orbital energies), and $F(i,j)$ is the off-diagonal NBO Fock matrix elements.

4.2 Structures and Vibrational Frequencies

The structures for the 27 hydrogenated Si, and SiN clusters and 32 acyclic Si and SiN species that were investigated in the present study were optimized using the B3LYP/6-31G(d) level of theory. The optimized structures for all of the clusters showed complex polycyclic properties with a varying number of nitrogen atoms in each species, as illustrated in Figure 1. High-energy sterically strained structural isomers were calculated in this study to capture the diverse range of strain energies possible in hydrogenated Si and SiN clusters. Acyclic Si and SiN structures were calculated for species comprised of one to six Si or Si + N atoms except the azo compound species. For the cluster structures, hydrogenated trigonal planar, square planar, substituted trigonal planar, pentagonal planar, hexagonal planar, trigonal pyramidal, trigonal bipyramidal, and prismane geometries comprised of varying numbers of three- and four-membered rings were calculated. All electronic wavefunctions for the structures were optimized in a singlet state. We also calculated all structures in this study in the triplet states (see Table 4.1 for selected structures). Dissociation was observed from most acyclic species and clusters due to excitation in the triplet state.

Using the nomenclature introduced in Figure 4.1, an analysis of the geometric parameters for the cluster species are presented. Comparison of our predicted values to experiment or predicted value from literatures for geometry parameters are presented here for the acyclic species. For disilane, the predicted Si-Si and Si-H bond lengths were 2.350 Å and 1.489 Å,[111] respectively, and experimental values were 2.331 Å and 1.492 Å, respectively. The H-Si-Si and H-Si-H bond angles were predicted as 110.6 and 108.3 degrees, respectively, and experimental values were 110.3 and 108.6 degrees, respectively.[111] For silylamine(A2N1), the predicted Si-N, Si-H and N-

H bond lengths were 1.738 Å , 1.487 Å and 1.104 Å, respectively. These are well matched with literature values[112, 113], which were 1.740 Å, 1.490 Å, and 1.021 Å. The H-Si-N, H-Si-H, HNH bond angles were predicted as 107.7, 107.0 and 110.0 degrees, respectively. For trisilane (A3N0), the predicted Si-Si and Si-H bond lengths were the same value as for disilane, The Si-Si-Si, HSi^1H and HSi^2H bond angles were predicted as 112.9, 108.4 and 107.1 degrees, respectively. In Si_2NH_7 species, for A3N1a the predicted Si-N and Si-Si bond lengths were 1.745 Å and 2.350 Å and the N-Si-Si bond angle was 108.9 degrees. For A3N1b, Si-N bond length was predicted slightly smaller than Si-N bond of A2N1 as 1.743 Å and the Si-N-Si bond angle was 129.4 degrees. For A3N2, the predicted Si-N bond length was 1.727 Å which was the shortest length among all Si-N lengths in this study. The predicted N-Si-N bond angle was 108.3 degrees. For A4N1bs, the predicted Si-N and Si-H bond length were 1.753 and 1.487 Å and the SiNSi bond angle was 120.0 degree. These are reasonably understandable parameters compared to the literature value by Beagley et al.[114] and Hedberg[115], which are 1.734 ~ 1.748 Å of Si-N bond, 1.485 ~ 1.506 Å of Si-H bond and 119.4 ~ 119.6 degree of SiNSi bond angle. All of our predicted values for geometry parameters are well matched to the experimental or literature data for the acyclic $Si_xN_yH_z$ species in this study. As with small acyclic species, it was predicted that there are similar bond lengths and angle values in larger acyclic species.

For trigonal planar Si_3H_6 (TN0), the equilateral triangle structure is suggested with a Si-Si bond length of 2.345 Å and a Si-H bond length of 1.486 Å. Addition of N atom to the TN0 geometry decreases the length of all the bonds in TN0, due to decreasing the size of the full cluster where the substituted N cluster is smaller than the Si cluster in geometric dimensions. For the TN1 geometry, the Si-Si bond length is 2.253 Å, the Si-N bond length is 1.745 Å, the Si-H bond length is 1.490 Å, N-H bond length is 1.011 Å, and Si-N-Si apex angle is 80.4 degrees. The size of the trigonal planar was shrunken compared to the size of TN0 and the apex angle increased. As observed with the trigonal planar structural series, all other structural geometries (i.e., substituted trigonal planar, trigonal pyramidal, trigonal bipyramidal, and prismane) showed a similar trend of diminishing bond lengths when exchanging Si atom with N atom. In addition, the N atom in all planar cluster species in the study is the sp^2 hybridized center which possesses planar trigonal structure. This is observed from the fact that the Si-N-Si angle has increased from 109.5 to 120 degree and atoms near N were placed on the same plane with N or the plane that is close to the N atom. This occurrence is most noticeable in A4N1s and STN1b. As we mentioned in our previous study, the cyclic rhombus structure(SN0) of four Si atoms which has slightly puckered character, has a Si-Si bond length of 2.371 Å and a Si-H bond length of 1.492 Å with the angles of the Si-Si-Si bonds at 87.7 and 92.3 degrees.[108] For the SN1 specie, the Si-N and Si-Si bond lengths are 1.760 Å and 2.360 Å. The Si-N-Si, N-Si-Si, Si-Si-Si bond angles are 109.9, 87.5 and 75.2 degrees. For SN geometry, the Si-N bond is 1.752 Å and the N-Si-N and Si-N-Si bond angles are 86.8 and 93.1 degrees. For the substituted trigonal planar structure (STN), which has the same number of Si and N atoms, the square planar type appeared to be more stable, this is because the NH substituent in a planar structure (SN) has less steric hindrance than substituted trigonal planar (STN) does. We also found that the similar trend, where the species becomes more planar and smaller as the number of N atoms increases, holds well for pentagonal and hexagonal planar geometry as well.

However, the average bond length of Si-N is increased to 1.821 Å in trigonal bipyramid (TBPyN). This bonding behavior happened due to the steric hindrance of 3D structure with neighboring atoms. As with the trigonal bipyramidal (TBPyN) geometries, the expansion of bond lengths are observed for trigonal pyramidal (TPyN) and prismane (PriN) species as the average length of 1.843 Å and 1.817 Å respectively.

Several structures in this study were hypothesized as resonance structures. However, NBO analysis confirmed that N atom of SiN species in present study has hybridization in various orbitals, sp^{λ}, which λ range is from 1.67 in acyclic or planar species to 3.62 in prismane geometry and Si atom has hybridized in λ from 1.86 to 5.83. It confirmed that a higher number λ occurs more in 3-dimensional geometry. The acyclic and planar structures are relatively more stable than 3-dimensional one, because most of N is the sp^2 hybridized center and lone pair electrons are in p orbitals, which can lead hyperconjugation phenomena with the neighboring Si atoms.

As far as we know, there are not many studies on hydrogenated silicon nitride nanocluster. From the literature reviews, most of silicon nitride is present in solid crystalline forms. Andrievskii[89] and Yashima et al.[116] compared the geometric characteristics of different phase Si_3N_4. Comparing these studies with our current study, we identified two match-points; 1) the Si-N bond lengths (1.73 - 1.75 Å) and 2) the fact that Si-N compounds prefer to be planar type structures than 3-dimensional cluster type.

At the level of theory considered in our study, modeling results have all real vibrational frequencies and represent stable minima on the potential energy surface. Experimental spectroscopic data for the vibrational frequencies of hydrogenated Si, and SiN clusters are limited. The unscaled harmonic vibrational frequencies for ammonia (NH_3) and amino silane (SiH_3NH_2) calculated using G3//B3LYP compared against available spectroscopic experimental data in Table 4.3. The unscaled harmonic frequencies for NH_3 and SiH_3NH_2 were determined to have mean percentage deviations from experimental values of -7.4 and -1.7 %, respectively.

Table 4.3. Comparison of Experimental Vibrational Modes for NH_3 and SiN_3NH_2 to Unscaled Harmonic Vibrational Modes Using the G3//B3LYP Composite Method

(a) Vibrational Modes of NH_3

type of mode	experimental frequency [a]	G3B3		
		calc. freq.	deviation (exp-calc)	% deviation
NH_3 a-stretch	3443.6	3568	-124.6	-3.6
NH_3 s-stretch	3336.2	3436	-100.3	-3.0
NH_2 scissors	1626.1	1727	-100.7	-6.2
N-H defrom	968.3	1132	-163.5	-16.9
average			-122.3	-7.4

(b) Vibrational Modes of SiH_3NH_2

type of mode	experimental frequency [b]	G3B3		
		calc. freq.	deviation (exp-calc)	% deviation
NH_2 a-stretch	3547	3645	-98.3	-2.8
NH_2 s-stretch	3445	3555	-110.1	-3.2
SiH stretch	2172	2191	-19.0	-0.9
NH_2 scissors	1564	1630	-65.8	-4.2
SiH_3 deform.	996	1012	-16.4	-1.7
SiH_3 deform.	983	993	-10.1	-1.0
SiH_3 deform.	970	942	27.6	2.8
SiN stretch	845	833	11.5	1.4
Deform.	670	709	-39.3	-5.9
average			-35.5	-1.7

a Ref[117]

b Ref[118]

4.4 Thermochemical Properties

The thermodynamic properties of ammonia (NH_3), disilane (AN20), trisilane (AN30) and SiN with experimental data available were estimated using the B3LYP with the various basis set. The deviations between the calculated and experimental values for standard enthalpy of formation, standard entropy, and constant pressure heat capacity are listed in Table 4.2 for the simple acyclic species. Among the methods used, the G3//B3LYP method was the most accurate for the standard enthalpy of formation calculation for silicon hydrides, with an average absolute deviation of 18.7 kJ mol^{-1} from experimental measurements. The G3//B3LYP method was more accurate for the prediction standard enthalpy of formation values for ammonia with an absolute deviation of 2.9 kJ mol^{-1} from experimental measurements. The largest deviation between experimental and calculated predictions for standard enthalpy of formation for ammonia was observed by B3LYP method can be attributed to factors not included in the composite methods discussed. Due to the correlation of semiconducting or non-local nature of electron of Si atom and lone pair electrons of N atom in the clusters, rigorous composite methods are required to predict trends in thermochemical properties, such as standard enthalpy of formation as function of Si and N composition.

To the best of our knowledge, there is no extensive investigation of thermochemical property estimation or even of vibrational frequency calculations for optimized hydrogenated Si and SiN clusters outside of the works cited in this paper. A total of 59 molecules up to a moderate cluster size, where $(Si + N) \leq 6$, were investigated in this study. The thermochemical properties of all 59 species studied here are reported in Table 4.4. The most stable ground electronic state for all molecules in this study was found to be the singlet state. As mentioned in the previous section, Structures and Vibrational Frequencies, a significant conformational change or spontaneous bond dissociation was observed during optimization of the electronic wavefunction to the triplet state. (Table 4.2)

In all geometries, the addition of N atoms to a species decreases the standard enthalpy of formation significantly, and also decreases standard entropy and constant pressure heat capacity values. This is the result of the conjugation effect of Si and N atoms. It is observed that a cyclic cluster is more stable than an acyclic molecule with the HN3 and A6N3a even though both have the same number of Si and N atoms. The stability of molecules depends on the position of N atom, so the structure with more Si-N bonds is significantly more stable than other isomers. It is shown to A5N2d and A5N2c in Table 4.4 and Figure 4.2. This can also be aligned the fact that the bond dissociation energy values of Si-N is much higher than the one of Si-Si, which are 439 kJ mol^{-1} and 327 kJ mol^{-1}, respectively.[119]

Table 4.4. Comparison of Calculated Thermodynamic Properties of Hydrogenated Si and SiN Clusters Using the G3//B3LYP Method.

Level of Theory									G3//B3LYP		
Atoms			Molecules	net charge	spin multi-plicity	Symmetry group	chirality	σ_{ext}	$\Delta H^{\circ}_{f,298K}$ KJ/mol	C_p J/mol.K	S J/mol.K
Si	Ge	H									
Acyclic species											
2	0	6	A2N0	0	1	D_{3d}		6	75.7	79.5	273.5
1	1	5	A2N1	0	1	C_s		1	-44.6	63.8	262.5
3	0	8	A3N0	0	1	C_{2v}		2	112.5	117.1	346.9
2	1	7	A3N1a	0	1	C_1		1	2.9	102.2	323.4
2	1	7	A3N1b	0	1	C_s		1	-60.2	94.3	328.1
1	2	6	A3N2	0	1	C_2		2	-147.1	87.6	288.1
4	0	10	A4N0	0	1	C_{2h}		2	147.7	154.8	412.3
3	1	9	A4N1a	0	1	C_1		1	39.0	139.9	387.7
3	1	9	A4N1b	0	1	C_1		1	-13.8	133.2	388.6
2	2	8	A4N2a	0	1	C_1		1	-163.1	117.8	356.3
2	2	8	A4N2b	0	1	C_{2h}		2	-70.1	124.6	351.1
5	0	12	A5N0	0	1	C_2		2	182.7	192.5	476.6
4	1	11	A5N1a	0	1	C_1		1	74.1	177.7	453.2
4	1	11	A5N1b	0	1	C_1		1	21.7	170.9	454.2
4	1	11	A5N1c	0	1	C_s		1	32.1	171.9	449.0
3	2	10	A5N2a	0	1	C_1		1	-116.9	156.7	416.8
3	2	10	A5N2b	0	1	C_1		1	-87.2	155.7	421.2
3	2	10	A5N2c	0	1	C_2		2	-33.9	162.5	415.6
3	2	10	A5N2d	0	1	C_2		2	-179.4	148.0	413.6
2	3	9	A5N3	0	1	C_s		1	-263.7	141.5	384.6
6	0	14	A6N0	0	1	C_{2h}		2	217.5	230.3	541.4
5	1	13	A6N1a	0	1	C_1		1	109.0	215.4	518.0
5	1	13	A6N1b	0	1	C_1		1	56.6	208.5	519.7
5	1	13	A6N1c	0	1	C_1		1	67.5	209.6	513.4
4	2	12	A6N2a	0	1	C_1		1	-81.4	194.4	481.8
4	2	12	A6N2b	0	1	C_1		1	-41.1	194.7	487.4
4	2	12	A6N2c	0	1	C_1		1	-51.4	193.5	487.6
4	2	12	A6N2d	0	1	C_1		1	0.6	200.4	488.9
4	2	12	A6N2e	0	1	C_1		1	-133.0	187.0	483.8

4	2	12	A6N2f	0	1	C_2		2	-104.2	186.7	479.9
3	3	11	A6N3a	0	1	C_1		1	-281.2	172.4	453.3
3	3	11	A6N3b	0	1	C_1		1	-190.0	179.1	449.3
3-dimentional clusters											
3	0	6	TN0	0	1	D3h		6	261.1	105.4	304.6
2	1	5	TN1	0	1	C_{2v}		2	121.8	81.3	282.0
4	0	8	SN0	0	1	D3d		4	205.2	137.9	339.4
3	1	7	SN1	0	1	Cs		2	53.7	114.8	350.9
2	2	6	SN2	0	1	C1		2	-128.9	95.8	290.1
4	0	8	STN0	0	1	C1		1	282.7	142.0	372.2
3	1	7	STN1a	0	1	C1		1	190.9	129.3	355.6
3	1	7	STN1b	0	1	C1		1	89.7	114.8	341.0
3	1	7	STN1c_ch	0	1	C2	o	2	158.5	120.6	353.0
2	2	6	STN2_ch	0	1	C2v	o	2	18.2	106.6	323.6
5	0	10	PN0	0	1	C2h		1	195.3	174.0	436.7
4	1	9	PN1	0	1	Cs		2	41.6	152.4	386.1
3	2	8	PN2	0	1	Td		2	-139.2	132.0	352.9
6	0	12	HN0	0	1	C3v		6	211.4	210.3	447.6
5	1	11	HN1	0	1	D3h		1	65.7	190.3	428.3
4	2	10	HN2a	0	1	C3v		1	-109.5	170.0	403.0
4	2	10	HN2b	0	1	Cs		2	-78.3	168.0	408.9
3	3	9	HN3	0	1	D3h		1	-327.0	148.0	369.9
4	0	4	TPyN0	0	1	D2d		12	644.0	122.0	347.1
3	1	3	TPyN1	0	1	C2v		3	540.6	98.5	310.7
5	0	8	TBPyN0	0	1	C2h		6	282.4	157.6	373.9
4	1	7	TBPyN1a	0	1	Cs		3	184.6	133.3	342.8
4	1	7	TBPyN1b	0	1	Cs		1	232.6	139.5	348.0
3	2	6	TBPyN2	0	1	Cs		6	145.6	114.0	318.5
6	0	6	PriN0	0	1	D3h		6	587.1	171.3	378.9
5	1	5	PriN1	0	1	C_s		1	477.7	147.3	365.0
4	2	4	PriN2	0	1	C_2		2	396.4	127.2	335.3

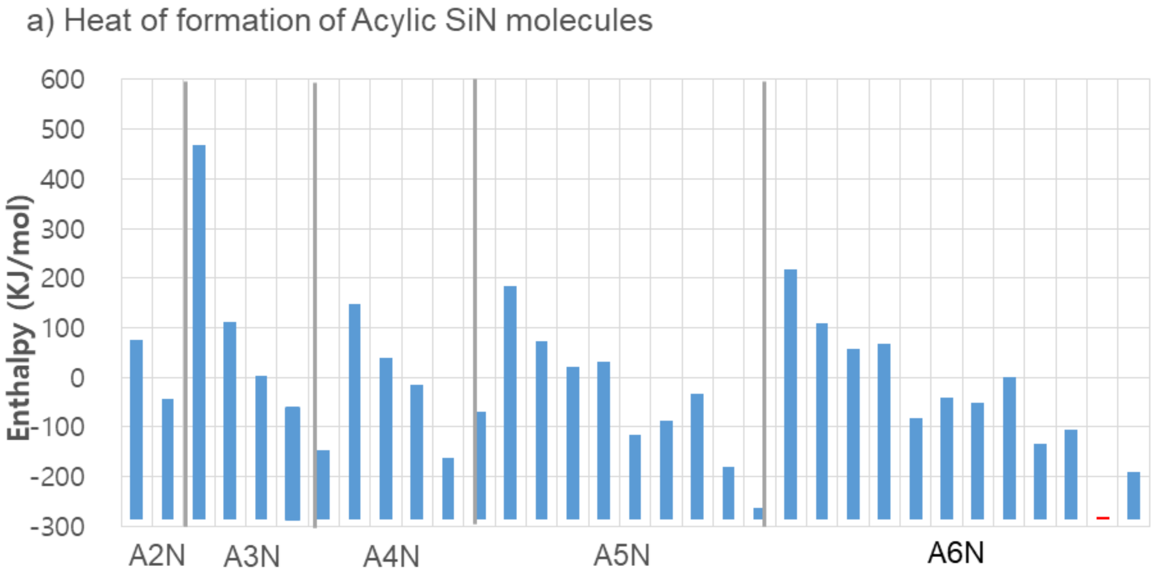

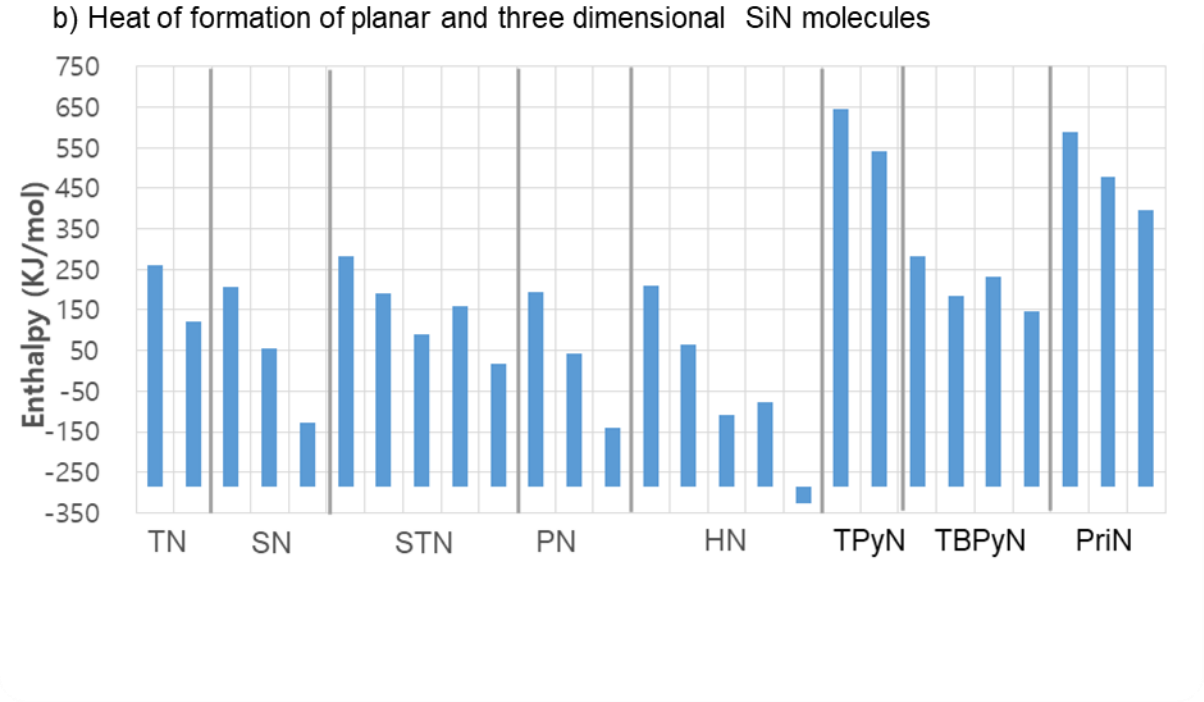

Figure 4.2. Heat of formation of (a) acyclic silicon nitride hydrides and (b) hydrogenated silicon nitride clusters in this study at 298.15 K using the G3//B3LYP level of theory.

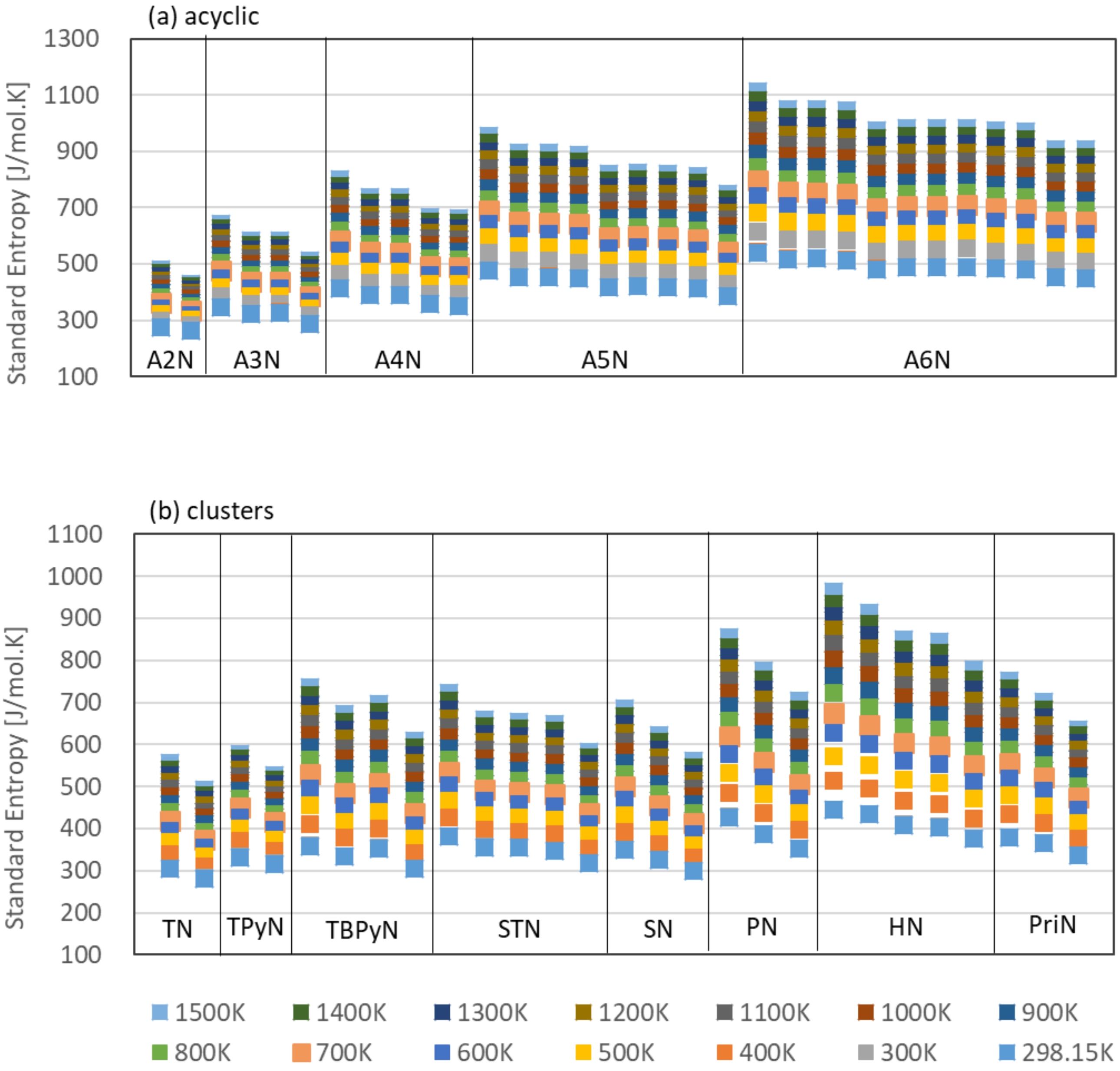

Figure 4.3. Standard entropies of (a) acyclic silicon nitride hydrides and (b) hydrogenated silicon nitride clusters in this study over the temperature range of 298.15 to 1500 K using the G3//B3LYP level of theory. The nomenclature to identify cluster geometries is the same as in Figure 4.1.

The standard entropies and constant pressure heat capacities for all clusters in this study over the temperature range of 298.15 K to 1500 K are presented graphically in Figure 4.3a-b prepared and in Appendix B1. The average percent deviations between experimental and calculated values of standard entropy and constant pressure heat capacity for the three acyclic Si and N hydrides were -4.5% and -5.8%, respectively, at the B3LYP level of theory.

It is noteworthy to mention that the external symmetry number was identified for all clusters to ensure that accurate standard entropy values were predicted. The effect of the external symmetry number on rotational entropy becomes less pronounced at elevated temperatures because the aforementioned correction factor, R ln σ_{rot}, is not a function of temperature. The clusters with the highest degree of symmetry were the trigonal pyramidal geometries, particularly the pure Si cluster (TPyN0) which possess a Td point group symmetry. The D3h point group symmetry was the next most common point group symmetry with a high degree of symmetry in this study, particularly for the trigonal planar (TN), trigonal bipyrimidal (TBPyN), hexagonal planar (HN) and prismane (PriN) geometries. Chiral clusters containing at least one Si/N atom with two nonidentical substituents were identified in our study. The presence of one chiral center was denoted in Table 4.4 for two substituted trigonal planar clusters (STN1c_ch and STN2_ch). The presence of a chiral center in a cluster increases the external symmetry number by a factor of two. Figure 4.3 and 4.4 displays standard entropy and constant pressure heat capacity values, respectively, as a function of temperature. It is interesting to note that standard entropy values are more sensitive to temperature variations than constant pressure heat capacity for all the clusters and variation of standard entropy values tends to decrease in the order of acyclic, planar, three-dimensional clusters in this study.

Figure 4.4. Constant pressure heat capacities of (a) acyclic silicon nitride hydrides and (b) hydrogenated silicon nitride clusters in this study over the temperature range of 298.15 to 1500 K using the G3//B3LYP level of theory. The nomenclature to identify cluster geometries is the same as in Figure 4.1.

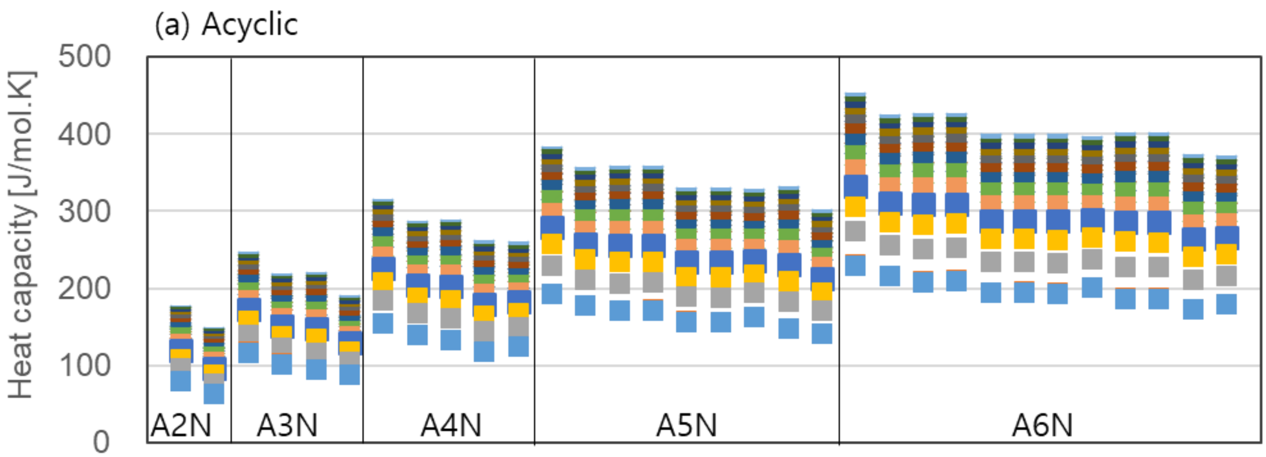
(a) Acyclic

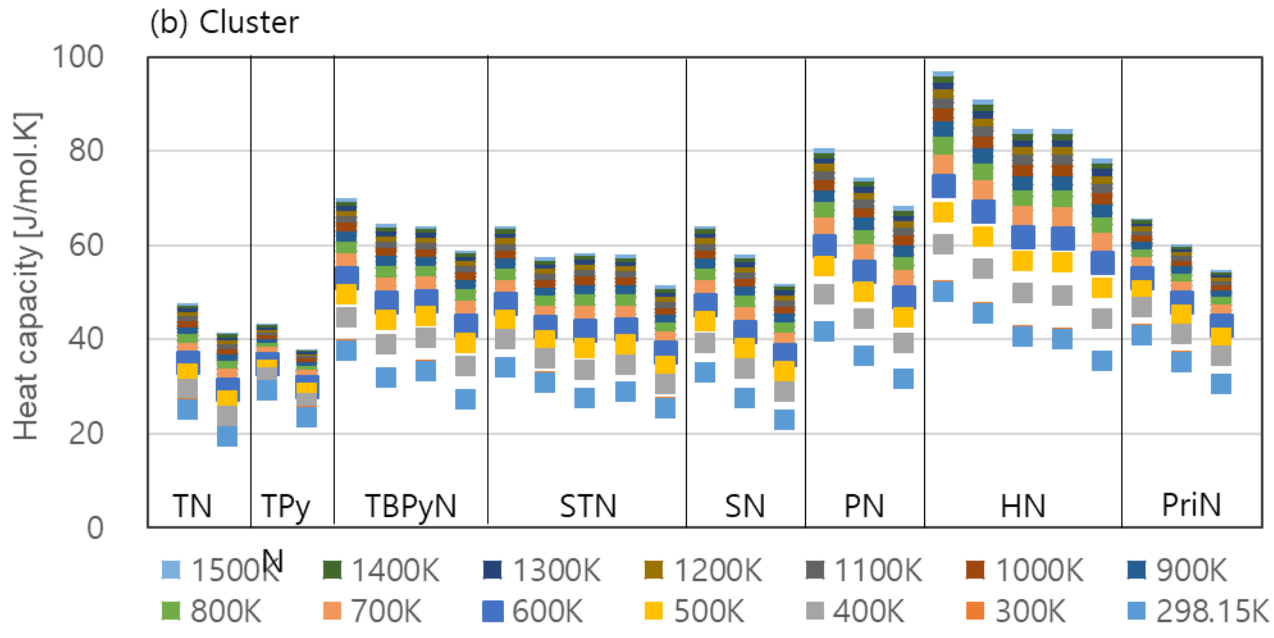
(b) Cluster

For all the planar-type geometries (trigonal, substituted trigonal, square, pentagonal and hexagonal planar), the range of standard entropy and constant pressure heat capacity values from 298 K to 1500 K is lower than the range of standard entropy and constant pressure heat capacity values over the same temperature range for the three-dimensional clusters (trigonal pyramidal, trigonal bipyrimidal and prismane geometries). This observation is likely due to the greater number of vibrational degrees of freedom for the larger Si and SiN clusters sizes.

If standard enthalpy of formation values are compared for isomers of a given cluster geometry, relative stabilities can be identified and ranked accordingly. Cluster isomers are present in this study for acyclic molecules (A3N, A4N, A5N and A6N), the substituted trigonal planar (STN), hexagonal planar (HN), and trigonal bipyramidal (TBPyN) geometries. For instance, in Table 4.4, for the acyclic 5 member molecule(A5N), one can observe that the isomer A5N2d is more stable than isomers A5N2a, A5N2b and A5N2c where standard enthalpies of formation are -179.4 kJ mol^{-1}, -116.9 kJ mol^{-1}, -87.2 kJ mol^{-1} and -33.9 kJ mol^{-1}, respectively. The isomer A5N2d differs from A5N2a, A5N2b and A5N2c due to the number of Si-N bonds in the molecules. Silicon is sp^{3}-hybridized to form a sigma bond with adjacent N and H. Due to the difference of electronegativity, Si has a relatively positive charge and N and H have relatively negative charges. Accordingly, the bond of Si-N is a polar covalent bond that is stronger than a non-polar covalent bond of Si-Si. A similar trend in cluster stabilities is also observed for the other STN isomers in the STN1a, STN1b, and STN1c_ch series of cluster geometries, but the differences between the most stable isomer and the least stable isomer in these geometry series are lower with values of 197.4 kJ mol^{-1}, 96.0 kJ mol^{-1}, and 165.0 kJ mol^{-1}, respectively.

The difference in stability of isomers is similarly pronounced for the hexagonal planar and trigonal bipyramidal geometry series; however, the greatest difference for the stability of isomers for this study is in the STN1 series where the STN1b isomer is most stable. The STN1b isomer has the molecular formula of $Si_3N_1H_7$ where the N is at the center of the cluster and bound to three Si atoms. The difference in stability of isomers is least pronounced for the hexagonal planar clusters with differences ranging -99.6 kJ $mol^{-1}$and -68.3 kJ mol^{-1} for the HN2a and HN2b, respectively.

Internal Rotation correction

In the thermodynamic or kinetic properties of molecules study, it is often approximated that molecules are rigid and hindered rotors. Because the rotation within the molecule is an intermediate motion between simple harmonic motion and free-rotation. However, treating internal rotations as free rotations is a valid approximation for pyrolytic conditions as the barriers to rotation for Si–Si and Si-N σ bonds in acyclic hydrogenated silicon nitrides are on average 4.22 kJ mol^{-1}. To assess the magnitude of the effects of internal rotation, potential energy scans at the B3LYP(d) level of theory were performed for the each Si-Si and Si-N σ bonds in acyclic molecules. The internal rotation in the molecules in this study was found to have a very low barrier to rotation, and the free rotor approximation is valid. The transition from a hindered to a free rotor was assumed to occur at the temperature at which k_BT equals the maximum barrier height to internal rotation. The thermochemistry properties with the internal rotation correction are presented in Appendix B2.

4.5 Electronic Properties and Chemical Stability

The Frontier Molecular Orbital, which can be calculated by quantum chemical methods, such as highest occupied molecular orbital (HOMO) and lowest unoccupied molecular orbital (LUMO), plays a significant part in the chemical stability of the molecule. Knowledge of the HOMO and LUMO contours is critical for understanding reactions of clusters, because HOMO represents the ability to donate an electron and LUMO represents ability to accept an electron. The energy gap between HOMO and LUMO determines optoelectronic properties, chemical hardness-softness of molecules as well as the chemical reactivities.

In our computational study, the HOMO–LUMO energy gap is considered to investigate the role of cluster composition on the chemical stability of hydrogenated Si and SiN clusters. This energy gap is a critical parameter which characterizes the chemical reactivity of the hydrogenated clusters. This chemical reactivity facilitates a molecule to participate in chemical reactions or to create a novel self-assembled material through intermolecular interactions. The HOMO–LUMO energy gap can describe the ability for electrons to move from HOMO to LUMO and consequently is considered as an important parameter to analyze the chemical stability of clusters. For instance, if the HOMO–LUMO energy gap were large for a given Si and SiN cluster, this value would correspond to a closed shell electronic configuration and high chemical stability. On the other hand, smaller HOMO–LUMO energy gaps for given Si and SiN clusters reflect that the respective cluster may interact easily with other molecules to form a covalent bond, and these types of molecules are on average more chemically reactive.

Calculated HOMO-LUMO energy gaps of hydrogenated Si and SiN clusters and acyclic Si and SiN hydrides at the G3//B3LYP level of theory are presented in Figure 4.5. The calculated HOMO-LUMO energy gaps for pure Si and SiN species are in the range from 8.19 to 12.35 eV. The HOMO-LUMO energy gaps of acyclic SiN hydrides are always higher than for pure Si and SiN cluster species. In acyclic hydrides, the HOMO-LUMO gaps decreases as the size of molecules increase, which indicates the reactivity of the acyclic hydrides increase. Also, it is worthy to note that the variation of HOMO-LUMO gaps in each geometries differs with the position of the N atom in the molecule. Generally, the HOMO-LUMO gap slightly decreases when the Si atom located at the end of the molecule is replaced with the N atom, which is shown in A2N1, A3N1a, A4N1a and so on. On the other hand, when a Si atom with two neighboring Si atoms was replaced with a N, the HOMO-LUMO energy gap increased with apparent examples of A3N1b and A4N2a. This can be explained by the difference of electronegativity between a Si and a N atom. When a N is located between Si atoms, the partially negative-charged N makes a stronger polar covalent bond with partially positive-charged neighboring Si atoms, which contributes to stability of the molecule. By contrast, When a N atom is located at the end of a molecule; the molecule behaves as a base due to amine functional group.

The largest absolute difference of 1.15 eV is observed for the square planar geometry and the smallest absolute difference of 0.18 eV between HOMO-LUMO energy gaps is observed for the two member acyclic hydrides. As the most strained structure, the trigonal pyramidal geometry showed the lowest HOMO-LUMO energy gap.

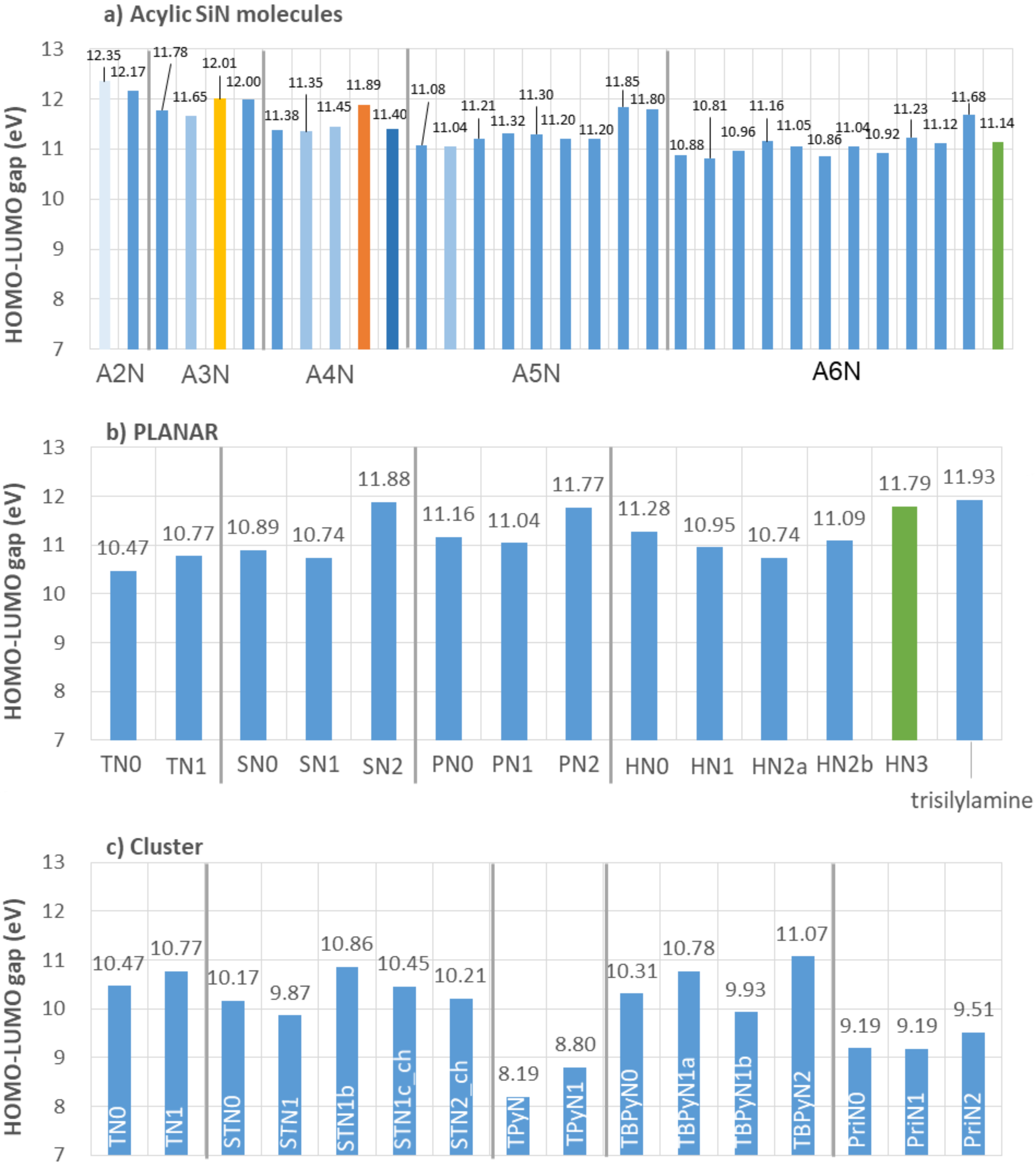

Figure 4.5. Comparison of calculated HOMO−LUMO energy gaps for all hydrogenated Si and SiN clusters in this study using the G3//B3LYP level of theory. The nomenclature to identify cluster geometries is the same as in Figure 4.1.

On average, the HOMO-LUMO energy gap decreases with increase in the polycyclic nature of the Si or SiN cluster. Figure 4.5a-5c present calculated HOMO-LUMO energy gaps of all clusters in our study, particularly highlighting the effects of alloy cluster composition and isomers. Figure 4.5a-5c present calculated HOMO-LUMO energy gaps of all clusters in our study, particularly highlighting the effects of alloy cluster composition and isomers. The most precipitous fall in the HOMO-LUMO energy gap is for the square planar geometry followed by the trigonal bipyramidal, hexagonal planar, substituted trigonal planar, six membered acyclic hydrides, five membered acyclic hydrides, pentagonal planar, trigonal pyramidal, four membered acyclic hydrides, three membered acyclic hydrides, prismane, trigonal planar and two membered acyclic hydrides,geometries at 1.15, 1.14, 1.04, 0.87, 0.81, 0.72, 0.60, 0.53, 0.36, 0.32, 0.30 and 0.18 eV, respectively. It is interesting to compare that the corresponding band gap energy of HN_3 and a $Si_3N_3H_3$ molecule. Nabati[120] and coworker investigated the stability and aromaticity of six-membered heterocyclic $Si_nN_{6-n}H_n$ (n=0-6), $Si_3N_3H_3$ showed relatively low aromaticity and lowest reactivity. This can be explained as the reason why HN_3 is the most stable here.

For acyclic Si and SiN hydrides and planar geometry clustes in this study, the HOMO is delocalized over the entire structure. By contrast, the LUMO is mostly localized over the N atom. Conseqeuntly, the HOMO-LUMO transition implies an electron density transfer to the limits of the molecular orbitals and this phenomena is consistent with stability results from SiN_Thermochemical Properties part. For the three–dimensional cluster, the HOMO and LUMO both are delocalized over the entire structure. The extreme delocalization of electron density suggests facile electron density transfer between neighboring clusters without forming a formal covalent bond which can be useful for the development of self-assembling nanomaterials. Examples of this LUMO behavior can be seen in Appendix B.3. for the trigonal pyramidal (TPyN), the trigonal bipyramidal (TBPyN) and prismane (PriN) geometries. On the other hand, the localization of electron density around a specific atom suggests the possibility of designing a particular nanomaterials or there is not much place to transfer electron density into LUMO which means reaction would hardly occur.

In the molecular orbital (MO) theory, predicting the reactivity of materials using the HOMO-LUMO energy gap is important to chemists or chemical engineers. That is, according to the notation introduced in the Computational Methodology section, hard molecules have a large HOMO-LUMO energy gap, and soft molecules have a small HOMO-LUMO energy gap. A small HOMO-LUMO energy gap is correlated to small vertical excitation energies to the manifold of excited energy states. Therefore, soft molecules, with a smaller energy gap than hard molecules, will be more polarizable by definition. As listed in Table 4.5, the trigonal pyramidal Si and SiN clusters are the softest species in this study, and thus most reactive due to smaller energy gaps than the remaining clusters and acyclic species. Consequently, these clusters also have a 1:1 Si-to-H or N-to-H atomic ratio, whereas the other species in this study have a lower Si or N atomic ratio to H. On average, less passivation with hydrogen will result in a more reactive cluster or acyclic species. As defined in the Computational Methodology section, molecular hardness, softness, and chemical potential calculated from the G3//B3LYP level of theory are presented in Table 4.5 and the reactivity index ΔN was presented in Figure 4.6.

Table 4.5. Calculated Quantum Chemical Molecular Descriptors for Hardness (η), Chemical Potential (μ), and Softness (σ) at the G3//B3LYP Level of Theory for All Hydrogenated Si and SiN Clusters and Acyclic Species in this study (Hardness in eV, chemical potential in eV, and softness in eV^{-1}). The nomenclature to identify molecular geometries is the same as in Figure 4.1

index		η (eV)	μ (eV)	σ (eV^{-1})
1	A2N0	6.2	-4.9	0.16
2	A2N1	6.1	-4.9	0.16
3	A3N0	5.9	-4.6	0.17
4	A3N1a	5.8	-4.7	0.17
5	A3N1b	6.0	-4.8	0.17
6	A3N2	6.0	-4.8	0.17
7	A4N0	5.7	-4.4	0.18
8	A4N1a	5.7	-4.5	0.18
9	A4N1b	5.7	-4.5	0.17
10	A4N2a	5.9	-4.8	0.17
11	A4N2b	5.7	-4.5	0.18
12	A5N0	5.5	-4.3	0.18
13	A5N1a	5.5	-4.4	0.18
14	A5N1b	5.6	-4.4	0.18
15	A5N1c	5.7	-4.5	0.18
16	A5N2a	5.6	-4.5	0.18
17	A5N2b	5.6	-4.4	0.18
18	A5N2c	5.6	-4.4	0.18
19	A5N2d	5.9	-4.8	0.17
20	A5N3	5.9	-4.8	0.17
21	A6N0	5.4	-4.2	0.18
22	A6N1a	5.4	-4.3	0.18
23	A6N1b	5.5	-4.3	0.18
24	A6N1c	5.6	-4.4	0.18
25	A6N2a	5.5	-4.4	0.18
26	A6N2b	5.4	-4.3	0.18
27	A6N2c	5.5	-4.4	0.18
28	A6N2d	5.5	-4.3	0.18
29	A6N2e	5.6	-4.5	0.18
30	A6N2f	5.6	-4.4	0.18
31	A6N3a	5.8	-4.8	0.17
32	A6N3b	5.6	-4.4	0.18
33	TN0	5.2	-3.8	0.19

34	TN1	5.4	-4.1	0.19
35	SN0	5.4	-4.1	0.18
36	SN1	5.4	-4.2	0.19
37	SN2	5.9	-4.6	0.17
38	STN0	5.1	-3.8	0.20
39	STN1a	4.9	-3.8	0.20
40	STN1b	5.4	-4.1	0.18
41	STN1c_ch	5.2	-4.0	0.19
42	STN2_ch	5.1	-3.9	0.20
43	PN0	5.6	-4.4	0.18
44	PN1	5.5	-4.4	0.18
45	PN2	5.9	-4.7	0.17
46	HN0	5.6	-4.4	0.18
47	HN1	5.5	-4.3	0.18
48	HN2a	5.4	-4.2	0.19
49	HN2b	5.5	-4.5	0.18
50	HN3	5.9	-4.7	0.17
51	TPyN0	4.1	-2.9	0.24
52	TPyN1	4.4	-4.0	0.23
53	TBPyN0	5.2	-3.9	0.19
54	TBPyN1a	5.4	-4.3	0.19
55	TBPyN1b	5.0	-3.7	0.20
56	TBPyN2	5.5	-4.3	0.18
57	PriN0	4.6	-3.4	0.22
58	PriN1	4.6	-3.5	0.22
59	PriN2	4.8	-3.6	0.21

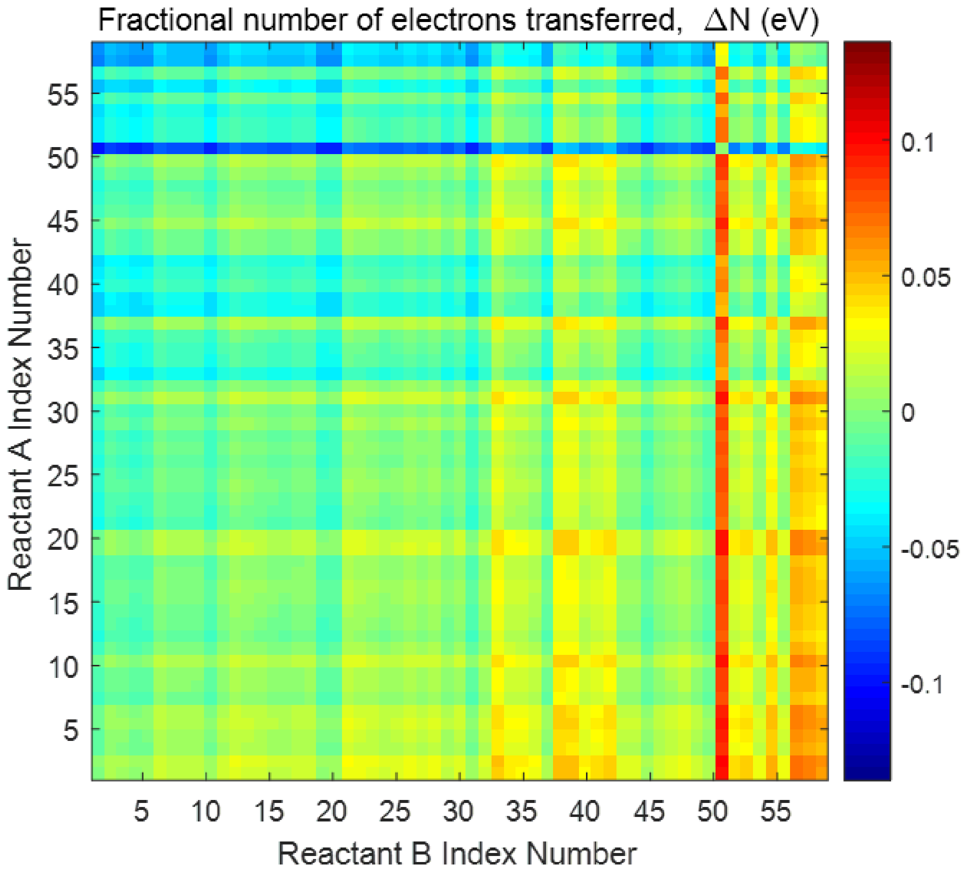

Figure 4.6. Contour map of the calculated fractional electrons transferred in eV (ΔN) for molecular interactions of all 59 molecules in this study. ΔN follows eq 4.8 where the frontier molecular orbital energies are calculated using the G3//B3LYP level of theory. The reactant index number follows the numbering scheme of Table 4.5.

4.6 Natural Bond Orbitals (NBO) analysis

The NBO analysis provide useful information for understanding of intra- and inter-molecular bonding, bond species and interactions among bonds. It is used for investigating of hyperconjugation interactions (or intramolecular charge transfers, ICT) between Lewis type (bonding or lone pair) filled orbitals and non-lewis type (antibonding and Rydgberg) vacancy orbitals in molecular system. The E(2) which is the energy of hypoerconjugative interactions (stabilization energy) shows the interaction between donor groups and acceptor groups. Delocalization of electron density between occupied Lewis type orbitals and formally unoccupied non-Lewis orbitals corresponding to a stabilizing donor–acceptor interaction.

The larger the magnitude of E(2), more intensive is the extent of interaction between electron donors and electron acceptors, which means conjugation of the whole system. The results of second-order perturbation theory analysis of Fock Matrix in NBO basis for A4N and HN group are presented in Appendix B3. The strong intramolecular hyperconjugation interactions or ICT could be found in σ to σ*, LP to σ* and LP to Rydgberg transitions. The strongest hyperconjugation interaction is from the lone pair electrons of N11 atoms to antibonding σ* electrons of Si8-H10 bond in A4N1a molecule. Similarly the interaction between lone pair electrons of N1 and each σ* electrons of neighboring Si-H bonds has 5.80 kcal mol^{-1}, which indicates well-delocalized electron density overall in A4N1s. It is interesting to note that ICT occurs from the lone pairs of N to not only Si-H antibonding but Si-N antibonding in the planar type molecular HN. The more N atoms in molecules, the greater the amount of stabilization energy that contributes to the antibonding. This charge transfer is also explained for the stability from the HOMO-LUMO energy gaps in Figure 4.5a-c.

Chapter 5 Summary of Conclusion

5.1 Si, Ge and SiGe nanomaterials properties

In summary, DFT calculations were performed to study the relative stabilities, thermodynamic properties and electronic properties of hydrogenated Si, Ge, and SiGe nanoclusters. For comparison, the properties of pure Si_xH_y and Ge_xH_y clusters are also investigated. The optimized geometries of the $Si_xGe_yH_z$ clusters were investigated systematically using quantum chemical calculations and conventional statistical thermodynamics. All electronic energies for the clusters were calculated using Gaussian-n methods, which use B3LYP geometries and higher-level corrections based on single point energies. To validate our approach, we compared our computational methodology to other composite methods such as the complete basis set (CBS-QB3) and G4//B3LYP methods, as well as to available experimental data. The geometry parameters of all the molecules increased nominally as Ge atoms were substituted for Si atoms; however, the geometric change was small when compared to the changes observed in the electronic properties. Detailed vibrational frequency analysis has confirmed that all species reported in this study are minima on the potential energy surface and possess all real vibrational frequencies. As Si atoms were exchanged for Ge atoms in a given cluster geometry, the calculated thermochemical properties increased proportionally with the number of Ge atoms in the cluster. The calculated HOMO-LUMO energy gaps are proportionally decreased, as the cluster size increases in total heavy atom count, Si or Ge atoms.

Standard enthalpy of formation at 298 K and standard entropy and constant pressure heat capacity at elevated temperatures, i.e., 298-1500 K, were calculated for the 46 hydrogenated Si, Ge, and SiGe clusters and 7 acyclic Si, Ge, and SiGe species in this study using the G3//B3LYP composite method and statistical thermodynamics with anharmonic vibrational frequency corrections. The hydrogenated Si, Ge, and SiGe clusters contained between one and six Si and/or Ge atoms and polycyclic nature by way of fused three- to four-membered rings, as well as different degrees of dehydrogenation or multifunctionality. Quantum chemical descriptors based on the G3//B3LYP method, electronic chemical potential, μ, and absolute hardness and softness, η and σ, respectively, were calculated and generalized using a machine learning approach to predict the reactivity of Si, Ge, and SiGe alloy clusters and acyclic species in the gas phase. A statistically significant predictive model at the 99.9% confidence interval was regressed to allow for nanomaterials design efforts independent of the need to perform computationally expensive quantum chemical calculations during the initial screening efforts of nanomaterials design.

5.2 Si and SiN nanomaterials properties

In Summary, DFT calculation were conducted to investigate the relative stabilities, thermodynamic properties and electronic properties of hydrogenated Si and SiN nanoclusters.[121] The optimized geometries of the $Si_xN_yH_z$ clusters were predicted systematically using quantum chemical calcuations and conventional statistical thermodynamics. All electronic energies for the clusters were calculated using G3//B3LYP method. To validate our approach, we compared our computational methodology to other level of theory such as B3LYP/6-31G(d,p), B3LYP/6-311G(d,p) and B3LYP/6-311++G(d,p), as well as to available literature data. On average, the geometry parameters such as bond distances and angles of all the molecules decreased as N atoms were substituted for Si atoms. Detailed vibrational frequency analysis has confirmed that all species in this study are minima on the potential energy surface and possess all real vibrational frequencies. As Si atoms were exchanged for N atoms in a given molecular geometry, the calculated thermochemical properties such as standard heat of formation, constand pressure heat capacity and standard entropy decreased proportionally with the number of N atoms in the cluster. The calculated HOMO-LUMO energy gaps are proportionally decreased, as the number of heavy atom, Si or N atoms, increases in planar type or cluster species.

Standard enthalpy of formation at 298 K and standard entropy and constant pressure heat capacity at elevated temperatures from 298 to 1500 K were calculated for the 59 hydrogenated Si and SiN nanospecies using the G3//B3LYP composite method and statistical thermodynamics with anharmonic vibrational frequency corrections. Quantum chemical descriptors based on the G3//B3LYP method, electronic chemical potential, μ, and absolute hardness and softness, η and σ, respectively, were calculated. To predict the stability of Si and SiN nanospieces, NBO analysis was performed to measure the degree of hyperconjugation for A4N and HN group species.

The structural and geometric information of doped silicon nanomaterials corresponding to their electronic properties which are given in this study would provide the fundamental understanding of the related material. Further, this information would be helpful for researcher to enhance performance of materials in microelectronics and energy-related application.

References

1. C. H. Lee, S. M., R. G. Southwick, J. Li, X. Miao, R. Bao, T. Ando, R. Galatage, S. Siddiqui, C. Labelle, A. Knorr, J. H. Stathis, D. Guo, V. Narayanan, B. Haran, H. Jagannathan, A Comparative Study of Strain and Ge Content in Si1-Xgex Channel Using Planar Fets, Finfets and Strained Relaxed Buffer Layer Finfets. In *2017 IEEE International Electron Devices Meeting (IEDM)*, IEEE: San Francisco, CA, USA 2017.
2. Pi, X. D.; Kortshagen, U., Nonthermal Plasma Synthesized Freestanding Silicon-Germanium Alloy Nanocrystals. *Nanotechnology* **2009,** *20*, 295602.
3. Ang, K.-W.; Lin, J.; Tung, C.-H.; Balasubramanian, N.; Samudra, G. S.; Yeo, Y.-C., Strained ${\Rm N}$-Mosfet with Embedded Source/Drain Stressors and Strain-Transfer Structure (Sts) for Enhanced Transistor Performance. *IEEE Transactions on Electron Devices* **2008,** *55*, 850-857.
4. Eberhard F. Krimmel, R. H., *Gmelin Handbook of Inorganic and Organometallic Chemistry_Silicon Nitride in Microelectronics and Solar Cells*. 1991.
5. Di Valentin, C.; Palma, G.; Pacchioni, G., Ab Initio Study of Transition Levels for Intrinsic Defects in Silicon Nitride. *The Journal of Physical Chemistry C* **2010,** *115*, 561-569.
6. Kim, J. E.; Lee, K. D.; Kang, Y.; Lee, H.-S.; Kim, D., Comparison of Passivation Property on Hydrogenated Silicon Nitrides Whose Antireflection Properties Are Identical. *Korean Journal of Materials Research* **2016,** *26*, 47-53.
7. Peter Eigen, H. K.-R., Wolfgang Kurtz, Peter Me rlet , Hans Schafer, Friedrich SchrOder, *Gmelin Handbook of Inorganic Chemistry_System Si-N. Binary and Ternary Silicon Nitrides*. 8th ed.; 1989; Vol. Supplement Volume B 4.
8. de Guzman, R. C.; Yang, J.; Ming-Cheng Cheng, M.; Salley, S. O.; Ng, K. Y. S., High Capacity Silicon Nitride-Based Composite Anodes for Lithium Ion Batteries. *J. Mater. Chem. A* **2014,** *2*, 14577-14584.
9. Weeks, S. L.; Leick, N.; Agarwal, S., Silicon Nitride Encapsulated Silicon Nanocrystals for Lithium Ion Batteries. *Plasma Processes and Polymers* **2016,** *13*, 116-123.
10. Ulvestad, A.; Mæhlen, J. P.; Kirkengen, M., Silicon Nitride as Anode Material for Li-Ion Batteries: Understanding the Sinx Conversion Reaction. *Journal of Power Sources* **2018,** *399*, 414-421.
11. Ulvestad, A.; Andersen, H. F.; Jensen, I. J. T.; Mongstad, T. T.; Maehlen, J. P.; Prytz, O.; Kirkengen, M., Substoichiometric Silicon Nitride - an Anode Material for Li-Ion Batteries Promising High Stability and High Capacity. *Sci Rep* **2018,** *8*, 8634.
12. Mouchet, C.; Latu-Romain, L.; Cayron, C.; Rouviere, E.; Celle, C.; Simonato, J. P., Growth of One-Dimensional Si/Sige Heterostructures by Thermal Cvd. *Nanotechnology* **2008,** *19*, 335603.
13. Lewars, E. G., *Computational Chemistry_Introduction to the Theory and Applications of Molecular and Quantum Mechanics*. 2nd ed.; Springer: 2010.
14. Cramer, C. J., *Essentials of Computational Chemistry; Theories and Models by Christopher J Cramer*. John Wiley & Sons: 2002.
15. Jensen, F., *Introduction to Computational Chemistry, 3rd Ed*. John Wiley and Sons: 2007.
16. Kohn, W.; Sham, L. J., Self-Consistent Equations Including Exchange and Correlation Effects. *Physical Review* **1965,** *140*, A1133-A1138.
17. John A. Pople, P. M. W. G. a. B. G. J., Kohn-Sham Density-Functional Theory within a

Finite Basis Set. *CHEMICAL PHYSICS LETTERS* **1992,** *199*, 557-560.
18. Warshel, A.; Karplus, M., Calculation of Ground and Excited State Potential Surfaces of Conjugated Molecules. I. Formulation and Parametrization. *Journal of the American Chemical Society* **1972,** *94*, 5612-5625.
19. *, M. L. A. W., Computer Simulation of Protein Folding. *Nature* **1975,** *253*, 694.
20. LEVITT, A. W. A. M., Theoritical Studies of Enzymic Reactions_Dielectric, Electrostatic and Steric Stabilizaion of the Carbonium Ion in the Reaction of Lysozyme. *J. Mol. Biol.* **1976,** *103*, 227-249.
21. Dewar, M. J. S.; Zoebisch, E. G.; Healy, E. F.; Stewart, J. J. P., Development and Use of Quantum Mechanical Molecular Models. 76. Am1: A New General Purpose Quantum Mechanical Molecular Model. *Journal of the American Chemical Society* **1985,** *107*, 3902-3909.
22. Stewart, J. J. P., Optimization of Parameters for Semiempirical Methods I. Method. *Journal of Computational Chemistry* **1989,** *10*, 209-220.
23. Stewart, J. J., Optimization of Parameters for Semiempirical Methods V: Modification of Nddo Approximations and Application to 70 Elements. *J Mol Model* **2007,** *13*, 1173-1213.
24. Hinchliffe, A., *Molecular Modelling for Beginners, 2nd Ed by Alan Hinchliffe*. 2nd ed.; A John Wiley and Sons: 2008; p 432.
25. M. Born and J. R. Oppenheimer, A., Zur Quantentheorie Der Molekeln. *annalen der physik* **1927,** *389*, 457-484.
26. Hartree, D. R., The Wave Mechanics of an Atom with a Non-Coulomb Central Field. Part I. Theory and Methods. *Mathematical Proceedings of the Cambridge Philosophical Society* **1928,** *24*, 89-110.
27. Hohenberg, P.; Kohn, W., Inhomogeneous Electron Gas. *Physical Review* **1964,** *136*, B864-B871.
28. Friedman, P. W. A. a. R. S., *Molecular Quantum Mechanics by Peter Atkins & Ronald Friedman*. 3rd ed.; Oxford University Press: 1997.
29. Weinhold, F.; Landis, C. R.; Glendening, E. D., What Is Nbo Analysis and How Is It Useful? *International Reviews in Physical Chemistry* **2016,** *35*, 399-440.
30. Glendening, E. D.; Landis, C. R.; Weinhold, F., Natural Bond Orbital Methods. *Wiley Interdisciplinary Reviews: Computational Molecular Science* **2012,** *2*, 1-42.
31. Harame, D. L.; Koester, S. J.; Freeman, G.; Cottrel, P.; Rim, K.; Dehlinger, G.; Ahlgren, D.; Dunn, J. S.; Greenberg, D.; Joseph, A. et al., The Revolution in Sige: Impact on Device Electronics. *Applied Surface Science* **2004,** *224*, 9-17.
32. Pham, D. P.; Kim, S.; Park, J.; Le, A. H. T.; Cho, J.; Jung, J.; Iftiquar, S. M.; Yi, J., Reduction in Photocurrent Loss and Improvement in Performance of Single Junction Solar Cell Due to Multistep Grading of Hydrogenated Amorphous Silicon Germanium Active Layer. *Silicon* **2018,** *10*, 759-767.
33. Ji, X. Y.; Cheng, H. Y.; Grede, A. J.; Molina, A.; Talreja, D.; Mohney, S. E.; Giebink, N. C.; Badding, J. V.; Gopalan, V., Conformal Coating of Amorphous Silicon and Germanium by High Pressure Chemical Vapor Deposition for Photovoltaic Fabrics. *Apl Materials* **2018,** *6*.
34. Leitz, C. W.; Currie, M. T.; Lee, M. L.; Cheng, Z. Y.; Antoniadis, D. A.; Fitzgerald, E. A., Hole Mobility Enhancements and Alloy Scattering-Limited Mobility in Tensile Strained Si/Sige Surface Channel Metal-Oxide-Semiconductor Field-Effect Transistors. *Journal of Applied Physics* **2002,** *92*, 3745-3751.
35. Yoffe, A. D., Semiconductor Quantum Dots and Related Systems: Electronic, Optical, Luminescence and Related Properties of Low Dimensional Systems. *Advances in Physics* **2001,**

50, 1-208.
36. Paul, D. J., Silicon-Germanium Strained Layer Materials in Microelectronics. *Advanced Materials* **1999,** *11*, 191-204.
37. Adamczyk, A. J.; Broadbelt, L. J., Thermochemical Property Estimation of Hydrogenated Silicon Clusters. *Journal of Physical Chemistry A* **2011,** *115*, 8969-8982.
38. Adamczyk, A. J.; Broadbelt, L. J., The Role of Multifunctional Kinetics During Early-Stage Silicon Hydride Pyrolysis: Reactivity of Si(2)H(2) Isomers with Sih(4) and Si(2)H(6). *Journal of Physical Chemistry A* **2011,** *115*, 2409-2422.
39. Adamczyk, A. J.; Reyniers, M.-F.; Marin, G. B.; Broadbelt, L. J., Exploring 1,2-Hydrogen Shift in Silicon Nanoparticles: Reaction Kinetics from Quantum Chemical Calculations and Derivation of Transition State Group Additivity Database. *Journal of Physical Chemistry A* **2009,** *113*, 10933-10946.
40. Adamczyk, A. J.; Reyniers, M. F.; Marin, G. B.; Broadbelt, L. J., Kinetic Correlations for H(2) Addition and Elimination Reaction Mechanisms During Silicon Hydride Pyrolysis. *Physical Chemistry Chemical Physics* **2010,** *12*, 12676-12696.
41. Adamczyk, A. J.; Reyniers, M. F.; Marin, G. B.; Broadbelt, L. J., Hydrogenated Amorphous Silicon Nanostructures: Novel Structure-Reactivity Relationships for Cyclization and Ring Opening in the Gas Phase. *Theoretical Chemistry Accounts* **2011,** *128*, 91-113.
42. Adamczyk, A. J.; Reyniers, M. F.; Marin, G. B.; Broadbelt, L. J., Kinetics of Substituted Silylene Addition and Elimination in Silicon Nanocluster Growth Captured by Group Additivity. *Chemphyschem* **2010,** *11*, 1978-1994.
43. Kovalenko, M. V.; Manna, L.; Cabot, A.; Hens, Z.; Talapin, D. V.; Kagan, C. R.; Klimov, V. I.; Rogach, A. L.; Reiss, P.; Milliron, D. J. et al., Prospects of Nanoscience with Nanocrystals. *Acs Nano* **2015,** *9*, 1012-1057.
44. Moss, S. J.; Ledwith, A., *The Chemistry of the Semiconductor Industry*. Chapman and Hall: New York, 1987.
45. Petkov, V.; Hessel, C. M.; Ovtchinnikoff, J.; Guillaussier, A.; Korgel, B. A.; Liu, X. F.; Giordano, C., Structure-Properties Correlation in Si Nanoparticles by Total Scattering and Computer Simulations. *Chemistry of Materials* **2013,** *25*, 2365-2371.
46. Yoo, S.; Shao, N.; Zeng, X. C., Reexamine Structures and Relative Stability of Medium-Sized Silicon Clusters: Low-Lying Endohedral Fullerene-Like Clusters Si-30-Si-38. *Physics Letters A* **2009,** *373*, 3757-3760.
47. Galashev, A. Y., Molecular Dynamics Study of Hydrogenated Silicon Clusters at High Temperatures. *Molecular Physics* **2009,** *107*, 2555-2568.
48. Singh, R., Effect of Hydrogen on Ground State Properties of Silicon Clusters (Sinhm; N=11-15, M=0-4): A Density Functional Based Tight Binding Study. *Journal of Physics-Condensed Matter* **2008,** *20*.
49. Li, C. P.; Li, X. J.; Yang, J. C., Silicon Hydride Clusters Si5h(N) (N=3-12) and Their Anions: Structures, Thermochemistry, and Electron Affinities. *Journal of Physical Chemistry A* **2006,** *110*, 12026-12034.
50. Zhao, M.; Gimarc, B. M., Strain Energies of Silicon Rings and Clusters. *Inorganic Chemistry* **1996,** *35*, 5378-5386.
51. Raghavachari, K., Theoretical-Study of Small Silicon Clusters - Equilibrium Geometries and Electronic-Structures of Si-2-7, Si-10. *Journal of Chemical Physics* **1986,** *84*, 5672-5686.
52. Bandyopadhyay, D., Study of Pure and Doped Hydrogenated Germanium Cages: A Density Functional Investigation. *Nanotechnology* **2009,** *20*, 275202.

53. Mahtout, S.; Tariket, Y., Electronic and Magnetic Properties of Crgen (15⩽N⩽29) Clusters: A Dft Study. *Chemical Physics* **2016,** *472*, 270-277.
54. Shi, S. P.; Liu, Y. L.; Zhang, C. Y.; Deng, B. L.; Jiang, G., A Computational Investigation of Aluminum-Doped Germanium Clusters by Density Functional Theory Study. *Computational and Theoretical Chemistry* **2015,** *1054*, 8-15.
55. Frisch, M. J.; Trucks, G. W.; Schlegel, H. B.; Scuseria, G. E.; Robb, M. A.; Cheeseman, J. R.; Scalmani, G.; Barone, V.; Petersson, G. A.; Nakatsuji, H. et al. *Gaussian 16 Rev. B.01*, Wallingford, CT, 2016.
56. Andzelm, J.; Russo, N.; Salahub, D. R., Ground and Excited-States of Group Iva Diatomics from Local-Spin-Density Calculations - Model Potentials for Si, Ge, and Sn. *Journal of Chemical Physics* **1987,** *87*, 6562-6572.
57. Curtiss, L. A.; Redfern, P. C.; Rassolov, V.; Kedziora, G.; Pople, J. A., Extension of Gaussian-3 Theory to Molecules Containing Third-Row Atoms K, Ca, Ga-Kr. *Journal of Chemical Physics* **2001,** *114*, 9287-9295.
58. Montgomery, J. A.; Frisch, M. J.; Ochterski, J. W.; Petersson, G. A., A Complete Basis Set Model Chemistry. Vi. Use of Density Functional Geometries and Frequencies. *Journal of Chemical Physics* **1999,** *110*, 2822-2827.
59. Kalcher, J.; Sax, A. F., Singlet Triplet Splittings and Electron-Affinities of Some Substituted Silylenes. *Theochem-J. Mol. Struct.* **1992,** *85*, 287-302.
60. Kassaee, M. Z.; Buazar, F.; Soleimani-Amiri, S., Triplet Germylenes with Separable Minima at Ab Initio and Dft Levels. *Journal of Molecular Structure-Theochem* **2008,** *866*, 52-57.
61. Apeloig, Y.; Pauncz, R.; Karni, M.; West, R.; Steiner, W.; Chapman, D., Why Is Methylene a Ground State Triplet While Silylene Is a Ground State Singlet? *Organometallics* **2003,** *22*, 3250-3256.
62. Brulin, Q.; Ning, N.; Vach, H., Hydrogen-Induced Crystallization of Amorphous Silicon Clusters in a Plasma Reactor. *J. Non-Cryst. Solids* **2006,** *352*, 1055-1058.
63. Scott, A. P.; Radom, L., Harmonic Vibrational Frequencies: An Evaluation of Hartree-Fock, Moller-Plesset, Quadratic Configuration Interaction, Density Functional Theory, and Semiempirical Scale Factors. *J. Phys. Chem.* **1996,** *100*, 16502-16513.
64. Alecu, I. M.; Zheng, J.; Zhao, Y.; Truhlar, D. G., Computational Thermochemistry: Scale Factor Databases and Scale Factors for Vibrational Frequencies Obtained from Electronic Model Chemistries. *Journal of Chemical Theory and Computation* **2010,** *6*, 2872-2887.
65. Katzer, G.; Sax, A. F., Beyond the Harmonic Approximation: Impact of Anharmonic Molecular Vibrations on the Thermochemistry of Silicon Hydrides. *Journal of Physical Chemistry A* **2002,** *106*, 7204-7215.
66. Vansteenkiste, P.; Speybroeck, V. V.; Verniest, G.; Kimpe, N. D.; Waroquier, M., Applicability of the Hindered Rotor Scheme to the Puckering Mode in Four-Membered Rings. *Journal of Physical Chemistry A* **2006,** *110*, 3838-3844.
67. McQuarrie, D. A.; Simon, J. D., *Molecular Thermodynamics*. University Science Book, Sausalito, CA: 1999.
68. Pfaendtner, J.; Yu, X.; Broadbelt, L. J., The 1-D Hindered Rotor Approximation. *Theoretical Chemistry Accounts* **2007,** *118*, 881-898.
69. Petersson, G. A.; Malick, D. K.; Wilson, W. G.; Ochterski, J. W.; Montgomery, J. A.; Frisch, M. J., Calibration and Comparison of the Gaussian-2, Complete Basis Set, and Density Functional Methods for Computational Thermochemistry. *J. Chem. Phys.* **1998,** *109*, 10570-10579.

70. Wong, H. W.; Nieto, J. C. A.; Swihart, M. T.; Broadbelt, L. J., Thermochemistry of Silicon-Hydrogen Compounds Generalized from Quantum Chemical Calculations. *Journal of Physical Chemistry A* **2004,** *108*, 874-897.
71. Geerlings, P.; De Proft, F.; Langenaeker, W., Conceptual Density Functional Theory. *Chemical Reviews* **2003,** *103*, 1793-1873.
72. Pearson, R. G., Absolute Electronegativity and Hardness - Application to Inorganic-Chemistry. *Inorganic Chemistry* **1988,** *27*, 734-740.
73. Parr, R. G.; Pearson, R. G., Absolute Hardness - Companion Parameter to Absolute Electronegativity. *Journal of the American Chemical Society* **1983,** *105*, 7512-7516.
74. Parr, R. G.; Donnelly, R. A.; Levy, M.; Palke, W. E., Electronegativity - Density Functional Viewpoint. *Journal of Chemical Physics* **1978,** *68*, 3801-3807.
75. Stein, T.; Autschbach, J.; Govind, N.; Kronik, L.; Baer, R., Curvature and Frontier Orbital Energies in Density Functional Theory. *The Journal of Physical Chemistry Letters* **2012,** *3*, 3740-3744.
76. Salzner, U.; Baer, R., Koopmans' Springs to Life. *The Journal of Chemical Physics* **2009,** *131*, 231101.
77. Wielgus, P.; Roszak, S.; Majumdar, D.; Saloni, J.; Leszczynski, J., Theoretical Studies on the Bonding and Thermodynamic Properties of Ge(N)Si(M) (M+N=5) Clusters: The Precursors of Germanium/Silicon Nanomaterials. *Journal of Chemical Physics* **2008,** *128*.
78. Chase, M. W., Nist-Janaf Thermochemical Tables for the Oxygen Fluorides. *Journal of Physical and Chemical Reference Data* **1996,** *25*, 551-603.
79. Swihart, M. T.; Girshick, S. L., Ab Initio Structures and Energetics of Selected Hydrogenated Silicon Clusters Containing Six to Ten Silicon Atoms. *Chemical Physics Letters* **1999,** *307*, 527-532.
80. Gordeychuk, M. V.; Katin, K. P.; Grishakov, K. S.; Maslov, M. M., Silicon Buckyballs Versus Prismanes: Influence of Spatial Confinement on the Structural Properties and Optical Spectra of the Si18
H12 and Si19 H12 Clusters. *International Journal of Quantum Chemistry* **2018,** *118*, e25609.
81. Coats, A. M., McKean, D.C., Steele, D., Infrared Intensities of Nu3 and Nu4 in Sih4, Geh4 and Snh4. *Journal of Molecular Structure* **1994,** *320*, 269-280.
82. Lattanzi, F.; Di Lauro, C.; Horneman, V. M., The N6, N8 3ν4+N12 Infrared System of Si2h6 under High Resolution: Rotational and Torsional Analysis. *Molecular Physics* **2003,** *101*, 2895-2906.
83. Bocanegra-Bernal, M. H.; Matovic, B., Mechanical Properties of Silicon Nitride-Based Ceramics and Its Use in Structural Applications at High Temperatures. *Materials Science and Engineering: A* **2010,** *527*, 1314-1338.
84. Julian-Jankowiak, A.; Valle, R.; Parlier, M., Potential of Innovative Ceramics for Turbine Applications. *Materials at High Temperatures* **2016,** *33*, 578-585.
85. Bocanegra-Bernal, M. H.; Matovic, B., Dense and near-Net-Shape Fabrication of Si3n4 Ceramics. *Materials Science and Engineering: A* **2009,** *500*, 130-149.
86. Zerr, A., Rapid Researchnote_a New High-Pressure D-Phaseof Si3n4. *Physica status solidi (b)* **2001,** *227*, R4-R6.
87. Andreas Zerr, G. M., George Serghiou, Marcus Schwarz, Edwin Kroke, Ralf Riedel, Hartmut Fueß, Peter Kroll, Reinhard Boehler, Synthesis of Cubic Silicon Nitride. *Nature* **1999,** *400*, 340-342.
88. Kroke, E., Novel Group 14 Nitrides. *Coordination Chemistry Reviews* **2004,** *248*, 493-

532.
89. Rostislav_A__Andrievskii, Silicon Nitride: Synthesis and Properties. *Russian Chemical Reviews* **1995,** *64*, 291-308.
90. Jaglarz, J.; Jurzecka-Szymacha, M.; Kluska, S., Film Materials Based on a-Sinx:H with High Refractive Index Obtained by Plasma Enhanced Chemical Vapour Deposition Technology. *Thin Solid Films* **2019,** *669*, 564-570.
91. Torchynska, T. V.; Casas Espinola, J. L.; Vergara Hernandez, E.; Khomenkova, L.; Delachat, F.; Slaoui, A., Effect of the Stoichiometry of Si-Rich Silicon Nitride Thin Films on Their Photoluminescence and Structural Properties. *Thin Solid Films* **2015,** *581*, 65-69.
92. Massines, F.; Silva, J.; Lelièvre, J.-F.; Bazinette, R.; Vallade, J.; Lecouvreur, P.; Pouliquen, S., Hydrogenated Silicon Nitride Sinx:H Deposited by Dielectric Barrier Discharge for Photovoltaics. *Plasma Processes and Polymers* **2016,** *13*, 170-183.
93. Edwin Kroke, Y.-L. L., Christoph Konetschny, Emmanuel Lecomte, Claudia Fasel, Ralf Riedel, Silazane Derived Ceramics and Related Materials. *Materials Science and Engineering* **2000,** *26*, 97-199.
94. F. Giorgis, C. F. P., E. Tresso, Structural Properties of a-Sil_Xn-H Films Grown by Plasma Enhanced Chemical Vapour Deposition by Sir 4 + Nh 3 + H 2 Gas Mixtures. *Thin Solid Films* **1997,** *307*, 298-305.
95. Karouta, F.; Vora, K.; Tian, J.; Jagadish, C., Structural, Compositional and Optical Properties of Pecvd Silicon Nitride Layers. *Journal of Physics D: Applied Physics* **2012,** *45*.
96. Brett D. Eustergerling, Y. S., Formation-of-Aminosilanes-in-the-Hot-Wire-Chemical-Vapor Deposition Process Using Sih4 – Nh3 Gas Mixtures. *ARKIVOC* **2009**, 75-89.
97. H. E. O'Neal, M. A. R., J. G. Martin, M. T. Navio, Kinetics of Silylene Insertion into N-H Bonds and the Mechanism and Kinetics of the Pyrolysis of Dimethylsilylamine. *J. Phys. Chem. A* **1998,** *102*, 8493-8497.
98. Yacoubi, K.; Azzaro, C.; Couderc, J. P., Low Pressure Cvd of Silicon Nitride from a Silane-Ammonia Mixture : Analysis of Preliminary Experimental and Simulation Results. *Le Journal de Physique IV* **1995,** *05*, C5-291-C295-298.
99. O. Parisel, M. H., Y. Ellinger, Interstellar Silicon-Nitrogen Chemistry. I. The Microwave and the Infrared Signatures of the Hsin, Hnsi, Hsinh 2, Hnsih 2 and Hsinh+ Species *Chemical Physics* **1996,** *212*, 331-351.
100. Shao-Wen Hu, Y. W., Xiang-Yun Wang, Ti-Wei Chu, Xin-Qi Liu, Gas Rxn Pathways from Sih4 to Si2h6. *Journal of Physical Chemistry A* **2003,** *107*, 2954-2963.
101. Kovacevic, G.; Pivac, B., Reactions in Silicon-Nitrogen Plasma. *Phys Chem Chem Phys* **2017,** *19*, 3826-3836.
102. Hsi-Wu Wong, J. C. A. N., ‡ Mark T. Swihart, Linda J. Broadbelt,, Thermochemistry of Silicon-Hydrogen Compounds Generalized from Quantum Chemical Calculations. *J. Phys. Chem. A* **2004,** *108*, 874-897.
103. Slakman, B. L.; Simka, H.; Reddy, H.; West, R. H., Extending Reaction Mechanism Generator to Silicon Hydride Chemistry. *Industrial & Engineering Chemistry Research* **2016,** *55*, 12507-12515.
104. Broadbelt, L. J.; Stark, S. M.; Klein, M. T., Computer Generated Reaction Modelling: Decomposition and Encoding Algorithms for Determining Species Uniqueness. *Computers & Chemical Engineering* **1996,** *20*, 113-129.
105. Curtiss, L. A.; Raghavachari, K.; Redfern, P. C.; Rassolov, V.; Pople, J. A., Gaussian-3 (G3) Theory for Molecules Containing First and Second-Row Atoms. *J. Chem. Phys.* **1998,** *109*,

7764-7776.

106. Baboul, A. G.; Curtiss, L. A.; Redfern, P. C.; Raghavachari, K., Gaussian-3 Theory Using Density Functional Geometries and Zero-Point Energies. *J. Chem. Phys.* **1999,** *110*, 7650-7657.

107. Curtiss, L. A.; Redfern, P. C.; Rassolov, V.; Kedziora, G.; Pople, J. A., Extension of Gaussian-3 Theory to Molecules Containing Third-Row Atoms K, Ca, Ga–Kr. *The Journal of Chemical Physics* **2001,** *114*, 9287-9295.

108. Choi, Y.; Adamczyk, A. J., Tuning Hydrogenated Silicon, Germanium, and Sige Nanocluster Properties Using Theoretical Calculations and a Machine Learning Approach. *J Phys Chem A* **2018,** *122*, 9851-9868.

109. Yang, R. C. P. a. W., Density-Functional Theory of the Electronic Structure of Molecules. Annu. Rev. Phys. Chem. 1995, 46, 701–728. Conceptual Dft.Pdf>. *Annu. Rev. Phys. Chern.* **1995,** *46*, 701-728.

110. Weinhold, F., Natural Bond Orbital Analysis: A Critical Overview of Relationships to Alternative Bonding Perspectives. *J Comput Chem* **2012,** *33*, 2363-2379.

111. Chase, M. W., *Nist-Janaf Thermochemical Tables*. Fourth Edition, Journal of Physical and Chemical Reference (Monograph 9): 1998.

112. Shao-Wen Hu, Y. W., Xiang-Yun Wang, Ti-Wei Chu, Xin-Qi Liu, Gas-Phase Reactions between Silane and Ammonia_ a Theoretical Study. *J. Phys. Chem. A* **2003,** *107,* 9189-9196.

113. Mo, Y.; Zhang, Y.; Gao, J., A Simple Electrostatic Model for Trisilylamine: Theoretical Examinations of the N→Σ* Negative Hyperconjugation, Pπ→Dπbonding, and Stereoelectronic Interaction. *Journal of the American Chemical Society* **1999,** *121*, 5737-5742.

114. B. BEAGLEY, A. R. C., New Electron-Diffraction Study of the Molecular Dimensions and Planarity of Trisilylamine. *Transactions of the Faraday Society* **1970,** *66*, 2740-2744.

115. Hedberg, K., The Molecular Structure of Trisilylamine (Sih3)3n1,2. *Journal of the American Chemical Society* **1955,** *77*, 6491-6492.

116. Masatomo Yashima, Y. A., Yasunori Tabira, Crystal Structure and Electron Density of R-Silicon Nitride: Experimental and Theoretical Evidence for the Covalent Bonding and Charge Transfer. *Journal of Physical Chemistry B* **2007,** *111*, 3609-3613.

117. Shimanouchi, T., *Tables of Molecular Vibrational Frequencies Consolidated Volume I, National Bureau of Standards*. 1972; Vol. 1.

118. Beach, D. B., Infrared and Mass Spectroscopic Study of the Reaction of Silyl Iodide and Ammonia. Infrared Spectrum of Silylamine. *Inorganic Chemistry* **1992,** *31*, 4174-4177.

119. Lange, N. A., *Lange's Handbook of Chemistry*. fifteenth edition ed.; McGRAW-HILL, INC: 1999.

120. Mahkam, M. N. a. M., Dft Study of the Six-Membered Heterocyclic Sinn6-Nhn (N = 0-6)_ Stability and Aromaticity. *Organic Chemistry Research* **2016,** *2*, 70-80.

121. Yeseul Choi, T. P., Andrew J. Adamczyk, Hydrogenated Si and Sin Molecules Properties Using Dft Calculation. *Journal of Physical Chemistry A* **2019**. in preparation

Appedix A.1. Calculated standard entropies and constant pressure heat capacities at elevated temperatures using the G3//B3LYP method for all hydrogenated Si, Ge, and SiGe clusters and acyclic species in this study.

		Entropy (J/mol-K)																
		Acyclic structure							Trigonal Planar				Trigonal Pyramidal				
		Si_1H_4	Si_2H_6	Si_3H_8	$SiGeH_6$	Ge_1H_4	Ge_2H_6	Ge_3H_8	T-0	T-1	T-2	T-3	TP-0	TP-1	TP-2	TP-3	TP-4
Temp (K)	Symmetry group	Td	D_{3d}	C_{2v}	C_{3v}	Td	D_{3d}	C_{2v}	D_{3h}	C_{2v}	C_{2v}	D_{3h}	Td	C_{3v}	C_{2v}	C_{3v}	Td
	σ_{ext}	12	6	2	3	12	6	2	6	2	2	6	12	3	2	3	12
298.15		204.5	273.4	346.9	294.2	217.5	304.0	418.9	304.5	333.3	352.8	363.1	331.9	350.2	361.9	366.9	363.8
300		204.8	273.9	347.7	294.7	217.7	304.5	419.8	305.2	334.0	353.5	363.9	332.6	351.0	362.6	367.7	364.6
400		218.4	299.3	385.1	321.1	232.0	331.8	460.2	338.5	368.6	389.2	400.6	369.8	388.4	400.2	405.5	402.7
500		230.7	322.3	418.8	344.8	245.0	356.2	495.9	367.9	398.7	420.0	432.0	400.8	419.5	431.5	436.9	434.3
600		242.2	343.3	449.3	366.4	257.0	378.3	528.1	394.1	425.4	447.2	459.7	427.4	446.1	458.3	463.9	461.4
800		262.9	380.7	503.3	404.5	278.6	417.2	584.3	439.4	471.5	493.9	507.1	471.6	490.6	502.9	508.8	506.6
900		272.3	397.5	527.4	421.6	288.4	434.6	609.3	459.4	491.8	514.4	527.8	490.5	509.6	522.1	528.0	526.0
1000		281.2	413.2	549.8	437.5	297.6	450.8	632.4	478.0	510.5	533.4	547.0	507.8	527.0	539.6	545.7	543.7
1100		289.6	427.9	570.9	452.5	306.2	465.9	654.1	495.3	528.0	551.0	564.8	523.9	543.1	555.8	561.9	560.1
1200		297.5	441.8	590.7	466.5	314.4	480.1	674.3	511.5	544.4	567.5	581.4	538.8	558.1	570.8	577.0	575.2
1300		305.0	454.9	609.4	479.8	322.0	493.5	693.4	526.8	559.7	583.0	597.0	552.7	572.1	584.8	591.1	589.4
1400		312.2	467.3	627.0	492.3	329.3	506.1	711.4	541.2	574.2	597.6	611.7	565.8	585.2	598.0	604.3	602.6
1500		318.9	479.0	643.7	504.1	336.2	518.1	728.4	554.8	587.9	611.4	625.6	578.1	597.5	610.4	616.7	615.1
		Constant Pressure Heat Capacity (J/mol-K)															
298.15		42.7	79.4	117.0	82.9	44.9	86.1	128.2	105.3	110.2	114.6	118.6	121.9	122.6	123.3	124.2	125.4
300		42.8	79.7	117.5	83.2	45.0	86.4	128.7	105.7	110.6	115.0	119.0	122.2	122.9	123.6	124.5	125.6
400		51.3	95.7	140.2	98.9	54.0	101.8	149.9	123.6	127.3	130.6	133.7	133.5	134.1	134.7	135.4	136.3
500		58.9	108.5	157.9	111.4	61.8	114.3	166.7	136.5	139.5	142.2	144.9	140.7	141.3	142.0	142.7	143.6
600		65.6	119.1	172.4	122.0	68.7	124.7	180.7	146.7	149.4	151.8	154.3	146.3	147.0	147.8	148.6	149.6
800		76.5	135.9	195.0	138.4	79.5	141.0	202.3	162.7	164.8	166.9	169.0	155.2	156.1	156.9	157.8	158.8
900		80.8	142.4	203.8	144.8	83.7	147.1	210.4	168.9	170.8	172.8	174.7	158.9	159.7	160.5	161.4	162.3
1000		84.5	147.9	211.1	150.1	87.1	152.2	217.2	174.1	175.9	177.6	179.4	162.0	162.7	163.5	164.4	165.2
1100		87.6	152.5	217.3	154.5	90.0	156.5	222.8	178.5	180.1	181.7	183.3	164.6	165.4	166.1	166.9	167.7
1200		90.2	156.4	222.4	158.2	92.4	160.0	227.4	182.2	183.7	185.1	186.5	166.9	167.6	168.2	168.9	169.7
1300		92.3	159.6	226.8	161.3	94.3	162.9	231.3	185.4	186.7	187.9	189.2	168.8	169.4	170.0	170.7	171.4
1400		94.2	162.4	230.5	163.9	96.0	165.3	234.5	188.0	189.2	190.3	191.5	170.4	171.0	171.6	172.2	172.8
1500		95.8	164.7	233.6	166.1	97.4	167.4	237.2	190.3	191.3	192.3	193.4	171.8	172.3	172.9	173.4	174.0

Appendix A.1 (continued)

		Entropy (J/mol-K)											
		Substituted trigonal planar											
		ST-0	ST-1a	ST-1b	ST-1c	ST-2a	ST-2b	ST-2c	ST-2d	ST-3a	ST-3b	ST-3c	ST-4
Temp. (K)	ymmetry group	Cs	Cs	Cs	C1	Cs	C1	C1	Cs	C1	Cs	Cs	Cs
	σ_{ext}	1	1	1	1	1	1	1	1	1	1	1	1
298.15		381.3	402.4	394.3	402.4	417.5	425.1	412.8	423.8	437.2	451.2	431.6	464.0
300		382.2	403.3	395.3	403.3	418.5	426.1	413.8	424.8	438.2	452.2	432.6	465.1
400		427.2	449.4	441.3	449.6	465.4	473.4	460.9	472.2	486.3	500.7	480.8	514.2
500		466.9	489.9	481.6	490.1	506.5	514.6	502.0	513.4	528.0	542.6	522.5	556.6
600		502.5	526.0	517.6	526.2	543.0	551.3	538.4	550.0	565.0	579.8	559.5	594.1
800		564.2	588.6	579.8	588.6	606.0	614.6	601.3	613.1	628.7	643.8	623.0	658.5
900		591.5	616.1	607.2	616.1	633.7	642.4	629.0	640.9	656.7	671.8	650.9	686.7
1000		616.8	641.7	632.6	641.6	659.4	668.1	654.6	666.6	682.6	697.8	676.8	712.8
1100		640.4	665.5	656.4	665.4	683.3	692.1	678.5	690.5	706.6	721.9	700.8	737.0
1200		662.5	687.8	678.6	687.6	705.7	714.6	700.8	712.9	729.2	744.5	723.3	759.7
1300		683.3	708.7	699.4	708.6	726.7	735.6	721.8	733.9	750.3	765.7	744.4	780.9
1400		702.9	728.5	719.1	728.3	746.5	755.5	741.6	753.8	770.2	785.6	764.3	800.9
1500		721.5	747.1	737.7	746.9	765.3	774.2	760.3	772.5	789.0	804.5	783.0	819.8
		Constant Pressure Heat Capacity (J/mol-K)											
298.15		141.9	145.7	146.1	146.9	149.5	150.7	150.5	151.5	153.9	155.2	154.8	158.1
300		142.5	146.2	146.6	147.4	150.0	151.2	151.1	152.0	154.4	155.7	155.3	158.6
400		167.0	170.3	170.0	170.7	173.1	174.0	173.3	174.1	176.4	177.5	176.6	179.6
500		184.8	188.0	187.1	187.9	190.1	191.0	190.0	190.8	192.9	193.9	192.7	195.6
600		199.1	202.1	201.0	201.8	203.9	204.8	203.6	204.4	206.4	207.3	206.1	208.9
800		221.2	223.8	222.6	223.4	225.2	226.0	224.7	225.5	227.4	228.2	226.9	229.5
900		229.7	232.2	231.0	231.7	233.4	234.2	232.9	233.6	235.3	236.1	234.9	237.3
1000		236.9	239.1	238.0	238.7	240.3	240.9	239.8	240.4	242.0	242.7	241.5	243.8
1100		242.9	245.0	243.9	244.5	246.0	246.6	245.5	246.1	247.5	248.2	247.1	249.1
1200		248.0	249.8	248.9	249.4	250.7	251.3	250.3	250.8	252.1	252.7	251.7	253.6
1300		252.2	253.9	253.0	253.5	254.7	255.2	254.3	254.8	256.0	256.5	255.6	257.3
1400		255.8	257.3	256.5	257.0	258.1	258.5	257.7	258.2	259.2	259.7	258.9	260.4
1500		258.9	260.3	259.5	259.9	260.9	261.3	260.6	261.0	261.9	262.4	261.6	263.0

Appendix A.1 (continued)

		Entropy (J/mol-K)											
		Trigonal Bipyramidal											
		TBP-0	TBP-1a	TBP-1b	TBP-2a	TBP-2b	TBP-2c	TBP-3a	TBP-3b	TBP-3c	TBP-4a	TBP-4b	TBP-5
Temp. (K)	Symmetry group	D_{3h}	C_{3v}	C_{2v}	D_{3h}	Cs	C_{2v}	C_{2v}	D_{3h}	Cs	C_{3v}	C_{2v}	D_{3h}
	σ_{ext}	6	3	2	6	1	2	2	6	1	3	2	6
298.15		358.8	376.3	386.2	381.1	403.1	405.4	406.5	417.2	421.9	433.1	424.1	433.9
300		359.8	377.3	387.2	382.2	404.1	406.5	407.6	418.4	423.0	434.2	425.2	435.0
400		410.0	428.2	438.9	433.5	456.3	459.5	460.1	472.7	476.5	489.0	478.8	489.9
500		454.6	473.2	484.3	478.8	502.1	505.8	506.1	519.9	523.0	536.3	525.5	537.3
600		494.4	513.3	524.7	519.0	542.7	546.8	546.8	561.4	564.2	578.1	566.8	579.1
800		563.2	582.4	594.2	588.5	612.6	617.1	616.9	632.5	634.8	649.5	637.6	650.6
900		593.4	612.7	624.7	618.9	643.2	647.8	647.6	663.5	665.7	680.6	668.5	681.8
1000		621.3	640.8	652.9	647.1	671.5	676.2	676.0	692.2	694.2	709.3	697.1	710.6
1100		647.4	666.9	679.1	673.3	697.8	702.6	702.4	718.7	720.7	736.0	723.7	737.3
1200		671.8	691.4	703.6	697.8	722.3	727.3	727.0	743.5	745.4	760.8	748.5	762.3
1300		694.6	714.3	726.6	720.8	745.4	750.4	750.1	766.8	768.6	784.1	771.7	785.6
1400		716.2	735.9	748.3	742.4	767.1	772.2	771.9	788.6	790.4	806.0	793.5	807.5
1500		736.6	756.3	768.7	762.9	787.6	792.7	792.4	809.3	811.0	826.7	814.1	828.2
		Constant Pressure Heat Capacity (J/mol-K)											
298.15		157.4	160.1	162.8	162.2	165.2	168.3	166.6	173.7	170.3	175.4	171.2	175.8
300		158.1	160.8	163.5	162.8	165.8	168.9	167.2	174.3	170.9	176.0	171.8	176.4
400		187.2	189.0	191.3	190.4	192.9	195.4	193.7	199.5	196.7	200.6	197.2	200.7
500		207.1	208.6	210.5	209.7	211.8	213.8	212.6	217.2	215.0	218.2	215.5	218.5
600		222.4	223.8	225.4	224.8	226.6	228.3	227.4	231.2	229.4	232.2	230.0	232.7
800		245.4	246.6	247.8	247.5	248.9	250.2	249.7	252.5	251.2	253.5	251.9	254.1
900		254.2	255.2	256.3	256.1	257.3	258.4	258.1	260.6	259.4	261.5	260.1	262.1
1000		261.5	262.5	263.4	263.3	264.3	265.3	265.0	267.2	266.2	268.1	266.9	268.7
1100		267.6	268.5	269.3	269.2	270.2	271.0	270.8	272.8	271.8	273.5	272.5	274.1
1200		272.8	273.5	274.3	274.2	275.0	275.8	275.6	277.3	276.5	278.0	277.1	278.6
1300		277.1	277.8	278.4	278.4	279.1	279.8	279.7	281.2	280.4	281.8	281.0	282.3
1400		280.7	281.3	281.9	281.9	282.5	283.1	283.0	284.4	283.7	285.0	284.2	285.4
1500		283.8	284.3	284.9	284.8	285.4	286.0	285.9	287.1	286.5	287.6	287.0	288.0

Appendix A.1 (continued)

		Entropy (J/mol-K)												
Temp (K)		Prismane Pri-0	Pri-1	Pri-2a	Pri-2b	Pri-2c	Pri-3a	Pri-3b	Pri-3c	Pri-4a	Pri-4b	Pri-4c	Pri-5	Pri-6
	Symmetry group	D_{3h}	Cs	Cs	C_{2v}	C2	C_{3v}	C1	Cs	Cs	C_{2v}	C2	Cs	D_{3h}
	σ_{ext}	6	1	1	2	4	3	2	1	1	2	4	1	6
298.15		378.7	405.5	416.5	409.7	411.8	417.9	427.0	428.7	437.9	430.9	432.8	448.3	443.9
300		379.8	406.6	417.6	410.8	412.9	419.0	428.1	429.8	439.1	432.1	434.0	449.5	445.0
400		433.3	460.8	472.3	465.3	467.7	474.2	483.2	485.1	494.7	487.4	489.6	505.4	501.3
500		479.3	507.2	519.0	511.9	514.4	521.2	530.1	532.1	541.9	534.6	536.8	552.9	549.0
600		519.4	547.6	559.7	552.5	555.1	562.1	571.0	573.0	583.0	575.6	577.9	594.2	590.5
800		587.1	615.7	628.1	620.9	623.5	630.9	639.8	641.9	652.1	644.6	647.0	663.6	660.3
900		616.3	645.0	657.6	650.4	653.1	660.5	669.4	671.5	681.9	674.4	676.8	693.5	690.3
1000		643.1	672.0	684.7	677.4	680.1	687.7	696.6	698.7	709.2	701.7	704.1	720.9	717.9
1100		668.0	696.9	709.7	702.5	705.2	712.8	721.7	723.8	734.4	726.9	729.3	746.2	743.3
1200		691.1	720.1	733.0	725.7	728.4	736.2	745.0	747.2	757.8	750.3	752.8	769.7	766.8
1300		712.7	741.8	754.7	747.4	750.2	758.0	766.8	769.0	779.7	772.1	774.6	791.7	788.8
1400		732.9	762.1	775.1	767.8	770.6	778.4	787.3	789.4	800.2	792.6	795.1	812.2	809.4
1500		752.0	781.3	794.3	787.0	789.8	797.7	806.5	808.7	819.5	811.9	814.4	831.5	828.8
		Constant Pressure Heat Capacity (J/mol-K)												
298.15		171.2	173.8	176.0	175.3	176.3	177.9	177.6	178.2	179.6	178.8	179.6	181.0	182.6
300		171.8	174.4	176.5	175.9	176.8	178.5	178.1	178.8	180.1	179.3	180.1	181.5	183.1
400		195.6	197.5	199.1	198.6	199.3	200.5	200.2	200.7	201.6	201.1	201.7	202.7	203.8
500		210.8	212.4	213.7	213.4	213.9	215.0	214.8	215.1	216.1	215.7	216.1	217.1	218.2
600		222.0	223.5	224.8	224.5	224.9	226.0	225.9	226.1	227.2	226.8	227.2	228.2	229.3
800		238.6	239.9	241.1	240.9	241.1	242.2	242.2	242.3	243.3	243.1	243.4	244.4	245.5
900		244.9	246.1	247.2	247.0	247.2	248.2	248.2	248.3	249.3	249.1	249.3	250.3	251.3
1000		250.1	251.2	252.2	252.1	252.2	253.2	253.1	253.2	254.2	254.0	254.2	255.1	256.1
1100		254.4	255.4	256.3	256.3	256.4	257.3	257.2	257.3	258.2	258.0	258.2	259.0	259.9
1200		258.1	259.0	259.8	259.7	259.8	260.6	260.6	260.7	261.4	261.3	261.5	262.2	263.0
1300		261.1	261.9	262.7	262.6	262.7	263.4	263.4	263.5	264.2	264.1	264.2	264.9	265.6
1400		263.7	264.4	265.1	265.1	265.1	265.8	265.8	265.8	266.5	266.4	266.5	267.1	267.7
1500		265.9	266.5	267.2	267.1	267.2	267.8	267.8	267.8	268.4	268.3	268.4	269.0	269.5

Appendix A2. Calculated contour surfaces of frontier molecular orbitals (HOMO, LUMO) for all hydrogenated Si, Ge, and SiGe clusters in Figure 3.1 using the G3//B3LYP level of theory. The HOMO and LUMO orbital distributions for all clusters are presented using an isovalue of 0.02. The nomenclature to identify cluster geometries is the same as in Figure 3.1.

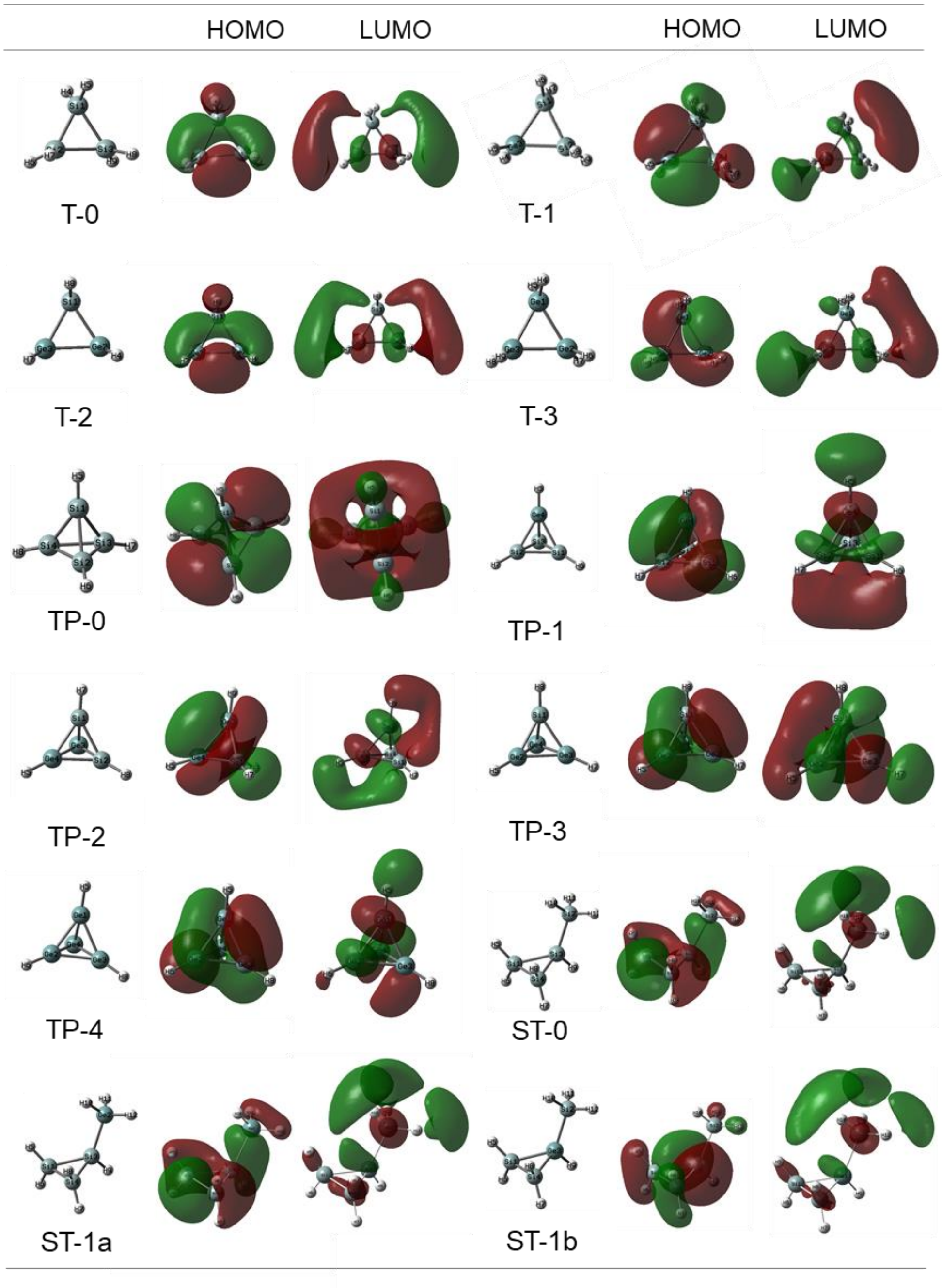

Appendix A.2. (continued)

	HOMO	LUMO		HOMO	LUMO
 ST-1c	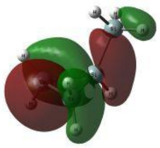	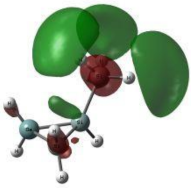	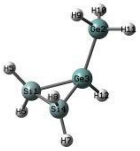 ST-2a	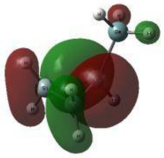	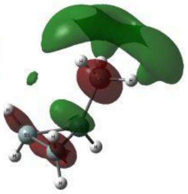
 ST-2b	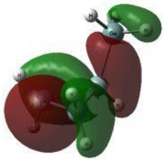	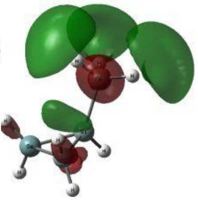	 ST-2c	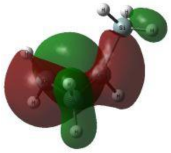	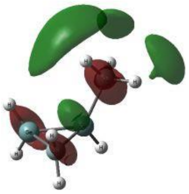
 ST-2d	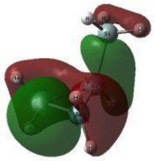	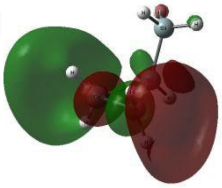	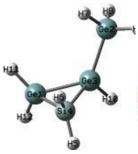 ST-3a	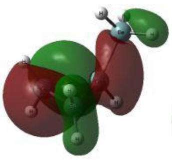	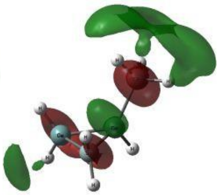
 ST-3b	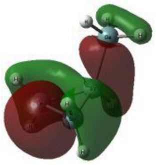	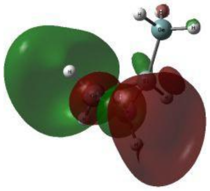	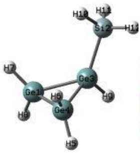 ST-3c	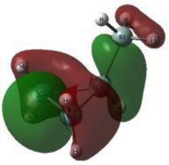	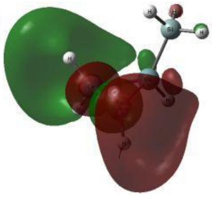
 ST-4	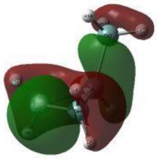	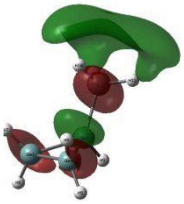	 TBP-0	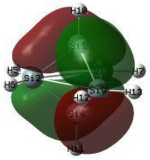	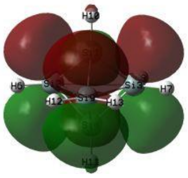
 TBP-1a	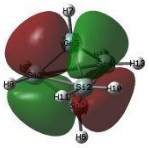	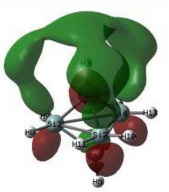	 TBP-1b	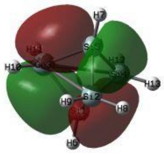	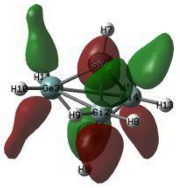

Appendix A.2. (continued)

	HOMO	LUMO		HOMO	LUMO
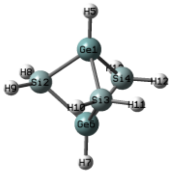 TBP-2a	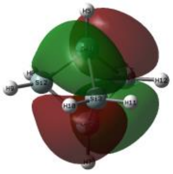	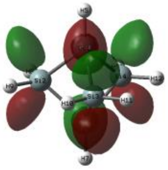	 TBP-2b	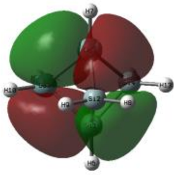	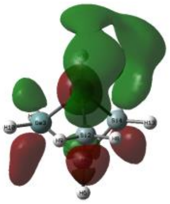
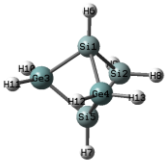 TBP-2c	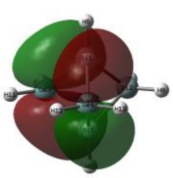	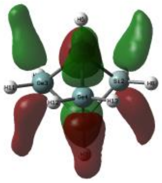	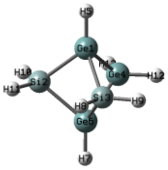 TBP-3a	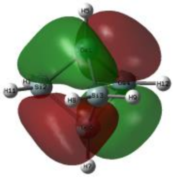	
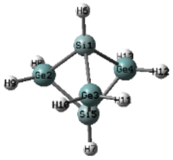 TBP-3b	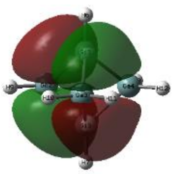	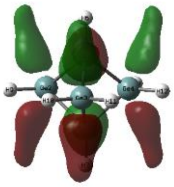	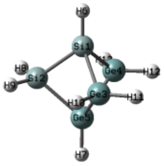 TBP-3c	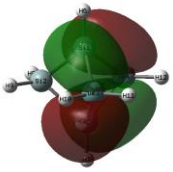	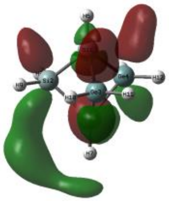
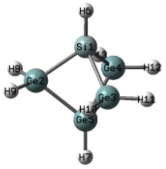 TBP-4a	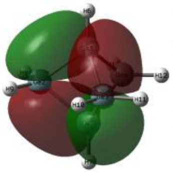	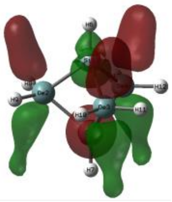	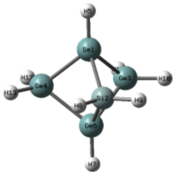 TBP-4b	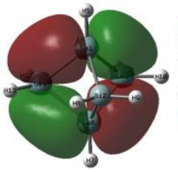	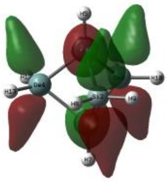
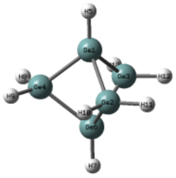 TBP-5	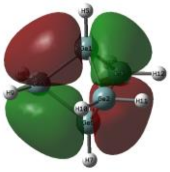	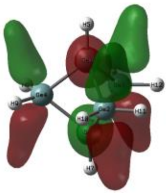	 Pri-0	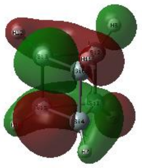	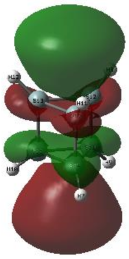
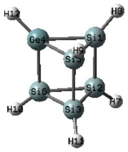 Pri-1	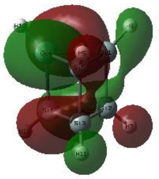	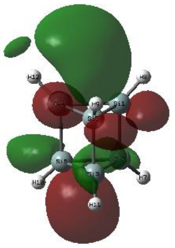	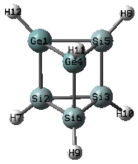 Pri-2a	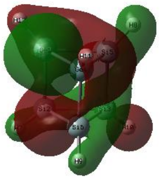	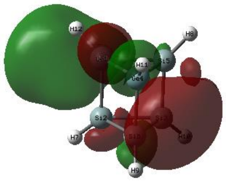

Appendix A.2. (continued)

	HOMO	LUMO		HOMO	LUMO
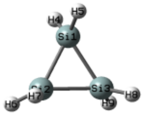 T-0	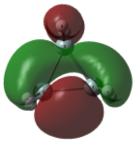	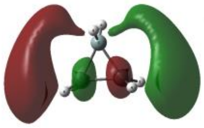	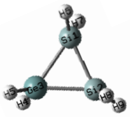 T-1	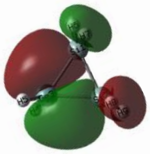	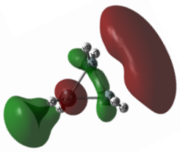
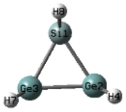 T-2	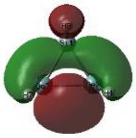	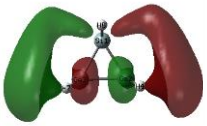	 T-3	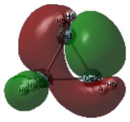	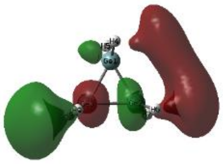
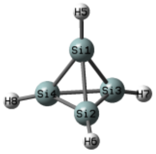 TP-0	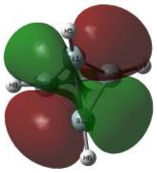	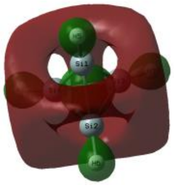	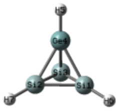 TP-1	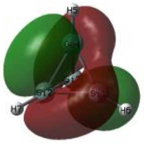	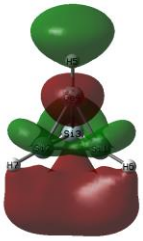
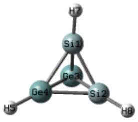 TP-2	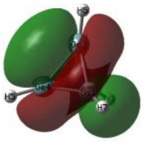	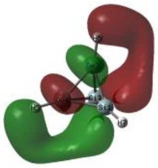	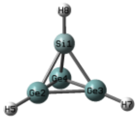 TP-3	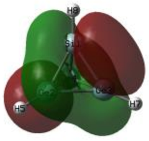	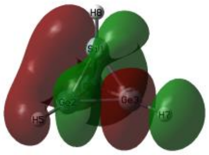
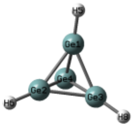 TP-4	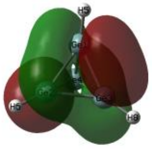	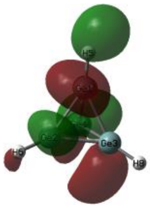	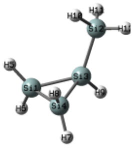 F-0	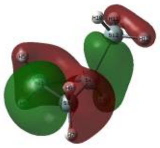	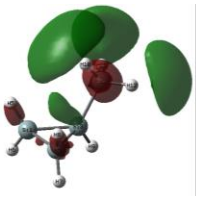
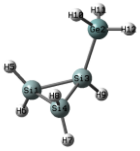 F-1a		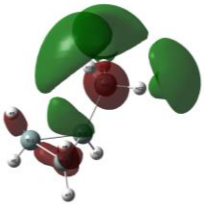	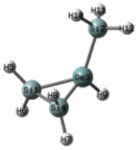 F-1b	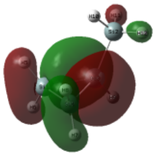	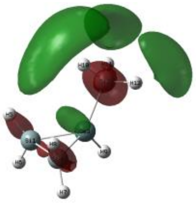

Appendix. B.1. Calculated standard entropies and constant pressure heat capacities at elevated temperatures using the G3//B3LYP method for all hydrogenated Si and SiN clusters and acyclic species in this study.

	Entropy (J/mol.K)															
Symmetry group	D3d	Cs	C2v	C1	Cs	C2	C2h	C1	C1	C1	C2h	C2	C1	C1	Cs	C1
σext	6	1	2	1	1	2	2	1	1	1	2	2	1	1	1	1
Temp. (K)	A2N0	A2N1	A3N0	A3N1a	A3N1b	A3N2	A4N0	A4N1a	A4N1b	A4N2a	A4N2b	A5N0	A5N1a	A5N1b	A5N1c	A5N2a
298.15	273.42	262.46	346.74	323.31	327.97	288.00	412.12	387.54	388.50	356.15	350.99	476.41	452.98	454.01	448.79	416.58
300	273.92	262.87	347.49	323.95	328.56	288.55	413.11	388.43	389.34	356.90	351.79	477.64	454.12	455.10	449.88	417.58
400	299.33	283.28	384.89	356.58	359.11	316.52	462.51	433.07	432.22	394.90	391.57	539.05	510.77	509.98	505.06	467.91
500	322.34	301.88	418.56	385.98	387.34	341.74	506.82	473.14	471.33	429.69	427.34	594.01	561.48	559.74	555.02	513.58
600	343.37	318.94	449.13	412.69	413.46	364.62	546.94	509.40	507.13	461.58	459.71	643.67	607.28	605.09	600.51	555.16
700	362.75	334.67	477.16	437.16	437.67	385.54	583.62	542.52	540.10	490.95	489.26	689.00	649.06	646.70	642.23	593.28
800	380.73	349.28	503.06	459.75	460.20	404.82	617.45	573.04	570.63	518.13	516.46	730.75	687.50	685.16	680.75	628.46
900	397.49	362.92	527.14	480.74	481.25	422.72	648.84	601.34	599.04	543.42	541.68	769.45	723.12	720.88	716.52	661.12
1000	413.19	375.70	549.62	500.35	500.97	439.44	678.10	627.74	625.59	567.06	565.19	805.50	756.29	754.21	749.89	691.59
1100	427.93	387.74	570.69	518.74	519.50	455.14	705.50	652.46	650.48	589.26	587.24	839.22	787.34	785.43	781.14	720.14
1200	441.80	399.10	590.49	536.06	536.97	469.95	731.22	675.70	673.90	610.16	607.99	870.87	816.51	814.77	810.51	747.00
1300	454.90	409.87	609.16	552.41	553.47	483.96	755.46	697.62	695.99	629.92	627.59	900.68	844.01	842.43	838.20	772.35
1400	467.29	420.08	626.81	567.90	569.10	497.27	778.37	718.36	716.90	648.64	646.17	928.84	870.00	868.59	864.37	796.34
1500	479.05	429.81	643.54	582.60	583.94	509.94	800.07	738.04	736.72	666.43	663.83	955.51	894.65	893.38	889.17	819.11
	Heat Capacity (J/mol.K)															
Temp. (K)	A2N0	A2N1	A3N0	A3N1a	A3N1b	A3N2	A4N0	A4N1a	A4N1b	A4N2a	A4N2b	A5N0	A5N1a	A5N1b	A5N1c	A5N2a
298.15	79.40	63.77	117.00	102.07	94.20	87.53	154.68	139.81	133.02	117.69	124.52	192.35	177.50	170.71	171.74	156.54
300	79.74	64.04	117.50	102.50	94.65	87.90	155.33	140.40	133.63	118.24	125.04	193.15	178.24	171.46	172.50	157.24
400	95.71	77.22	140.23	122.46	116.30	105.08	184.76	167.05	161.90	143.86	149.08	229.29	211.59	206.43	207.41	189.47
500	108.47	87.97	157.90	138.02	133.93	118.43	207.31	187.48	184.23	164.11	167.48	256.72	236.90	233.65	234.47	214.42
600	119.10	96.81	172.40	150.64	148.31	129.03	225.67	203.95	202.31	180.30	182.11	278.94	257.22	255.58	256.26	234.30
700	128.16	104.26	184.64	161.19	160.24	137.79	241.10	217.67	217.30	193.58	194.17	297.55	274.14	273.75	274.31	250.64
800	135.88	110.62	195.01	170.15	170.22	145.24	254.14	229.29	229.84	204.69	204.38	313.25	288.41	288.95	289.42	264.31
900	142.40	116.10	203.77	177.80	178.59	151.73	265.11	239.17	240.36	214.11	213.17	326.45	300.51	301.69	302.09	275.88
1000	147.90	120.84	211.12	184.36	185.63	157.45	274.32	247.58	249.19	222.16	220.80	337.52	310.79	312.39	312.73	285.72
1100	152.51	124.96	217.28	190.00	191.57	162.52	282.04	254.76	256.63	229.08	227.45	346.79	319.52	321.37	321.67	294.14
1200	156.38	128.54	222.45	194.84	196.59	167.02	288.50	260.90	262.90	235.04	233.27	354.55	326.95	328.94	329.20	301.35
1300	159.64	131.65	226.80	199.02	200.84	171.01	293.94	266.16	268.21	240.19	238.36	361.08	333.30	335.34	335.56	307.56
1400	162.40	134.36	230.47	202.63	204.46	174.55	298.53	270.68	272.72	244.65	242.82	366.58	338.74	340.77	340.97	312.91
1500	164.74	136.74	233.58	205.75	207.56	177.69	302.42	274.59	276.57	248.53	246.74	371.25	343.42	345.40	345.58	317.54

Appendix. B.1. Continued

	Entropy (J/mol.K)															
Symmetry group	C1	C2	C2	Cs	C2h	C1	C1	C1	C1	C1	C1	C1	C1	C2	C1	C1
σext	1	2	2	1	2	1	1	1	1	1	1	1	1	2	1	1
Temp. (K)	A5N2b	A5N2c	A5N2d	A5N3	A6N0	A6N1a	A6N1b	A6N1c	A6N2a	A6N2b	A6N2c	A6N2d	A6N2e	A6N2f	A6N3a	A6N3b
298.15	421.04	415.42	413.38	384.40	541.11	517.75	519.49	513.14	481.55	487.13	487.41	488.63	483.57	479.67	453.08	449.12
300	422.04	416.46	414.33	385.31	542.58	519.13	520.82	514.48	482.80	488.38	488.65	489.92	484.77	480.86	454.18	450.27
400	472.08	468.27	462.35	430.81	615.98	587.78	587.69	581.65	545.14	550.79	550.71	553.79	545.17	541.15	509.89	507.75
500	517.56	514.69	506.71	472.17	681.60	649.15	648.09	642.26	601.45	607.15	606.85	610.90	600.42	596.33	560.93	559.76
600	559.03	556.61	547.61	509.85	740.79	704.50	702.97	697.29	652.58	658.32	657.86	662.38	651.02	646.90	607.70	607.00
700	597.08	594.81	585.41	544.37	794.78	754.93	753.24	747.65	699.35	705.14	704.56	709.24	697.59	693.45	650.70	650.20
800	632.22	629.93	620.49	576.20	844.45	801.29	799.61	794.10	742.45	748.28	747.62	752.29	740.67	736.53	690.46	689.98
900	664.86	662.45	653.17	605.74	890.45	844.21	842.64	837.18	782.42	788.28	787.57	792.13	780.72	776.58	727.41	726.86
1000	695.32	692.75	683.73	633.30	933.28	884.17	882.75	877.33	819.67	825.56	824.81	829.22	818.12	813.98	761.91	761.23
1100	723.86	721.12	712.41	659.16	973.33	921.55	920.30	914.91	854.55	860.47	859.68	863.92	853.16	849.03	794.26	793.44
1200	750.72	747.80	739.41	683.50	1010.91	956.64	955.56	950.20	887.33	893.28	892.46	896.52	886.11	881.98	824.71	823.73
1300	776.07	772.97	764.91	706.51	1046.29	989.71	988.80	983.45	918.25	924.22	923.37	927.27	917.20	913.07	853.46	852.33
1400	800.06	796.81	789.04	728.32	1079.70	1020.96	1020.21	1014.88	947.49	953.48	952.62	956.36	946.60	942.48	880.69	879.42
1500	822.83	819.43	811.94	749.06	1111.34	1050.58	1049.97	1044.65	975.23	981.24	980.36	983.96	974.48	970.37	906.54	905.14

	Heat Capacity (J/mol.K)															
Temp. (K)	A5N2b	A5N2c	A5N2d	A5N3	A6N0	A6N1a	A6N1b	A6N1c	A6N2a	A6N2b	A6N2c	A6N2d	A6N2e	A6N2f	A6N3a	A6N3b
298.15	155.52	162.32	147.79	141.36	230.03	215.21	208.34	209.39	194.23	194.50	193.32	200.25	186.80	186.47	172.18	178.92
300	156.21	162.99	148.50	142.00	230.98	216.10	209.24	210.29	195.07	195.35	194.16	201.08	187.67	187.33	172.99	179.70
400	188.53	193.65	182.61	171.53	273.81	256.13	250.92	251.92	234.00	234.22	233.11	238.36	228.33	227.95	210.85	216.02
500	213.71	216.90	209.78	194.36	306.12	286.32	283.03	283.87	263.84	264.07	263.13	266.45	260.18	259.91	240.47	243.83
600	233.80	235.37	231.54	212.32	332.20	310.50	308.83	309.51	287.57	287.83	287.06	288.74	285.61	285.46	263.90	265.73
700	250.29	250.61	249.34	226.93	354.00	330.59	330.18	330.75	307.08	307.37	306.73	307.14	306.44	306.39	282.96	283.58
800	264.08	263.49	264.11	239.17	372.36	347.53	348.05	348.52	323.42	323.71	323.18	322.66	323.76	323.76	298.79	298.52
900	275.74	274.50	276.46	249.63	387.79	361.86	363.02	363.42	337.21	337.51	337.06	335.89	338.25	338.28	312.14	311.23
1000	285.64	283.99	286.84	258.69	400.72	373.99	375.58	375.92	348.91	349.21	348.83	347.23	350.42	350.47	323.49	322.15
1100	294.10	292.20	295.59	266.58	411.53	384.27	386.11	386.41	358.88	359.16	358.83	356.98	360.67	360.72	333.20	331.59
1200	301.34	299.32	303.01	273.48	420.60	393.00	394.98	395.23	367.39	367.66	367.38	365.39	369.34	369.40	341.54	339.78
1300	307.56	305.50	309.32	279.53	428.21	400.44	402.47	402.69	374.68	374.94	374.69	372.65	376.70	376.75	348.72	346.90
1400	312.93	310.88	314.71	284.84	434.63	406.80	408.82	409.01	380.96	381.19	380.98	378.95	382.98	383.02	354.94	353.11
1500	317.57	315.58	319.33	289.50	440.08	412.26	414.23	414.40	386.37	386.59	386.40	384.42	388.35	388.39	360.34	358.54

Appendix. B.1. Continued

	Entropy (J/mol.K)															
Symmetry group	D3h	C2v	Td	C3v	D3h	C3v	Cs	D3h	Cs	Cs	Cs	C1	C1	D2d	C2v	C2h
σext	6	2	12	3	6	3	1	6	1	1	1	2	2	4	2	2
Temp. (K)	TN0	TN1	TPyN0	TPyN1	TBPyN0	TBPyN1a	TBPyN1b	TBPyN2	STN0	STN1a	STN1b	STN1c_ch	STN2_ch	SN0	SN1	SN2
298.15	304.46	281.95	332.08	316.37	358.80	333.47	353.57	303.44	381.21	355.46	355.25	347.18	317.62	348.33	324.56	299.07
300	305.13	282.47	332.85	316.99	359.80	334.32	354.46	304.16	382.11	356.29	355.98	347.94	318.29	349.21	325.29	299.68
400	338.44	308.75	370.07	347.47	410.06	377.55	399.30	341.71	427.10	397.06	393.06	386.58	352.42	393.26	362.52	331.16
500	367.80	332.76	401.04	373.50	454.66	416.88	439.52	376.58	466.86	432.92	426.95	421.39	383.13	432.59	396.55	360.55
600	394.00	354.63	427.59	396.15	494.47	452.52	475.60	408.52	502.42	464.85	457.91	452.88	410.85	467.92	427.56	387.64
700	417.69	374.64	450.91	416.22	530.42	484.99	508.27	437.79	534.64	493.66	486.37	481.58	436.04	500.03	455.95	412.60
800	439.36	393.06	471.79	434.28	563.23	514.79	538.10	464.74	564.15	519.96	512.66	507.95	459.13	529.48	482.12	435.66
900	459.36	410.12	490.73	450.70	593.43	542.30	565.56	489.68	591.39	544.19	537.08	532.34	480.44	556.69	506.37	457.06
1000	477.92	426.00	508.08	465.77	621.40	567.84	591.00	512.86	616.68	566.67	559.84	555.02	500.26	581.98	528.94	477.01
1100	495.24	440.85	524.11	479.68	647.45	591.66	614.69	534.49	640.29	587.65	581.14	576.20	518.78	605.58	550.06	495.68
1200	511.46	454.79	539.01	492.62	671.81	613.96	636.86	554.76	662.40	607.32	601.14	596.07	536.16	627.70	569.87	513.23
1300	526.72	467.93	552.93	504.70	694.69	634.92	657.68	573.81	683.20	625.83	619.98	614.78	552.55	648.50	588.54	529.78
1400	541.11	480.33	566.00	516.03	716.24	654.67	677.31	591.78	702.83	643.31	637.76	632.44	568.05	668.13	606.17	545.43
1500	554.72	492.09	578.31	526.69	736.62	673.35	695.88	608.77	721.40	659.87	654.61	649.17	582.75	686.70	622.87	560.27

	Heat Capacity (J/mol.K)															
Temp. (K)	TN0	TN1	TPyN0	TPyN1	TBPyN0	TBPyN1a	TBPyN1b	TBPyN2	STN0	STN1a	STN1b	STN1c_ch	STN2_ch	SN0	SN1	SN2
298.15	25.16	19.40	29.15	23.52	37.62	31.81	33.32	27.21	33.92	30.87	27.40	28.79	25.46	32.94	27.41	22.87
300	25.26	19.49	29.22	23.59	37.79	31.97	33.47	27.37	34.05	30.98	27.53	28.92	25.57	33.08	27.55	22.99
400	29.54	23.83	31.92	26.56	44.74	39.07	40.19	34.38	39.91	36.08	33.55	34.68	30.62	39.33	33.72	28.88
500	32.61	27.03	33.63	28.53	49.50	44.06	44.81	39.34	44.18	39.76	38.14	38.96	34.35	43.82	38.26	33.30
600	35.06	29.50	34.96	30.01	53.17	47.86	48.29	43.07	47.59	42.65	41.80	42.31	37.21	47.37	41.78	36.66
700	37.12	31.50	36.11	31.20	56.16	50.91	51.07	46.00	50.44	45.05	44.80	45.04	39.50	50.31	44.64	39.32
800	38.87	33.15	37.10	32.17	58.66	53.40	53.36	48.38	52.86	47.09	47.28	47.31	41.41	52.79	47.00	41.49
900	40.36	34.53	37.97	32.98	60.75	55.45	55.27	50.32	54.90	48.83	49.35	49.22	43.04	54.86	48.97	43.28
1000	41.61	35.69	38.72	33.65	62.50	57.15	56.87	51.91	56.61	50.34	51.06	50.82	44.43	56.60	50.62	44.78
1100	42.67	36.67	39.35	34.20	63.97	58.55	58.22	53.23	58.05	51.63	52.48	52.16	45.65	58.05	52.00	46.06
1200	43.55	37.50	39.89	34.66	65.19	59.72	59.36	54.32	59.26	52.75	53.66	53.30	46.71	59.27	53.17	47.15
1300	44.30	38.22	40.35	35.05	66.22	60.70	60.32	55.23	60.28	53.72	54.65	54.27	47.63	60.30	54.16	48.09
1400	44.94	38.82	40.74	35.37	67.09	61.53	61.15	56.00	61.14	54.55	55.48	55.10	48.44	61.16	55.01	48.89
1500	45.48	39.35	41.07	35.65	67.82	62.22	61.85	56.65	61.88	55.28	56.19	55.81	49.15	61.89	55.73	49.59

Appendix. B.1. Continued

	Entropy (J/mol.K)										
Symmetry group	C1	C2	C2v	D3d	Cs	C1	C2h	Cs	D3h	Cs	C2
σext	1	2	2	6	1	1	2	1	6	1	2
Temp. (K)	PN0	PN1	PN2	HN0	HN1	HN2a	HN2b	HN3	PriN0	PriN1	PriN2
298.15	426.97	385.89	352.76	444.00	433.80	408.57	402.95	375.50	378.71	364.80	335.19
300	428.08	386.86	353.60	445.35	435.02	409.66	404.02	376.45	379.81	365.74	336.00
400	483.71	436.01	396.58	512.62	496.21	464.72	458.55	424.94	433.33	412.39	376.79
500	533.46	480.61	436.20	572.81	551.47	515.05	508.55	470.07	479.31	453.26	413.14
600	578.20	521.09	472.54	626.97	601.50	560.96	554.26	511.68	519.41	489.32	445.48
700	618.88	558.08	505.93	676.22	647.16	603.02	596.22	550.03	555.02	521.54	474.50
800	656.19	592.13	536.77	721.42	689.14	641.78	634.92	585.49	587.09	550.66	500.79
900	690.67	623.66	565.39	763.18	727.99	677.70	670.80	618.43	616.30	577.24	524.80
1000	722.71	653.00	592.06	801.98	764.12	711.14	704.24	649.15	643.14	601.69	546.90
1100	752.62	680.43	617.02	838.20	797.88	742.43	735.52	677.92	667.97	624.31	567.35
1200	780.65	706.16	640.47	872.15	829.55	771.79	764.89	704.96	691.07	645.37	586.39
1300	807.01	730.39	662.57	904.08	859.35	799.46	792.56	730.47	712.66	665.06	604.18
1400	831.88	753.27	683.46	934.20	887.49	825.60	818.71	754.60	732.94	683.55	620.89
1500	855.42	774.94	703.27	962.70	914.13	850.37	843.49	777.48	752.05	700.97	636.63
	Heat Capacity (J/mol.K)										
Temp. (K)	PN0	PN1	PN2	HN0	HN1	HN2a	HN2b	HN3	PriN0	PriN1	PriN2
298.15	41.54	36.38	31.52	50.21	45.44	40.58	40.10	35.32	40.91	35.17	30.38
300	41.72	36.55	31.68	50.43	45.65	40.77	40.30	35.51	41.05	35.31	30.52
400	49.68	44.27	39.08	60.07	54.94	49.79	49.40	44.33	46.76	41.25	36.46
500	55.43	49.97	44.69	67.05	61.80	56.55	56.25	51.05	50.37	45.10	40.34
600	59.95	54.43	49.04	72.55	67.18	61.80	61.60	56.23	53.06	47.91	43.10
700	63.69	58.06	52.53	77.10	71.57	66.03	65.90	60.35	55.23	50.10	45.20
800	66.83	61.07	55.40	80.89	75.22	69.52	69.44	63.71	57.02	51.86	46.86
900	69.45	63.59	57.78	84.07	78.26	72.43	72.38	66.49	58.52	53.30	48.19
1000	71.65	65.69	59.77	86.72	80.81	74.86	74.85	68.83	59.77	54.48	49.28
1100	73.48	67.45	61.45	88.94	82.94	76.91	76.91	70.81	60.81	55.46	50.16
1200	75.02	68.94	62.88	90.79	84.74	78.65	78.66	72.50	61.68	56.27	50.89
1300	76.31	70.20	64.09	92.34	86.25	80.13	80.14	73.94	62.41	56.94	51.50
1400	77.40	71.26	65.13	93.65	87.54	81.39	81.41	75.18	63.03	57.50	52.00
1500	78.32	72.17	66.03	94.76	88.63	82.47	82.49	76.26	63.55	57.98	52.43

Appendix. B.2. Thermodynamic properties with internal rotation correction

Thermochemistry properties with internal rotation correction: Enthalpy (kcal/mol) S (cal/mol-K) Cp (cal/mol-k)

	A2N0			A2N1			A3N0			A3N1a			A3N1b			A3N2		
Temp. (K)	H^o_f	S	C_p	H^o_f	S	C_p	H^o_f	S	C_p	H^o_f	S	C_p	H^o_f	S	C_p	H^o_f	S	C_p
298.15	101.50	274.95	73.60	1.34	265.11	58.21	161.58	363.39	113.03	68.58	336.11	98.99	12.08	341.71	88.42	-57.18	296.35	86.87
300	101.64	275.42	73.93	1.45	265.49	58.47	161.80	364.13	113.52	68.77	336.76	99.43	12.26	342.29	88.87	-57.00	296.94	87.24
400	110.15	299.75	90.10	7.24	285.12	70.72	174.91	401.63	136.93	80.33	369.84	120.16	22.85	372.55	111.06	-46.63	326.62	105.40
500	118.86	322.03	101.92	15.11	302.62	81.60	187.91	435.54	153.21	92.06	399.45	134.97	35.37	400.38	129.23	-34.88	352.76	119.78
600	129.81	341.93	112.73	23.93	318.67	90.63	204.40	465.52	168.26	104.94	426.17	146.63	49.46	425.99	144.18	-22.06	376.09	131.41
700	141.71	360.25	121.99	33.55	333.45	98.30	222.19	492.90	181.07	120.48	450.08	157.78	64.83	449.63	156.69	-8.38	397.14	141.14
800	154.44	377.21	129.94	43.83	347.16	104.90	241.09	518.09	192.04	136.97	472.07	167.36	81.27	471.55	167.30	6.03	416.35	149.53
900	167.86	392.99	136.74	54.69	359.93	110.64	260.92	541.42	201.45	154.28	492.42	175.67	98.60	491.94	176.33	21.06	434.04	156.92
1000	181.86	407.73	142.54	66.04	371.87	115.67	281.53	563.11	209.50	172.27	511.36	182.91	116.69	510.97	184.08	36.65	450.44	163.51
1500	257.93	469.15	161.32	128.25	422.07	133.30	392.69	652.89	235.94	269.68	590.01	208.10	214.93	590.29	209.93	120.96	518.50	188.08
3000	510.38	585.23	181.50	339.81	519.19	154.99	758.45	821.15	266.97	594.70	739.37	240.52	541.99	740.64	241.42	396.95	649.44	213.95
6000	1038.16	707.01	198.10	790.18	623.03	172.69	1520.40	996.98	297.40	1279.33	897.29	272.01	1228.11	898.93	272.27	1004.06	789.40	246.57

	A4N0			A4N1a			A4N1b			A4N1s			A4N2a			A4N2b		
Temp. (K)	H^o_f	S	C_p	H^o_f	S	C_p	H^o_f	S	C_p	H^o_f	S	C_p	H^o_f	S	C_p	H^o_f	S	C_p
298.15	221.41	435.76	161.92	127.52	415.47	138.52	79.25	419.73	129.52	30.44	411.19	123.77	-54.69	336.01	109.42	36.98	369.73	125.55
300	221.71	436.76	162.52	127.80	416.39	139.11	79.50	420.59	130.12	30.68	412.02	124.38	-54.49	336.68	109.94	37.24	370.60	126.09
400	238.29	487.88	185.70	142.92	463.11	165.94	94.89	464.60	159.42	45.50	454.36	154.83	-42.16	371.91	135.23	52.25	413.57	151.89
500	256.38	533.18	198.30	160.24	504.11	186.48	112.73	504.24	182.76	62.89	493.02	179.69	-27.58	404.32	155.18	69.06	450.97	171.81
600	278.41	573.25	216.31	178.49	540.93	202.18	131.13	540.54	200.45	80.27	528.85	198.05	-11.21	434.07	171.08	87.32	484.19	187.81
700	302.09	609.69	231.42	199.92	573.90	216.87	152.46	573.34	216.39	101.42	561.38	215.14	6.59	461.45	184.09	102.00	514.80	196.37
800	327.16	643.11	244.18	222.59	604.12	229.47	175.13	603.56	229.91	124.01	591.49	229.58	25.58	486.76	194.97	122.37	541.96	207.71
900	353.39	673.97	254.93	246.30	632.02	240.38	198.92	631.55	241.47	147.81	619.48	241.81	45.57	510.27	204.18	143.64	566.98	217.61
1000	380.62	702.63	263.98	270.91	657.91	249.86	223.66	657.58	251.39	172.61	645.58	252.21	66.41	532.20	212.05	162.57	590.51	223.24
1500	526.86	820.77	291.87	403.40	764.92	282.72	357.12	765.37	284.74	306.73	753.89	286.25	179.75	623.70	237.96	281.29	686.38	254.86
3000	1005.94	1041.20	315.03	841.73	966.46	325.98	797.63	967.97	326.94	748.97	957.32	327.72	560.61	798.66	262.99	678.87	869.02	299.53
6000	2002.06	1271.08	321.88	1760.52	1178.43	371.30	1718.00	1180.33	371.59	1670.62	1170.00	371.82	1366.10	984.43	271.34	1520.34	1063.08	345.91

	A5N0			A5N1a			A5N1b			A5N1c			A5N2a			A5N2b		
Temp. (K)	H^o_f	S	C_p	H^o_f	S	C_p	H^o_f	S	C_p	H^o_f	S	C_p	H^o_f	S	C_p	H^o_f	S	C_p
298.15	221.41	435.76	161.92	127.52	415.47	138.52	79.25	419.73	129.52	30.44	411.19	123.77	-54.69	336.01	109.42	36.98	375.50	125.55
300	221.71	436.76	162.52	127.80	416.39	139.11	79.50	420.59	130.12	30.68	412.02	124.38	-54.49	336.68	109.94	37.24	376.36	126.09
400	238.29	487.88	185.70	142.92	463.11	165.94	94.89	464.60	159.42	45.50	454.36	154.83	-42.16	371.91	135.23	52.25	419.33	151.89
500	256.38	533.18	198.30	160.24	504.11	186.48	112.73	504.24	182.76	62.89	493.02	179.69	-27.58	404.32	155.18	69.06	456.73	171.81
600	278.41	573.25	216.31	178.49	540.93	202.18	131.13	540.54	200.45	80.27	528.85	198.05	-11.21	434.07	171.08	87.32	489.96	187.81
700	302.09	609.69	231.42	199.92	573.90	216.87	152.46	573.34	216.39	101.42	561.38	215.14	6.59	461.45	184.09	102.00	520.56	196.37
800	327.16	643.11	244.18	222.59	604.12	229.47	175.13	603.56	229.91	124.01	591.49	229.58	25.58	486.76	194.97	122.37	547.72	207.71
900	353.39	673.97	254.93	246.30	632.02	240.38	198.92	631.55	241.47	147.81	619.48	241.81	45.57	510.27	204.18	143.64	572.74	217.61
1000	380.62	702.63	263.98	270.91	657.91	249.86	223.66	657.58	251.39	172.61	645.58	252.21	66.41	532.20	212.05	162.57	596.28	223.24
1500	526.86	820.77	291.87	403.40	764.92	282.72	357.12	765.37	284.74	306.73	753.89	286.25	179.75	623.70	237.96	281.29	692.15	254.86
3000	1005.94	1041.20	315.03	841.73	966.46	325.98	797.63	967.97	326.94	748.97	957.32	327.72	560.61	798.66	262.99	678.87	874.79	299.53
6000	2002.06	1271.08	321.88	1760.52	1178.43	371.30	1718.00	1180.33	371.59	1670.62	1170.00	371.82	1366.10	984.43	271.34	1520.34	1068.84	345.91

Appendix. B.2. Continued

	A5N2c			A5N2d			A5N3		
Temp. (K)	H^o_f	S	C_p	H^o_f	S	C_p	H^o_f	S	C_p
298.15	94.07	447.61	175.61	-37.73	459.14	150.17	-105.74	424.89	161.04
300	94.39	448.70	176.22	-37.44	460.12	150.84	-105.45	425.89	161.56
400	113.54	503.52	204.94	-19.79	510.57	183.74	-87.94	475.99	187.08
500	132.65	552.41	217.31	0.81	556.36	210.05	-68.15	520.01	207.46
600	156.17	595.18	235.21	21.48	598.56	222.01	-46.54	559.33	223.77
700	178.36	634.27	240.96	46.27	636.70	239.47	-23.44	594.86	237.19
800	204.78	669.51	253.55	72.65	671.87	253.94	-1.76	627.79	239.30
900	232.38	701.97	264.31	100.36	704.46	266.05	23.53	657.54	249.22
1000	260.96	732.06	273.57	129.17	734.78	276.24	49.75	685.13	257.82
1500	414.78	856.29	304.55	284.76	860.44	308.35	184.49	799.55	278.49
3000	925.67	1091.10	335.13	799.84	1097.27	336.98	656.56	1016.41	309.53
6000	2001.31	1339.21	345.45	1878.51	1346.14	346.00	1656.26	1246.95	320.30

	A6N0			A6N1a			A6N1b			A6N1c			A6N2a			A6N2b		
Temp. (K)	H^o_f	S	C_p	H^o_f	S	C_p	H^o_f	S	C_p	H^o_f	S	C_p	H^o_f	S	C_p	H^o_f	S	C_p
298.15	340.88	601.52	248.35	235.07	490.11	206.90	198.35	580.15	221.31	206.18	576.03	222.51	78.62	536.19	213.76	114.57	535.38	211.57
300	341.34	603.06	249.22	235.46	491.39	207.75	198.77	581.55	222.14	206.61	577.43	223.35	79.02	537.51	214.54	114.97	536.71	212.31
400	365.87	681.33	279.58	258.35	556.87	247.32	222.33	652.64	256.95	230.56	648.84	258.14	100.56	605.14	241.77	138.50	604.06	247.78
500	392.83	749.85	296.81	284.66	615.39	277.06	248.59	715.87	278.54	256.43	712.35	279.39	127.09	664.15	270.39	163.51	663.66	270.75
600	425.95	810.09	322.41	313.63	668.08	300.80	278.09	772.24	299.06	286.20	768.89	299.76	154.90	717.32	288.46	191.26	716.93	288.44
700	461.40	864.64	343.76	344.76	715.97	320.49	311.19	823.16	319.99	319.36	819.91	320.57	185.99	765.16	307.25	222.34	764.77	307.14
800	498.81	914.52	361.73	377.69	759.88	337.06	346.20	869.84	337.49	354.42	866.66	337.97	217.05	809.10	318.48	252.91	808.79	318.13
900	537.87	960.47	376.86	412.14	800.41	351.08	382.81	912.91	352.17	391.08	909.78	352.58	251.27	849.36	331.81	284.42	849.28	326.85
1000	578.32	1003.04	389.56	447.89	838.03	362.97	420.77	952.86	364.50	429.08	949.77	364.85	286.73	886.67	343.14	319.80	886.51	338.31
1500	794.72	1177.90	428.64	640.16	993.34	400.78	624.39	1117.36	402.80	632.82	1114.37	402.99	473.93	1040.66	374.93	509.81	1040.00	375.17
3000	1500.42	1502.68	461.03	1273.94	1284.81	434.56	1291.51	1424.30	435.53	1300.10	1421.38	435.59	1100.26	1328.68	409.06	1136.36	1328.13	409.14
6000	2964.87	1840.65	470.60	2598.71	1590.48	445.19	2680.21	1744.76	445.49	2688.87	1741.86	445.50	2411.58	1631.22	420.08	2447.82	1630.70	420.11

	A6N2c			A6N2d			A6N2e			A6N2f			A6N3a			A6N3b		
Temp. (K)	H^o_f	S	C_p	H^o_f	S	C_p	H^o_f	S	C_p	H^o_f	S	C_p	H^o_f	S	C_p	H^o_f	S	C_p
298.15	105.45	541.25	206.67	152.44	536.64	218.09	29.67	542.28	199.99	58.56	538.42	196.28	-94.26	509.15	187.70	-12.31	493.04	208.52
300	105.84	542.56	207.44	152.84	537.99	218.83	30.05	543.54	200.79	58.94	539.68	197.06	-93.90	510.33	188.42	-11.93	494.33	209.15
400	128.96	608.69	244.24	175.56	606.23	249.23	51.84	608.21	234.91	78.54	604.94	225.51	-72.79	570.74	223.64	10.60	558.83	239.51
500	154.18	667.61	268.18	200.20	666.26	266.93	77.78	665.90	265.46	104.39	662.42	256.43	-48.53	624.69	251.48	34.37	615.23	258.84
600	178.90	720.87	277.41	226.70	719.69	279.18	105.54	718.28	285.34	133.01	714.47	281.16	-21.78	673.33	273.64	61.71	664.97	278.42
700	209.75	768.33	296.69	257.65	767.32	297.21	133.91	766.25	296.30	163.87	761.94	301.42	5.29	717.77	287.15	87.32	710.24	285.50
800	242.35	811.80	312.80	290.26	810.80	312.39	166.52	809.73	313.27	196.57	805.55	318.26	32.56	758.75	293.12	117.86	750.95	299.39
900	276.44	851.89	326.39	324.26	850.81	325.32	200.69	849.92	327.48	230.82	845.83	332.35	61.07	796.22	301.55	149.68	788.39	311.28
1000	311.77	889.08	337.91	359.47	887.86	336.40	236.15	887.25	339.42	266.35	883.22	344.20	93.90	830.77	312.66	179.50	823.49	316.54
1500	501.64	1042.45	374.96	548.37	1040.45	372.95	426.97	1041.38	376.95	454.72	1037.70	376.99	270.87	973.69	348.91	355.96	966.01	351.70
3000	1128.02	1330.50	409.09	1172.58	1327.45	408.13	1055.52	1330.47	410.04	1083.30	1326.81	410.05	858.47	1243.79	383.50	937.46	1235.38	382.61
6000	2439.40	1633.05	420.09	2482.39	1629.61	419.81	2368.45	1633.41	420.37	2396.25	1629.75	420.37	2093.94	1528.79	394.95	2171.46	1520.01	394.69

Appendix. B.2. Continued

	STN0			STN1a			STN1b			STN1c			STN2		
Temp. (K)	H^o_f	S	C_p	H^o_f	S	C_p	H^o_f	S	C_p	H^o_f	S	C_p	H^o_f	S	C_p
298.15	362.03	379.99	140.33	280.81	352.55	126.20	191.22	343.30	106.36	251.69	346.95	117.52	131.27	312.55	106.20
300	362.30	380.86	140.85	281.05	353.33	126.66	191.43	343.98	106.89	251.91	347.68	118.03	131.46	313.20	106.64
400	377.64	424.77	164.15	294.83	392.79	147.37	203.85	379.50	131.73	264.96	385.01	141.41	143.24	346.88	127.38
500	393.47	463.88	176.01	310.37	427.36	162.31	218.45	411.94	150.68	278.98	418.79	154.17	156.79	377.02	142.54
600	412.23	498.00	190.00	325.59	458.25	169.50	234.73	441.55	165.72	295.54	448.92	167.95	171.66	404.06	154.02
700	432.26	528.84	201.69	343.48	485.77	179.31	252.37	468.69	178.03	313.35	476.32	179.16	187.55	428.51	163.13
800	453.37	556.98	211.57	362.27	510.83	187.64	271.14	493.70	188.22	332.18	501.43	188.47	204.26	450.80	170.64
900	475.39	582.89	219.93	381.83	533.84	194.77	290.83	516.87	196.68	351.86	524.58	196.26	221.67	471.28	177.00
1000	498.18	606.87	226.98	402.05	555.13	200.91	311.29	538.40	203.73	372.26	546.04	202.83	239.66	490.22	182.46
1500	620.02	705.32	248.81	510.32	642.60	221.21	421.39	627.34	225.08	481.64	634.42	223.47	336.06	568.09	200.91
3000	1017.25	888.14	267.07	867.00	806.61	240.68	782.28	793.39	242.53	840.70	799.59	241.71	649.83	715.02	215.23

Appendix. B.3 Calculated contour surfaces of frontier molecular orbitals (HOMO, LUMO) for all Hydrogenated Si and SiN clusters using the G3//B3LYP level of theory. The HOMO and LUMO orbital distributions for all clusters are presented using an isovalue of 0.02. The nomenclature to identify cluster geometries is the same as in Figure 4.1.

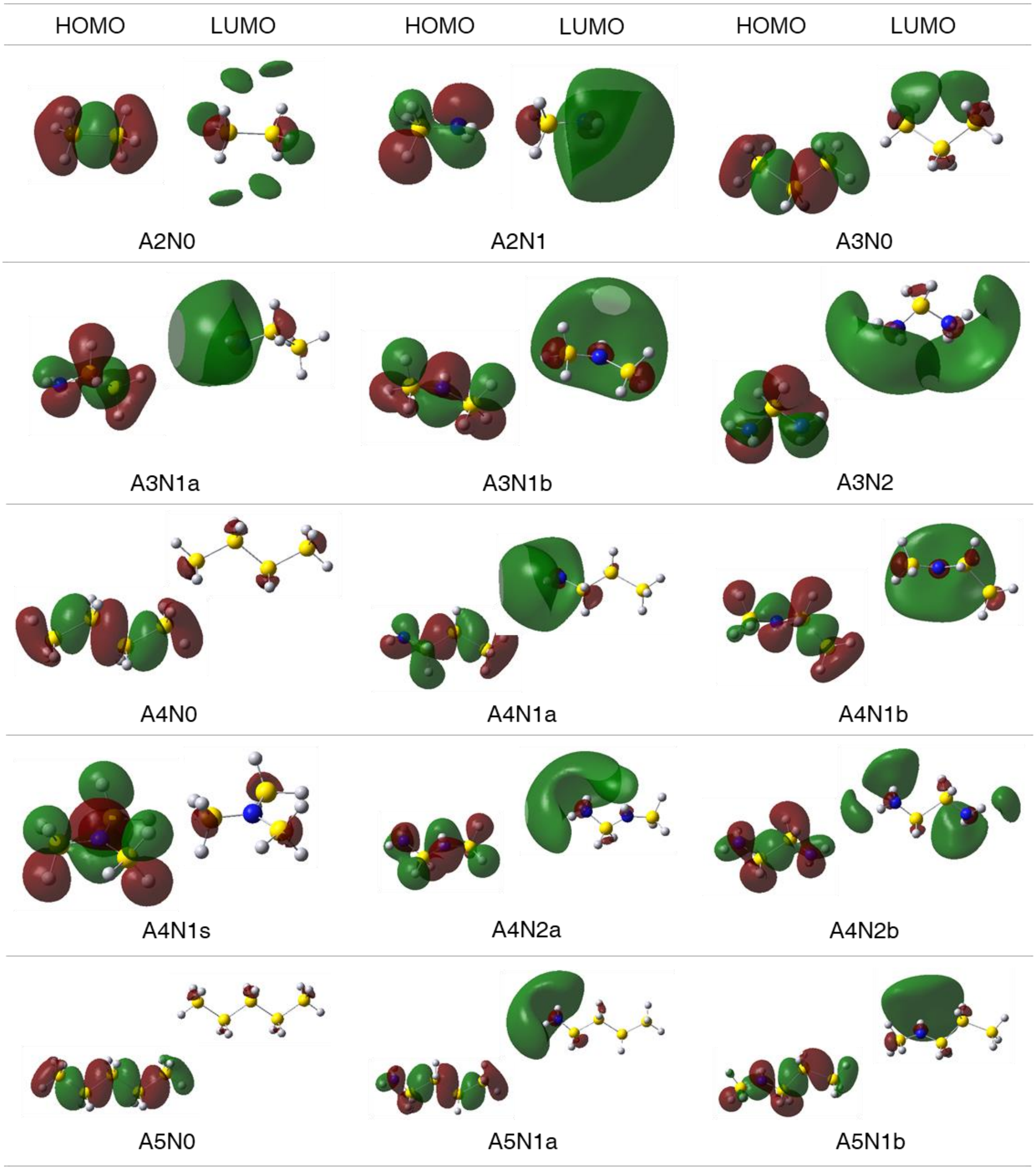

Appendix. B.3. (continued)

HOMO LUMO HOMO LUMO HOMO LUMO

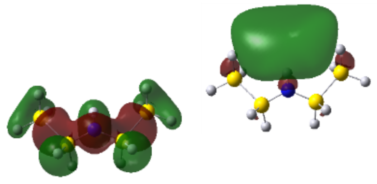
A5N1

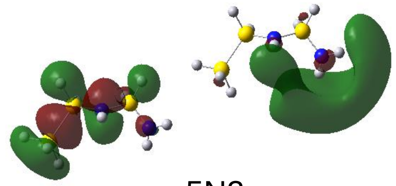
A5N2

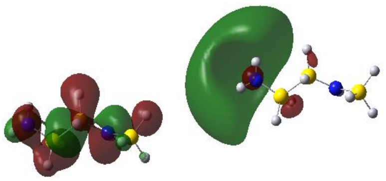
A5N2

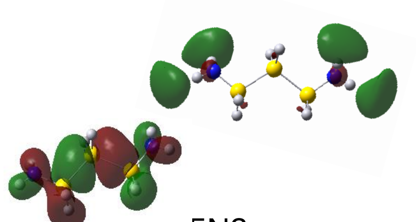
A5N2

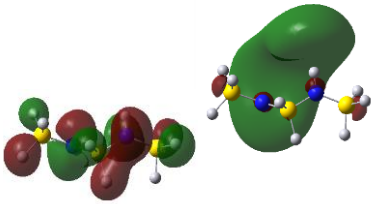
A5N2

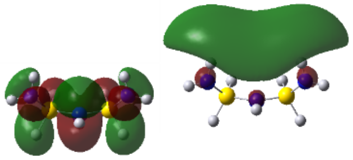
A5N

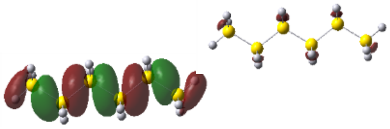
A6N

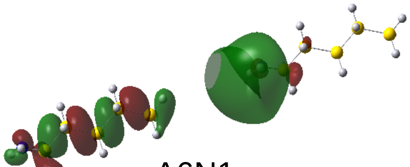
A6N1

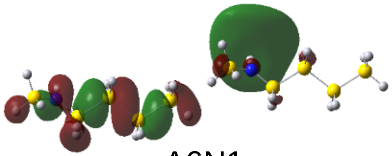
A6N1

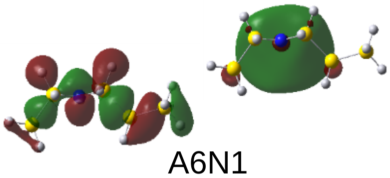
A6N1

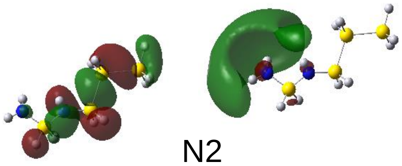
N2

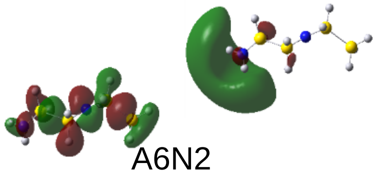
A6N2

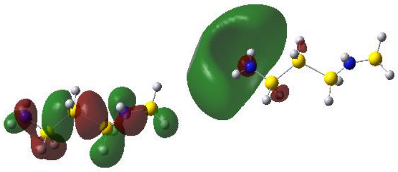
A6N2

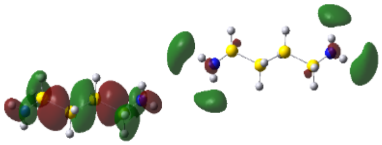
A6N2

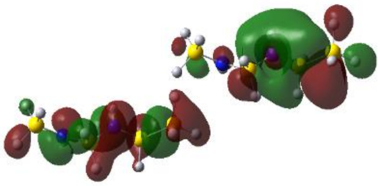
A6N2

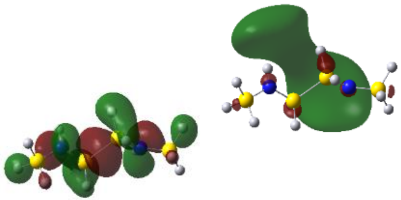
A6N

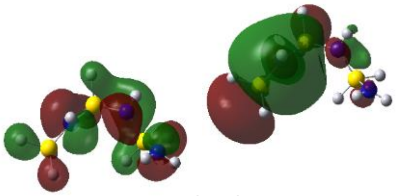
A6N3

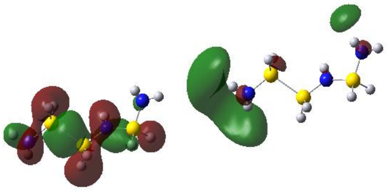
A6N3

Appendix. B.3. (continued)

HOMO LUMO	HOMO LUMO	HOMO LUMO
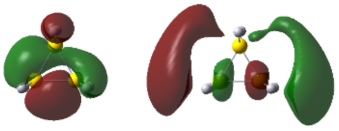 TN0	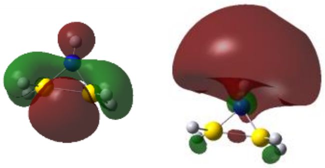 TN1	
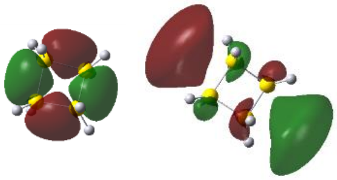 SN0	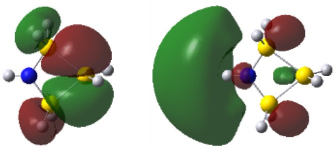 SN1	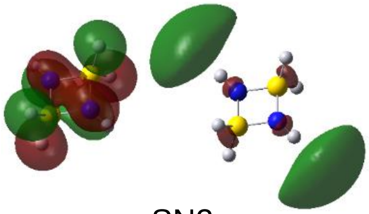 SN2
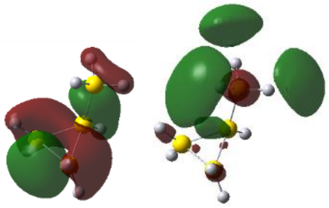 STN0	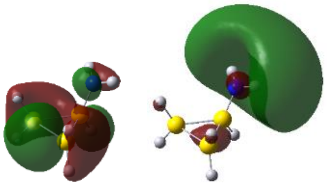 STN1a	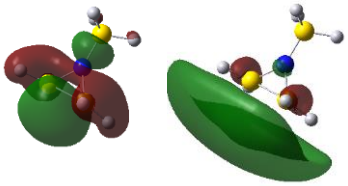 STN1b
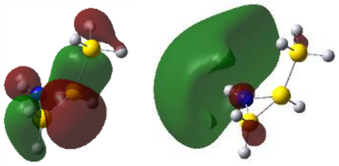 STN1c_ch	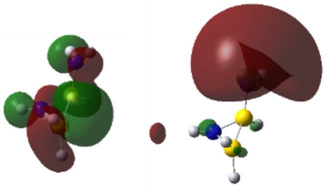 STN2_ch	
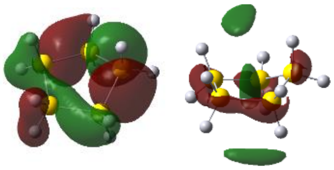 PN0	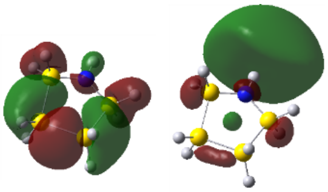 PN1	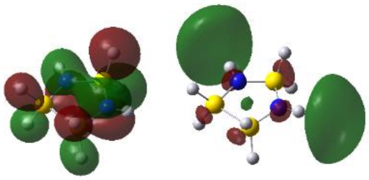 PN2

Appendix. B.3. (continued)

<table>
<tr><th>HOMO</th><th>LUMO</th><th>HOMO</th><th>LUMO</th><th>HOMO</th><th>LUMO</th></tr>
<tr><td colspan="2">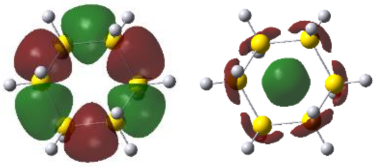
HN0</td><td colspan="2">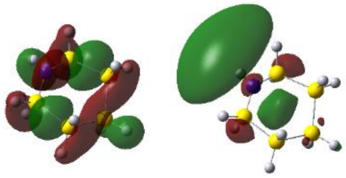
HN1</td><td colspan="2">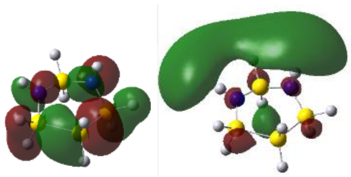
HN2a</td></tr>
<tr><td colspan="2">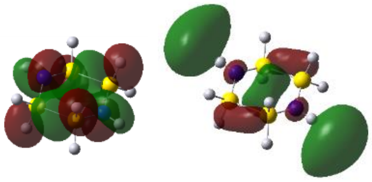
HN2b</td><td colspan="2">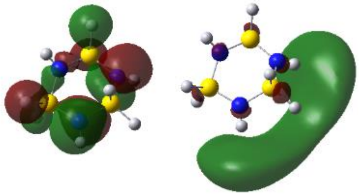
HN3</td><td colspan="2"></td></tr>
<tr><td colspan="2">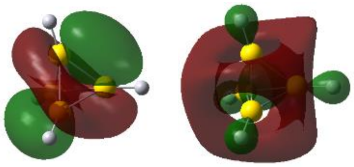
TPyN0</td><td colspan="2">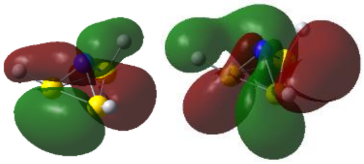
TPyN1</td><td colspan="2">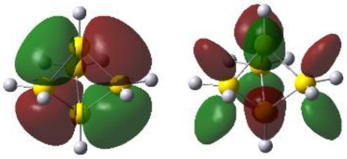
TBPyN0</td></tr>
<tr><td colspan="2">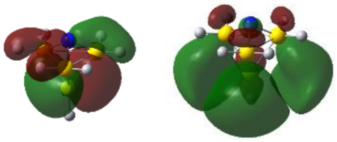
TBPyN1a</td><td colspan="2">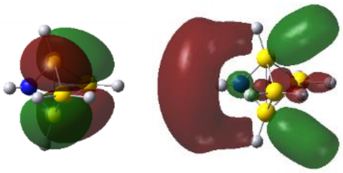
TBPyN1b</td><td colspan="2">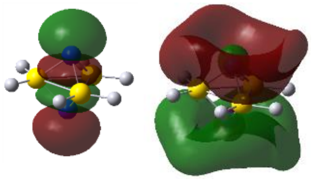
TBPyN2</td></tr>
<tr><td colspan="2">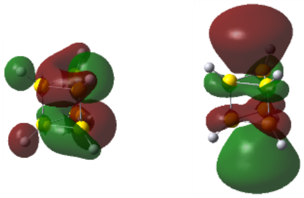
PriN0</td><td colspan="2">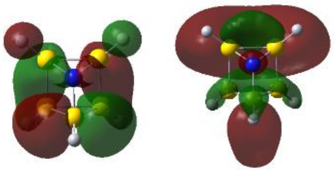
PriN1</td><td colspan="2">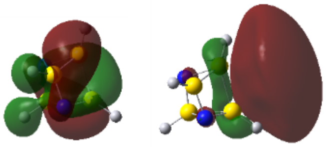
PriN2</td></tr>
</table>

Appendix. B.4.

a) Second order perturbation theory analysis of Fock matrix in NBO basis for A4N0

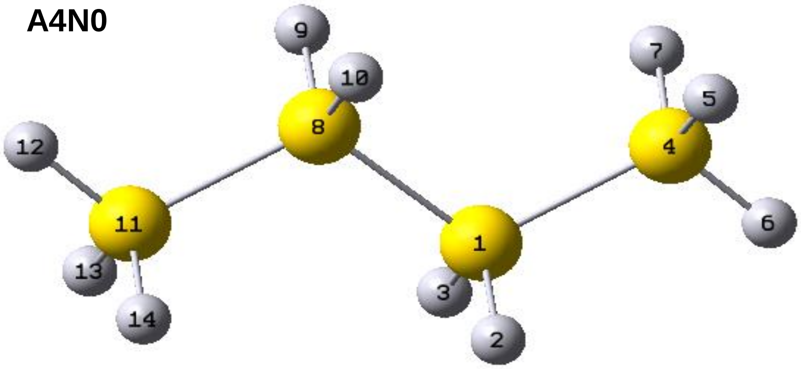

A4N0

Donor (i)				type	Acceptor (j)						type	E(2) kcal/mol	E(j)-E(i) a.u.	F(i,j) a.u.
Si	1			CR(2)	36	Si	1	-	Si	4	σ*	0.67	5.72	0.055
Si	1			CR(2)	57	H	2	-			RY*(1)	0.66	6.48	0.058
Si	1			CR(2)	58	H	3	-			RY*(1)	0.66	6.48	0.058
Si	4			CR(2)	36	Si	1	-	Si	4	σ*	0.62	5.78	0.053
Si	4			CR(2)	69	H	5	-			RY*(1)	0.64	6.53	0.058
Si	4			CR(2)	70	H	6	-			RY*(1)	0.62	6.53	0.057
Si	4			CR(2)	71	H	7	-			RY*(1)	0.64	6.53	0.058
Si	8			CR(2)	43	Si	8	-	Si	11	σ*	0.67	5.72	0.055
Si	8			CR(2)	82	H	9	-			RY*(1)	0.66	6.48	0.058
Si	8			CR(2)	83	H	10	-			RY*(1)	0.66	6.48	0.058
Si	11			CR(2)	43	Si	8	-	Si	11	σ*	0.62	5.78	0.053
Si	11			CR(2)	94	H	12	-			RY*(1)	0.62	6.53	0.057
Si	11			CR(2)	95	H	13	-			RY*(1)	0.64	6.53	0.058
Si	11			CR(2)	96	H	14	-			RY*(1)	0.64	6.53	0.058
Si1	-	H	2	σ	35	Si	1	-	H	3	σ*	1.36	0.67	0.027
Si1	-	H	2	σ	36	Si	1	-	Si	4	σ*	1.37	0.56	0.025
Si1	-	H	2	σ	37	Si	1	-	Si	8	σ*	1.27	0.56	0.024
Si1	-	H	2	σ	40	Si	4	-	H	7	σ*	1.05	0.66	0.024
Si1	-	H	2	σ	41	Si	8	-	H	9	σ*	1.20	0.67	0.025
Si1	-	H	3	σ	34	Si	1	-	H	2	σ*	1.36	0.67	0.027
Si1	-	H	3	σ	36	Si	1	-	Si	4	σ*	1.37	0.56	0.025
Si1	-	H	3	σ	37	Si	1	-	Si	8	σ*	1.27	0.56	0.024
Si1	-	H	3	σ	38	Si	4	-	H	5	σ*	1.05	0.66	0.024
Si1	-	H	3	σ	42	Si	8	-	H	10	σ*	1.20	0.67	0.025
Si1	-	Si	4	σ	34	Si	1	-	H	2	σ*	1.02	0.68	0.024
Si1	-	Si	4	σ	35	Si	1	-	H	3	σ*	1.02	0.68	0.024
Si1	-	Si	4	σ	37	Si	1	-	Si	8	σ*	0.79	0.57	0.019
Si1	-	Si	4	σ	38	Si	4	-	H	5	σ*	1.17	0.68	0.025
Si1	-	Si	4	σ	39	Si	4	-	H	6	σ*	1.28	0.68	0.026
Si1	-	Si	4	σ	40	Si	4	-	H	7	σ*	1.17	0.68	0.025
Si1	-	Si	4	σ	43	Si	8	-	Si	11	σ*	1.26	0.57	0.024
Si1	-	Si	4	σ	72	Si	8				RY	0.54	0.89	0.02

Si1	-	Si	8	σ	34	Si	1	-	H	2	σ*	0.91	0.68	0.022
Si1	-	Si	8	σ	35	Si	1	-	H	3	σ*	0.91	0.68	0.022
Si1	-	Si	8	σ	36	Si	1	-	Si	4	σ*	1.12	0.58	0.023
Si1	-	Si	8	σ	39	Si	4	-	H	6	σ*	0.98	0.68	0.023
Si1	-	Si	8	σ	41	Si	8	-	H	9	σ*	0.91	0.68	0.022
Si1	-	Si	8	σ	42	Si	8	-	H	10	σ*	0.91	0.68	0.022
Si1	-	Si	8	σ	43	Si	8	-	Si	11	σ*	1.12	0.58	0.023
Si1	-	Si	8	σ	44	Si	11	-	H	12	σ*	0.98	0.68	0.023
Si4	-	H	5	σ	35	Si	1	-	H	3	σ*	1.23	0.67	0.026
Si4	-	H	5	σ	36	Si	1	-	Si	4	σ*	1.55	0.56	0.026
Si4	-	H	5	σ	39	Si	4	-	H	6	σ*	1.55	0.66	0.029
Si4	-	H	5	σ	40	Si	4	-	H	7	σ*	1.58	0.66	0.029
Si4	-	H	6	σ	36	Si	1	-	Si	4	σ*	1.34	0.56	0.024
Si4	-	H	6	σ	37	Si	1	-	Si	8	σ*	1.26	0.56	0.024
Si4	-	H	6	σ	38	Si	4	-	H	5	σ*	1.58	0.67	0.029
Si4	-	H	6	σ	40	Si	4	-	H	7	σ*	1.58	0.67	0.029
Si4	-	H	7	σ	34	Si	1	-	H	2	σ*	1.23	0.67	0.026
Si4	-	H	7	σ	36	Si	1	-	Si	4	σ*	1.55	0.56	0.026
Si4	-	H	7	σ	38	Si	4	-	H	5	σ*	1.58	0.66	0.029
Si4	-	H	7	σ	39	Si	4	-	H	6	σ*	1.55	0.66	0.029
Si8	-	H	9	σ	34	Si	1	-	H	2	σ*	1.20	0.67	0.025
Si8	-	H	9	σ	37	Si	1	-	Si	8	σ*	1.27	0.56	0.024
Si8	-	H	9	σ	42	Si	8	-	H	10	σ*	1.36	0.67	0.027
Si8	-	H	9	σ	43	Si	1	-	Si	11	σ*	1.37	0.56	0.025
Si8	-	H	9	σ	46	Si	11	-	H	14	σ*	1.05	0.66	0.024
Si8	-	H	10	σ	35	Si	1	-	H	3	σ*	1.20	0.67	0.025
Si8	-	H	10	σ	37	Si	1	-	Si	8	σ*	1.27	0.56	0.024
Si8	-	H	10	σ	41	Si	8	-	H	9	σ*	1.36	0.67	0.027
Si8	-	H	10	σ	43	Si	1	-	Si	11	σ*	1.37	0.56	0.025
Si8	-	H	10	σ	45	Si	11	-	H	13	σ*	1.05	0.66	0.024
Si8	-	Si	11	σ	36	Si	1	-	Si	4	σ*	1.26	0.57	0.024
Si8	-	Si	11	σ	37	Si	1	-	Si	8	σ*	0.79	0.57	0.019
Si8	-	Si	11	σ	41	Si	8	-	H	9	σ*	1.02	0.68	0.024
Si8	-	Si	11	σ	42	Si	8	-	H	10	σ*	1.02	0.68	0.024
Si8	-	Si	11	σ	44	Si	11	-	H	12	σ*	1.28	0.68	0.026
Si8	-	Si	11	σ	45	Si	11	-	H	13	σ*	1.17	0.68	0.025
Si8	-	Si	11	σ	46	Si	11	-	H	14	σ*	1.17	0.68	0.025
Si8	-	Si	11	σ	47	Si	1				RY	0.54	0.89	0.02
Si11	-	H	12	σ	37	Si	1	-	Si	8	σ*	1.26	0.56	0.024
Si11	-	H	12	σ	43	Si	8	-	Si	11	σ*	1.34	0.56	0.024
Si11	-	H	12	σ	45	Si	11	-	H	13	σ*	1.58	0.67	0.029
Si11	-	H	12	σ	46	Si	11	-	H	14	σ*	1.58	0.67	0.029
Si11	-	H	13	σ	42	Si	8	-	H	10	σ*	1.23	0.67	0.026
Si11	-	H	13	σ	43	Si	8	-	Si	11	σ*	1.55	0.56	0.026
Si11	-	H	13	σ	44	Si	11	-	H	12	σ*	1.55	0.66	0.029
Si11	-	H	13	σ	46	Si	11	-	H	14	σ*	1.58	0.66	0.029
Si11	-	H	14	σ	41	Si	8	-	H	9	σ*	1.23	0.67	0.026
Si11	-	H	14	σ	43	Si	8	-	Si	11	σ*	1.55	0.56	0.026
Si11	-	H	14	σ	44	Si	11	-	H	12	σ*	1.55	0.66	0.029
Si11	-	H	14	σ	45	Si	11	-	H	13	σ*	1.58	0.66	0.029

b) Second order perturbation theory analysis of Fock matrix in NBO basis for A4N1a

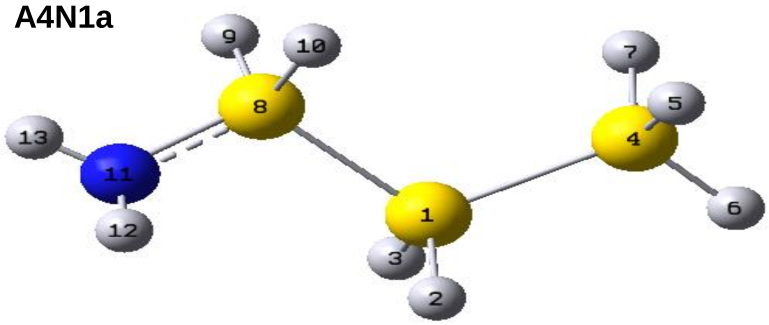

A4N1a

Donor (i)					type	Acceptor (j)						type	E(2)	E(j)-E(i)	F(i,j)
													kcal/mol	a.u.	a.u.
Si	1				CR(2)	32	Si	1	-	Si	4	σ*	0.54	5.7	0.05
Si	1				CR(2)	33	Si	1	-	Si	8	σ*	0.62	5.71	0.053
Si	1				CR(2)	52	H	2				RY*(1)	0.65	6.46	0.058
Si	1				CR(2)	53	H	3				RY*(1)	0.67	6.46	0.059
Si	4				CR(2)	32	Si	1	-	Si	4	σ*	0.63	5.78	0.054
Si	4				CR(2)	42	Si	1				RY*(1)	0.64	5.95	0.055
Si	4				CR(2)	64	H	5				RY*(1)	0.64	6.53	0.058
Si	4				CR(2)	65	H	6				RY*(1)	0.63	6.54	0.057
Si	4				CR(2)	66	H	7				RY*(1)	0.63	6.53	0.057
Si	8				CR(2)	39	Si	8	-	N	11	σ*	1.37	5.99	0.081
Si	8				CR(2)	40	N	11	-	H	12	σ*	0.99	6.24	0.07
Si	8				CR(2)	41	N	11	-	H	13	σ*	0.96	6.24	0.069
Si	8				CR(2)	77	H	9				RY*(1)	0.58	6.66	0.055
Si	8				CR(2)	78	H	10				RY*(1)	0.53	6.67	0.053
N	11				LP(1)	33	Si	1	-	Si	8	σ*	1.73	0.43	0.024
N	11				LP(1)	37	Si	8	-	H	9	σ*	1.88	0.54	0.028
N	11				LP(1)	38	Si	8	-	H	10	σ*	10.03	0.53	0.065
N	11				LP(1)	67	Si	8				RY*(1)	3.56	0.87	0.05
N	11				LP(1)	74	Si	8				RY*(8)	0.66	0.74	0.02
Si	1	-	H	2	σ	31	Si	1	-	H	3	σ*	1.33	0.67	0.027
Si	1	-	H	2	σ	32	Si	1	-	Si	4	σ*	1.27	0.56	0.024
Si	1	-	H	2	σ	33	Si	1	-	Si	8	σ*	1.41	0.57	0.025
Si	1	-	H	2	σ	36	Si	4	-	H	7	σ*	1.11	0.66	0.024
Si	1	-	H	2	σ	37	Si	8	-	H	9	σ*	0.89	0.69	0.022
Si	1	-	H	3	σ	30	Si	1	-	H	2	σ*	1.29	0.66	0.026
Si	1	-	H	3	σ	32	Si	1	-	Si	4	σ*	1.41	0.56	0.025
Si	1	-	H	3	σ	33	Si	1	-	Si	8	σ*	1.28	0.57	0.024
Si	1	-	H	3	σ	34	Si	4	-	H	5	σ*	1.09	0.66	0.024
Si	1	-	H	3	σ	38	Si	8	-	H	10	σ*	0.86	0.68	0.022
Si	1	-	Si	4	σ	30	Si	1	-	H	2	σ*	0.94	0.68	0.023
Si	1	-	Si	4	σ	31	Si	1	-	H	3	σ*	1.02	0.68	0.023
Si	1	-	Si	4	σ	33	Si	1	-	Si	8	σ*	1.28	0.59	0.024
Si	1	-	Si	4	σ	34	Si	4	-	H	5	σ*	1.16	0.67	0.025
Si	1	-	Si	4	σ	35	Si	4	-	H	6	σ*	1.28	0.67	0.026
Si	1	-	Si	4	σ	36	Si	4	-	H	7	σ*	1.15	0.67	0.025

Si	1	-	Si	4	σ	39	Si	8	-	N	11	σ*	1.17	0.66	0.025
Si	1	-	Si	8	σ	30	Si	1	-	H	2	σ*	0.97	0.67	0.023
Si	1	-	Si	8	σ	31	Si	1	-	H	3	σ*	1.01	0.68	0.023
Si	1	-	Si	8	σ	32	Si	1	-	Si	4	σ*	1.05	0.57	0.022
Si	1	-	Si	8	σ	35	Si	4	-	H	6	σ*	1.1	0.67	0.024
Si	1	-	Si	8	σ	37	Si	8	-	H	9	σ*	1.14	0.69	0.025
Si	1	-	Si	8	σ	38	Si	8	-	H	10	σ*	1.84	0.69	0.032
Si	1	-	Si	8	σ	39	Si	8	-	N	11	σ*	1.12	0.66	0.024
Si	1	-	Si	8	σ	41	N	11	-	H	13	σ*	1.65	0.91	0.035
Si	1	-	Si	8	σ	54	Si	4				RY*(1)	0.53	0.86	0.019
Si	1	-	Si	8	σ	79	N	11				RY*(1)	0.52	1.37	0.024
Si	4	-	H	5	σ	31	Si	1	-	Si	3	σ*	1.17	0.67	0.025
Si	4	-	H	5	σ	32	Si	1	-	Si	4	σ*	1.55	0.56	0.026
Si	4	-	H	5	σ	35	Si	4	-	H	6	σ*	1.54	0.66	0.029
Si	4	-	H	5	σ	36	Si	4	-	H	7	σ*	1.56	0.66	0.029
Si	4	-	H	6	σ	32	Si	1	-	Si	4	σ*	1.29	0.56	0.024
Si	4	-	H	6	σ	33	Si	1	-	Si	8	σ*	1.13	0.58	0.023
Si	4	-	H	6	σ	34	Si	4	-	H	5	σ*	1.57	0.66	0.029
Si	4	-	H	6	σ	36	Si	4	-	H	7	σ*	1.56	0.66	0.029
Si	4	-	H	7	σ	30	Si	1	-	H	2	σ*	1.16	0.66	0.025
Si	4	-	H	7	σ	32	Si	1	-	Si	4	σ*	1.58	0.56	0.027
Si	4	-	H	7	σ	34	Si	4	-	H	5	σ*	1.57	0.66	0.029
Si	4	-	H	7	σ	35	Si	4	-	H	6	σ*	1.52	0.66	0.028
Si	8	-	H	9	σ	30	Si	1	-	H	2	σ*	1.19	0.66	0.025
Si	8	-	H	9	σ	33	Si	1	-	Si	8	σ*	1.45	0.57	0.026
Si	8	-	H	9	σ	38	Si	8	-	H	10	σ*	2.31	0.68	0.035
Si	8	-	H	9	σ	39	Si	8	-	N	11	σ*	1.37	0.64	0.027
Si	8	-	H	9	σ	40	N	11	-	H	12	σ*	1.81	0.9	0.036
Si	8	-	H	10	σ	31	Si	1	-	H	3	σ*	1.31	0.66	0.026
Si	8	-	H	10	σ	33	Si	1	-	Si	8	σ*	2.12	0.57	0.031
Si	8	-	H	10	σ	37	Si	8	-	H	9	σ*	2.12	0.68	0.034
Si	8	-	H	10	σ	39	Si	8	-	N	11	σ*	2.19	0.64	0.033
Si	8	-	N	11	σ	32	Si	1	-	Si	4	σ*	0.57	0.78	0.019
Si	8	-	N	11	σ	33	Si	1	-	Si	8	σ*	1.2	0.79	0.028
Si	8	-	N	11	σ	37	Si	8	-	H	9	σ*	1.92	0.91	0.037
Si	8	-	N	11	σ	38	Si	8	-	H	10	σ*	1.67	0.9	0.035
Si	8	-	N	11	σ	40	N	11	-	H	12	σ*	0.69	1.13	0.025
Si	8	-	N	11	σ	41	N	11	-	H	13	σ*	0.73	1.12	0.026
N	11	-	H	12	σ	37	Si	8	-	H	9	σ*	0.68	0.9	0.022
N	11	-	H	13	σ	33	Si	1	-	Si	8	σ*	0.94	0.78	0.024
N	11	-	H	13	σ	37	Si	8	-	H	9	σ*	0.62	0.89	0.021
	Si11	-	H	13	σ	44	Si	11	-	H	12	σ*	1.55	0.66	0.029
	Si11	-	H	13	σ	46	Si	11	-	H	14	σ*	1.58	0.66	0.029
	Si11	-	H	14	σ	41	Si	8	-	H	9	σ*	1.23	0.67	0.026
	Si11	-	H	14	σ	43	Si	8	-	Si	11	σ*	1.55	0.56	0.026
	Si11	-	H	14	σ	44	Si	11	-	H	12	σ*	1.55	0.66	0.029
	Si11	-	H	14	σ	45	Si	11	-	H	13	σ*	1.58	0.66	0.029

c) Second order perturbation theory analysis of Fock matrix in NBO basis for

A4N1s

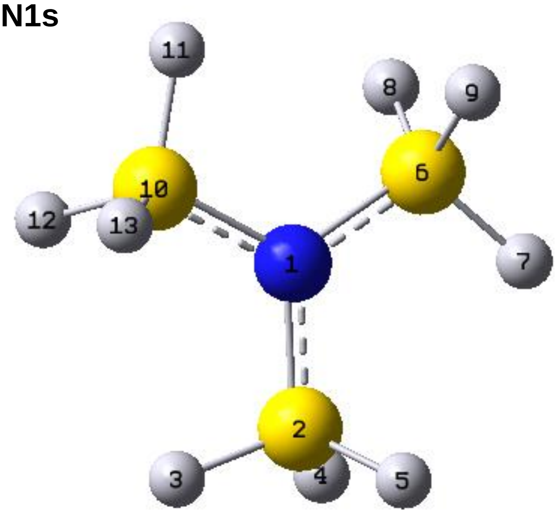

A4N1s

Donor (i)					type	Acceptor (j)						type	E(2)	E(j)-E(i)	F(i,j)
													kcal/mol	a.u.	a.u.
Si	2				CR(2)	30	N	1	-	Si	2	σ*	1.11	5.99	0.073
Si	2				CR(2)	31	N	1	-	Si	6	σ*	2.35	5.99	0.106
Si	2				CR(2)	32	N	1	-	Si	10	σ*	2.29	5.99	0.105
Si	2				CR(2)	34	Si	2	-	H	4	σ*	0.52	6.05	0.05
Si	2				CR(2)	35	Si	2	-	H	5	σ*	0.52	6.05	0.05
Si	2				CR(2)	62	H	3				RY*(1)	0.51	6.69	0.052
Si	2				CR(2)	63	H	4				RY*(1)	0.57	6.68	0.055
Si	2				CR(2)	64	H	5				RY*(1)	0.57	6.68	0.055
Si	6				CR(2)	30	N	1	-	Si	2	σ*	2.29	5.99	0.105
Si	6				CR(2)	31	N	1	-	Si	6	σ*	1.1	5.99	0.073
Si	6				CR(2)	32	N	1	-	Si	10	σ*	2.35	5.99	0.106
Si	6				CR(2)	37	Si	6	-	H	8	σ*	0.52	6.05	0.05
Si	6				CR(2)	38	Si	6	-	H	9	σ*	0.52	6.05	0.05
Si	6				CR(2)	75	H	7				RY*(1)	0.51	6.69	0.052
Si	6				CR(2)	76	H	8				RY*(1)	0.57	6.68	0.055
Si	6				CR(2)	77	H	9				RY*(1)	0.57	6.68	0.055
Si	10				CR(2)	30	N	1	-	Si	2	σ*	2.35	5.99	0.106
Si	10				CR(2)	31	N	1	-	Si	6	σ*	2.29	5.99	0.105
Si	10				CR(2)	32	N	1	-	Si	10	σ*	1.1	5.99	0.073
Si	10				CR(2)	40	Si	10	-	H	12	σ*	0.52	6.05	0.05
Si	10				CR(2)	41	Si	10	-	H	13	σ*	0.52	6.05	0.05
Si	10				CR(2)	88	H	11				RY*(1)	0.51	6.69	0.052
Si	10				CR(2)	89	H	12				RY*(1)	0.57	6.68	0.055
Si	10				CR(2)	90	H	13				RY*(1)	0.57	6.68	0.055
N	1				LP(1)	34	Si	2	-	H	4	σ*	5.8	0.51	0.049
N	1				LP(1)	35	Si	2	-	H	5	σ*	5.8	0.51	0.049
N	1				LP(1)	37	Si	6	-	H	8	σ*	5.8	0.51	0.049
N	1				LP(1)	38	Si	6	-	H	9	σ*	5.8	0.51	0.049
N	1				LP(1)	40	Si	10	-	H	12	σ*	5.81	0.51	0.049
N	1				LP(1)	41	Si	10	-	H	13	σ*	5.81	0.51	0.049
N	1				LP(1)	52	Si	2				RY*(1)	2.51	0.94	0.043
N	1				LP(1)	55	Si	2				RY*(4)	1.34	0.56	0.024
N	1				LP(1)	65	Si	6				RY*(1)	2.53	0.94	0.044
N	1				LP(1)	68	Si	6				RY*(4)	1.33	0.56	0.024
N	1				LP(1)	78	Si	10				RY*(1)	2.5	0.94	0.043
N	1				LP(1)	81	Si	10				RY*(4)	1.33	0.56	0.024
N	1	-	Si	2	σ	30	N	1	-	Si	2	σ*	0.51	0.84	0.018
N	1	-	Si	2	σ	31	N	1	-	Si	6	σ*	1.91	0.84	0.036
N	1	-	Si	2	σ	32	N	1	-	Si	10	σ*	1.87	0.84	0.035

N	1	-	Si	2	σ	33	Si	2	-	H	3	σ*	2.38	0.89	0.041
N	1	-	Si	2	σ	34	Si	2	-	H	4	σ*	2.08	0.9	0.039
N	1	-	Si	2	σ	35	Si	2	-	H	5	σ*	2.08	0.9	0.039
N	1	-	Si	2	σ	36	Si	6	-	H	7	σ*	1.3	0.89	0.03
N	1	-	Si	2	σ	39	Si	10	-	H	11	σ*	0.74	0.89	0.023
N	1	-	Si	6	σ	30	N	1	-	Si	2	σ*	1.88	0.84	0.035
N	1	-	Si	6	σ	31	N	1	-	Si	6	σ*	0.51	0.84	0.018
N	1	-	Si	6	σ	32	N	1	-	Si	10	σ*	1.91	0.84	0.036
N	1	-	Si	6	σ	33	Si	2	-	H	3	σ*	0.74	0.89	0.023
N	1	-	Si	6	σ	36	Si	6	-	H	7	σ*	2.38	0.89	0.041
N	1	-	Si	6	σ	37	Si	6	-	H	8	σ*	2.09	0.9	0.039
N	1	-	Si	6	σ	38	Si	6	-	H	9	σ*	2.09	0.9	0.039
N	1	-	Si	6	σ	39	Si	10	-	H	11	σ*	1.3	0.89	0.03
N	1	-	Si	10	σ	30	N	1	-	Si	2	σ*	1.9	0.84	0.036
N	1	-	Si	10	σ	31	N	1	-	Si	6	σ*	1.87	0.84	0.035
N	1	-	Si	10	σ	32	N	1	-	Si	10	σ*	0.51	0.84	0.019
N	1	-	Si	10	σ	33	Si	2	-	H	3	σ*	1.3	0.89	0.03
N	1	-	Si	10	σ	36	Si	6	-	H	7	σ*	0.74	0.89	0.023
N	1	-	Si	10	σ	39	Si	10	-	H	11	σ*	2.38	0.89	0.041
N	1	-	Si	10	σ	40	Si	10	-	H	12	σ*	2.08	0.9	0.039
N	1	-	Si	10	σ	41	Si	10	-	H	13	σ*	2.08	0.9	0.039
Si	2	-	H	3	σ	30	N	1	-	Si	2	σ*	1.66	0.62	0.029
Si	2	-	H	3	σ	31	N	1	-	Si	6	σ*	1.71	0.62	0.029
Si	2	-	H	3	σ	32	N	1	-	Si	10	σ*	0.83	0.62	0.02
Si	2	-	H	3	σ	34	Si	2	-	H	4	σ*	2.2	0.68	0.035
Si	2	-	H	3	σ	35	Si	2	-	H	5	σ*	2.2	0.68	0.035
Si	2	-	H	3	σ	39	Si	10	-	H	11	σ*	0.87	0.68	0.022
Si	2	-	H	4	σ	30	N	1	-	Si	2	σ*	1.63	0.62	0.028
Si	2	-	H	4	σ	31	N	1	-	Si	6	σ*	0.72	0.62	0.019
Si	2	-	H	4	σ	32	N	1	-	Si	10	σ*	1.05	0.62	0.023
Si	2	-	H	4	σ	33	Si	2	-	H	3	σ*	2.04	0.68	0.033
Si	2	-	H	4	σ	35	Si	2	-	H	5	σ*	2.65	0.68	0.038
Si	2	-	H	5	σ	30	N	1	-	Si	2	σ*	1.63	0.62	0.028
Si	2	-	H	5	σ	31	N	1	-	Si	6	σ*	0.72	0.62	0.019
Si	2	-	H	5	σ	32	N	1	-	Si	10	σ*	1.05	0.62	0.023
Si	2	-	H	5	σ	33	Si	2	-	H	3	σ*	2.04	0.68	0.033
Si	2	-	H	5	σ	34	Si	2	-	H	4	σ*	2.65	0.68	0.038
Si	6	-	H	7	σ	30	N	1	-	Si	2	σ*	0.83	0.62	0.02
Si	6	-	H	7	σ	31	N	1	-	Si	6	σ*	1.66	0.62	0.029
Si	6	-	H	7	σ	32	N	1	-	Si	10	σ*	1.71	0.62	0.029
Si	6	-	H	7	σ	33	Si	2	-	H	3	σ*	0.87	0.68	0.022
Si	6	-	H	7	σ	37	Si	6	-	H	8	σ*	2.2	0.68	0.035
Si	6	-	H	7	σ	38	Si	6	-	H	9	σ*	2.2	0.68	0.035
Si	6	-	H	8	σ	30	N	1	-	Si	2	σ*	1.05	0.62	0.023
Si	6	-	H	8	σ	31	N	1	-	Si	6	σ*	1.63	0.62	0.028
Si	6	-	H	8	σ	32	N	1	-	Si	10	σ*	0.72	0.62	0.019
Si	6	-	H	8	σ	36	Si	6	-	H	7	σ*	2.04	0.68	0.033
Si	6	-	H	8	σ	38	Si	6	-	H	9	σ*	2.65	0.68	0.038
Si	6	-	H	9	σ	30	N	1	-	Si	2	σ*	1.05	0.62	0.023
Si	6	-	H	9	σ	31	N	1	-	Si	6	σ*	1.63	0.62	0.028
Si	6	-	H	9	σ	32	N	1	-	Si	10	σ*	0.72	0.62	0.019
Si	6	-	H	9	σ	36	Si	6	-	H	7	σ*	2.04	0.68	0.033
Si	6	-	H	9	σ	37	Si	6	-	H	8	σ*	2.65	0.68	0.038
Si	10	-	H	11	σ	30	N	1	-	Si	2	σ*	1.71	0.62	0.029
Si	10	-	H	11	σ	31	N	1	-	Si	6	σ*	0.83	0.62	0.02
Si	10	-	H	11	σ	32	N	1	-	Si	10	σ*	1.66	0.62	0.029
Si	10	-	H	11	σ	36	Si	6	-	H	7	σ*	0.87	0.68	0.022
Si	10	-	H	11	σ	40	Si	10	-	H	12	σ*	2.19	0.68	0.035
Si	10	-	H	11	σ	41	Si	10	-	H	13	σ*	2.19	0.68	0.035
Si	10	-	H	12	σ	30	N	1	-	Si	2	σ*	0.72	0.62	0.019
Si	10	-	H	12	σ	31	N	1	-	Si	6	σ*	1.05	0.62	0.023
Si	10	-	H	12	σ	32	N	1	-	Si	10	σ*	1.63	0.62	0.028
Si	10	-	H	12	σ	39	Si	10	-	H	11	σ*	2.04	0.68	0.033
Si	10	-	H	12	σ	41	Si	10	-	H	13	σ*	2.65	0.68	0.038
Si	10	-	H	13	σ	30	N	1	-	Si	2	σ*	0.72	0.62	0.019
Si	10	-	H	13	σ	31	N	1	-	Si	6	σ*	1.05	0.62	0.023
Si	10	-	H	13	σ	32	N	1	-	Si	10	σ*	1.63	0.62	0.028
Si	10	-	H	13	σ	39	Si	10	-	H	11	σ*	2.04	0.68	0.033
Si	10	-	H	13	σ	40	Si	10	-	H	12	σ*	2.65	0.68	0.038

d) Second order perturbation theory analysis of Fock matrix in NBO basis for A4N2a

A4N2a

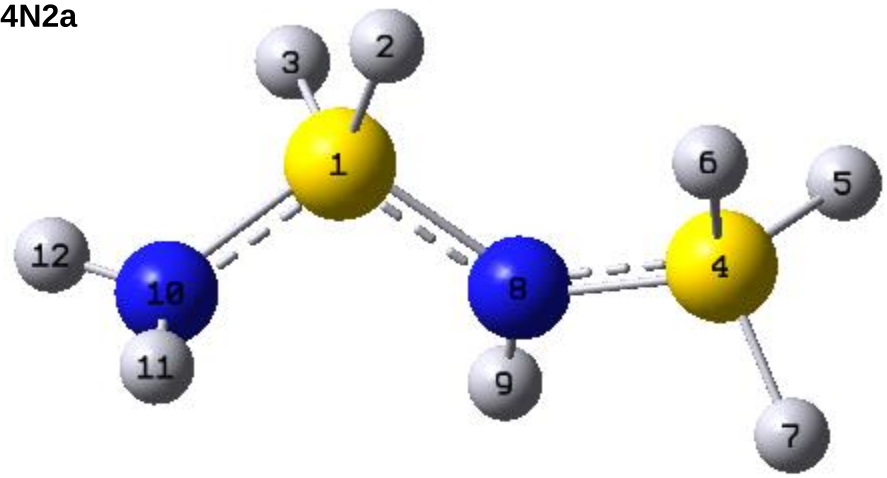

A4N2a

Donor (i)					type	Acceptor (j)						type	E(2)	E(j)-E(i)	F(i,j)
													kcal/mol	a.u.	a.u.
Si	1				CR(2)	28	Si	1	-	N	8	σ*	0.85	6.15	0.065
Si	1				CR(2)	29	Si	1	-	N	10	σ*	1.09	6.16	0.073
Si	1				CR(2)	33	Si	4	-	N	8	σ*	2.65	6.12	0.114
Si	1				CR(2)	34	N	8	-	H	9	σ*	0.74	6.37	0.061
Si	1				CR(2)	35	N	10	-	H	11	σ*	1.17	6.38	0.077
Si	1				CR(2)	36	N	10	-	H	12	σ*	1.03	6.38	0.072
Si	4				CR(2)	28	Si	1	-	N	8	σ*	2.41	6.08	0.108
Si	4				CR(2)	33	Si	4	-	N	8	σ*	1.23	6.05	0.077
Si	4				CR(2)	34	N	8	-	H	9	σ*	0.78	6.3	0.063
Si	4				CR(2)	59	H	5				RY*(1)	0.54	6.72	0.054
Si	4				CR(2)	60	H	6				RY*(1)	0.57	6.71	0.055
Si	4				CR(2)	61	H	7				RY*(1)	0.54	6.71	0.054
N	8				LP(1)	27	Si	1	-	H	3	σ*	7.05	0.53	0.055
N	8				LP(1)	29	Si	1	-	N	10	σ*	5.91	0.51	0.049
N	8				LP(1)	30	Si	4	-	H	5	σ*	8.34	0.51	0.058
N	8				LP(1)	31	Si	4	-	H	6	σ*	1.2	0.51	0.022
N	8				LP(1)	32	Si	4	-	H	7	σ*	3.52	0.5	0.038
N	8				LP(1)	38	Si	1				RY*(2)	2.56	1.01	0.045
N	8				LP(1)	49	Si	4				RY*(1)	2.86	0.9	0.045
N	8				LP(1)	52	Si	4				RY*(4)	1.19	0.67	0.025
N	10				LP(1)	26	Si	1	-	H	2	σ*	8.48	0.54	0.061
N	10				LP(1)	27	Si	1	-	H	3	σ*	0.65	0.54	0.017
N	10				LP(1)	28	Si	1	-	N	8	σ*	6.84	0.52	0.053
N	10				LP(1)	37	Si	1				RY*(1)	2.27	0.94	0.041
N	10				LP(1)	38	Si	1				RY*(2)	0.86	1.03	0.027
N	10				LP(1)	44	Si	1				RY*(8)	0.58	0.95	0.021
Si	1	-	H	2	σ	27	Si	1	-	H	3	σ*	2.64	0.7	0.038
Si	1	-	H	2	σ	28	Si	1	-	N	8	σ*	2.02	0.67	0.033
Si	1	-	H	2	σ	29	Si	1	-	N	10	σ*	2.22	0.68	0.035
Si	1	-	H	2	σ	33	Si	4	-	N	8	σ*	0.75	0.64	0.019

Si	1	-	H	2	σ	34	N	8	-	H	9	σ*	1.66	0.89	0.034
Si	1	-	H	3	σ	26	Si	1	-	H	2	σ*	2.74	0.69	0.039
Si	1	-	H	3	σ	28	Si	1	-	N	8	σ*	1.66	0.67	0.03
Si	1	-	H	3	σ	29	Si	1	-	N	10	σ*	1.87	0.68	0.032
Si	1	-	H	3	σ	33	Si	4	-	N	8	σ*	0.97	0.64	0.022
Si	1	-	H	3	σ	35	N	10	-	H	11	σ*	2.27	0.9	0.04
Si	1	-	N	8	σ	26	Si	1	-	H	2	σ*	3.1	0.93	0.048
Si	1	-	N	8	σ	27	Si	1	-	H	3	σ*	1.53	0.93	0.034
Si	1	-	N	8	σ	29	Si	1	-	N	10	σ*	1.38	0.91	0.032
Si	1	-	N	8	σ	31	Si	4	-	H	6	σ*	0.75	0.9	0.023
Si	1	-	N	8	σ	33	Si	4	-	N	8	σ*	1.37	0.87	0.031
Si	1	-	N	8	σ	34	N	8	-	H	9	σ*	1.12	1.12	0.032
Si	1	-	N	8	σ	36	N	10	-	H	12	σ*	0.56	1.13	0.022
Si	1	-	N	10	σ	26	Si	1	-	H	2	σ*	1.62	0.93	0.035
Si	1	-	N	10	σ	27	Si	1	-	H	3	σ*	2.97	0.93	0.047
Si	1	-	N	10	σ	28	Si	1	-	N	8	σ*	1.61	0.9	0.034
Si	1	-	N	10	σ	33	Si	4	-	N	8	σ*	0.75	0.87	0.023
Si	1	-	N	10	σ	35	N	10	-	H	11	σ*	0.76	1.14	0.026
Si	1	-	N	10	σ	36	N	10	-	H	12	σ*	0.74	1.13	0.026
Si	4	-	H	5	σ	28	Si	1	-	N	8	σ*	0.74	0.68	0.02
Si	4	-	H	5	σ	31	Si	4	-	H	6	σ*	2.24	0.68	0.035
Si	4	-	H	5	σ	32	Si	4	-	H	7	σ*	2.51	0.68	0.037
Si	4	-	H	5	σ	33	Si	4	-	N	8	σ*	1.78	0.64	0.03
Si	4	-	H	6	σ	30	Si	4	-	H	5	σ*	2.34	0.68	0.036
Si	4	-	H	6	σ	32	Si	4	-	H	7	σ*	1.98	0.68	0.033
Si	4	-	H	6	σ	33	Si	4	-	N	8	σ*	1.63	0.65	0.029
Si	4	-	H	6	σ	34	N	8	-	H	9	σ*	1.36	0.9	0.031
Si	4	-	H	7	σ	28	Si	1	-	N	8	σ*	1.5	0.68	0.028
Si	4	-	H	7	σ	30	Si	4	-	H	5	σ*	2.66	0.68	0.038
Si	4	-	H	7	σ	31	Si	4	-	H	6	σ*	1.92	0.68	0.032
Si	4	-	H	7	σ	33	Si	4	-	N	8	σ*	1.46	0.65	0.027
Si	4	-	N	8	σ	26	Si	1	-	H	2	σ*	0.78	0.93	0.024
Si	4	-	N	8	σ	28	Si	1	-	N	8	σ*	1.06	0.9	0.028
Si	4	-	N	8	σ	29	Si	1	-	N	10	σ*	0.53	0.91	0.02
Si	4	-	N	8	σ	30	Si	4	-	H	5	σ*	1.92	0.9	0.037
Si	4	-	N	8	σ	31	Si	4	-	H	6	σ*	2.1	0.9	0.039
Si	4	-	N	8	σ	32	Si	4	-	H	7	σ*	2.02	0.9	0.038
Si	4	-	N	8	σ	34	N	8	-	H	9	σ*	1.12	1.12	0.032
N	8	-	H	9	σ	28	Si	1	-	N	8	σ*	0.51	0.88	0.019
N	8	-	H	9	σ	31	Si	4	-	H	6	σ*	0.68	0.88	0.022
N	8	-	H	9	σ	32	Si	4	-	H	7	σ*	0.52	0.88	0.019
N	10	-	H	12	σ	27	Si	1	-	H	3	σ*	0.74	0.91	0.023
N	10	-	H	12	σ	28	Si	1	-	N	8	σ*	0.73	0.89	0.023

e) Second order perturbation theory analysis of Fock matrix in NBO basis for HN0

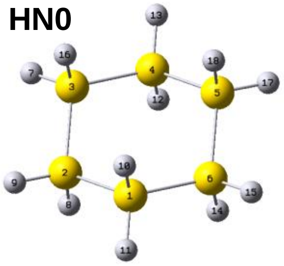

HN0

Donor (i)					type	Acceptor (j)						type	E(2)	E(j)-E(i)	F(i,j)
													kcal/mol	a.u.	a.u.
Si	1				CR(2)	130	H	10				RY*(1)	0.66	6.51	0.058
Si	1				CR(2)	131	H	11				RY*(1)	0.64	6.52	0.058
Si	2				CR(2)	128	H	8				RY*(1)	0.66	6.51	0.058
Si	2				CR(2)	129	H	9				RY*(1)	0.64	6.52	0.058
Si	3				CR(2)	127	H	7				RY*(1)	0.64	6.52	0.058
Si	3				CR(2)	136	H	16				RY*(1)	0.66	6.51	0.058
Si	4				CR(2)	132	H	12				RY*(1)	0.66	6.51	0.058
Si	4				CR(2)	133	H	13				RY*(1)	0.64	6.52	0.058
Si	5				CR(2)	137	H	17				RY*(1)	0.64	6.52	0.058
Si	5				CR(2)	138	H	18				RY*(1)	0.66	6.51	0.058
Si	6				CR(2)	134	H	14				RY*(1)	0.66	6.51	0.058
Si	6				CR(2)	135	H	15				RY*(1)	0.64	6.52	0.058
Si	1	-	Si	2	σ	50	Si	1	-	Si	6	σ*	0.94	0.57	0.021
Si	1	-	Si	2	σ	51	Si	1	-	H	10	σ*	0.93	0.68	0.022
Si	1	-	Si	2	σ	52	Si	1	-	H	11	σ*	1.01	0.68	0.023
Si	1	-	Si	2	σ	53	Si	2	-	Si	3	σ*	0.95	0.57	0.021
Si	1	-	Si	2	σ	54	Si	2	-	H	8	σ*	0.93	0.68	0.022
Si	1	-	Si	2	σ	55	Si	2	-	H	9	σ*	1.01	0.68	0.023
Si	1	-	Si	2	σ	57	Si	3	-	H	7	σ*	1.23	0.68	0.026
Si	1	-	Si	2	σ	66	Si	6	-	H	15	σ*	1.22	0.68	0.026
Si	1	-	Si	2	σ	117	Si	6	-			RY*(1)	0.50	1.02	0.02
Si	1	-	Si	6	σ	49	Si	1	-	Si	2	σ*	0.94	0.57	0.021
Si	1	-	Si	6	σ	51	Si	1	-	H	10	σ*	0.93	0.68	0.022
Si	1	-	Si	6	σ	52	Si	1	-	H	11	σ*	1.02	0.68	0.023
Si	1	-	Si	6	σ	55	Si	2	-	H	9	σ*	1.23	0.68	0.026
Si	1	-	Si	6	σ	62	Si	5	-	Si	6	σ*	0.95	0.57	0.021
Si	1	-	Si	6	σ	63	Si	5	-	H	17	σ*	1.23	0.68	0.026
Si	1	-	Si	6	σ	65	Si	6	-	H	14	σ*	0.93	0.68	0.022
Si	1	-	Si	6	σ	66	Si	6	-	H	15	σ*	1.02	0.68	0.023
Si	1	-	Si	6	σ	77	Si	2	-			RY*(1)	0.50	1.02	0.02
Si	1	-	H	10	σ	49	Si	1	-	Si	2	σ*	1.27	0.56	0.024
Si	1	-	H	10	σ	50	Si	1	-	Si	6	σ*	1.27	0.56	0.024
Si	1	-	H	10	σ	52	Si	1	-	H	11	σ*	1.34	0.67	0.027
Si	1	-	H	10	σ	54	Si	2	-	H	8	σ*	1.18	0.67	0.025
Si	1	-	H	10	σ	65	Si	6	-	H	14	σ*	1.18	0.67	0.025
Si	1	-	H	11	σ	49	Si	1	-	Si	2	σ*	1.07	0.56	0.022
Si	1	-	H	11	σ	50	Si	1	-	Si	6	σ*	1.08	0.56	0.022
Si	1	-	H	11	σ	51	Si	1	-	H	10	σ*	1.37	0.67	0.027
Si	1	-	H	11	σ	53	Si	2	-	Si	3	σ*	1.16	0.56	0.023
Si	1	-	H	11	σ	62	Si	5	-	Si	6	σ*	1.16	0.56	0.023
Si	2	-	Si	3	σ	49	Si	1	-	Si	2	σ*	0.95	0.57	0.021
Si	2	-	Si	3	σ	52	Si	1	-	H	11	σ*	1.22	0.68	0.026
Si	2	-	Si	3	σ	54	Si	2	-	H	8	σ*	0.93	0.68	0.022
Si	2	-	Si	3	σ	55	Si	2	-	H	9	σ*	1.00	0.68	0.023
Si	2	-	Si	3	σ	56	Si	3	-	Si	4	σ*	0.95	0.57	0.021
Si	2	-	Si	3	σ	57	Si	3	-	H	7	σ*	1.00	0.68	0.023
Si	2	-	Si	3	σ	58	Si	3	-	H	16	σ*	0.93	0.68	0.022
Si	2	-	Si	3	σ	61	Si	4	-	H	13	σ*	1.21	0.68	0.026
Si	2	-	H	8	σ	49	Si	1	-	Si	2	σ*	1.27	0.56	0.024

Si	2	-	H	8	σ	51	Si	1	-	H	10	σ*	1.19	0.67	0.025
Si	2	-	H	8	σ	53	Si	2	-	Si	3	σ*	1.27	0.56	0.024
Si	2	-	H	8	σ	55	Si	2	-	H	9	σ*	1.34	0.67	0.027
Si	2	-	H	8	σ	58	Si	3	-	H	16	σ*	1.19	0.67	0.025
Si	2	-	H	9	σ	49	Si	1	-	Si	2	σ*	1.07	0.56	0.022
Si	2	-	H	9	σ	50	Si	1	-	Si	6	σ*	1.16	0.56	0.023
Si	2	-	H	9	σ	53	Si	2	-	Si	3	σ*	1.07	0.56	0.022
Si	2	-	H	9	σ	54	Si	2	-	H	8	σ*	1.37	0.67	0.027
Si	2	-	H	9	σ	56	Si	3	-	Si	4	σ*	1.16	0.56	0.023
Si	3	-	Si	4	σ	53	Si	2	-	Si	3	σ*	0.95	0.57	0.021
Si	3	-	Si	4	σ	55	Si	2	-	H	9	σ*	1.23	0.68	0.026
Si	3	-	Si	4	σ	57	Si	3	-	H	7	σ*	1.02	0.68	0.023
Si	3	-	Si	4	σ	58	Si	3	-	H	16	σ*	0.93	0.68	0.022
Si	3	-	Si	4	σ	59	Si	4	-	Si	5	σ*	0.94	0.57	0.021
Si	3	-	Si	4	σ	60	Si	4	-	H	12	σ*	0.93	0.68	0.022
Si	3	-	Si	4	σ	61	Si	4	-	H	13	σ*	1.02	0.68	0.023
Si	3	-	Si	4	σ	63	Si	5	-	H	17	σ*	1.23	0.68	0.026
Si	3	-	Si	4	σ	107	Si	5	-			RY*(1)	0.50	1.02	0.02
Si	3	-	H	7	σ	49	Si	1	-	Si	2	σ*	1.16	0.56	0.023
Si	3	-	H	7	σ	53	Si	2	-	Si	3	σ*	1.07	0.56	0.022
Si	3	-	H	7	σ	56	Si	3	-	Si	4	σ*	1.08	0.56	0.022
Si	3	-	H	7	σ	58	Si	3	-	H	16	σ*	1.37	0.67	0.027
Si	3	-	H	7	σ	59	Si	4	-	Si	5	σ*	1.16	0.56	0.023
Si	3	-	H	16	σ	53	Si	2	-	Si	3	σ*	1.27	0.56	0.024
Si	3	-	H	16	σ	54	Si	2	-	H	8	σ*	1.19	0.67	0.025
Si	3	-	H	16	σ	56	Si	3	-	Si	4	σ*	1.27	0.56	0.024
Si	3	-	H	16	σ	57	Si	3	-	H	7	σ*	1.34	0.67	0.027
Si	3	-	H	16	σ	60	Si	4	-	H	12	σ*	1.19	0.67	0.025
Si	4	-	Si	5	σ	56	Si	3	-	Si	4	σ*	0.94	0.57	0.021
Si	4	-	Si	5	σ	57	Si	3	-	H	7	σ*	1.22	0.68	0.026
Si	4	-	Si	5	σ	60	Si	4	-	H	12	σ*	0.93	0.68	0.022
Si	4	-	Si	5	σ	61	Si	4	-	H	13	σ*	1.01	0.68	0.023
Si	4	-	Si	5	σ	62	Si	5	-	Si	6	σ*	0.95	0.57	0.021
Si	4	-	Si	5	σ	63	Si	5	-	H	17	σ*	1.01	0.68	0.023
Si	4	-	Si	5	σ	64	Si	5	-	H	18	σ*	0.93	0.68	0.022
Si	4	-	Si	5	σ	66	Si	6	-	H	15	σ*	1.23	0.68	0.026
Si	4	-	Si	5	σ	87	Si	3	-			RY*(1)	0.50	1.02	0.02
Si	4	-	H	12	σ	56	Si	3	-	Si	4	σ*	1.27	0.56	0.024
Si	4	-	H	12	σ	58	Si	3	-	H	16	σ*	1.18	0.67	0.025
Si	4	-	H	12	σ	59	Si	4	-	Si	5	σ*	1.27	0.56	0.024
Si	4	-	H	12	σ	61	Si	4	-	H	13	σ*	1.34	0.67	0.027
Si	4	-	H	12	σ	64	Si	5	-	H	18	σ*	1.18	0.67	0.025
Si	4	-	H	13	σ	53	Si	2	-	Si	3	σ*	1.16	0.56	0.023
Si	4	-	H	13	σ	56	Si	3	-	Si	4	σ*	1.07	0.56	0.022
Si	4	-	H	13	σ	59	Si	4	-	Si	5	σ*	1.07	0.56	0.022
Si	4	-	H	13	σ	60	Si	4	-	H	12	σ*	1.37	0.67	0.027
Si	4	-	H	13	σ	62	Si	5	-	Si	6	σ*	1.16	0.56	0.023
Si	5	-	Si	6	σ	50	Si	1	-	Si	6	σ*	0.95	0.57	0.021
Si	5	-	Si	6	σ	52	Si	1	-	H	11	σ*	1.21	0.68	0.026
Si	5	-	Si	6	σ	59	Si	4	-	Si	5	σ*	0.95	0.57	0.021
Si	5	-	Si	6	σ	61	Si	4	-	H	13	σ*	1.22	0.68	0.026
Si	5	-	Si	6	σ	63	Si	5	-	H	17	σ*	1.00	0.68	0.023
Si	5	-	Si	6	σ	64	Si	5	-	H	18	σ*	0.93	0.68	0.022
Si	5	-	Si	6	σ	65	Si	6	-	H	14	σ*	0.93	0.68	0.022
Si	5	-	Si	6	σ	66	Si	6	-	H	15	σ*	1.01	0.68	0.023
Si	5	-	H	17	σ	50	Si	1	-	Si	6	σ*	1.16	0.56	0.023
Si	5	-	H	17	σ	56	Si	3	-	Si	4	σ*	1.16	0.56	0.023
Si	5	-	H	17	σ	59	Si	4	-	Si	5	σ*	1.07	0.56	0.022
Si	5	-	H	17	σ	62	Si	5	-	Si	6	σ*	1.07	0.56	0.022
Si	5	-	H	17	σ	64	Si	5	-	H	18	σ*	1.37	0.67	0.027
Si	5	-	H	18	σ	59	Si	4	-	Si	5	σ*	1.27	0.56	0.024
Si	5	-	H	18	σ	60	Si	4	-	H	12	σ*	1.19	0.67	0.025
Si	5	-	H	18	σ	62	Si	5	-	Si	6	σ*	1.27	0.56	0.024
Si	5	-	H	18	σ	63	Si	5	-	H	17	σ*	1.34	0.67	0.027
Si	5	-	H	18	σ	65	Si	6	-	H	14	σ*	1.19	0.67	0.025
Si	6	-	H	14	σ	50	Si	1	-	Si	6	σ*	1.27	0.56	0.024

Si	6	-	H	14	σ	51	Si	1	-	H	10	σ*	1.19	0.67	0.025
Si	6	-	H	14	σ	62	Si	5	-	Si	6	σ*	1.27	0.56	0.024
Si	6	-	H	14	σ	64	Si	5	-	H	18	σ*	1.19	0.67	0.025
Si	6	-	H	14	σ	66	Si	6	-	H	15	σ*	1.34	0.67	0.027
Si	6	-	H	15	σ	49	Si	1	-	Si	2	σ*	1.16	0.56	0.023
Si	6	-	H	15	σ	50	Si	1	-	Si	6	σ*	1.08	0.56	0.022
Si	6	-	H	15	σ	59	Si	4	-	Si	5	σ*	1.16	0.56	0.023
Si	6	-	H	15	σ	62	Si	5	-	Si	6	σ*	1.07	0.56	0.022
i	6	-	H	15	σ	65	Si	6	-	H	14	σ*	1.37	0.67	0.027

f) Second order perturbation theory analysis of Fock matrix in NBO basis for HN1

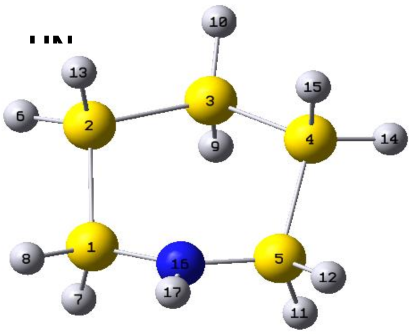

HN1

Donor (i)		type	Acceptor (j)						type	E(2)	E(j)-E(i)	F(i,j)
										kcal/mol	a.u.	a.u.
Si	1	CR(2)	48	Si	1	-	N	16	σ*	1.2	5.96	0.075
Si	1	CR(2)	60	Si	5	-	N	16	σ*	2.79	5.96	0.115
Si	1	CR(2)	61	N	16	-	H	17	σ*	0.62	6.21	0.055
Si	1	CR(2)	113	H	7				RY*(1)	0.57	6.65	0.055
Si	1	CR(2)	114	H	8				RY*(1)	0.55	6.65	0.054
Si	2	CR(2)	45	Si	1	-	Si	2	σ*	0.56	5.73	0.051
Si	2	CR(2)	112	H	6				RY*(1)	0.65	6.5	0.058
Si	2	CR(2)	119	H	13				RY*(1)	0.67	6.5	0.059
Si	3	CR(2)	115	H	9				RY*(1)	0.66	6.5	0.058
Si	3	CR(2)	116	H	10				RY*(1)	0.65	6.5	0.058
Si	4	CR(2)	55	Si	4	-	Si	5	σ*	0.56	5.73	0.051
Si	4	CR(2)	120	H	14				RY*(1)	0.65	6.5	0.058
Si	4	CR(2)	121	H	15				RY*(1)	0.67	6.5	0.059
Si	5	CR(2)	48	Si	1	-	N	16	σ*	2.79	5.96	0.115
Si	5	CR(2)	60	Si	5	-	N	16	σ*	1.2	5.96	0.075
Si	5	CR(2)	61	N	16	-	H	17	σ*	0.62	6.21	0.055
Si	5	CR(2)	117	H	11				RY*(1)	0.57	6.65	0.055

Si	5				CR(2)	118	H	12				RY*(1)	0.55	6.65	0.054
N	16				LP(1)	45	Si	1	-	Si	2	σ*	3.66	0.4	0.034
N	16				LP(1)	46	Si	1	-	H	7	σ*	8.38	0.51	0.059
N	16				LP(1)	55	Si	4	-	Si	5	σ*	3.67	0.4	0.034
N	16				LP(1)	58	Si	5	-	H	11	σ*	8.38	0.51	0.059
N	16				LP(1)	62	Si	1				RY*(1)	3.01	0.9	0.046
N	16				LP(1)	67	Si	1				RY*(6)	0.96	0.73	0.024
N	16				LP(1)	102	Si	5				RY*(1)	3.01	0.9	0.046
N	16				LP(1)	107	Si	5				RY*(6)	0.96	0.73	0.024
Si	1	-	Si	2	σ	46	Si	1	-	H	7	σ*	1.82	0.69	0.032
Si	1	-	Si	2	σ	47	Si	1	-	H	8	σ*	1.37	0.69	0.027
Si	1	-	Si	2	σ	48	Si	1	-	N	16	σ*	1.21	0.64	0.025
Si	1	-	Si	2	σ	49	Si	2	-	Si	3	σ*	0.87	0.57	0.020
Si	1	-	Si	2	σ	50	Si	2	-	H	6	σ*	0.96	0.68	0.023
Si	1	-	Si	2	σ	51	Si	2	-	H	13	σ*	1.04	0.68	0.024
Si	1	-	Si	2	σ	54	Si	3	-	H	10	σ*	1.59	0.68	0.029
Si	1	-	Si	2	σ	60	Si	5	-	N	16	σ*	0.76	0.64	0.020
Si	1	-	Si	2	σ	61	N	16	-	H	17	σ*	0.89	0.9	0.025
Si	1	-	H	7	σ	45	Si	1	-	Si	2	σ*	2.23	0.56	0.032
Si	1	-	H	7	σ	47	Si	1	-	H	8	σ*	1.91	0.68	0.032
Si	1	-	H	7	σ	48	Si	1	-	N	16	σ*	1.74	0.63	0.030
Si	1	-	H	7	σ	51	Si	2	-	H	13	σ*	1.24	0.66	0.026
Si	1	-	H	7	σ	60	Si	5	-	N	16	σ*	0.74	0.63	0.019
Si	1	-	H	8	σ	45	Si	1	-	Si	2	σ*	1.37	0.57	0.025
Si	1	-	H	8	σ	46	Si	1	-	H	7	σ*	2.13	0.68	0.034
Si	1	-	H	8	σ	48	Si	1	-	N	16	σ*	1.45	0.64	0.027
Si	1	-	H	8	σ	49	Si	2	-	Si	3	σ*	1.08	0.56	0.022
Si	1	-	H	8	σ	60	Si	5	-	N	16	σ*	2.09	0.64	0.033
Si	1	-	N	16	σ	45	Si	1	-	Si	2	σ*	1.37	0.79	0.029
Si	1	-	N	16	σ	46	Si	1	-	H	7	σ*	1.8	0.91	0.036
Si	1	-	N	16	σ	47	Si	1	-	H	8	σ*	1.87	0.91	0.037
Si	1	-	N	16	σ	50	Si	2	-	H	6	σ*	0.52	0.89	0.019
Si	1	-	N	16	σ	60	Si	5	-	N	16	σ*	1.44	0.86	0.031
Si	1	-	N	16	σ	61	N	16	-	H	17	σ*	1.05	1.12	0.031
Si	2	-	Si	3	σ	45	Si	1	-	Si	2	σ*	1.08	0.58	0.022
Si	2	-	Si	3	σ	47	Si	1	-	H	8	σ*	0.96	0.69	0.023
Si	2	-	Si	3	σ	50	Si	2	-	H	6	σ*	0.98	0.68	0.023
Si	2	-	Si	3	σ	51	Si	2	-	H	13	σ*	0.88	0.68	0.022
Si	2	-	Si	3	σ	52	Si	3	-	Si	4	σ*	0.91	0.57	0.020
Si	2	-	Si	3	σ	53	Si	3	-	H	9	σ*	0.92	0.68	0.022
Si	2	-	Si	3	σ	54	Si	3	-	H	10	σ*	0.98	0.68	0.023
Si	2	-	Si	3	σ	56	Si	4	-	H	14	σ*	1.46	0.68	0.028
Si	2	-	Si	3	σ	92	Si	4				RY*(1)	0.55	0.99	0.021
Si	2	-	H	6	σ	45	Si	1	-	Si	2	σ*	1.51	0.57	0.026
Si	2	-	H	6	σ	48	Si	1	-	N	16	σ*	1.28	0.64	0.026
Si	2	-	H	6	σ	49	Si	2	-	Si	3	σ*	1.04	0.56	0.022
Si	2	-	H	6	σ	51	Si	2	-	H	13	σ*	1.38	0.67	0.027
Si	2	-	H	6	σ	52	Si	3	-	Si	4	σ*	0.97	0.56	0.021
Si	2	-	H	13	σ	45	Si	1	-	Si	2	σ*	1.26	0.57	0.024
Si	2	-	H	13	σ	46	Si	1	-	H	7	σ*	0.88	0.68	0.022
Si	2	-	H	13	σ	49	Si	2	-	Si	3	σ*	1.19	0.56	0.023
Si	2	-	H	13	σ	50	Si	2	-	H	6	σ*	1.42	0.67	0.028
Si	2	-	H	13	σ	53	Si	3	-	H	9	σ*	1.18	0.66	0.025
Si	3	-	Si	4	σ	49	Si	2	-	Si	3	σ*	0.91	0.57	0.020
Si	3	-	Si	4	σ	50	Si	2	-	H	6	σ*	1.46	0.68	0.028
Si	3	-	Si	4	σ	53	Si	3	-	H	9	σ*	0.92	0.68	0.022
Si	3	-	Si	4	σ	54	Si	3	-	H	10	σ*	0.98	0.68	0.023

Si	3	-	Si	4	σ	55	Si	4	-	Si	5	σ*	1.08	0.58	0.022
Si	3	-	Si	4	σ	56	Si	4	-	H	14	σ*	0.98	0.68	0.023
Si	3	-	Si	4	σ	57	Si	4	-	H	15	σ*	0.88	0.68	0.022
Si	3	-	Si	4	σ	59	Si	5	-	H	12	σ*	0.96	0.69	0.023
Si	3	-	Si	4	σ	72	Si	2				RY*(1)	0.55	0.99	0.021
Si	3	-	H	9	σ	49	Si	2	-	Si	3	σ*	1.22	0.56	0.023
Si	3	-	H	9	σ	51	Si	2	-	H	13	σ*	1.16	0.67	0.025
Si	3	-	H	9	σ	52	Si	3	-	Si	4	σ*	1.22	0.56	0.023
Si	3	-	H	9	σ	54	Si	3	-	H	10	σ*	1.47	0.67	0.028
Si	3	-	H	9	σ	57	Si	4	-	H	15	σ*	1.16	0.67	0.025
Si	3	-	H	10	σ	45	Si	1	-	Si	2	σ*	0.93	0.57	0.021
Si	3	-	H	10	σ	49	Si	2	-	Si	3	σ*	1.11	0.56	0.022
Si	3	-	H	10	σ	52	Si	3	-	Si	4	σ*	1.11	0.56	0.022
Si	3	-	H	10	σ	53	Si	3	-	H	9	σ*	1.41	0.67	0.027
Si	3	-	H	10	σ	55	Si	4	-	Si	5	σ*	0.93	0.57	0.021
Si	4	-	Si	5	σ	48	Si	1	-	N	16	σ*	0.76	0.64	0.020
Si	4	-	Si	5	σ	52	Si	3	-	Si	4	σ*	0.87	0.57	0.020
Si	4	-	Si	5	σ	54	Si	3	-	H	10	σ*	1.59	0.68	0.029
Si	4	-	Si	5	σ	56	Si	4	-	H	14	σ*	0.96	0.68	0.023
Si	4	-	Si	5	σ	57	Si	4	-	H	15	σ*	1.04	0.68	0.024
Si	4	-	Si	5	σ	58	Si	5	-	H	11	σ*	1.82	0.69	0.032
Si	4	-	Si	5	σ	59	Si	5	-	H	12	σ*	1.37	0.69	0.027
Si	4	-	Si	5	σ	60	Si	5	-	N	16	σ*	1.21	0.64	0.025
Si	4	-	Si	5	σ	61	N	16	-	H	17	σ*	0.89	0.9	0.025
Si	4	-	H	14	σ	49	Si	2	-	Si	3	σ*	0.97	0.56	0.021
Si	4	-	H	14	σ	52	Si	3	-	Si	4	σ*	1.04	0.56	0.022
Si	4	-	H	14	σ	55	Si	4	-	Si	5	σ*	1.51	0.57	0.026
Si	4	-	H	14	σ	57	Si	4	-	H	15	σ*	1.38	0.67	0.027
Si	4	-	H	14	σ	60	Si	5	-	N	16	σ*	1.28	0.64	0.026
Si	4	-	H	15	σ	52	Si	3	-	Si	4	σ*	1.19	0.56	0.023
Si	4	-	H	15	σ	53	Si	3	-	H	9	σ*	1.18	0.66	0.025
Si	4	-	H	15	σ	55	Si	4	-	Si	5	σ*	1.26	0.57	0.024
Si	4	-	H	15	σ	56	Si	4	-	H	14	σ*	1.43	0.67	0.028
Si	4	-	H	15	σ	58	Si	5	-	H	11	σ*	0.88	0.68	0.022
Si	5	-	H	11	σ	48	Si	1	-	N	16	σ*	0.74	0.63	0.019
Si	5	-	H	11	σ	55	Si	4	-	Si	5	σ*	2.23	0.56	0.032
Si	5	-	H	11	σ	57	Si	4	-	H	15	σ*	1.24	0.66	0.026
Si	5	-	H	11	σ	59	Si	5	-	H	12	σ*	1.91	0.68	0.032
Si	5	-	H	11	σ	60	Si	5	-	N	16	σ*	1.74	0.63	0.030
Si	5	-	H	12	σ	48	Si	1	-	N	16	σ*	2.09	0.64	0.033
Si	5	-	H	12	σ	52	Si	3	-	Si	4	σ*	1.08	0.56	0.022
Si	5	-	H	12	σ	55	Si	4	-	Si	5	σ*	1.37	0.57	0.025
Si	5	-	H	12	σ	58	Si	5	-	H	11	σ*	2.13	0.68	0.034
Si	5	-	H	12	σ	60	Si	5	-	N	16	σ*	1.45	0.64	0.027
Si	5	-	N	16	σ	48	Si	1	-	N	16	σ*	1.44	0.86	0.031
Si	5	-	N	16	σ	55	Si	4	-	Si	5	σ*	1.37	0.79	0.029
Si	5	-	N	16	σ	56	Si	4	-	H	14	σ*	0.52	0.89	0.019
Si	5	-	N	16	σ	58	Si	5	-	H	11	σ*	1.8	0.91	0.036
Si	5	-	N	16	σ	59	Si	5	-	H	12	σ*	1.87	0.91	0.037
Si	5	-	N	16	σ	61	N	16	-	H	17	σ*	1.05	1.12	0.031
N	16	-	H	17	σ	45	Si	1	-	Si	2	σ*	0.74	0.77	0.021
N	16	-	H	17	σ	47	Si	1	-	H	8	σ*	0.99	0.89	0.026
N	16	-	H	17	σ	48	Si	1	-	N	16	σ*	0.54	0.84	0.019
N	16	-	H	17	σ	55	Si	4	-	Si	5	σ*	0.73	0.77	0.021
N	16	-	H	17	σ	59	Si	5	-	H	12	σ*	0.99	0.89	0.026
N	16	-	H	17	σ	60	Si	5	-	N	16	σ*	0.54	0.84	0.019

g) Second order perturbation theory analysis of Fock matrix in NBO basis for HN3

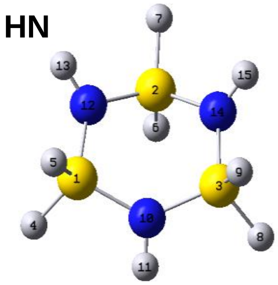

HN3

Donor (i)		type	Acceptor (j)						type	E(2) kcal/mol	E(j)-E(i) a.u.	F(i,j) a.u.
Si	1	CR(2)	39	Si	1	-	N	10	σ*	0.9	6.12	0.066
Si	1	CR(2)	40	Si	1	-	N	12	σ*	0.92	6.12	0.067
Si	1	CR(2)	43	Si	2	-	N	12	σ*	2.5	6.12	0.110
Si	1	CR(2)	47	Si	3	-	N	10	σ*	2.52	6.12	0.111
Si	1	CR(2)	49	N	10	-	H	11	σ*	0.7	6.35	0.059
Si	1	CR(2)	50	N	12	-	H	13	σ*	0.91	6.36	0.068
Si	1	CR(2)	82	H	4	-			RY*(1)	0.5	6.77	0.052
Si	1	CR(2)	83	H	5	-			RY*(1)	0.51	6.77	0.052
Si	2	CR(2)	40	Si	1	-	N	12	σ*	2.49	6.12	0.110
Si	2	CR(2)	43	Si	2	-	N	12	σ*	1.08	6.11	0.072
Si	2	CR(2)	44	Si	2	-	N	14	σ*	1.08	6.11	0.072
Si	2	CR(2)	48	Si	3	-	N	14	σ*	2.49	6.12	0.110
Si	2	CR(2)	50	N	12	-	H	13	σ*	0.84	6.35	0.065
Si	2	CR(2)	51	N	14	-	H	15	σ*	0.84	6.35	0.065
Si	2	CR(2)	84	H	6	-			RY*(1)	0.55	6.77	0.054
Si	3	CR(2)	39	Si	1	-	N	10	σ*	2.52	6.12	0.111
Si	3	CR(2)	44	Si	2	-	N	14	σ*	2.5	6.12	0.110
Si	3	CR(2)	47	Si	3	-	N	10	σ*	0.9	6.12	0.066
Si	3	CR(2)	48	Si	3	-	N	14	σ*	0.93	6.12	0.067
Si	3	CR(2)	49	N	10	-	H	11	σ*	0.7	6.35	0.059
Si	3	CR(2)	51	N	14	-	H	15	σ*	0.91	6.36	0.068
Si	3	CR(2)	86	H	8	-			RY*(1)	0.5	6.77	0.052
Si	3	CR(2)	87	H	9	-			RY*(1)	0.51	6.77	0.052
N	10	LP(1)	37	Si	1	-	H	4	σ*	0.87	0.53	0.019
N	10	LP(1)	38	Si	1	-	H	5	σ*	7.61	0.53	0.057
N	10	LP(1)	40	Si	1	-	N	12	σ*	5.31	0.5	0.046
N	10	LP(1)	42	Si	2	-	H	7	σ*	0.7	0.53	0.017
N	10	LP(1)	45	Si	3	-	H	8	σ*	0.87	0.53	0.019
N	10	LP(1)	46	Si	3	-	H	9	σ*	7.61	0.53	0.057
N	10	LP(1)	48	Si	3	-	N	14	σ*	5.31	0.5	0.046
N	10	LP(1)	52	Si	1	-			RY*(1)	0.91	0.97	0.026
N	10	LP(1)	53	Si	1	-			RY*(2)	1.97	1.02	0.040
N	10	LP(1)	58	Si	1	-			RY*(7)	0.78	0.77	0.022
N	10	LP(1)	72	Si	3	-			RY*(1)	0.91	0.97	0.027
N	10	LP(1)	73	Si	3	-			RY*(2)	1.97	1.02	0.040
N	10	LP(1)	78	Si	3	-			RY*(7)	0.78	0.77	0.022
N	12	LP(1)	37	Si	1	-	H	4	σ*	7.83	0.53	0.057
N	12	LP(1)	38	Si	1	-	H	5	σ*	3.16	0.53	0.036
N	12	LP(1)	39	Si	1	-	N	10	σ*	1.75	0.49	0.026
N	12	LP(1)	41	Si	2	-	H	6	σ*	5.46	0.54	0.048
N	12	LP(1)	44	Si	2	-	N	14	σ*	8.27	0.49	0.057
N	12	LP(1)	52	Si	1	-			RY*(1)	1.59	0.97	0.035
N	12	LP(1)	53	Si	1	-			RY*(2)	1.74	1.02	0.038
N	12	LP(1)	62	Si	2	-			RY*(1)	1.71	0.97	0.036
N	12	LP(1)	63	Si	2	-			RY*(2)	0.63	1.01	0.023
N	12	LP(1)	68	Si	2	-			RY*(7)	0.8	0.67	0.021
N	14	LP(1)	41	Si	2	-	H	6	σ*	5.45	0.54	0.048
N	14	LP(1)	43	Si	2	-	N	12	σ*	8.29	0.49	0.057
N	14	LP(1)	45	Si	3	-	H	8	σ*	7.83	0.53	0.057

N	14				LP(1)	46	Si	3	-	H	9	σ*	3.15	0.53	0.036
N	14				LP(1)	47	Si	3	-	N	10	σ*	1.76	0.49	0.026
N	14				LP(1)	62	Si	2	-			RY*(1)	1.71	0.97	0.036
N	14				LP(1)	63	Si	2	-			RY*(2)	0.63	1.01	0.023
N	14				LP(1)	68	Si	2	-			RY*(7)	0.8	0.67	0.021
N	14				LP(1)	72	Si	3	-			RY*(1)	1.58	0.97	0.035
N	14				LP(1)	73	Si	3	-			RY*(2)	1.74	1.02	0.038
Si	1	-	H	4	σ	38	Si	1	-	H	5	σ*	3.32	0.7	0.043
Si	1	-	H	4	σ	39	Si	1	-	N	10	σ*	1.74	0.66	0.030
Si	1	-	H	4	σ	40	Si	1	-	N	12	σ*	1.6	0.67	0.029
Si	1	-	H	4	σ	43	Si	2	-	N	12	σ*	0.86	0.66	0.021
Si	1	-	H	4	σ	47	Si	3	-	N	10	σ*	2	0.66	0.032
Si	1	-	H	5	σ	37	Si	1	-	H	4	σ*	3.19	0.7	0.042
Si	1	-	H	5	σ	39	Si	1	-	N	10	σ*	1.77	0.66	0.031
Si	1	-	H	5	σ	40	Si	1	-	N	12	σ*	2.11	0.67	0.034
Si	1	-	H	5	σ	43	Si	2	-	N	12	σ*	1.53	0.66	0.028
Si	1	-	H	5	σ	47	Si	3	-	N	10	σ*	0.63	0.66	0.018
Si	1	-	N	10	σ	37	Si	1	-	H	4	σ*	2.61	0.93	0.044
Si	1	-	N	10	σ	38	Si	1	-	H	5	σ*	1.61	0.92	0.034
Si	1	-	N	10	σ	40	Si	1	-	N	12	σ*	2.08	0.89	0.038
Si	1	-	N	10	σ	43	Si	2	-	N	12	σ*	0.56	0.89	0.020
Si	1	-	N	10	σ	47	Si	3	-	N	10	σ*	1.26	0.89	0.030
Si	1	-	N	10	σ	48	Si	3	-	N	14	σ*	0.58	0.89	0.020
Si	1	-	N	10	σ	49	N	10	-	H	11	σ*	1.11	1.12	0.031
Si	1	-	N	10	σ	50	N	12	-	H	13	σ*	0.73	1.13	0.026
Si	1	-	N	12	σ	37	Si	1	-	H	4	σ*	1.57	0.92	0.034
Si	1	-	N	12	σ	38	Si	1	-	H	5	σ*	2.78	0.92	0.045
Si	1	-	N	12	σ	39	Si	1	-	N	10	σ*	1.99	0.88	0.037
Si	1	-	N	12	σ	42	Si	2	-	H	7	σ*	0.66	0.92	0.022
Si	1	-	N	12	σ	43	Si	2	-	N	12	σ*	1.27	0.88	0.030
Si	1	-	N	12	σ	50	N	12	-	H	13	σ*	1.12	1.12	0.032
Si	2	-	H	6	σ	40	Si	1	-	N	12	σ*	0.78	0.67	0.020
Si	2	-	H	6	σ	42	Si	2	-	H	7	σ*	2.47	0.7	0.037
Si	2	-	H	6	σ	43	Si	2	-	N	12	σ*	2.17	0.66	0.034
Si	2	-	H	6	σ	44	Si	2	-	N	14	σ*	2.17	0.66	0.034
Si	2	-	H	6	σ	48	Si	3	-	N	14	σ*	0.78	0.66	0.020
Si	2	-	H	6	σ	50	N	12	-	H	13	σ*	0.71	0.9	0.022
Si	2	-	H	6	σ	51	N	14	-	H	15	σ*	0.71	0.9	0.023
Si	2	-	H	7	σ	40	Si	1	-	N	12	σ*	1.76	0.67	0.031
Si	2	-	H	7	σ	41	Si	2	-	H	6	σ*	2.62	0.71	0.039
Si	2	-	H	7	σ	43	Si	2	-	N	12	σ*	2.01	0.67	0.033
Si	2	-	H	7	σ	44	Si	2	-	N	14	σ*	2.01	0.67	0.033
Si	2	-	H	7	σ	48	Si	3	-	N	14	σ*	1.76	0.67	0.031
Si	2	-	N	12	σ	39	Si	1	-	N	10	σ*	1.5	0.88	0.032
Si	2	-	N	12	σ	40	Si	1	-	N	12	σ*	1.51	0.89	0.033
Si	2	-	N	12	σ	41	Si	2	-	H	6	σ*	2.62	0.93	0.044
Si	2	-	N	12	σ	42	Si	2	-	H	7	σ*	2.03	0.92	0.039
Si	2	-	N	12	σ	43	Si	2	-	N	12	σ*	0.54	0.88	0.019
Si	2	-	N	12	σ	44	Si	2	-	N	14	σ*	1.84	0.88	0.036
Si	2	-	N	12	σ	50	N	12	-	H	13	σ*	1.01	1.12	0.030
Si	2	-	N	14	σ	41	Si	2	-	H	6	σ*	2.62	0.93	0.044
Si	2	-	N	14	σ	42	Si	2	-	H	7	σ*	2.03	0.92	0.039
Si	2	-	N	14	σ	43	Si	2	-	N	12	σ*	1.84	0.88	0.036
Si	2	-	N	14	σ	44	Si	2	-	N	14	σ*	0.54	0.88	0.019
Si	2	-	N	14	σ	47	Si	3	-	N	10	σ*	1.5	0.88	0.032
Si	2	-	N	14	σ	48	Si	3	-	N	14	σ*	1.51	0.89	0.033
Si	2	-	N	14	σ	51	N	14	-	H	15	σ*	1.01	1.12	0.030
Si	3	-	H	8	σ	39	Si	1	-	N	10	σ*	2	0.66	0.032
Si	3	-	H	8	σ	44	Si	2	-	N	14	σ*	0.86	0.66	0.021
Si	3	-	H	8	σ	46	Si	3	-	H	9	σ*	3.31	0.7	0.043
Si	3	-	H	8	σ	47	Si	3	-	N	10	σ*	1.74	0.66	0.030
Si	3	-	H	8	σ	48	Si	3	-	N	14	σ*	1.6	0.67	0.029
Si	3	-	H	9	σ	39	Si	1	-	N	10	σ*	0.63	0.66	0.018
Si	3	-	H	9	σ	44	Si	2	-	N	14	σ*	1.53	0.66	0.028
Si	3	-	H	9	σ	45	Si	3	-	H	8	σ*	3.19	0.7	0.042
Si	3	-	H	9	σ	47	Si	3	-	N	10	σ*	1.77	0.66	0.031
Si	3	-	H	9	σ	48	Si	3	-	N	14	σ*	2.11	0.67	0.034
Si	3	-	N	10	σ	39	Si	1	-	N	10	σ*	1.26	0.89	0.030
Si	3	-	N	10	σ	40	Si	1	-	N	12	σ*	0.58	0.89	0.020
Si	3	-	N	10	σ	44	Si	2	-	N	14	σ*	0.56	0.89	0.020

Si	3	-	N	10	σ	45	Si	3	-	H	8	σ*	2.61	0.93	0.044
Si	3	-	N	10	σ	46	Si	3	-	H	9	σ*	1.61	0.92	0.034
Si	3	-	N	10	σ	48	Si	3	-	N	14	σ*	2.08	0.89	0.038
Si	3	-	N	10	σ	49	N	10	-	H	11	σ*	1.11	1.12	0.031
Si	3	-	N	10	σ	51	N	14	-	H	15	σ*	0.73	1.13	0.026
Si	3	-	N	14	σ	42	Si	2	-	H	7	σ*	0.66	0.92	0.022
Si	3	-	N	14	σ	44	Si	2	-	N	14	σ*	1.27	0.88	0.030
Si	3	-	N	14	σ	45	Si	3	-	H	8	σ*	1.57	0.92	0.034
Si	3	-	N	14	σ	46	Si	3	-	H	9	σ*	2.78	0.92	0.045
Si	3	-	N	14	σ	47	Si	3	-	N	10	σ*	1.99	0.88	0.037
Si	3	-	N	14	σ	51	N	14	-	H	15	σ*	1.12	1.12	0.032
N	10	-	H	11	σ	37	Si	1	-	H	4	σ*	0.77	0.91	0.024
N	10	-	H	11	σ	45	Si	3	-	H	8	σ*	0.77	0.91	0.024
N	12	-	H	13	σ	39	Si	1	-	N	10	σ*	0.59	0.88	0.020
N	12	-	H	13	σ	42	Si	2	-	H	7	σ*	0.65	0.91	0.022
N	14	-	H	15	σ	42	Si	2	-	H	7	σ*	0.65	0.91	0.022
N	14	-	H	15	σ	47	Si	3	-	N	10	σ*	0.59	0.88	0.020